EXPERIMENTAL STUDY OF LOW PRESSURE HEAT TRANSFER ON TUBES AND WALL

Elsaye Abdulhafiz Elsaye

A Thesis Submitted for the Degree of Doctor of Philosophy

Heriot-Watt University

Institute of Mechanical, Process and Energy Engineering

School of Engineering and Physical Sciences

2017

ABSTRACT

Experimental data are reported for water boiling at 850, 450 and 50 mbar pressures on the shell-side of a model industrial boiler slice. The boiler test section was 1 m high, 0.75 m wide and contained 36 electrically heated tubes. The tubes were 28.5 mm in diameter and 98 mm long. The design of the boiler ensured that the tubes were submerged in a liquid pool. The height of the liquid pool could be varied. The pool height was set to approximately 0.8 m for the tests carried out at a pressure of 850 mbar, submerging the top of the tube bundle by about 200 mm. Two pool heights were used for the tests carried out at a pressure of 50 mbar, one at approximately 0.8 m and another at approximately 2 m. The later submerged the top of the tube bundle by about 1.6 m. The tube heat flux was varied from 10-65 kW/m^2 for the tests at pressures 50 mbar and was varied within the range 10-70 kW/m^2 for the test of 450 and 850 mbar. A near-symmetrical half of the tube bundle contained wall thermocouples. An additional 29 thermocouples were located throughout the liquid pool.

The liquid pool temperature was found to be reasonably uniform and controlled by the pressure at the free surface. This led to a small amount of sub-cooling at a pressure of 850 mbar, up to 3 K, and a significant amount of sub-cooling at a pressure of 50 mbar, up to 16 K for the smaller pool height and up to 31 K at the larger pool height. The reasonably uniform pool temperature suggests that the liquid re-circulates within it. Boiling is found to occur at all heat fluxes at a pressure of 450 and 850 mbar, with the measured heat-transfer coefficients shown to be in broad agreement with nucleate boiling correlations available in the open literature. However, it is also consistent with a flow boiling process involving natural convection and nucleation, where the convection is driven by variations in liquid temperature on the walls of the tubes. This natural convection relies on an interaction between the tubes that produces mass fluxes in the range 46-87 kg/m^{2}s, based on the approach area to the tube bundle. Boiling occurs only at the higher heat fluxes during the low level tests at a pressure of 50 mbar, with interactive natural convection being the dominant heat-transfer mechanism. The mass fluxes produced are in the range 28-70 kg/m^{2}s. Boiling also occurs only at the higher heat fluxes during the high level tests at a pressure of 50 mbar. However, the convective heat transfer was more compatible with little interaction between the tubes, although some evidence suggests that the evaporator oscillates between interaction and isolated tube behaviour.

Solids can come out of solution when some process fluids are evaporated. These solids can form beds of particles on the heated base of the evaporator vessel. The effect on base temperature of increasing the bed depth is experimentally investigated for water boiling at a pressure of 50 mbar absolute. The bed depth is varied from 0-32 mm using glass particles 500-600 μm in diameter. The evaporator used was a model industrial boiler slice. The tube heat flux was maintained at 65 kW/m^2 and the base heat flux varied within the range 0-45 kW/m^2. Out with the solid bed, the liquid temperature in the liquid pool is shown to be reasonably constant and close to the free surface saturation temperature. This indicates that fluid recirculation is taking place, with fluid flashing to the saturation temperature at the free surface before returning to the depths of the pool. The liquid temperature within to the solid bed is shown to be greater than that in the pool and to decrease with increasing base heat flux. The temperature of the base is shown to be subcooled in the absence of a solids bed. The presence of the bed induces boiling at most conditions, indicating that a strong convection current normally cools the base and that the base is insulated from this cooling by the bed. The bubbles formed within the bed increase in size with increasing bed depth and heat flux. Beneath the bed, the base temperatures decrease with increasing base heat flux and the base superheat increases with increasing bed depth until 16 mm, decreases at 24 mm and increase again at 32 mm.

DEDICATION

I remember when I was a lad, times were hard and things were difficult, but there's a silver linin' behind every cloud.

Dad, you were working to change our life, you did, and you were teaching us how to be a nice family, supporting each other to live a good life; and you managed.

Your dream was to see me as a doctor, as I promised you to do, I know you will be happy although you are not in this life.

Dad, I fulfil your dream, and promise to let you feel happy and a proud always.

Thanks dad.

ACKNOWLEDGEMENTS

First of all, I would like to thank Allah (God) for giving me health to continue my education.

No words sufficient to express my sincere gratitude to my supervisor Dr David A. McNeil for the great and continuous support of my Ph.D. study and related research, for his patience, motivation, and immense knowledge. His guidance helped me in all the time of research and writing of this thesis. I could not have imagined having a better advisor and mentor for my Ph.D. study.

My deep appreciation to all members of school of engineering and physical science who support me to complete this work spatially Dr Burnside B.M., Alistair, Richard, Kenny, Robert and Aftab Aziz.

I acknowledge the funding provided for this work by Sellafield Sites Ltd and the National Nuclear Laboratory.

Last but not the least, I would like to thank my family: my mum and to my brothers, sisters, my sons and daughters for supporting me spiritually throughout writing this thesis and my life in general. Also a great appreciation to my wife for her unconditional support and unlimited help,

ACADEMIC REGISTRY
Research Thesis Submission

Name:	ELSAYE ABDULHAFIZ ELSAYE		
School/PGI:	School of Engineering and Physical Sciences		
Version: *(i.e. First, Resubmission, Final)*	First	Degree Sought (Award and Subject area)	PhD Mechanical Engineering

Declaration

In accordance with the appropriate regulations I hereby submit my thesis and I declare that:

1) the thesis embodies the results of my own work and has been composed by myself
2) where appropriate, I have made acknowledgement of the work of others and have made reference to work carried out in collaboration with other persons
3) the thesis is the correct version of the thesis for submission and is the same version as any electronic versions submitted*.
4) my thesis for the award referred to, deposited in the Heriot-Watt University Library, should be made available for loan or photocopying and be available via the Institutional Repository, subject to such conditions as the Librarian may require.
5) I understand that as a student of the University I am required to abide by the Regulations of the University and to conform to its discipline.

* *Please note that it is the responsibility of the candidate to ensure that the correct version of the thesis is submitted.*

Signature of Candidate*:*		Date:	

Submission

Submitted By *(name in capitals):*	ELSAYE ABDULHAFIZ ELSAYE
Signature of Individual Submitting:	
Date Submitted:	

For Completion in the Student Service Centre (SSC)

Received in the SSC by *(name in capitals):*			
Method of Submission *(Handed in to SSC; posted through internal/external mail):*			
E-thesis Submitted (***mandatory for final theses***)			
Signature:		Date:	

TABLE OF CONTENTS

LIST OF TABLES

NOMENCLATURE

A	Area	m^2
a_l	Liquid thermal diffusivity	m^2/s
β	The thermal expansion coefficient	-
C_{sf}	Surface-fluid combinations	-
c_{pl}	Specific heat capacity at constant pressure	J/kg. K
cap	Capillary number	-
D	The outside diameter of a tube	m
d_{bub}	Bubble diameter	m
g	Standard gravity	m/s^2
Gr	Grashof number	-
H	The depth of the tube centre line from the free surface	m
h	Heat transfer coefficient	$W/m^2.K$
h_b	Bundle heat transfer coefficient	$W/m^2.K$
h_{fg}	The enthalpy of evaporation	J/kg
h_{nb}	Nucleate boiling heat transfer coefficient	$W/m^2.K$
h_{nc}	Natural convection heat transfer coefficient	$W/m^2.K$
Fl	Single phase friction factor	-
F_{fi}	Flow inclination correction factor	-
F_{pr}	A non-dimensional pressure correction factor	-
F_r	Froude number	-
F_{RC}	Surface roughness correction factor	-
F_v	Viscosity correction factor	-
j_g^*	Gas phase superficial velocity	-
Kb	Thermal conductivity of brass	W/m °C
k_l	The liquid thermal conductivity	W/m °C
L_{tc}	Depth of the thermocouple from the tube surface	m
m	Mass flux	$kg/s.m^2$
M	Molecular weights	g/mole
N_R	Number of tubes	-
Nu	Nusselt number	-
p	Local pressure	bar
P_{crit}	Critical pressure	bar

Pe	Pelclet number	-
p_h	Horizontal tube pitch	m
$P_{LC\ ref}$	Reference pressure loss coefficient	
p_{pool}	The measured pool pressure	bar
Pr	Prandtle number	-
P_r	Reduced pressure	-
P_s	The measured shell pressure	bar
p_v	Vertical tube pitch	m
q	Heat flux	W/m^2
Q	Heat flow	W
Ra	Rayleigh number	-
Re	Reynolds number	-
Ri	Richardson number	-
R_p	Surface roughness	m
S	Slip ratio	-
T_F	Fluid temperature	K
T_f	Film temperature	K
T_H	Heat transfer temperature	K
T_L	The liquid temperature	K
T_S	The stream temperature	K
T_{tc}	The measured wall temperature	K
T_{sat}	The saturation temperature	K
T_w	Wall temperature	K
u_g	Superficial vapour velocity	m/s
u_l	Superficial liquid velocity	m/s
X_{tt}	Martinelli parameter	-
x	Quality	-
μ_l	Dynamic Liquid viscosity	kg /m.s
ρ_g	Vapour density	kg/m^3
ρ_H	Homogeneous density	kg/m^3
ρ_l	Density of liquid	kg/m^3
ρ_{LB}	The bulk fluid liquid density	kg/m^3
ρ_{lw}	The liquid density at the wall temperature	kg/m^3
σ	Surface tension	N/m

ΔP_f	Frictional pressure drop	-
ΔP_l	Single phase pressure drop	-
ΔP_m	Momentum pressure drop	-
ΔP_{net}	Net pressure drop	-
ΔP_t	Total pressure drop	-
ΔP_s	Static pressure drop	-
$\triangle T_{sub}$	Liquid sub-cooling	K
$\triangle T_{sup}$	Wall superheat	K
ϵ	Void fraction	-
ϵ_H	Homogeneous void fraction	-
Φ_L^2	Two-phase friction multiplier	-

LIST OF FIGURES

LIST OF PUBLICATIONS

ELSAYE E.A., MCNEIL D.A., BURNSIDE B.M., RYLATT D.I., & BAKER *S,* 2015, An Experimental Study Of Solids Deposited On The Base Of A Heated Vessel At Low Pressure. *Journal of Applied Thermal Engineering, accepted.*

ELSAYE E.A., MCNEIL D.A., BURNSIDE B.M., RYLATT D.I., AND BAKER *S,* 2015, The Effect Of Solids On The Heated Base Of The Evaporator Vessel For Water Boiling At Sub-Atmospheric pressure*’14th UK Heat Transfer, Edinburgh. 7-8 Sept, 2015.*

MCNEIL, D. A., BURNSIDE, B., RYLATT, D., ELSAYE, E., BAKER, S. 2015. Shell Side Boiling Of Water At Sub-Atmospheric Pressures. *International Journal of Heat and Mass Transfer,* 85, 488-504.

MCNEIL, D. A., BURNSIDE, B., ELSAYE, E., SALEM, S M. 2015, Shell-Side boiling of a Glycerol-Water Mixture at Low Sub-Atmospheric Pressures. *Journal of Applied Thermal Engineering,* 115(2017)1438-1450.

D.A. MCNEIL., B.M. BURNSIDE., D.I. RYLATT., E. ELSAYE., S. BAKER., C. ROBERTSON, A Comparison of Shell-side Boiling At Atmospheric And Vacuum Pressures *13th UK Heat Transfer, Edinburgh. 2-3 Sept, 2013.*

D A MCNEIL, B M BURNSIDE, E A ELSAYE, S M SALEM, S BAKER, Shell-Side Boiling Of A Glycerol-Water Mixture At Low Sub-Atmospheric Pressures*’14th UK Heat Transfer, Edinburgh. 7-8 Sept, 2015.*

Chapter 1– **INTRODUCTION**

At the Sellafield site in Cumbria, three evaporators A, B and C were built since 1970; evaporators A and B were out of service. Evaporator C is still running but an assessment of the remnant life of an evaporator is needed, based on the level of corrosion that the metalwork has received. New evaporator, D, Figure 1.1, is in the final stages of construction and will be ready for operations by 2017; it is one of the biggest industrial projects currently underway in UK. The cost of the new evaporator is about £700 million. These evaporators are used to process the nuclear waste that comes from reprocessing operations. They produce a more concentrated form of waste known as Highly Active Liquor or HAL. This HAL is subsequently vitrified, i.e., combined with molten glass, to make it suitable for long-term safe storage [1].

These evaporators are stainless steel pressure vessels with dual heat transfer capability as shown in Figure 1.2, consisting of six heating coils, Figure 1.3, and a thick-walled heating jacket. Low Pressure steam is used to heat the radioactive effluents that produce the more concentrated liquid. The evaporator has a unique role in reprocessing in that it is currently the only evaporator that can process effluent arising from the Thermal Oxide Reprocessing Plant (THORP). This makes it strategically important to the UK. It is the only evaporator capable of supporting the reprocessing of irradiated fuel from UK's advanced gas cooled reactor fleet.

The corrosive nature of the reprocessed liquors results in a progressive thinning of the stainless steel heating surfaces, which ultimately dictates the remnant life of the evaporator [2]. This process is temperature dependent, with increasing corrosion rates occurring at increased temperatures. To continue its operations, Sellafield has to show that the evaporator has sufficient wall thickness to support the operating vacuum pressure. To assess this, knowledge of the surface temperature of the evaporator is needed. Additionally, the life expectancy of the new evaporator will depend on how it is operated. This study was initiated in support of that assessment and to provide information that will maximise the life of the new evaporator.

This study involves boiling liquids at a very low pressure. Chapter 2 presents a literature review of heat transfer and pressure drop in similar evaporators and of low pressure boiling. As the liquor in the evaporator becomes more concentrated, some solids come out of solution and settle on the evaporator base. The effects of solids on boiling surfaces are also reviewed in Chapter 2.

This investigation was carried out on a one-quarter scale, thin slice model of the actual evaporator. Additionally, the model evaporator has the capability to vary the depth of the liquid pool in it from the one-quarter scale level up to the depth that occurs in the actual evaporator. The model evaporator could operate at any free surface pressure from close to total vacuum to atmospheric pressure. The test facility is described in Chapter 3.

Evaporator behaviour was investigated through two experimental campaigns. The first campaign investigates the effect of pressure on the thermal performance of the evaporator and the second campaign investigates the effect on the wall temperature of solids being deposited on the evaporator base.

The campaign to investigate the effect of pressure on the thermal performance contains four tests series. These series varied the coil heating at different conditions. The first series, the LLLP, low liquid level at low pressure series, was carried out at a surface pressure of 50 mbar absolute and at the scaled pool depth. The second series, the HLLP, high liquid level at low pressure series, was carried out at the same pressure but at the actual evaporator's pool depth. The third series, the LLMP, low liquid level at medium pressure series, was carried out at a surface pressure of 450 mbar and at the scaled pool depth and the fourth series, the LLHP, low liquid level at high pressure series, was carried out at pressure of 850 mbar and at the scaled pool depth. This campaign is presented and discussed in Chapter 4.

Two modelling approaches were investigated, one that assumed that the coils behaved independently and one that assumes an interaction between them. The models are presented and discussed in Chapter 5.

The campaign to investigate the effect of solids on the evaporator base is presented in Chapter 6. The investigation was carried out by boiling water at a surface pressure of 50 mbar absolute with the scaled pool depth. Experimental data are reported for solid bed depths of 0-32 mm. The solids used were glass particles 0.5-0.6 mm in diameter. These are a stimulant for Barium Nitrate, a solid that occurs in the actual evaporator. The effect on the wall temperature of solids being deposited on the evaporator base is discussed and analysed in Chapter 7.

Chapter 8 summarises and concludes on the finding achieved in the study. It also gives some suggestions of some further work that could be done in the future.

Figure 1-1: Evaporator D

Figure 1-2: The coils

Figure 1-3: The vessel

Chapter 2– **LITERATURE REVIEW**

2.1 Introduction

Some evaporators boil fluids that are highly corrosive. The corrosion rate of the materials used to construct these evaporators depends on their temperature. Thus, the life of the evaporator can be extended if the wall temperatures of the evaporator are kept low. One way of achieving this is to boil the fluid at a low pressure, and hence a low saturation temperature. This chapter reviews the literature relative to the kettle reboiler and the correlations that are used in prediction of the heat transfer coefficient, void fraction, pressure drops, boiling at low pressure and the effect of the solid particles.

2.2 Fundamentals of Boiling

Boiling is defined as the process of phase changing the state of a substance from liquid to vapour by adding heat at its saturation point. Different types of boiling can be defined according to the geometric situation and to the mechanism occurring. Regarding the geometry, it is possible to distinguish between pool boiling, where the heat is transferred to a stagnant fluid; and flow boiling, where the fluid has a velocity relative to the heating surface. The three different boiling heat transfer mechanisms are nucleate boiling, where heat is transferred by means of vapour bubbles nucleating, growing and finally detaching from the surface; convective boiling, where heat is conducted through the liquid to produce evaporation at the liquid-vapour interface without bubble formation; and film boiling, where the heat is transferred by conduction and radiation through a film of vapour that covers the heated surface and the liquid vaporizes at the vapour-liquid interface. Nucleate boiling and film boiling may occur in both pool boiling and flow boiling, while forced convective boiling occurs only in flow boiling. In addition, if the temperature of the bulk liquid is below the saturation temperature, the process is called subcooled boiling, whereas if the liquid is maintained at the saturation temperature, the process is known as saturated boiling.

2.3 Pool Boiling

When a surface is heated to a temperature that is higher than the surrounding liquid's saturation temperature, the process is known as pool boiling. Pool boiling is similar to natural convection, in that there is no external mechanism that causes fluid motion. On the other hand, active fluid motion exists during pool boiling as a result of the difference in the density that exists between the vapour that is created by the evaporation process and the surrounding liquid density.

2.3.1 *Nucleate Pool Boiling Correlations*

To design heat transfer equipment, such as heat exchangers, accurate heat transfer correlations are required. The boiling heat transfer coefficient is defined as

$$h = \frac{q''_w}{T_w - T_{sat}} \qquad \text{2-1}$$

Nucleate pool boiling heat transfer has a close relationship to the activities of the bubbles and results from a combination of several interacting mechanisms:

- Transient heat conduction; the thermal boundary layer created by conduction into the liquid in the vicinity of the heated surface is periodically removed by the hydrodynamic drag during bubble growth and departure.

- Enhanced heat Convection; liquid movement is generated by the growing and departing bubbles. This creates convective streams that contribute in the heat transfer.

- Evaporation; vaporization of the super-heated liquid surrounding the bubbles in layer between the bubble and the microlayer.

Generally, the heat transfer coefficient can be predicted by knowing the frequency of the bubbles, the heat transfer in every cycle and the density of active nucleation sites [3]. However, the contribution to heat transfer by each mechanism has not been firmly proven and analytical treatments are not completely developed for effective applications. Therefore many experimental correlations are available in the literature. Rohsenow [4] correlation was one of the first correlations based on the bubble agitation mechanism. It was formulated as a single phase forced convection correlation.

$$\frac{C_{pl}\Delta T}{h_{fg}} = C_{sf}\left[\frac{q}{\mu_l h_{fg}}\left(\frac{\sigma}{g(\rho_l - \rho_g)}\right)^{1/2}\right]^n Pr_l^{m+1} \qquad \text{2-2}$$

Where the specific heat of the liquid is C_{pl} , σ is the surface tension, $\rho_{l,}$ ρ_g are liquid and gas density and Pr_l is the liquid Prandtl number; h_{nb} is obtained from the definition of the heat transfer coefficient.

$$h_{nb} = q/\Delta T \qquad 2\text{-}3$$

The values of the exponents are m = 0.7 and n = 0.33 for all fluids except for water for which Rohsenow [4] recommended setting m = 0. Values of C_{sf} for various surface-fluid combinations of Rohsenow [4] and additional values proposed by R.I.Vachon [5] for water are Water on polished copper 0.0128, water on lapped copper 0.0147 water on scored copper 0.0068, Water on ground and polished stainless steel 0.08 Water on PTFE pitted stainless steel 0.0058, Water on chemically etched stainless steel 0.0133, Water on mechanically polished stainless steel 0.0132.

Montinski ignored surface effects and applied the principle of corresponding states to nucleate pool boiling heat transfer [6], correlating data as a function of the reduced pressure of the fluid F_{pr} and its critical pressure P_{crit}. His dimensional reduced pressure correlation gives h_{nb} in *W/m²K* through

$$h_{nb} = 0.00417 q^{0.7} P_{crit}^{0.69} F_{pr} \qquad 2\text{-}4$$

The correlation must be used with q in W/m^2 and P_{crit} in kN/m^2 (i.e. in KPa, not in N/m^2). F_{pr} is a non-dimensional pressure correction factor that characterizes pressure effects on nucleate boiling as:

$$F_{pr} = 1.8P_r^{0.17} + 4P_r^{1.2} + 10P_r^{10} \qquad 2\text{-}5$$

where is $P_r = \frac{p}{P_{crit}}$ 2-6

Equation 2.3 is valid for q ≤ 0.9P_{crit}, where the critical heat flux, q_{crit} is defined by

$$q_{crit} = 3.2 \times 10^4 \, P_{crit} P_r^{0.35} (1 - P_r)^{0.9} \qquad 2\text{-}7$$

Montinski fitted the above correlation to a large bank of experiment data and found that this correlation predicted the heat transfer coefficient to an accuracy of ±30%.

Rice and Calus investigated pool boiling for toluene, methanol, water and water- isopropanol azeotrope at atmospheric pressure on a wire [7]. The wire had diameter of 0.315 mm and was made a nickel-aluminium alloy. They correlated their data in the form of equation as

$$Nu = EPe^{0.7}K_P^{0.7}\left[\frac{T_{sw}}{T_{sat}}\right]^4 \qquad 2\text{-}8$$

Rice and Calus used the modified version of Pelclet, *Pe*, Nusselt, *Nu* and K_p which is a function of absolute pressure, that modified by Borishanskii V. M. [8] . The bubble growth diameter was equivalent to $\sqrt{\frac{\sigma}{g(\rho_l-\rho_g)}}$ and the modified versions are stated in the Equations (2.9, 2.10, and 2.11).

$$Pe = \frac{\rho_l Cp_l\, q}{k_l \rho_g h_{fg}}\left[\frac{\sigma}{g(\rho_l-\rho_g)}\right]^{0.5} \qquad 2\text{-}9$$

$$K_p = \frac{P}{[g\sigma(\rho_l-\rho_g)]^{0.5}} \qquad 2\text{-}10$$

$$Nu = \frac{q}{k_l\ \Delta T}\left[\frac{\sigma}{g(\rho_l-\rho_g)}\right]^{0.5} \qquad 2\text{-}11$$

where T_{sw} refers to the absolute boiling temperature of water at the system pressure and E is a factor depending on the liquid/surface conditions. The value of E was chosen to be 9.9×10^{-4} for water boiling on a stainless steel surface.

Stephan and Abdelsalam developed a nucleation boiling correlation for various fluids, including water [9], hydrocarbons, cryogenics and refrigerants. This correlation was based on fluid and thermal properties combined in various dimensionless groups. Their water correlation is given as:

$$\frac{h_{nb}d_{bub}}{K_l} = 0.246\ \times 10^7\ \left(\frac{qd_{bub}}{K_lT_{sat}}\right)^{0.673}\left(\frac{h_{fg}d_{bub}^2}{a_l^2}\right)^{-1.58}\left(\frac{C_pT_{sat}d_{bub}^2}{a_l^2}\right)^{1.26}\left(\frac{\rho_l-\rho_g}{\rho_l}\right)^{5.22} \qquad 2\text{-}12$$

The expression to the left of the equal sign is a Nusselt number and their bubble departure diameter d_{bub} is obtained from

$$d_{bub} = 0.0146\beta\left[\frac{2\sigma}{g(\rho_l-\rho_g)}\right]^{1/2} \qquad 2\text{-}13$$

The contact angle β assigned a fixed value of 45, $10^{-4} \le P/P_{crit} \le 0.886$, T_{sat} is the saturation temperature of the fluid in *K*, and a_l is the liquid thermal diffusivity.

Nishikawa introduced a correlation that was determined by curve fitting to experimental results as [10]:

$$h = 3.14 \frac{Pcrit^{0.2}}{M^{0.1} Tcrit^{0.9}} (8. R_{p.old})^{\frac{1-P_r}{5}} . \frac{{P_r}^{0.23}}{(1-0.99 \,. P_r)^{0.9}} \,. q^{0.8} \qquad \textit{2-14}$$

where P_r is the reduced pressure, $R_{p.old}$ is the old standard of surface roughness of the heating surface, M is the molar mass, P_{crit} is the critical pressure and the T_{crit} is the critical temperature of the evaporating fluid. The surface roughness $R_{p.old}$ can be updated by

$$R_{p.old} = \frac{R_p}{0.4} \qquad \textit{2-15}$$

Cooper proposed a correlation [11], which earned the reputation for its accuracy in predicting heat transfer coefficient of nucleate pool boiling. In his correlation, the heat transfer coefficient was presented as a function of the reduced pressure, heat flux, molecular weight of the liquid and the surface roughness.

$$h_{nb} = 55{P_r}^{0.12-0.2log_{10}R_p} (-0.4343lnP_r)^{-0.55} \, M^{-0.5} q^{0.67} \qquad \textit{2-16}$$

This is a dimensional correlation in which h_{nb} is in W/m^{2}K, q is in W/m^2 and R_p is the surface roughness in μm. When R_p is unknown, it is set to 1.0 μm. Cooper recommended multiplying the above heat transfer coefficient by 1.7 for horizontal copper cylinders; however, the correlation seems to be more accurate for boiling of refrigerants on copper tubes without this correction and that approach is recommended here. The Cooper correlation covers reduced pressures from 0.001 to 0.9 and molecular weights from 2 to 200.

Gorenflo proposed a fluid specific reduced pressure correlation and included the effect of surface roughness [12]. His method uses a reference heat transfer coefficient h_o, specified for each fluid at the following fixed reference conditions of P_r=0.1, R_{po}=0.4 μm and q_0 = 20,000 W/m^2. The nucleate boiling heat transfer coefficient h_{nb} at other conditions of pressure, heat flux and roughness is then calculated relative to the reference heat transfer coefficient using the following expression

$$h_{nb} = h_o F_{Pr} \left(\frac{q}{q_0}\right)^{nf} \left(\frac{R_p}{R_{po}}\right)^{0.133} \qquad \textit{2-17}$$

His pressure correction factor F_{Pr} is

$$F_{Pr} = 1.2P_r^{0.27} + 2.5P_r + \frac{P_r}{1-P_r} \qquad \textit{2-18}$$

The effect of reduced pressure on his exponent nf for the heat flux term is given by:

$$nf = 0.9 - 0.3P_r^{0.3} \qquad \textit{2-19}$$

Its value decreases with increasing reduced pressure, which is typical of experimental data. The surface roughness is R_p in μm and is set to 0.4 μm when unknown. The above method is for all fluids except water and helium; for water the corresponding equations are:

$$F_{Pr} = 1.73\, P_r^{0.27}\, \left[6.1 + \frac{0.68}{1-P_r}\right] P_r^2 \qquad \textit{2-20}$$

$$And \quad nf = 0.9 - 0.3\, P_r^{0.15} \qquad \textit{2-21}$$

This method is applicable over the reduced pressure range from about 0.0005 to 0.95. References values of [12] with h_o for water 5600 W/m^{2}K at P_r = 0.1, q_0 = 20,000 W/m^2 and R_{po}= 0.4 μm with P_{crit} for water 220.6 bar and M for water 18.02.

Cornwell and Houston [13] correlation is presented in the following form

$$h = \frac{N_u k_l}{\sqrt{\frac{\sigma}{g(\rho_l-\rho_g)}}} \qquad \textit{2-22}$$

$$N_u = 9.7\, P_{crit}^{0.5} F_{pr} Re^{0.67} (\frac{P}{P_{crit}})^{0.4} \qquad \textit{2-23}$$

And F_{pr} is as shown in Equation 2.5.

Pioro [14] correlation suggests that the heat transfer coefficient can be found from Equation 2.23, where C_{sf} is a constant that depends on the nature of the heating surface- fluid combination and can be taken as 0.016 for water and copper. m suggested to be 1.0.

$$h = \frac{k_l}{\sqrt{\frac{\sigma}{g.\rho_l}}} C_{sf} \left[\frac{q}{{\rho_g}^{0.5} h_{fg} [\sigma.g.(\rho_l - \rho_g)]^{0.25}}\right]^{\frac{2}{3}} Pr_l^m \qquad \textit{2-24}$$

where Pr_l is the Prandtle number which is

$$Pr_l = c_{pl}\mu_l/k_l \tag{2-25}$$

Choon [15] modified Rohsenow [4] correlation, Using the water properties at the working pressures as well as measured boiling fluxes and ΔT, a multi-variable regression was conducted to give Equation 2.25. The coefficients C_{sf} and index n remain unchanged from the Rohsenow [4] correlation, i.e., 0.0132 and 0.33, respectively, but the exponent L for the low pressure correction is best fitted by 0.293 and E is -0.098

$$\Delta T = \left(\frac{C_{sf} h_{fg} Pr_l^{m+1}}{c_{pl}}\right)\left[\frac{q}{\mu_l h_{fg}}\left(\frac{\sigma}{g(\rho_{l-}\rho_g)}\right)^{1/2}\right]^n \left(\frac{p}{p_{atm}}\right)^L \left(\frac{A_{wetted}}{A_{base}}\right)^E \tag{2-26}$$

2.4 Natural convection on horizontal tube:

When a horizontal tube with temperature T_w is submerged in a fluid with temperature T_∞ ($T_w > T_\infty$) a boundary layer develops along the curved surface. The boundary layer thickness is a function of the angle ϕ ($\phi = 0^0$ is at the bottom of the tube), as shown in Figure 2.1. The similarity solution that worked for the case of the vertical plate does not work for natural convection over a horizontal tube. Merk [16] assumed the momentum and thermal boundary layer thicknesses are identical, they found an integral solution depending on this assumption. The results show that the local Nusselt number at the bottom where the boundary layer is thinnest is highest. As the angle φ increases, the thickness of the boundary layer increases and the local Nusselt number decreases. Although the integral solution can produce results all the way to the top where $\phi = 180^0$ and $Nu_\phi = 0$, the result beyond $\phi = 165^0$ is no longer applicable because boundary layer separation occurred and plume flow takes place. Merk [17] recommended the following empirical correlation for natural convection over a horizontal tube based on the integral solution:

$$Nu_D = C\ Ra\ D^{0.25} \tag{2-27}$$

where is the diameter of the tube the characteristic length in the average Nusselt number and Rayleigh number. The constant C is a function of Prandtl number

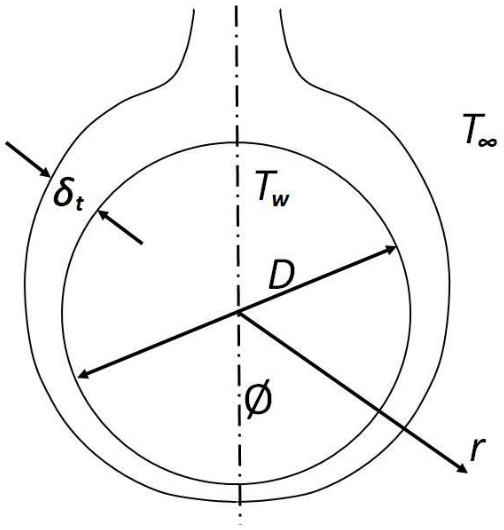

Figure 2-1: boundary layer for natural convection over horizontal cylinder

Practically, the empirical correlations based on experimental results are more useful. Churchill and Chu [18] recommended the following correlation for horizontal cylinders (tubes):

$$Nu = \left\{ 0.6 + \frac{0.387 Ra^{\frac{1}{6}}}{\left[1+\left(\frac{0.559}{Pr}\right)^{\frac{9}{16}}\right]^{\frac{8}{27}}} \right\}^2 \qquad 2\text{-}28$$

And

$$Ra = GrPr = \frac{\rho_L^2 g \beta (T_W - T_L) D^3}{{\mu_l}^2} Pr \qquad 2\text{-}29$$

when $Ra<10^{12}$

2.5 Flow Boiling on Tube Bundles

The boiling on the outside of horizontal tube bundles is used in several systems such as thermosiphons and kettle reboilers, waste heat boilers, fire-tube steam generators and flooded evaporators in refrigeration systems. A simplified tube bundle is shown in Figure 2.2, with tube uniform heating in up flow boiling. The Figure also shows different flow patterns encountered from the bottom to the top, with corresponding regimes of heat transfer. A sub-cooled liquid flows from the inlet nozzle upwards to the bottom of heated tubes. The liquid is heated up to the saturation temperature and the temperature of the wall remains lower than that needed for nucleation, the process of the heat transfer is a single phase convection [19].

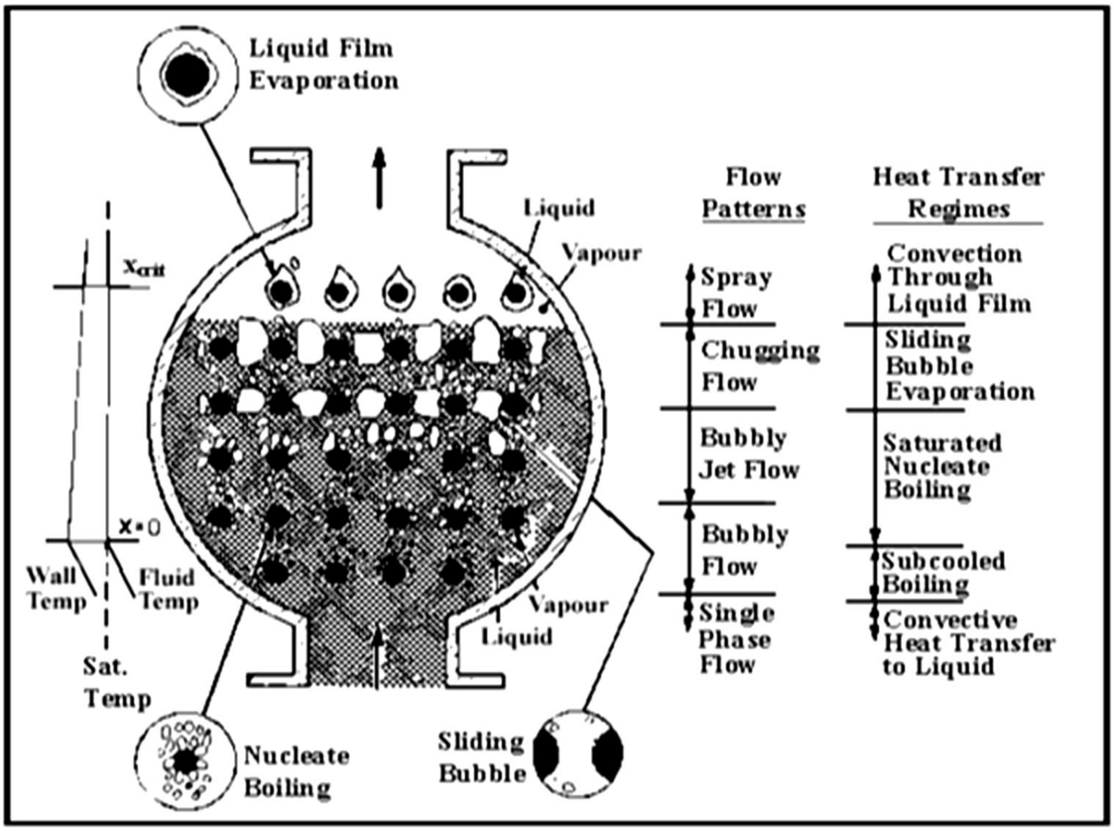

Figure 2-2: Boiling on horizontal tube bundle [19]

As the nucleation conditions are met, vapour is generated, the sub-cooled boiling regime is started and remains until the saturated boiling regime begins. This occurs when the liquid reaches the saturation temperature, similar to that for pool billing on a single tube. Bubbly flow occurs in the lower part of the bundle up until transition to bubble jet flow. Bubbly jet flow forms when a two-phase jet impinges on the tubes above. As the local void fraction increases, large vapour plugs are formed and pass between adjacent tubes, trapping thin layers of evaporating liquid on the sides of tubes. This is the sliding bubble phenomenon observed by Cornwel [20]. Higher up in the bundle, the vapour becomes the continuous phase and liquid is evaporated from thin films covering the tubes, producing a frothy spray type of flow [19]. At some critical value of quality and heat flux, dry out of the tube can occur with a substantial decrease in heat transfer performance. The liquid flow regime on the tube bundle of a kettle reboiler was observed by Cornwel [20]. The flow contained large bubbles that could be described as slugs interspersed with other smaller bubbles that could be characterize as plug flow or chugging. At the same critical conditions, the flow changes into spray flow with large droplets on the tube forming a liquid film.

2.6 Heat Transfer on Tube Bundles

Flow boiling across tube bundles is similar to in-tube flow boiling, with models for tube bundles requiring correlations for convective and boiling heat transfer. The flow velocity, bundle geometry and fluid properties govern the heat transfer of forced convective flow across a tube bundle. Experimental result for convective heat transfer in tube bundles are correlated with expressions of the form

$$Nu = cRe^{m}Pr^{n}\left({}^{Pr}/_{Pr_w}\right)^{0.25} \tag{2-30}$$

where c is an empirical constant, m and n are dependent on the tube geometry and Reynolds number.

Models for boiling on tube bundles are available in the open literature, but most of them have been developed with a limited database. Palen [21] presented a simple method to estimate the coefficients for bundle, h_b. It was obtained by superposition of the natural convection and boiling contributions.

$$h_b = F_b F_c h_{nb} + h_{nc} \tag{2-31}$$

where h_{nb} is the nucleate pool boiling coefficient, F_b, F_c are the bundle boiling and the mixture boiling correction factors respectively and h_{nc} is the heat transfer coefficient for single- phase natural convection on the tube bundle.

Fujita et al, Jensen et al and Cornwell et al [22-24] have shown that by using theory of two-phase flow for in-tube flow they can estimate the pressure drop and the heat transfer through the bundle, in an appropriate manner modified for the different flow regimes and the different geometry.

Applying the corrections to tube boiling directly for the tube bundles obtains poor results, it is therefore required to calculate the local heat transfer coefficients within a tube bundle, either as a function of local vapour quality or by position. Different adaptions have been done. For instance, Hwang and Yao [25] modified the Chen [26] correlation.

$$h_{TP} = Sh_{nb} + Fh_{sp} \tag{2-32}$$

Applying a new empirical expression for F and the Bennett et al [27] expression for boiling suppression factor S.

$$S = \frac{k_f}{Fh_{sp}Y}\left[1 - exp\left(\frac{Fh_{sp}Y}{K_l}\right)\right] \quad 2\text{-}33$$

where Y is a dimensionless variable.

Convective and nucleate boiling contributions were assumed to be additive without a boiling suppression factor by Cornwell et al [28]

$$Nu_b = cRe^m Pr^n + CRe_b^{0.67} \quad 2\text{-}34$$

The Zukauskas and Ziugzda [29] parameters were applied for c, m and n . The local Nusselt number in the bundle is based on the tube parameters

$$Nu_b = \frac{h_b D}{k_l} \quad 2\text{-}35$$

and the Reynolds number is calculated based on the velocity of the liquid phase as:

$$Re = \frac{\rho_l u_l D}{\mu_l} \quad 2\text{-}36$$

The coefficient of bundle boiling was proposed by Nukiyama [30] as the summation of nucleate boiling and thin-film evaporation. The general correlation for the coefficient of local heat transfer on the *N* the tube row from the bottom of the bundle is expressed as:

$$h_b = (1 - \epsilon)h_{nb} + \epsilon h_{tl} \quad 2\text{-}37$$

where ϵ the void fraction is used to weight the two contributions. Therefore nucleate boiling will be dominant at low void fraction while at higher void fraction, thin-film evaporation becomes controlling. The coefficient for thin film heat transfer is proposed as the dimensional equation [30].

$$h_{tl} = 2326 + 1512\, exp\left[-\left(\frac{0.5556}{u_g}\right)^{1.5}\right] \quad 2\text{-}38$$

The unit of h_{tf} is $W/m^2\ K$, and u_g is the superficial vapour velocity in $\mathrm{m/s}$, calculated from the energy input of the lower tube rows as

$$u_g = \sum_N^{N-1} \frac{\emptyset \pi D}{i_{fg}\rho_g N s_1} \quad 2\text{-}39$$

where s_1 is the transvers tube pitch.

2.7 Void Fraction Prediction Methods

In the tube bundles similar to flow in tubes, the void fraction has been expressed as:

$$\epsilon = 1 - \frac{1}{\Phi_L^2} \qquad \textit{2-40}$$

where Φ_L^2 is the two phase multiplier. The method of Ishihara et al [31], Equation 2.41, is such a method which is expressed as a function of the Martinelli parameter, Equation 2.42. Cornwell et al [32] suggested similar approach, Equation 2.42, as did Fair and Klip [33] suggested a method based on a different two-phase friction multiplier, Equation 2.43.

$$\frac{1}{1-\epsilon} = 1 + \frac{8}{X_{tt}} + \frac{1}{X_{tt}^2} \qquad \textit{2-41}$$

$$\frac{1}{1-\epsilon} = 1 + \left(\frac{6}{X_{tt}}\right)^{0.71} \qquad \textit{2-42}$$

$$\frac{1}{(1-\epsilon)^2} = 1 + \frac{20}{X_{tt}} + \frac{1}{X_{tt}^2} \qquad \textit{2-43}$$

All equations are based on Martinelli parameter, X_{tt},

$$X_{tt} = \left(\frac{1-x}{x}\right)^{0.9} \left(\frac{\rho_g}{\rho_l}\right)^{0.5} \left(\frac{\mu_l}{\mu_g}\right)^{0.1} \qquad \textit{2-44}$$

The prediction method of Schrage et al [34] used a correction factor based on the liquid Froude number as a multiplier to the homogeneous model. This model of Schrage et al [34] was one of the earliest models that involved the important effect of mass flux directly:

$$\frac{\epsilon}{\epsilon_{\boldsymbol{H}}} = 1 + 0.123\left(\frac{ln\, x}{Fr_l^{0.191}}\right) \qquad \textit{2-45}$$

$$\text{with} \quad Fr_l = \frac{m}{\rho_l\,(gD)^{0.5}} \qquad \textit{2-46}$$

Dowlati et al [35] suggested a void fraction model based on data from R113 flow at mass velocities higher than 50 *kg/m*^{2}*s*. Dowlati method is based on two constants ($C_1 = 30$ and $C_2 = 50$) and dimensionless gas phase superficial velocity

$$\epsilon = 1 - \frac{1}{\left(1+C_1 j_g^* + C_2 j_g^*\right)^{0.5}} \qquad \textit{2-47}$$

with

$$j_g^* = \frac{\rho_g^{0.5} j_g}{\sqrt{gD\,(\rho_l - \rho_g)}} \qquad \text{2-48}$$

The Feenstra et al [36] method is based on dimensionless parameters that were identified and used to fit to their database. The models proposed in the literature were reviewed by Ribatski and Thome [37] and found that the Feenstra et al [36] model is the most suitable method to predict the void fraction for tube bundles.

By combining liquid and gas phase's continuity equations, accounting the definition of cross-sectional vapour quality, velocity or slip ratio $S = \frac{u_g}{u_l}$, the void fraction ϵ is derived as follow:

$$\epsilon = \left[1 + S\,\frac{\rho_g}{\rho_l}\left(\frac{1-x}{x}\right)\right]^{-1} \qquad \text{2-49}$$

Dimensional analysis [36] was used to identify four dimensionless groups governing the velocity ratio's. Equation 2.50 is theoretical result from their separated flow model.

$$S = 1 + 25.7\,(Ri\,.\,cap)^{0.5}\left(\frac{P}{D}\right)^{-1} \qquad \text{2-50}$$

If the basic length scale, (a) is assumed to be the narrowest gap between two tubes and the pitch velocity u_g is evaluated in the flow area in the gap, it follows that:

$$Ri = \frac{(\rho_l - \rho_g)^2\, ga}{m^2} \quad and\ cap = \frac{\mu_l u_g}{\sigma} \quad with \quad u_g = \frac{xm}{\epsilon\,\rho_g} \qquad \text{2-51}$$

where the Richardson number (Ri) is the ratio between buoyancy force and the inertial force and the capillary number (cap) is the ratio between the viscous force and the surface tension force. An iterative procedure is needed for the computation.

2.8 Pressure Drop in Tube Bundle

2.8.1 *Single Phase Pressure Drop Prediction Methods*

The pressure drop for single phase flow over tube bundles was expressed by Zukauskas [38] as:

$$\Delta p_l = Eu\,N_R\,\frac{m^2}{2\rho} \qquad \text{2-52}$$

For 3 < $Re \leq 10^3$

$$\frac{Eu}{k_1} = 0.795 + \frac{0.247\ 10^3}{Re} + \frac{0.335\ 10^3}{Re^2} - \frac{0.155\ 10^4}{Re^3} + \frac{0.241\ 10^4}{Re^4} \qquad 2\text{-}53$$

For 10^3 < Re < 2.10^6

$$\frac{Eu}{k_1} = 0.245 + \frac{0.339\ 10^4}{Re} + \frac{0.984\ 10^7}{Re^2} - \frac{0.132\ 10^{11}}{Re^3} + \frac{0.599\ 10^{13}}{Re^4} \qquad 2\text{-}54$$

where k_1, the geometric factor is a function of the aspect ratio($\frac{a}{b}$), The relative transverse (*a*) and longitudinal (*b*). $k_1 \approx 1$, the influence of this parameter can be neglected.

ESDU [39] proposed

$$\Delta p_l = \frac{f_l}{2D\ \rho_L} m^2 l \qquad 2\text{-}55$$

f_L the single phase friction factor for the tube bundle and m is mass flux. The single phase friction factor for the tube bundles expresses by ESDU [39]:

$$f_l = Plc_{ref}\ .F_v.F_{fi}.F_{RC} \qquad 2\text{-}56$$

where $\mathrm{Plc}_{\mathrm{ref}}$ is the reference pressure loss coefficient.

$$P_{LC\ ref} = Y.F.b_f.\left(\frac{1}{P_i - 1}\right)^3 \qquad 2\text{-}57$$

where F factor =1.0, $P_i = P/D$ and the blockage factor b_f is

$$b_f = \frac{4P_i^2}{\pi} - \frac{Re}{Re+1000} \qquad 2\text{-}58$$

$$Y = \left(\frac{X_{CA}}{X_{CC} - X_{CC}} + X_{CD}\right)^{0.5} \qquad 2\text{-}59$$

$$X_{CA} = \left(\frac{0.1\ Re}{Re+100}\right)^2,\ \ X_{CB} = \left(\frac{A}{0.5(1.0+0.6A)}\right)^2,\ X_{CC} = \frac{1.0}{(1000+3A)^2}\ ,And\ \ X_{CD} = \frac{49}{(Re)^{1.95}} \qquad 2\text{-}60$$

The viscosity correction factor F_v given by

$$F_v = \left(\frac{\nu_w}{\nu_l}\right)^{\frac{0.38}{(Re)^{0.24}}} \qquad 2\text{-}61$$

The flow inclination correction factor F_{fi} =1.0 and the surface roughness correction factor F_{RC} = 1.0 as well.

2.8.2 *Two-Phase Pressure Drop Prediction Methods*

The total pressure drop ΔP_{total} of the two-phase fluid following in cross-flow over a tube bundle is the sum of the frictional pressure drop,ΔP_{f}, the momentum pressure drop, ΔP_{m}, and the gravitational pressure drop ΔP_{G},:

$$\Delta P_{total} = \Delta P_{G} + \Delta P_{m} + \Delta P_{f} \tag{2-62}$$

for a shell-side flow, the gravitational pressure drop is

$$\Delta P_{G} = \rho g\, H \tag{2-63}$$

where H is the height through the boiling. The ρ is

$$\rho = \rho_{L}(1-\epsilon) + \rho_{g}\epsilon \tag{2-64}$$

The vapour and liquid densities are ρ_{g} and ρ_{L}, respectively.

The momentum pressure drop is

$$\Delta P_{m} = m_{total}^{2}\left\{\left(\frac{(1-x)^{2}}{\rho_{L}(1-\epsilon)} + \frac{x^{2}}{\rho_{g}\epsilon}\right)_{out} - \left(\frac{(1-x)^{2}}{\rho_{L}(1-\epsilon)} + \frac{x^{2}}{\rho_{g}\epsilon}\right)_{in}\right\} \tag{2-65}$$

The momentum pressure drop results in a decrease in pressure of the fluid when $x_{out} > x_{in}$ (evaporation). The two-phase multiplier, Φ_{L}^{2}, crossflow over a tube bundles is defined by

$$\Delta P_{f} = \Phi_{L}^{2}\Delta p_{l} \tag{2-66}$$

Ishihara et al [31] and Huang [40] based their two-phase multiplier correlations on the Martinelli parameter

$$\Phi_{L}^{2} = 1 + \frac{C}{X_{tt}} + \frac{1}{X_{tt}^{2}} \tag{2-67}$$

For two-phase flow Ishihara et al [31] set the parameter C to a value of 8.0 The Martinelli parameter X_{tt} is given by Equation.2.44. For flooded evaporators, the gravitation head ΔP_{G} typically dominates as low mass velocities. Hence, the influence of the void fraction is particularly significant on the value of the total pressure drop especially at low quality.

2.9 Boiling at Sub-Atmospheric Pressures

Boiling at low pressure can be useful when low temperatures are required, keep the temperature of a boiling surface low and thus reduce its corrosion rate; low temperatures can be achieved by reducing the saturation pressure. A reduction in the saturation pressure causes a corresponding decrease in the saturation or boiling temperature. This temperature decrease is translated to the boiling surface. This is particularly useful when water is used as the boiling liquid. Water is a desirable liquid since it has such a high thermal conductivity, a high heat of vaporization and is non-toxic non-flammable Boiling in sealed vessels is a typical application of low pressure boiling. Heat pipes, thermosiphons, and some thermodynamic cycles may depend on low pressures to provide low surface temperatures while moving significant quantities of heat.

Research on the boiling of liquids at sub-atmospheric pressures has mainly focused on the reduced pressure effect on the bubble nucleation process, critical heat flux, incipient superheat and surface temperature. Water boiling at sub-atmospheric pressures has been done in most cases on plain surfaces or wires, and in some cases on roughened machine surfaces. Van Stralen [41], studied boiling of water and a mixture of methyl-ethyl ketone on an electrically heated platinum wire within a pressure range of 0.13-1.0 bar. He found a reduction in heat transfer during boiling at sub atmospheric pressures. He observed that a decrease in pressure delayed the onset of nucleate boiling, led to increase in the bubble size and reduced the maximum heat flux attained.

I. A. Raben [42] investigated saturated nucleate pool boiling of water at sub-atmospheric pressures from a 38.1 *mm* diameter horizontal heated surface. The reported experimental data included the number of bubbles on the surface, frequency of bubble departure and bubble departure diameter for pressures ranging from 0 .013 to 1.0 bar. The objective of their investigation was to identify the dominant energy transport mechanisms of nucleate boiling and to understand how they are affected by pressure. By applying the energy equation to a simple heat transfer model, a theoretical analysis of nucleate boiling was discussed. They postulated that free convection, vapour-liquid exchange, and the latent heat of vaporization are the modes in which energy is transferred during saturated nucleate boiling. For very low pressures, they found that the contribution of latent heat was insignificant compared to the vapour-liquid exchange. Measured heat fluxes ranged from about 8 W/cm^2 at 13 mbar to about 19 W/cm^2 at 1.01 bar. Heat fluxes were not extended into the regimes of vapour slugs and columns or critical heat fluxes.

Enhancement strategies were not considered either. However, the investigation of I. A. Raben [42] did reveal the vapour bubble formation characteristics for water at low pressure in a large vessel.

Ponter [43] visualized boiling of water for the pressure range of 0.133-1.013bar with a tubular stainless steel heater in a stainless steel cylinder. Similar to Van Stralen [41], they also observed a reduction in potentially active bubble nucleation sites. Further, they also observed that the increase in pressure led to an increase in the critical heat flux. Another notable study on the mechanism of nucleate boiling at atmospheric and sub-atmospheric pressures was by Miyauchi [44] who tried to explain the suppressed bubble growth rates at sub-atmospheric pressures. They suggested that a rapidly growing bubble would accelerate the liquid surrounding the bubble, which will increase the pressure inside the bubble with respect to the outside pressure. They believed that this process would induce a higher saturation pressure inside the bubble and thus a higher wall superheat, which will suppress the bubble growth rate.

Later, Van Stralen et al [45] experimentally investigated the growth rate of vapour bubbles in water using a nickel-plated copper-heating surface for a pressure range of 20- 267 mbar. They observed that the bubble departure time and departure bubble radius increased substantially with a decrease in operating pressure.

Joudi and James [46] focused on a pressure range of 0.25-1.013 bar for boiling water, R- 113 and methanol, they observed fluctuations in the surface temperature during incipience and noted that decreasing pressure initiated a decrease in the onset superheat.

Fath and Judd [47] investigated micro-layer evaporation and found higher wall superheats with decrease in operating pressure. With an increase in surface heat flux, they found an increase in the bubble generation site density, which helped transfer of additional heat. Tewari et al [48] observed that the heat transfer coefficient decreased with a decrease in saturation pressure in the nucleate boiling regime within a pressure range of 0.6-1 bar. They studied nucleate boiling on a horizontal tube at atmospheric and sub-atmospheric pressure with water and NaCl solution. Later, McGillis [49] investigated the boiling of water in a thermosiphon configuration at sub-atmospheric pressures using a plain surface with surface enhancements. They observed that lower pressure generated larger nucleation bubbles, which impeded growth in active nucleation sites, resulting in larger wall superheats. However, surface enhancements improved the heat transfer with lower wall superheat and increased the critical heat flux. Rainey et al [50] did experiments with FC-72 at reduced pressures and observed that increase in pressure brings an increase in CHF with a decrease in boiling onset. Boiling from enhanced surfaces produced wall superheat that remained at much lower than those of plain surfaces for the range of heat flux applied to the experiments.

Figure.2.3 shows the variation of heat flux with temperature difference data was compiled by Choon et al [15]. The range of heat fluxes varied from 1 to 5 W/cm^2 in their experiments whilst the ΔT varies up to 5.4 K. Included in the Figure are the nucleate pool boiling experimental data for water of McGillis et al [51] at pressures of 4 and 9 Kpa. These data were obtained at heat fluxes from 5 to 10 W/cm^2.

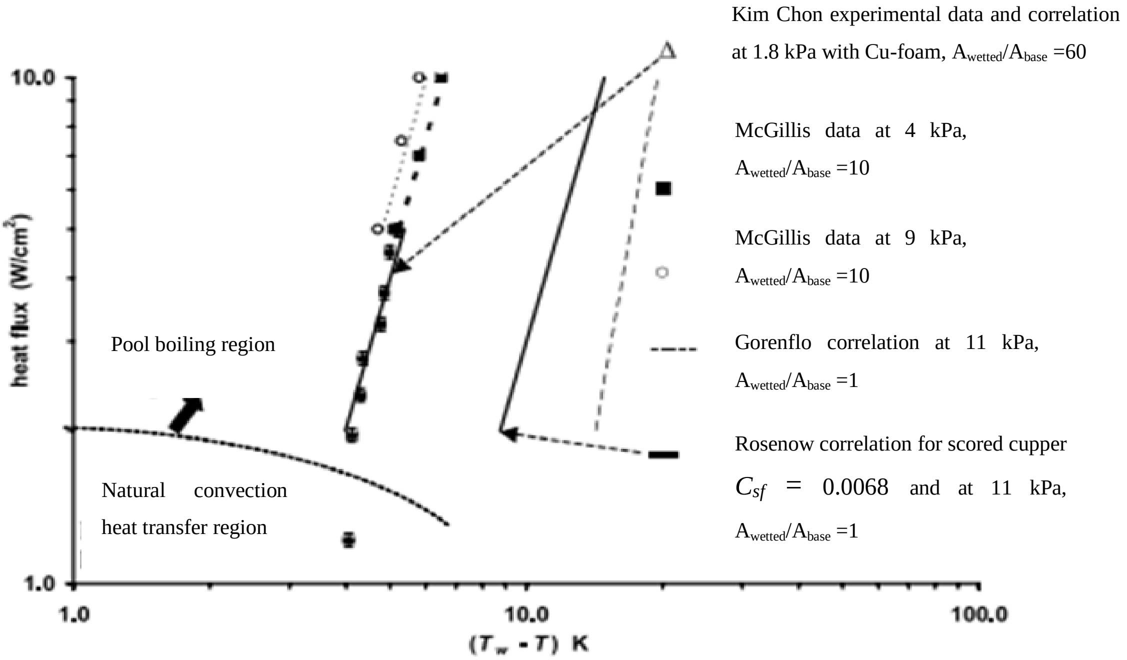

Figure 2-3: Heat flux versus temperature difference for water at 18 mbar [15] experiment), 4 , 9 Kpa [51]and 11Kpa [12]. The bottom most data of 1.8 Kpa is observed to have insignificant boiling, i.e., mainly convective heat transfer by water.

The modified Rohsenow [4] correlation, Equation 2.26 is applicable at low absolute pressures from 1.8 to 10 Kpa. Extrapolation beyond these pressures may not reasonable as higher system pressures tend to delay the onset of pool boiling [15] highlighted that the lowest data point in Figure. 2.3, falls far from the modified correlation and was observed to have no boiling at low heat flux, i.e., the rise in ΔT was refer to natural convective heat transfer. Due to the high A_{wetted}/A_{base} of copper-foam, the effect of the capillary is found to be excellent and these effects enhance the boiling heat transfer coefficients at higher heat fluxes. The analysis of Rohsenow [4] pool boiling correlation of scored copper surfaces (C_{sf} = 0.0068 and n = 0.33) at a working pressure 1.8 Kpa, is included in Figure 2.3 for comparison. This correlation does not match with the Choon et al [15] experimental data.

The reduced pressure correlation of Gorenflo [12] for polished copper with pure water is also shown in Figure 2.3. Choon et al. [15] observed that, at the sub-atmospheric pressures, the Gorenflo [12] correlation did not agree with the experimental data of McGillis et al. [51] as well as Choon et al. [15] measured data.

Liu and Liao [52] reported that the test pressure has a marked effect on the boiling heat transfer performance of in line tube bundles. The heat transfer enhancement effect decreases with decreasing test pressure for the same tube spacing and the position of the test tube in the bundle had a clear effect on its heat transfer characteristics. The heat transfer enhancement effect of the top tube was the best.

Flow boiling of water in a vertical tube at sub-atmospheric pressure was studied by Barbosa Jr et al. [53]. The experiments were conducted at 250, 500 and 1000 mbar. They observed an enhancement of local heat transfer at near zero quality and postulated that the heat transfer enhancement was due to the formation of a large Taylor bubble at the onset of nucleate boiling.

The comparison of several sets of experimental data for boiling water done by Feldmann and Luke [54], Figure 2.4. The Nishikawa [10], Equation 2.13, Gorenflo [12], Equation 2.16, and Cooper [11], Equation 2.14, calculation methods for water boiling on copper surfaces with R_p = 0,4μm are included in Figure 2.4. Feldmann and Luke [54] conclude that the Gorenflo [12] equation predicts a stronger rise of the heat transfer coefficient than Nishikawa, as shown in Figure 2.4. Both methods seem to be more accurate for water than the correlation of Cooper, especially for intermediate and high reduced pressures. The Gorenflo [12] correlation shows a good agreement with the experimental results. For low pressures there is a large deviation within the experimental results. Cooper overestimates the heat transfer coefficient for the whole pressure range.

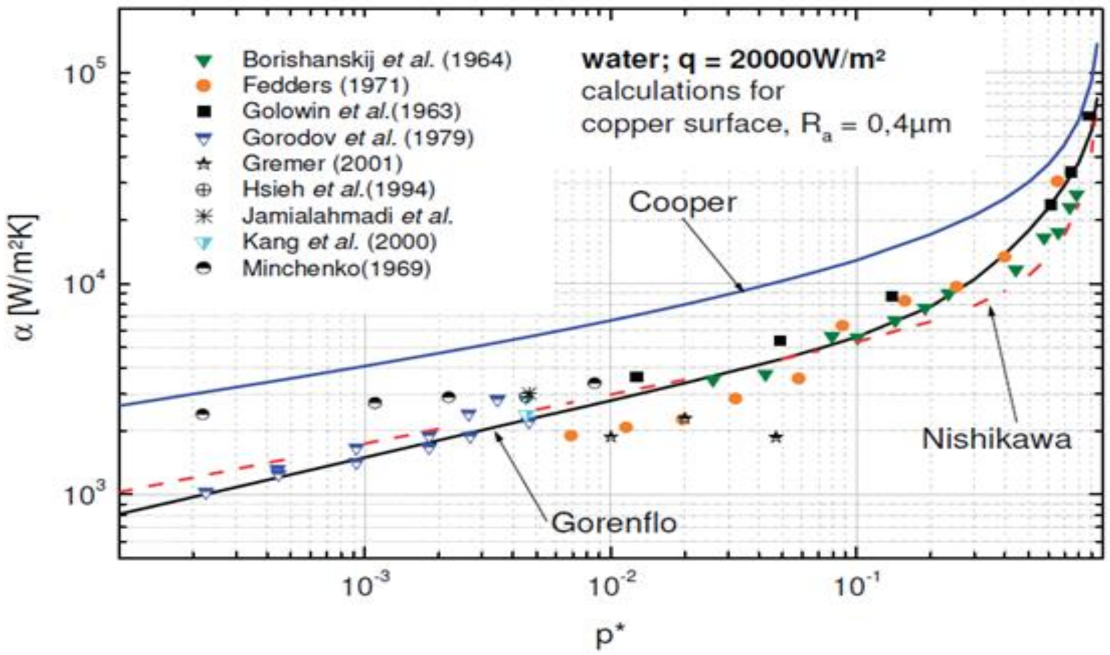

Figure 2-4: Comparison of experimental data for water calculated by [54] with the Methods of [10, 12] and [11]

A study of boiling heat transfer from a longitudinal rectangular finned surface immersed in saturated water at near vacuum pressure was presented by Chan et al. [55], they found that boiling at low pressure causes the formation of vapour films (compressed bubbles) inside the narrow fin spacing. At high heat flux, vapour films were present in all of the fin spaces, impeding the return of the liquid and leading to a decline in the slope of the boiling curve. Boiling at very low pressure between 1.2 kPa and 1.8 kPa was studied by Giraud et al. [56], they focused on a special boiling flow pattern, large bubble departure followed by the generation of many bubbles of different sizes which collapsed before leaving the wall. They explained that increasing the liquid height above the surface leads to an increase in the minimum wall superheat required to maintain nucleation and to a decrease in heat transfer.

Experimental research on water boiling on a horizontal copper rod surface was done by Yu et al [57] at sub-atmospheric pressure. The test conditions were 1.8–3.3 kPa and 4000–10,000 W/m^2.

They concluded the follows:

- ❖ At sub-atmospheric pressure, when the heat flux is constant, the boiling heat transfer coefficient of water increases with increasing pressure.

- When the pressure is low, the increase of boiling heat transfer coefficient with increasing pressure is slow. When the pressure reaches a certain value, the increase is enhanced.

- The Cooper correlation used for calculating the pool boiling heat transfer coefficient for refrigerants, is not consistent for their experiments, i.e., this correlation is not suitable for the calculation of evaporator heat transfer coefficients in water vapour compression refrigeration and heat pump systems.

Giraud et al [58] studied pool boiling of water over a large range of pressures from (0.85- 100) kPa on a horizontal heated copper disk. They presented a boiling curve that showed that as the pressure decrease, a new boiling regime appeared. The regime is specific to sub-atmospheric pool boiling and is referred to as the cyclic boiling regime. Fluctuation in the wall temperature in this regime reached 20 K affecting the heat transfer coefficient and causing material fatigue.

The influence of sub-atmospheric pressure on nucleate boiling was studied by Zajaczkowski et al [59]. Sixteen correlations were calculated and compared to the experimental data within pressure range of 1.0-10 kPa for heat flux of 10-45 kW/m^2, they found that the Montinski [6] correlation was the most accurate approximation for the heat transfer coefficient and that the Stephan and Abdelsalam [9] correlation showed reasonable agreement. The experiments were conducted by using an isolated glass cylinder with water boiling above the cooper plate. Their results showed that low pressures adjust the character of the boiling curve. The curve flattened and the region of natural convection shifted towards higher wall superheat because of the influence of low pressure on the bubble creation and bubble departure processes.

2.10 The Effect of Using Free Particles

As the liquid is evaporated in the actual evaporator, the solid can come out of solution and settle on the evaporator base, this solid can form different bed sizes. The effect of these particles on the base requires more understanding from the previous researches. Yang and Maa, Yamaguchi and James, Ma et al [60-62] reported that when a suitable amount of solid particles were present in a boiling liquid, the pool boiling heat transfer can be enhanced and the boiling hysteresis, is partly, or even completely, removed.

Chuah and Carey [63] presented the effects of a thin layer of free particles on saturated pool boiling heat transfer from a horizontal surface. They used two different types of particles, the first was glass spheres 0.275 and 0.475 mm in diameter, which have a low thermal conductivity and density, and the second was copper spheres 0.1 and 0.2 mm in diameter, which have a high thermal conductivity and density. They used water at a pressure of 1 atm with heat fluxes of 20-100 kW/m^2. For both types of particles, they observed that vapour moves vertically through chimneys in the particle layers that tended to fluidize the layer. Comparisons with normal pool boiling at the same level of heat flux showed that the addition of light and low conductivity particles significantly increases the wall superheat. However, the heavier and high conductivity particles decreased the wall superheat. Chuah and Carey [63] measured the coefficients of heat transfer with a layer of copper particles and found that for same heat flux, they were as much as a factor of two larger than those measured in normal pool boiling. Furthermore, the results obtained, showed that the boiling curve was insensitive to the thickness of the layer at least for thin layers.

McGillis et al [51] studied the pool boiling enhancement techniques for water at low pressure, [51]. They suggested that the presence of copper beads of 0.2 mm did not contribute to bubble nucleation and did not significantly enhance the nucleation behaviour. This was probably because additional large critical cavity sites were not introduced by adding small copper beads.

The experimental results for Shi et al [64] show that the boiling behaviour is significantly different from water pool boiling and that boiling heat transfer can be enhanced greatly for both a fixed particle or fluidized bed. Visual observations show that there are additional nucleation sites in the gaps between the particles and the heated surface. The onset boiling temperature is much lower than that of pure water boiling, especially for fixed particle beds. The boiling hysteresis phenomena almost disappear in all the boiling cases tested. Experimental observations also show that the average bubble size in nucleate pool boiling with solid particles are generally greater than those without particles, especially if the solid particles are static on the heated wall (that is, in a fixed bed) or not been fully fluidized. Bubble sizes are usually between 10 and 20 mm in diameter for water boiling on a copper surface under atmosphere pressure.

Shi et al [64] suggest that boiling heat transfer can be enhanced greatly by adding solid particles into the liquid, whether in a fixed particle bed or a fluidized bed. Their experimental results show that the boiling heat transfer enhancement is closely related to the particle size, the initial bed depth (in fluidized case) and the heat flux applied. The boiling heat transfer characteristics are greatly changed when a particle layer is put on the heated surface. Shi et al [64] concluded that the major effects of a fixed particle bed on nucleate pool boiling heat transfer is the nucleation sites, bubble motion and the thermal conductivity.

A free-particles-based, boiling enhancement technique was studied using water as the working fluid by Kim and Garimella [65]. Free metal particles placed on a heated surface were found to improve the boiling heat transfer by providing additional active nucleation sites. The enhancement was a function of the number and size of the particles introduced. An optimum particle size of 3 mm to 6 mm, depending on the heat flux, was identified. For the uniform particle size test cases, the largest average heat transfer coefficient over the range of heat fluxes tested was provided by the 3 mm particles. They also produced the lowest wall superheat at the onset of nucleate boiling. Models developed for vapour bubble embryo growth and incipience were consistent with these experimentally observed particles sizes. In order to maximize the boiling heat transfer performance, and invest the mechanistic compromise between a large particle size for simplicity of bubble growth/departure and a small particle size for more effective superheating of the surrounding liquid, mixtures of different sizes of particles were tested. A mixture of 3 mm and 6 mm particles was shown to improve the average heat transfer coefficient by 115% compared to a polished surface over a heat flux range of 20 to 100kW/m^2.

The concept of a free-particle technique for boiling heat transfer enhancement was also proposed in the companion paper by Kim et al [66]. They experimentally investigated the concept using the wetting fluid FC-72 as the working fluid. This technique introduces free-standing metal particles, which may be orders of magnitude larger than nanoparticles, on to the immersed boiling surface. The primary function of the particles was to change the local surface topography by forming narrow corner gaps between the particle and the surface. These cavities help for bubble nucleation and consequently enhance nucleate boiling at low heat fluxes. This nucleation enhancement mechanism is similar to conventional porous structure attached promoters, except that the particles are not fixed to the heated surface and are free to move.

2.11 The surface aging

The duration or history of the boiling may affect considerably the heat transfer coefficient in nucleate pool boiling, i.e. the age of the surface. The ageing of solid surfaces may be because of any or all of the following reasons:

- Changeable activity of minute pits, grooves.
- Deposition of a fouling film on the heated surface
- Corrosion of the surface.
- Fluctuations of the temperature during boiling, (hysteresis).
- The gradual expulsion of dissolved gases from the liquid.
- The release of gases occluded on the solid surface.

The time elapse required to reach steady state heat transfer rates will differ, being affected by all these factors and other conditions such as the purity of the liquid, the material and the heating surface initial condition. Jakob [67] first stated the ageing effect; following studies have implied that the attainment of steady state heat transfer depends mainly on the type of surface used, and to a lesser extent on its initial condition [68]. No general agreement, however, exists on the influence of heat flux on the ageing rate of a heating surface. In addition, rather little attention has been given to ageing in the boiling of organic liquids. In the chemical and petroleum industries the design of boiling equipment for organic liquids is of considerable importance.

Bergles and Chyu [69] observed the Hysteresis behaviour in nucleate pool boiling on porous metallic coatings, with reasonably wetting liquids, such as water, and highly wetting liquids, such as R-113. The surface aging, surface sub cooling and heat flux change affected the range of the temperature overshoot and resultant boiling curve hysteresis. The hysteresis was supposed to have occurred due to flooding of the porous matrix with liquid so that only relatively small sites are available for nucleation. Introduction of foreign gas was found to be effective to overcome this behaviour but the way it works was not well understood. Boiling hysteresis was observed with Gewa-T tubes but to a significantly lower degree to that observed with Thermoexcel-E and High Flux as described by Ayub and Bergles [70]. Chyu and Bergles [71] also confirmed that boiling on structured surfaces started readily with no hysteresis.

2.12 The One-Dimensional Model

The geometry of thin slice model used in this study is similar to those used in the study of kettle reboilers. A review of these studies is given by Bamardouf and McNeil [72] Most of these studies were carried out using pentane and refrigerant R113. This study used water.

The kettle reboiler is one of the most commonly used shell and tube heat exchangers in the process industry and consists of a tube bundle placed in a shell. The conventional one-dimensional model is applied in sections of the shell where the flow is at right angles to the tube bundle. This approach is frequently used in the design of kettle reboilers [73-76]. A recirculation model [75, 77] was developed by Burnside et al [78] to predict the flow and heat transfer in the bundle for a uniform heat flux. Each column, with the appropriate number of tubes, was treated separately as a column of square cells with boundaries half way between the tube centres. The tubes were immersed in a pool of saturated liquid. The recirculation mass flux, *m*, was based on equating the head of liquid in the pool against the sum of the gravitational, ΔP_G frictional, ΔP_f and momentum, ΔP_m.

(Bamardouf and McNeil,2009), the model assumed that a constant vertical mass flux, m_v, passed upwards through a column, and that the total vertical pressure drop across it was the static liquid value for the height of the column. The horizontal mass flux was taken to be zero. The pressure gradient for each tube within the column had a frictional, gravitational and acceleration component. However, the acceleration component was negligible. The momentum equation for the one-dimensional model of a two-phase mixture with a liquid density of ρ_l, a vapour density of ρ_g and a void fraction of Є was therefore given by

$$\frac{\partial p}{\partial y} = -\rho_{TP} g + F_{sf} \qquad \textit{2-68}$$

where p is the pressure, y is the distance up the column, ρ_{TP} is the two-phase density, given by Equation 2.64, g is the acceleration due to gravity and F_{sf} is the force on the fluid by the tubes and is given by

$$F_{sf} = \Delta P_f \qquad \textit{2-69}$$

where ΔP_f is given by Equation 2.68. Bamardouf and McNeil [72] investigated the relevant available pressure drop data for one-dimensional flow across tube bundles and recommended that, for kettle reboilers, the tube friction factor be evaluated from ESDU [39] Equation 2.55, the void fraction from Feenstra et al [36] et al. Equation 2.50 and the two-phase multiplier from Ishihara et al [31] Equation 2.67. It is assumed that the flow enters the base of a column of tubes as a saturated liquid. The energy equation is therefore

$$\frac{dx}{dy} = \frac{\pi D q}{m_v p_v p_h h_{fg}} \tag{2-70}$$

where D is the tube diameter, q is the heat flux, $h_{fg}$is the enthalpy of evaporation and p_v and p_h are the vertical and horizontal tube pitches, respectively.

2.13 Conclusion

There are many research papers on the boiling at high pressure. Boiling at low (vacuum level) pressures has not had very much attention in the literature. Some pool boiling data has been reported, most of the studies focus on enhancement of the heat transfer, bubbles behaviour, and agreement of some correlation to the experimental results, the important points of the boiling at low pressure can be concluded as:

- Reduction in heat transfer
- Decrease in pressure delayed the onset of nucleate boiling, led to increase in the bubble size and reduced the CHF.
- The contribution of latent heat was insignificant compared to the vapour-liquid exchange.

- Higher wall superheat required
- Cooper [11], Gorenflo [12] and Stephan and Abdelsalam correlations [9] showed reasonable agreement.
- The heat transfer enhancement effect decreases with decreasing test pressure
- A special boiling flow pattern, new boiling regime
- The increase of boiling heat transfer coefficient with increasing pressure is slow**.**

But there is a lack of data on the characteristics at low pressures, especially, the tube bundle effect, thermal fluid process at low pressure and the boiling mechanism. This study was initiated to investigate the changes that occur in evaporator operation as the pressure is reduced and because of the geometry of the evaporator used in this study is similar to those used in the study stated above of kettle reboilers, so one dimensional model can be used for more understanding.

Most of the research papers used the solid particles as enhancement techniques for the boiling heat transfer. Most of them used metal particles at atmospheric and concentrate on the particle sizes effect at atmospheric pressure and higher pressures. All the reported results are still insufficient to define the effect of solid particles on the evaporator base at vacuum. This study is to investigate the influence of glass particles on evaporator base using range of 0-32 mm bed depth.

Chapter 3: EXPERIMENTAL APPARATUS AND DATA PROCESSING

3.1 Experimental Apparatus

The layout of the test facility is shown in Figure 3.1. Deionised water flows from the hot-well to the test section via the pump. Heat was supplied to the evaporator by Joule heating that generated vapour within the three part test section. Vapour from the test section was condensed and sub-cooled to approximately 12°C in the condenser before being returned to the hot-well. The entry point to the test section could be selected as shown in Figure 3.1. The Vacuum pump was used to control the pressure of the system.

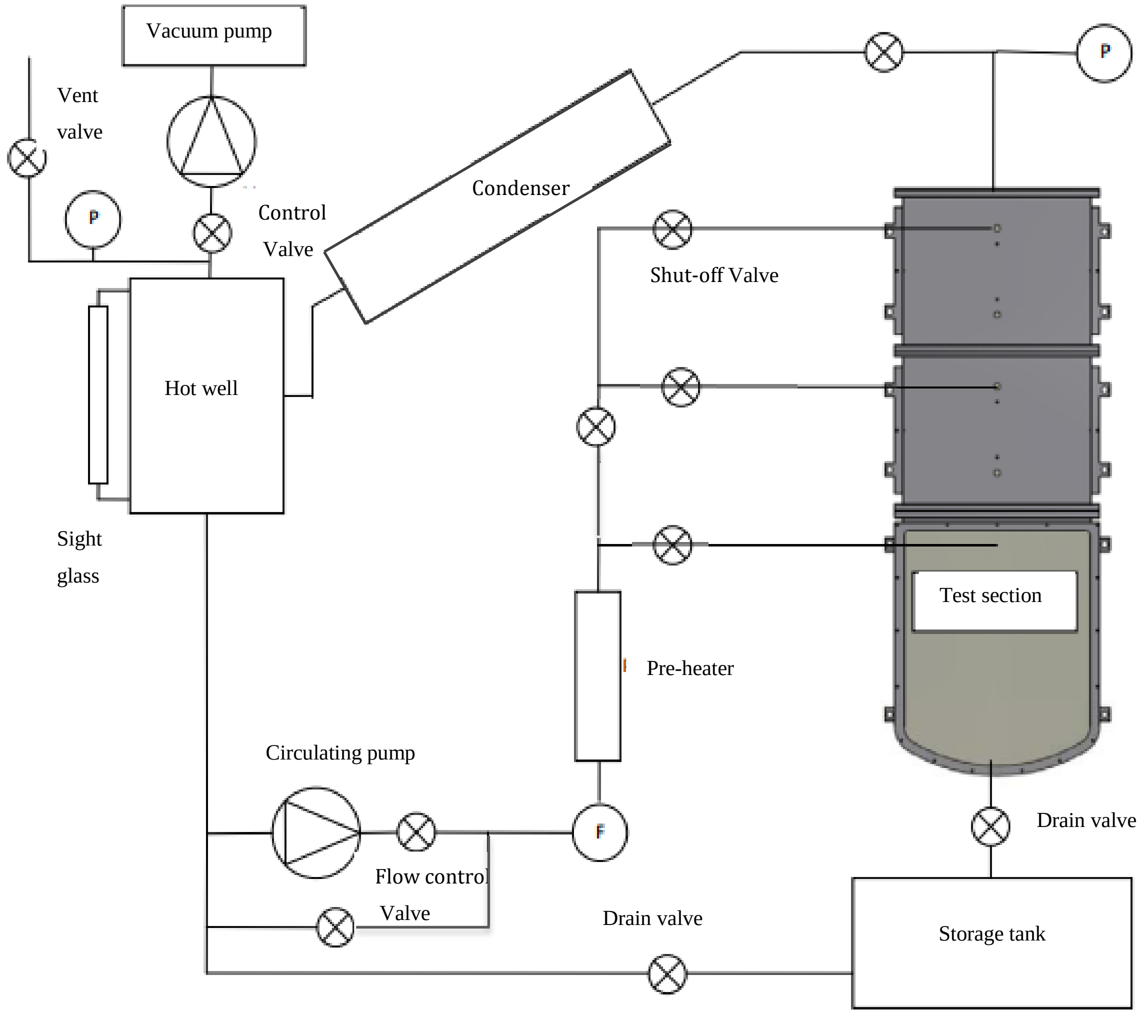

Figure 3-1: plane layout

3.1.1 ***Test Section***

The test section was manufactured from stainless steel and is shown in Figures 3.2 and 3.3. The main vessel was 1 m high, 0.75 m wide and 98 mm deep. The two smaller vessels were 0.6 m high and were used to vary the pool height from quarter scale up to the level attained in the actual evaporator. The mid and upper sections were identical and are shown in Figures 3.2 and 3.4.

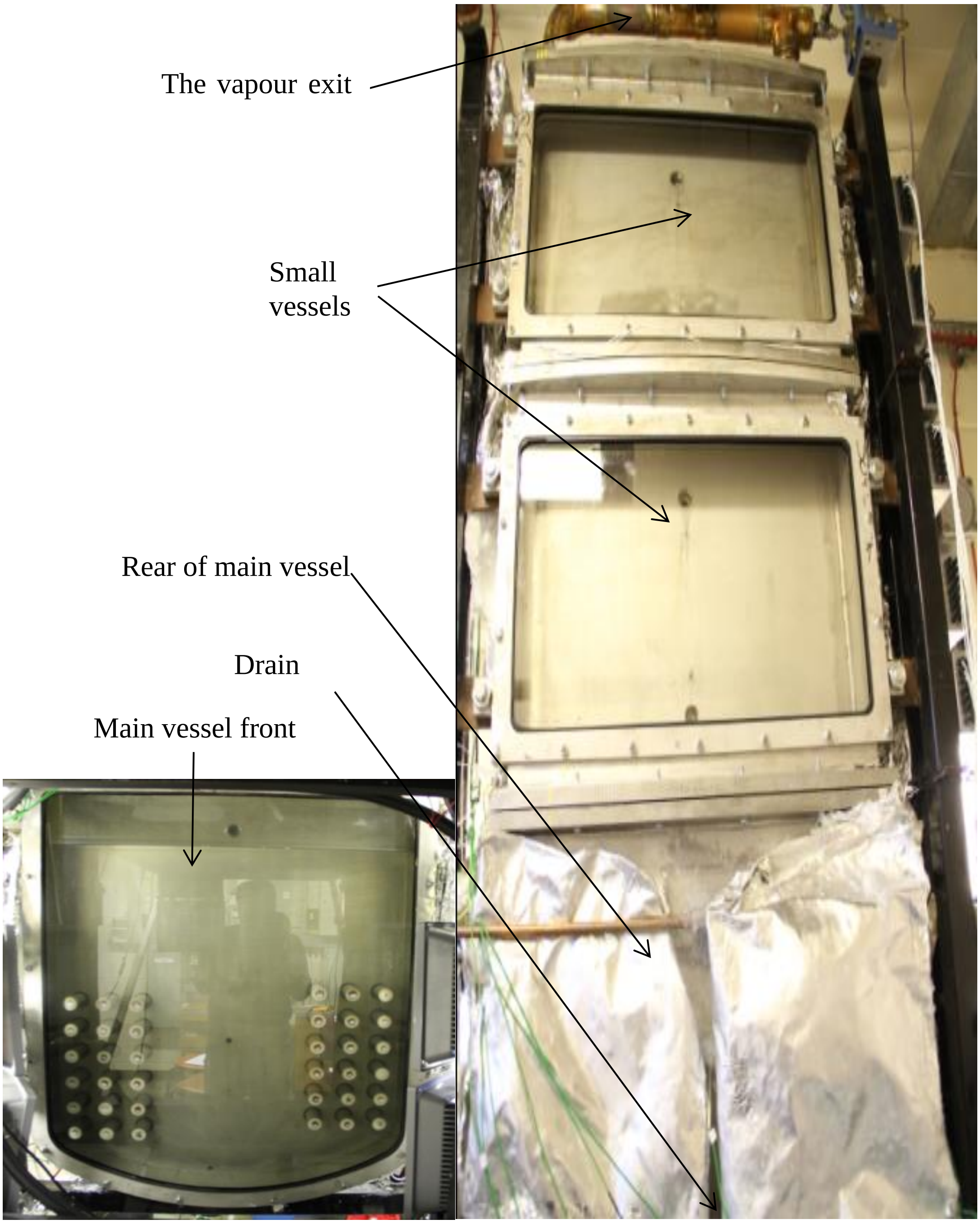

Figure 3-2: test sections

The vapour exit port was 50 mm at diameter and was situated in the top of the third vessel. The feed was introduced through one of three possible inlet ports. They were all located on the shell centre line as shown in Figure 3.3 and 3.4 and were connected to the hot-well via the preheater. A forth port, the drain was situated in the bottom of the main test section; this was connected to the water storage tank. All four ports had a diameter of 13 mm. The vessels in Figure 3.2 were fitted with viewing windows. These windows were made from toughened glass, 25 mm thick. The glass was compressed against a 3 mm rubber seal by a stainless steel flange. After assembly, the shell and accompanying pipe-work were insulated with 30 mm thick glass wool.

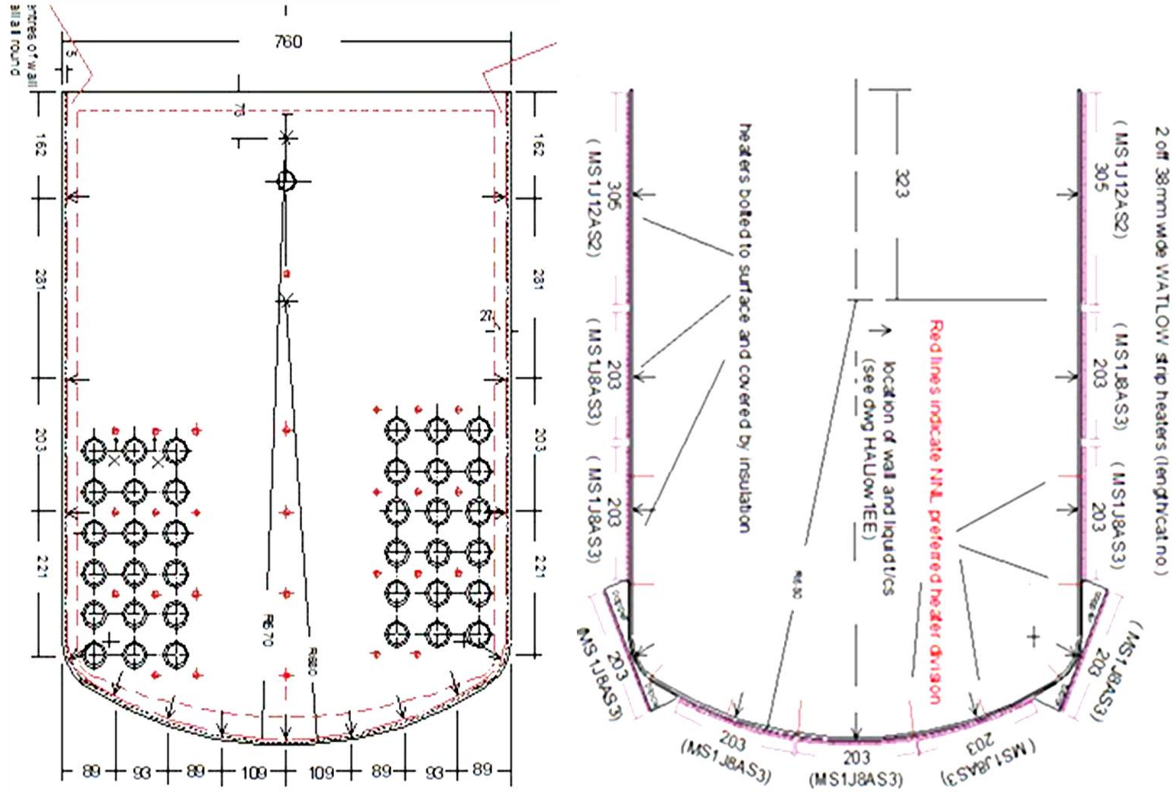

Figure 3-3: test section

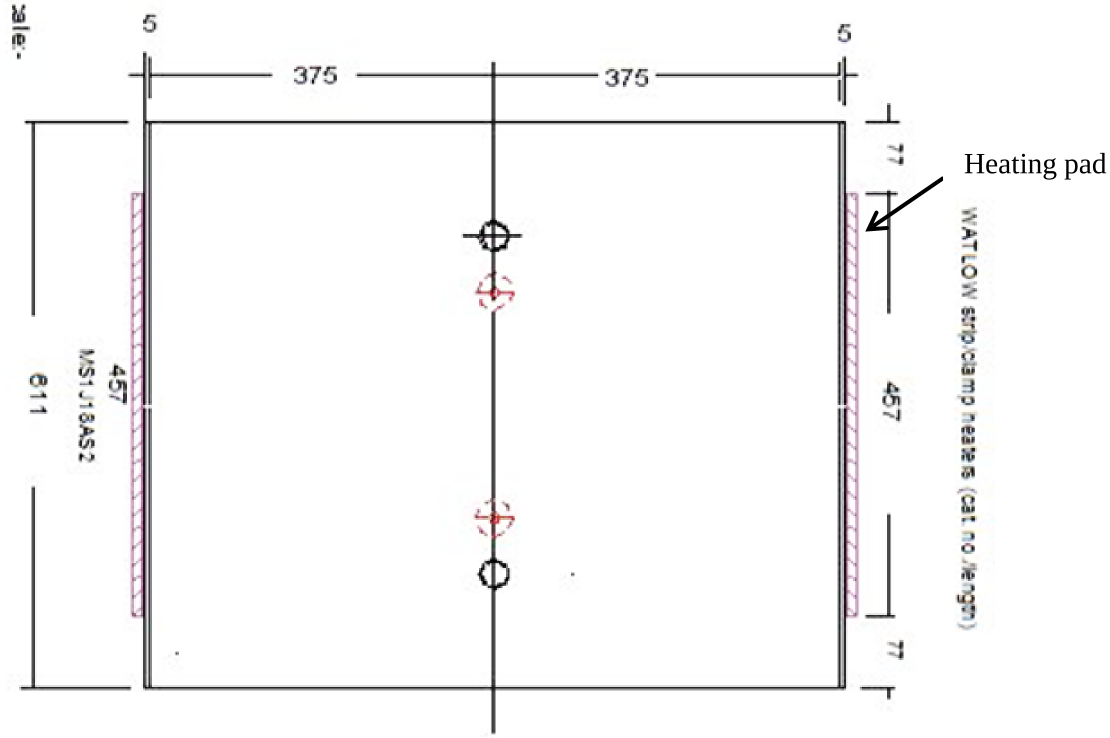

Figure 3-4: mid and upper section

3.1.2 *Tube Bundle*

The two tube bundles each contained 18 tubes in an in-line configuration, with a horizontal tube pitch of 69 mm and a vertical tube pitch of 62.5 mm. The tubes were made of brass, had an outside diameter of 28.5 mm, a length of 98 mm, were 5 mm thick and were electrically heated. The tubes in the left hand bundle of Figure 3.2 were offset by 32 mm above those in the right to replicate a thin slice through tube coils. Each tube contained a rod heater. The rod heater had a diameter of 15 mm, and was 90 mm in length as shown in Figure 3.5. The tube heater arrangement is shown in Figure 3.6. The tube bank is divided into six sectors, 1-6, each with 6 tubes, 3 on either side, dividing the bundle volume into six blocks, representing the six coils in the evaporator.

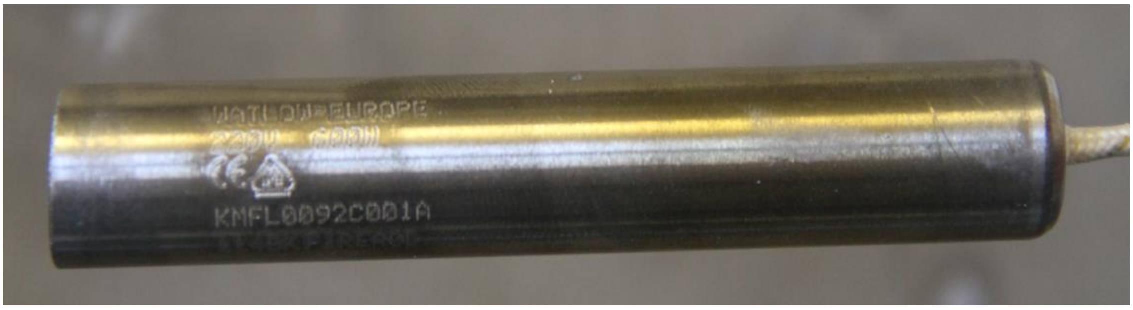

Figure 3-5: The tube cartridge heater

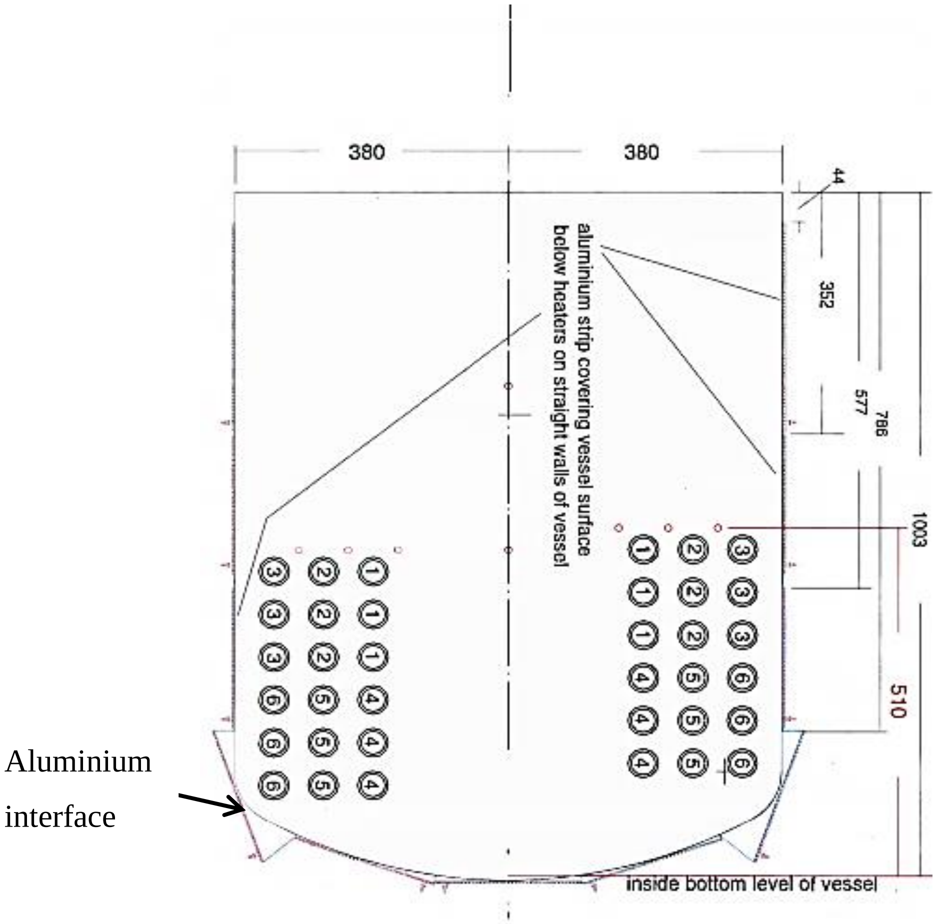

Aluminium interface

Figure 3-6: tube and wall heaters arrangement

3.1.3 ***Wall Heater***

Wall heating was provided by pairs of 38mm wide, Watlow MS1J18A strip heaters, shown in Figure 3.7. They were uniformly spaced on the walls of the vessels, as shown in Figure 3.3. Because of variable curvature of the walls of the lower vessel, as shown in Figure 3.6, and because the heaters were rigid, the assembly contained aluminium adaptors between the walls and the heaters. The straight walls in the upper vessels and in the upper part of the lower vessel had adaptors that were 1.5 mm deep and wide 92 mm strips of aluminium. On the lower vessel these strips covered the whole length of the surface and were longer than the heaters, Figure 3.2 and 3.3. On the upper vessel walls the length of the strips are the same as the heaters, Figure 3.4.

Figure 3-7: wall heaters

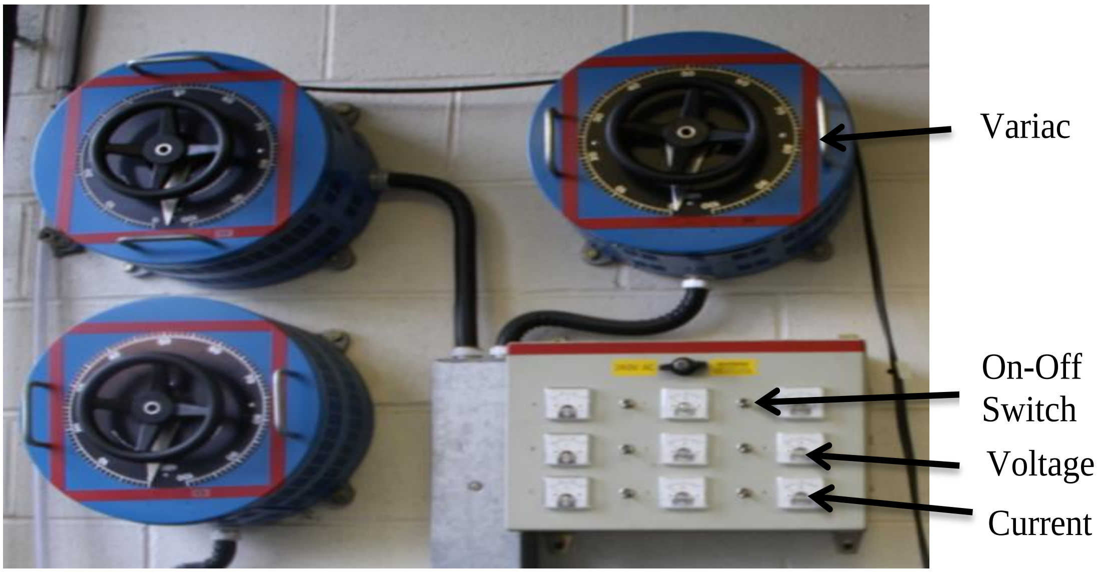

Figure 3-8: variacs

3.1.4 ***Power Supply***

The 240 V, 50 Hz supply to the heaters was taken from a 440 V, 3 phase 50 Hz supply. Power to the heaters was controlled by 11 variac variable transformers. Six variacs controlled the power to the tube heaters, with each variac supplying six cartridge heaters. Five variacs supplied power to the wall heaters. Dial gauge meters indicated the voltage and current in each circuit. These were mounted on the supply box, one box per phase, that housed fuses and on/off switches as shown in the Figure 3.8. The switches allowed any particular tube bank to be isolated.

All the measurement and control circuitry were located in the same laboratory. Wires to the heaters were routed through ducting that terminating on sealed die-cast boxes that were mounted on the boiler support framework.

The bottom three sets of the wall heater pairs were connected to a single power controller, controller F. The next four mirror-imaged heater pairs were on controller E. The top four heater pairs were also on a single controller, controller D. However, a switch was in place that allowed the top pairs to be switched off, as the MS1J12AS2 heaters were only used in high level tests.

3.1.5 ***Vacuum Pump***

The rig operates at a pressure of 50 to 850 mbar absolute. Inevitably for a vacuum system, air leaked in and had to be removed to allow the operating pressure to be maintained. To avoid removal of excessive amounts of vapour from the rig while removing the air, the method chosen was to reduce the temperature of the condensate to a level where the vapour partial pressure was low and hence the vapour air mixture was predominantly air. Removal of the air was accomplished by pumping away only a small amount of vapour. This method is commonly used in modified Rankine cycle steam plant. However, the problem in this study was that the flowrate of condensate was very low, a maximum of 0.0143 kg/s. Therefore a CVC 3000 vacuum pump was used for this purpose. The CVC 3000 vacuum pump manages the vacuum by working to a set point and altering the pump speed to maintain it.

3.1.6 ***Circulating Pump***

The circulating pump used was a GRUDFOS 25-80. This pump is a single phase pump, it provided a head of up to 8 metres, with a flow rate of up to 5.7 m^3/h and a system pressure of up to 10 bar.

3.1.7 ***Feed System***

The feed flow system is shown in Figure 3.9, and was controlled by the Crane D934 15 mm valve. The maximum flow rate corresponding to all wall heaters on at a heat flux of 45 kW/m^2 and the maximum tube heating of 70 kW/m^2 is 0.0175 kg/s or 0.0176l/s. The bypass flow, Figure 3.9, was controlled by Crane D931 (DN20) 20 mm, fixed orifice double regulating valve (DRV), which combines control and orifice metering of the flow. The pressure drope over the range of flow rates and handwheel setting of the bypass and the feed control valves were plotted from the K_V values provided by the manufacturer.

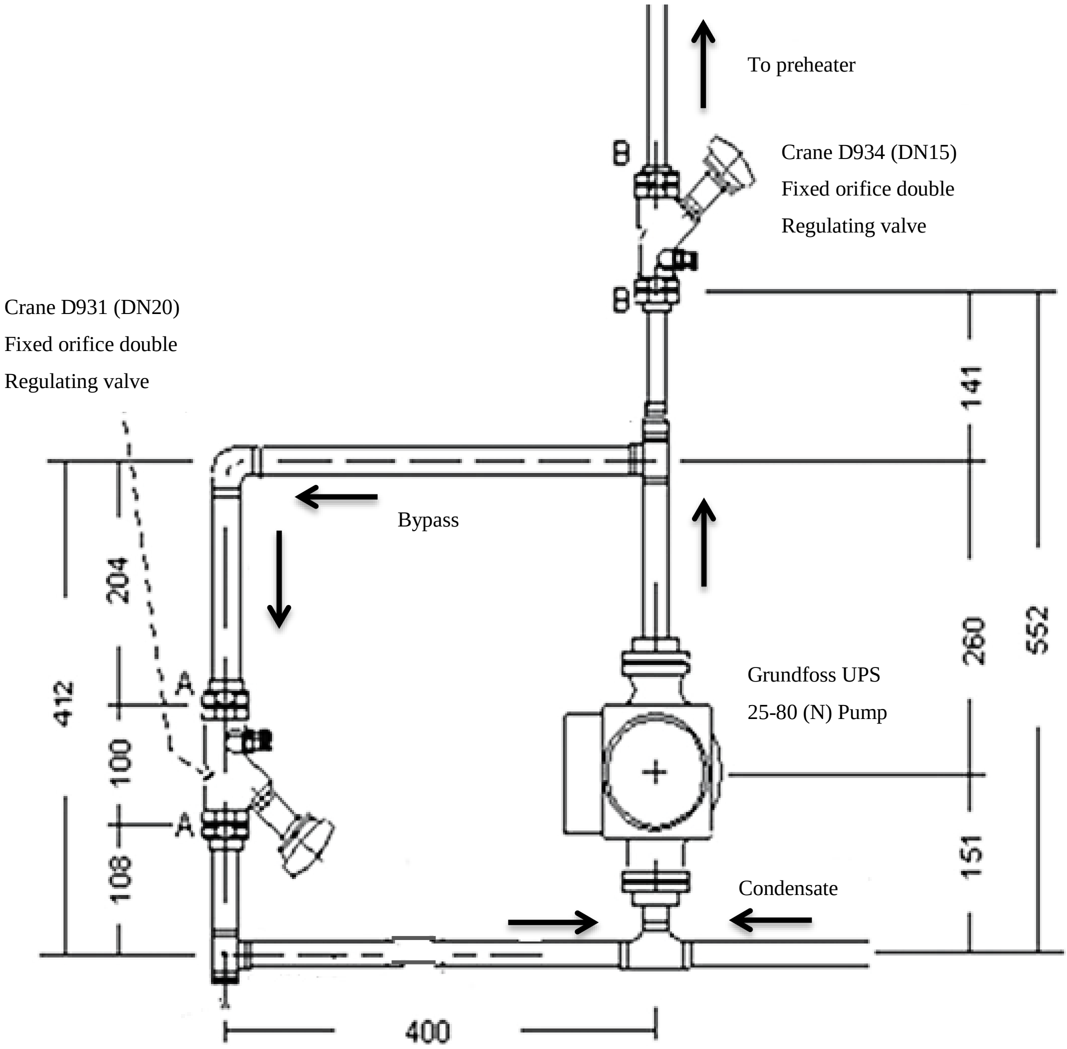

Figure 3-9: Rig feed pump circuit

3.1.8 *The Condenser*

The condenser was a Serck ZA396 heat exchanger. This is a single pass condenser with condensation on the tube side. A cooling water flow rate of up to 85 l/min was available for cooling the condenser.

3.1.9 *The Hot-Well Tank*

The hot-well tank was made of stainless steel was 40 cm high, 20 cm wide and 20 cm deep. It had a sight glass to observe the water level as shown in Figure 3.10. The hot- well was connected to the atmosphere via a valve. This valve used to allow air into the rig and increase the pressure back to atmospheric pressure.

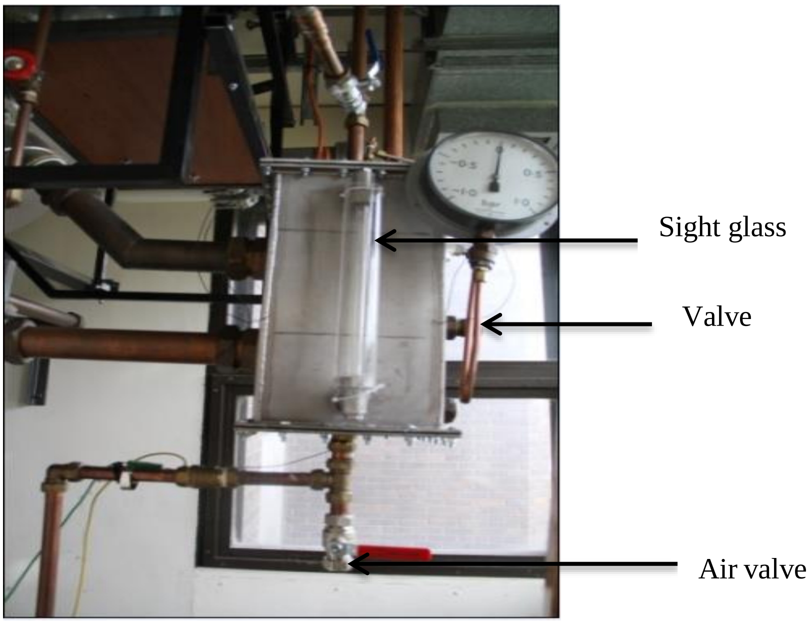

Figure 3-10: Hot-well tank

3.2 Instrumentation

3.2.1 ***Pressure***

The test-section and pool pressures were measured by Rosemount 1151 absolute pressure transducers. These smart pressure transducers were accurate to ± 0.25% of range and the range was set by a HART communicator. A Rosemount 1151 differential transducer was available to measure the pressure difference across the tube bundle. This was a fixed range transducer, accurate to ±0.5% of range.

3.2.2 ***Flow Rate***

The flow rate was set by adjusting the pump control valves until a steady level was obtained in the hot-well sight glass. The flow rate was measured by a Pelton wheel turbine meter, accurate to ±1% of reading.

3.2.3 ***Temperature***

TC Direct thermocouples were positioned in the shell to measure the liquid and wall temperatures. The thermocouple locations in the test section are shown in Figure 3.11. Only the right-hand-side of the evaporator contained thermocouples. The thermocouples were classified into 4 groups. The first group are referred to as the stream thermocouples. The ‘stream’ was considered to start at the free surface in the top section, flow down the centre line through the mid-section and on to the base of the test section, move across the base and up the side walls of all three sections, before returning to the free surface. These thermocouples were numbered T_{S1}-T_{S18} and are shown in Figure 3.11.

The second group are referred to as the wall thermocouples. They began in the centre of the wall at the base of the test section, moved across it and up through the other sections. These thermocouples were numbered T_{W1}-T_{W10}, and are also shown in Figure 3.11.

The third group are the tube thermocouples. These are numbered from right to left going top to bottom as T_{T1-T18} in Figure 3.11. The fourth and final groups are the fluid thermocouples. These were the thermocouples located in the fluid between the tubes and were also numbered right to left going from top to bottom as T_{F1}-T_{F11} in Figure 3.11.

All temperatures within the evaporator were measured by k-type thermocouples and were connected to the data logger system. The same system was used in the calibrations and in the tests.

3.2.4 ***Data Logger***

The National Instrument data logging equipment was linked to a PC and controlled through LABVIEW software. All instruments, except the power meter, were connected to NI data logging equipment that was linked to a PC, Figure 3.12, and. The software allowed monitoring of the instruments during operation and logging of the data when required.

3.2.5 ***Power***

For the tube bundle, inner most tubes were on a single power controller, coil 1, with the upper 3 middle tubes on coil 2 and the upper 3 outer tubes on coil 3. The lower tubes were similarly powered as coils 4-6. This allowed each coil to operate independently, as is possible on the actual evaporator. A uniform heat flux was applied to the tubes in this study. The power to each left (three tubes) and right (three tubes) for each coil was measured by a power meter. Each sector is controlled by one variable transformer. The object of this arrangement is to enable the imposition of non-uniform heat flux patterns.

For the wall heaters, Controllers D, E, and F, the mid and upper sections were powered independently through controllers P2 and P5. These independent controllers allowed a distribution of wall heat to be applied. The power measured by the power meter. The data was entered into a computer file manually. The power meter was accurate to ±1% of reading.

3.2.6 ***Cameras***

Two webcam cameras (Logitech) Tessar 2.0/3.7, 2 MP Autofocus, were used. One was used to monitor the test section and the other to monitor the mid and upper sections. These were controlled through Lab view software and recordings of each test condition were made prior to measurement being taken. Another camera, SLR EOS 7D CANON, was used to monitor the test section to get more detailed pictures and videos. This camera used to record the visual images had a resolution of 5184 x 3456 pixels.

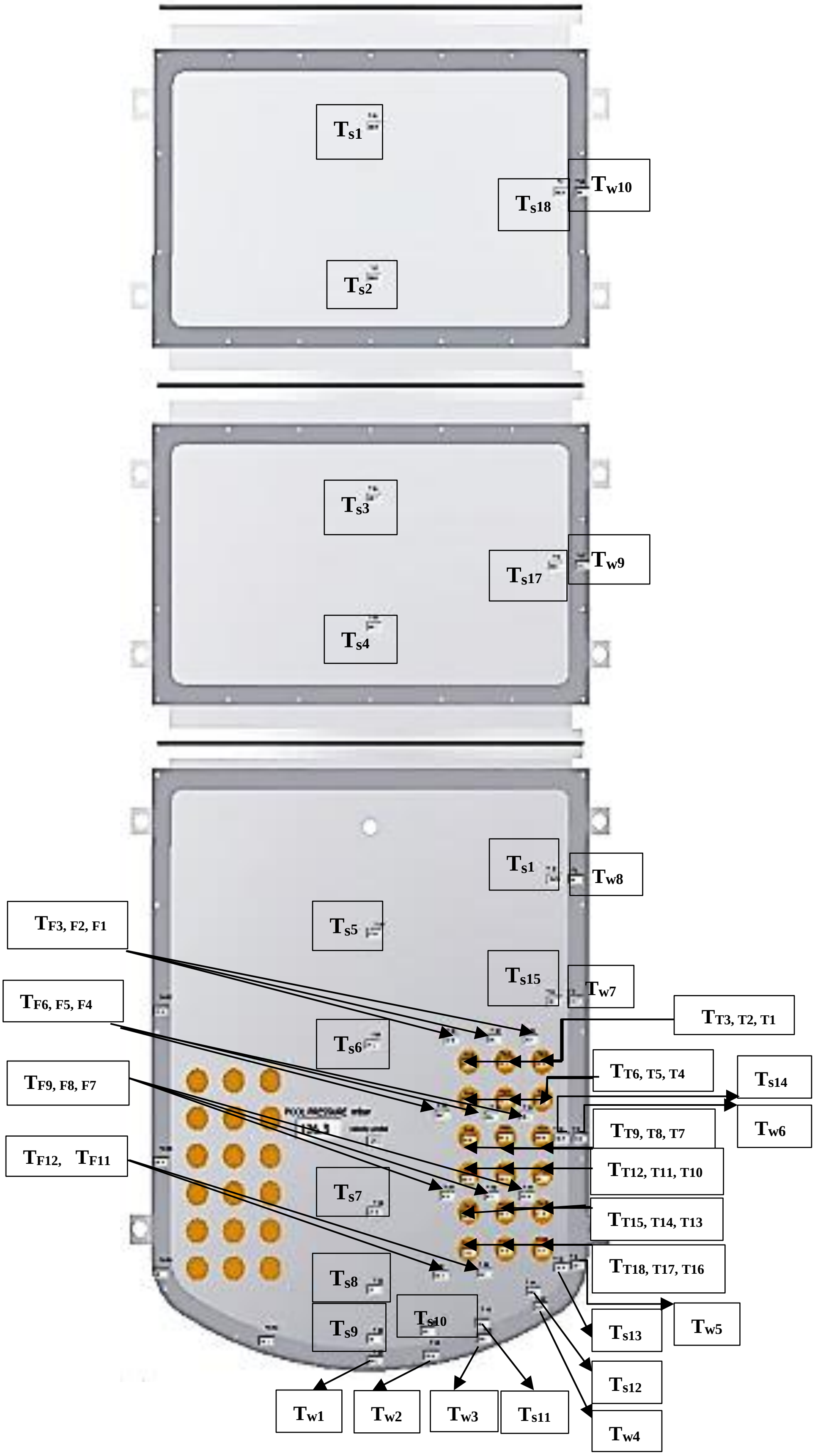

Figure 3-11: Thermocouple locations

3.3 Operation Procedure

To fill the rig with deionised water, both drain valves and the vent valve were closed and the vacuum pump control valve was opened, Figure 3.1. The vacuum pump was switched on until the test section pressure was reduced to 500 mbar. The drain valve to the test section was opened, allowing water to flow from the storage tank to the evaporator. The drain valve was closed when the desired water level was achieved in the evaporator. The drain valve from the hot well was opened, allowing water to flow from the storage tank to the hot well. The drain valve was closed when the water reached the desired height in the hot-well sight glass. The circulating pump, water control valves and the evaporator entry shut-off valve were opened, allowing water to flow from the hot well to the vessel, purging any air from the pipe work. The shut-off valve was closed when a steady flow of water was evident in the evaporator.

To operate the rig, the vacuum pump was switched on and adjusted until the required test section pressure was achieved. Heat was supplied to the evaporator by Joule heating of rod heaters contained within the tubes. Initially, the tube heaters were switched on at 90% of full power. After some time, steam was generated. This pushed any remaining air into the hot well before it was expelled to the atmosphere. When condensate began to accumulate in the hot well, the liquid entry shut-off valve was opened and the circulating pump was started. The flow rate was set by adjusting the pump control valves until a steady level was obtained in the hot-well sight glass. Water from the hot-well was pumped by the circulating pump into the test section via the pre-heater. The inlet temperature can be set by adjustment of the pre-heater. However, this was not used in these tests. Vapour from the vessel was condensed and subcooled before being returned to the hot-well. Steady conditions were achieved in about 3 hours, whence the power controllers were set to produce the required heat flux for the test. Test conditions were achieved in a further 30 minutes. To obtain data set a, each instrument was read once per second over a 2 minute period. The readings were obtained a second time, ten minutes later, to obtain data set b. Thereafter, the power controllers were set to the next condition and the procedure repeated until the necessary heat-flux range had been achieved.

3.4 Adding the Glass Particles

The glass particles obtained has similar properties to barium nitrate, it’s contained a range of particle sizes and all less than 1.0 mm. The particle size is compatible to the particle size in the actual evaporator. A sieving machine with different meshes was used to obtain particles 0.5-0.6 mm in diameter. Sieving was repeated many times to obtain this range. A volume of glass particles size 0.5-0.6 mm was measured in a measuring cylinder. These particles were weighted to establish a mass-volume relationship. The volume of the base of the evaporator against the centre line height, H, was obtained from the test sections geometry. Measured masses of particles were positioned on the base of the test section to achieve the required bed depth as shown in Table 3.1. To add the particles to the test section, the required mass of glass particles was mixed with some water. The drain valve from the test section, Figure 3.1, was opened, allowing the mixture to flow into the vessel where the glass beads separated from the water to form the required bed. When the tube heat flux was applied, the convection current within the test section produces a flatbed surface, an example is shown in Figure 3.14.

Table 3-1: mass of glass particles required for each bed depth

bed depth	Total particles weight
04 mm	**60 gram**
08 mm	**168 gram**
12 mm	**310 gram**
16 mm	**475 gram**
24 mm	**876 gram**
32 mm	**1346 gram**

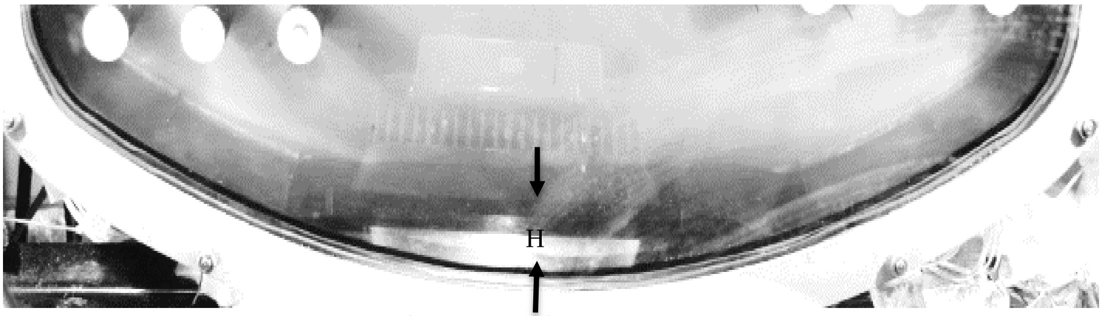

Figure 3-12: flatbed surface at a 32 mm bed depth

3.5 Data Processing:

The heat transfer mechanism could fall into one of three categories, single phase, sub-cooled boiling or saturated boiling. The difference between the first and the other two is the heat transfer temperature. For single phase flow this is the liquid value, for the others it is the saturation value. The onset of nucleate boiling was taken to occur when the heat flux, q, was related to the wall temperature through, [79],

$$q = \frac{Q}{A} = \frac{K_l h_{fg} \rho_v (T_w - T_{sat})^2}{8\sigma T_{sat}} \qquad \textit{3-1}$$

where K_l is the liquid thermal conductivity, $h_{fg}$is the enthalpy of evaporation, ρ_v is the vapour density, T_{sat} is the saturation temperature and σ is the liquid surface tension. If the wall temperature fell below the value from Equation 3.1, the local liquid temperature was used otherwise the saturation value was used.

The heat-transfer area was taken as the outside surface area of a tube A. The heat flow, Q, to the tubes on the right hand side of a coil, i.e. 3 tubes, was measured. The tube heat flux, q, was therefore found from $q = \frac{Q}{3A}$. For the tube heat transfer coefficients, the heat transfer area is the outside surface area of the tubes on the right hand side of a coil, i.e. 3 tubes. The power to the right side of each coil was measured. The surface temperature of each tube surface can be found from

$$T_w = T_{tc} - \frac{qD}{2K_B} ln(\frac{D}{D-2L_{tc}}) \qquad \textit{3-2}$$

where T_w is the measured wall temperature, D is the outside diameter of a tube,K_B is the thermal conductivity of brass, 190 W/mK, and L_{tc} is the depth of the thermocouple from the tube surface, i.e. 2.5 mm.

The coil heat fluxes can be found as shown in the Table 3.2.

Table 3-2: The coil heat fluxes

Coil	Tube no	Heat flux
Coil 1	12	$\mathrm{PTR}(1)/(3\Pi \mathrm{D}\, L_{tc})$
	15	$\mathrm{PTR}(1)/(3\Pi \mathrm{D}\, L_{tc})$
	18	$\mathrm{PTR}(1)/(3\Pi \mathrm{D}\, L_{tc})$
Coil 2	11	$\mathrm{PTR}(2)/(3\pi \mathrm{D}\, L_{tc})$
	14	$\mathrm{PTR}(2)/(3\pi \mathrm{D}\, L_{tc})$
	17	$\mathrm{PTR}(2)/(3\pi \mathrm{D}\, L_{tc})$
Coil 3	10	$\mathrm{PTR}(3)/(3\pi \mathrm{D}\, L_{tc})$
	13	$\mathrm{PTR}(3)/(3\pi \mathrm{D}\, L_{tc})$
	16	$\mathrm{PTR}(3)/(3\pi \mathrm{D}\, L_{tc})$
Coil 4	3	$\mathrm{PTR}(4)/(3\pi \mathrm{D}\, L_{tc})$
	6	$\mathrm{PTR}(4)/(3\pi \mathrm{D}\, L_{tc})$
	9	$\mathrm{PTR}(4)/(3\pi \mathrm{D}\, L_{tc})$
Coil 5	2	$\mathrm{PTR}(5)/(3\pi \mathrm{D}\, L_{tc})$
	5	$\mathrm{PTR}(5)/(3\pi \mathrm{D}\, L_{tc})$
	8	$\mathrm{PTR}(5)/(3\pi \mathrm{D}\, L_{tc})$
Coil 6	1	$\mathrm{PTR}(6)/(3\pi \mathrm{D}\, L_{tc})$
	4	$\mathrm{PTR}(6)/(3\pi \mathrm{D}\, L_{tc})$
	7	$\mathrm{PTR}(6)/(3\pi \mathrm{D}\, L_{tc})$

where PTR are power variables for right tubes, Figure 3.11.

The analyses, of the evaporator is considered in columns and rows as shown in Figure.3.13.

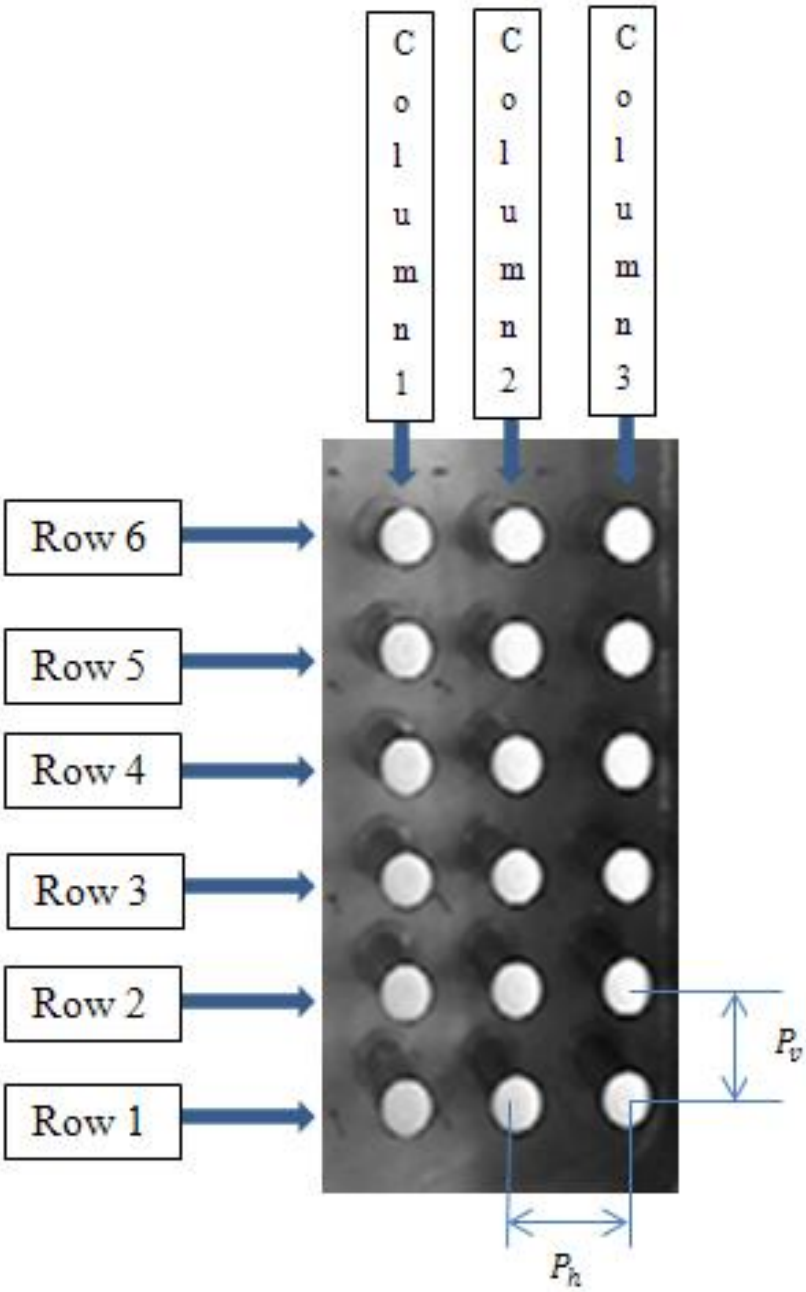

Figure 3-13: columns and rows numbering

The liquid temperatures were distributed throughout the pool. The temperature for each tube was found as shown in the Table 3.3.

Table 3-3: The liquid temperature at tubes

Row	Tube nu	Liquid temperature at tube
Row 1	16	$T_{L16} = (T_{F7} + T_{F13})/2.0$
	17	$T_{L17} = (T_{F8} + T_{F10})/2.0$
	18	$T_{L18} = (T_{F9} + T_{F11})/2.0$
Row 2	13	$T_{L13} = T_{F7}$
	14	$T_{L14} = T_{F8}$
	15	$T_{L15} = T_{F9}$
Row 3	10	$T_{L10} = (T_{F4} + T_{F7})/2.0$
	11	$T_{L11} = (T_{F5} + T_{F8})/2.0$
	12	$T_{L12} = (T_{F6} + T_{F9})/2.0$
Row 4	7	$T_{L7} = T_{F4}$
	8	$T_{L8} = T_{F5}$
	9	$T_{L9} = T_{F6}$
Row 5	4	$T_{L4} = (T_{F1} + T_{F4})/2.0$
	5	$T_{L5} = (T_{F2} + T_{F5})/2.0$
	6	$T_{L6} = (T_{F3} + T_{F6})/2.0$
Row 6	1	$T_{L1} = T_{F1}$
	2	$T_{L2} = T_{F2}$
	3	$T_{L3} = T_{F3}$

The saturation temperature was evaluated from the local pressure, p, found from

$$p = p_s + \rho_l g H \tag{3-3}$$

where p_s is the measured shell pressure, ρ_l is the density of liquid and H is the depth of the tube centre line from the free surface. The height of the free surface above the pool measurement location was found from

$$H_{pool} = \frac{(p_{pool} - p_s)}{\rho_L g} \tag{3-4}$$

where p_{pool} was the measured pool pressure. Liquid properties were evaluated at the liquid temperature with vapour properties evaluated at the local saturation conditions deduced from the local pressure.

For the walls, the heat transfer area depended on the heat spreaders used. The heat was assumed to spread across the full width of the wall, i.e. 92 mm, and the total length of the heat spreaders controlled by a given power controller. These were 0.5964 m for controller F, 0.8065 m for controller E, 0.45 m for controller D during low level tests and 1.144 m during high level tests, 0.9141 m for controller P2 and 0.9141 m for controller P5. The supplied power was as measured. The wall temperature at each wall location was found from:

$$T_W = T_{tc} - \frac{q\,L_{tc}}{K_s} \qquad 3\text{-}5$$

where K_s is the thermal conductivity of stainless steel, 16 W/mK. The depth of the thermocouple from the wall surface, L_{tc}, was 2.5 mm. The liquid temperature at each wall location can be found as, Figure 3.11,

$T_{WL1} = T_{S9}$ $T_{WL2} = T_{S10}$
$T_{WL3} = T_{S11}$ $T_{WL4} = T_{S12}$
$T_{WL5} = T_{S13}$ $T_{WL6} = T_{S14}$
$T_{WL7} = T_{S15}$ $T_{WL8} = T_{S16}$
$T_{WL9} = T_{S17}$ $T_{WL10} = T_{S18}$.

A heat balance was obtained by measuring the volume of condensate collected in the hot-well and comparing the associated cooling power with the power supplied to the tubes. The cooling power was found to be 96% of the heating power. For the wall, the cooling power was found to be 92% of the heating power.

3.6 Uncertainty

All of the thermocouples were calibrated in a water bath. The water bath contained a heater, a stirrer and a resistance thermometer accurate to ±0.1°C. The thermocouples, with the necessary compensation cable attached. The thermocouple holes were located at better than ±0.5 mm on their pitch circle radius. The uncertainty in the wall temperature therefore varied from ±0.1 K to ±0.2 K as the heat flux increased from 10 to 70 kW/m^2. The pressure in the test-section vapour space was measured by an absolute pressure transducer, accurate to 0.25% of range. With this uncertainty in the pressure at the free surface, the uncertainty in the corresponding calculated saturation temperature is ±0.9 K for the 50 mbar tests and ±0.1 K for the 850 mbar tests. A second, similar pressure transducer measured the pool pressure. The uncertainties in the pressure at the free surface and in the pool combined to give an uncertainty in the calculated pool height of ±51 mm.

Chapter 4: EXPERIMENTAL THERMAL RESULTS FOR VARIOUS PRESSURES

4.1 Introduction

The campaign to investigate the effect of pressure on the thermal performance of the evaporator contained four tests series. The first series, the LLLP, low pressure low liquid level series, was carried out at 50 mbar absolute pressure and at a low liquid level. The second series, the HLLP, low pressure high liquid level series, was carried out at a pressure of 50 mbar and at a high liquid level. The third series, the LLMP, medium pressure low liquid level series, was carried out at a pressure of 450 mbar at low liquid level. The fourth series, the LLHP, high pressure low liquid level series, series, was carried out at a pressure of 850 mbar and at a low liquid level. The tube heat flux was varied from 10-65 kW/m^2 for the LPLL series and the LPHL series, and varied from 10- 70 kW/m^2 for the LLMP series and the HPLL series. The tests were carried out at two pool heights, one at approximately 0.8 m, the low level tests, and one at approximately 2m, the high level tests. The stream temperature locations are shown in Figure 3.11 and the rows and columns are obtained in Figure 3.13

4.2 LLLP Series (50 mbar)

These tests was carried out at 50 mbar absolute pressure at low liquid level, the pool height was approximately 0.8 m. The tube heat flux in this test was varied from 10- 65 kW/m^2.

4.2.1 *Stream Temperature for the LLLP Series (50 mbar)*

Tests with the tube heat flux within the range of (10-65) kW/m^2 produced the stream temperatures shown in Figures 4.1. Included in Figure 4.1 are the saturation temperatures corresponding to the pressure at the free surface and the evaporator base. The saturation temperature varies from 32^{o}C at the free surface to 49^{o}C at the evaporator base. Figures 4.1 shows that the stream temperatures are close to the free surface saturation temperature for all heat fluxes. However, for heat fluxes of 10, 25, 40 and 55 kW/m^2, they are slightly below the free surface saturation temperature, while they are slightly above at a heat flux of 65 kW/m^2. The stream temperatures are well distributed throughout the pool. These results are therefore indicative of fluid recirculation taking place, with fluid flashing to the saturation temperature at the free surface before returning to the depths of the pool.

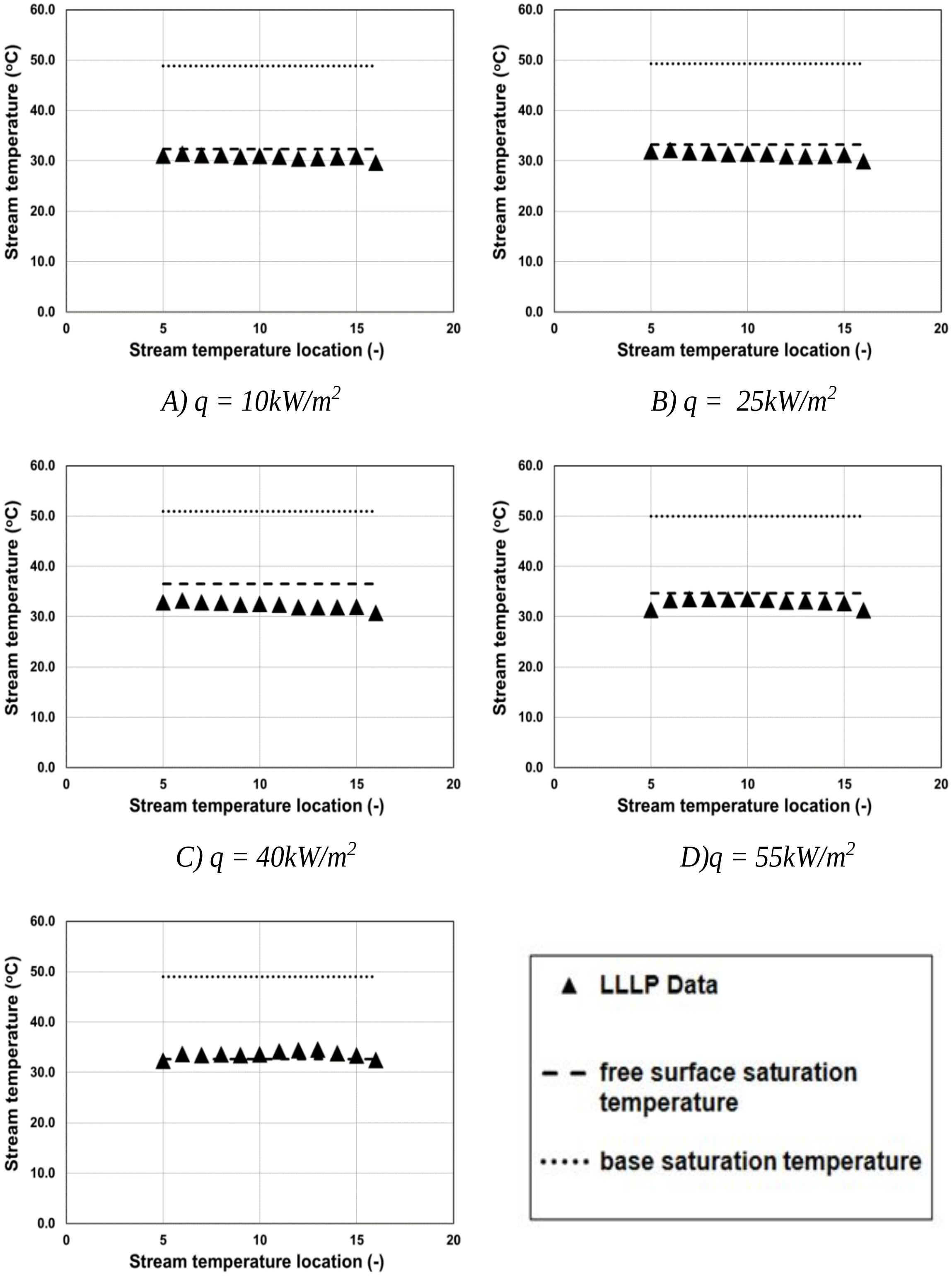

A) q = 10kW/m^2

B) q = 25kW/m^2

C) q = 40kW/m^2

D)q = 55kW/m^2

E) q = 65kW/m^2

Figure 4-1: Variation of stream temperature with stream location

4.2.2 ***Tube and Liquid Temperatures for the LLLP Series (50 mbar)***

Tube and fluid temperature are shown in Figure 4.2a for a tube heat flux of 10 kW/m^2. Included in the Figure are the saturation temperature and the boiling onset temperature. The boiling onset temperature was found from the applied heat flux so that it represents the maximum temperature that can occur without boiling happening. The saturation and boiling onset temperatures increase with pool pressure (depth). Reasonably constant fluid temperatures are shown. These temperatures are below the local saturation temperature and are consistent with the stream temperatures, Figure 4.1, and therefore support the concept of re-circulation within the evaporator. The liquid has a large degree of subcooling, typically 11K. All tube temperatures are below the saturation temperature except tubes in rows 3 and 4 of column 3 and row 4 of column 2. Figure 4.2a, shows that all of the tube temperatures are less than the onset boiling temperature, therefore convective heat transfer is taking place.

Figure 4.2b shows the temperatures for a heat flux of 25 kW/m^2. All of the tube temperatures are higher than the saturation temperature and the degree of sub-cooling is similar to the 10 kW/m^2 case. Most of the tube temperatures are below the onset boiling temperature, and are therefore in the single phase regime. However, the temperatures of the tubes in rows 3, 4, and 5 of columns 3 are above the onset boiling temperature, indicating that boiling is likely on these tubes. The tube temperatures differ about 9 K.

Figure 4.2c shows the temperatures for a heat flux of 40 kW/m^2. The liquid temperatures are below the saturation temperature with a sub-cooling of about 10.4 K. The liquid temperatures vary within 2.3 K. Tube temperatures in rows 2, 3, and 4 of column 3, and in row 1of column 1 are above the onset boiling temperature. Therefore, these tubes are in the sub-cooled boiling regime. The other tube temperatures are less than the boiling onset temperature and are therefore in the single phase regime. The tube temperatures vary within 9.1 K.

Figure 4.2d shows the temperature for a heat flux of 55 kW/m^2. The liquid temperatures are reasonably uniform varying by about 1.7 K and are less than the saturation temperature. The tube temperatures of the rows 2, 3, 5 and 6 in column 1 and row 6 in columns 2 and 3 are below the onset boiling temperature. Therefore these tubes are in the single phase regime. The others are above, and are in the sub-cooled boiling regime.

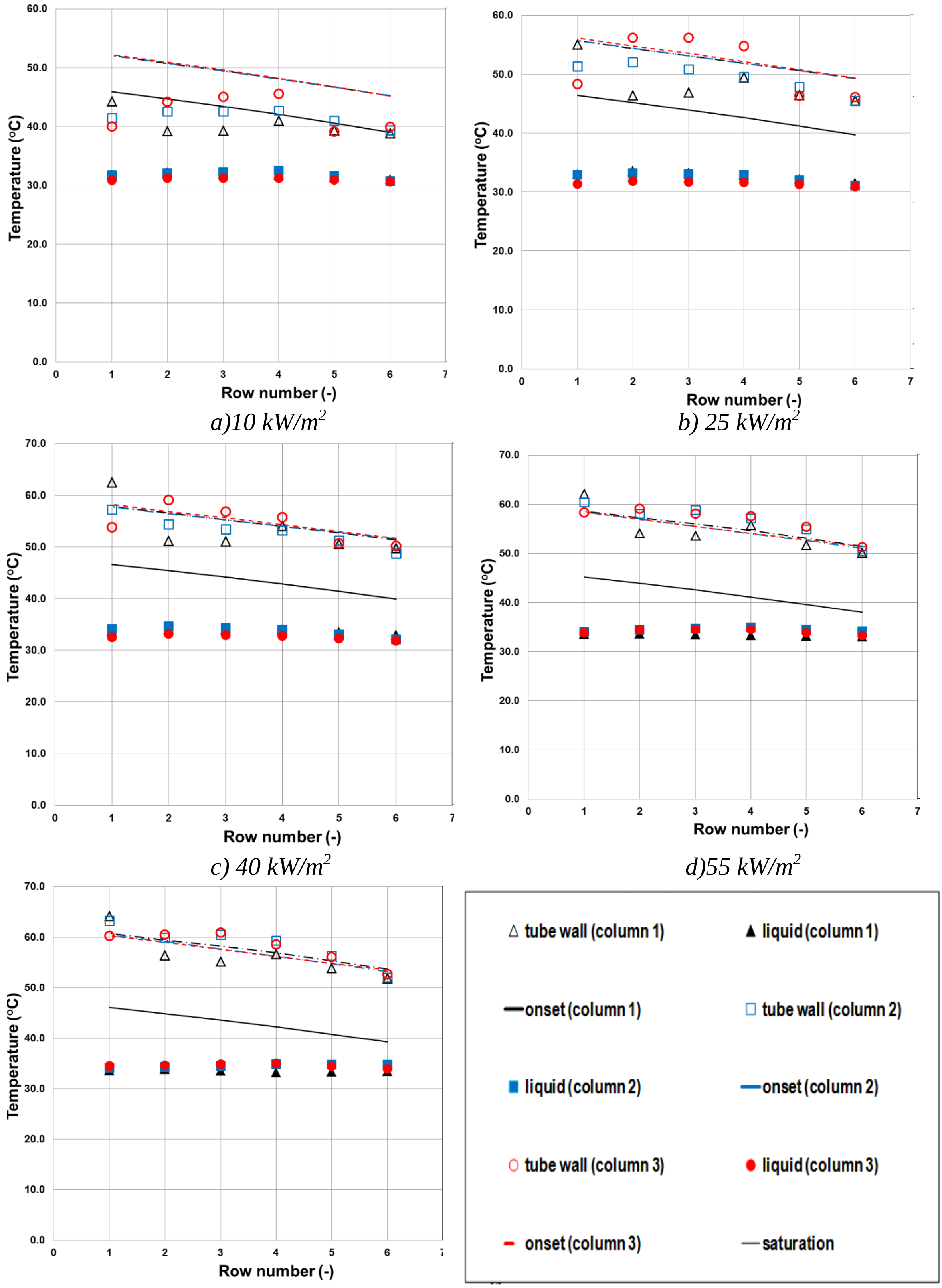

a)10 kW/m^2 b) 25 kW/m^2

c) 40 kW/m^2 d)55 kW/m^2

f) 65 kW/m^2

Figure 4-2: Variation of tube and liquid temperatures with row number for a heat flux

Tube and fluid temperature are shown in figure 4.2f for a heat flux of 65 kW/m^2. The liquid temperatures vary within 0.8 K, so they are practically constant. The degree of subcooling is typically 8.6 K. All tubes are shown to be boiling except row 5 of column

1 and row 6 of columns 1, 2 and 3, which are in single phase convection. Overall, all the liquid temperatures for all heat fluxes are below the local saturation temperature and are reasonably close to the stream temperatures. The liquid temperatures are approximately constant and therefore support the concept of re-circulation within the evaporator. The LLLP data have a reasonably large degree of sub-cooling, typically 11 K, and have a tube temperatures that vary by about 8.6 K. Most tube temperatures for heat fluxes of 10, 25 and 40 kW/m^2 are shown to be below the boiling onset temperature and therefore most tubes are in the single phase regime. For heat fluxes of 55 and 65 kW/m^2, most tube temperatures are above the boiling onset temperature, so most of the tubes are in the subcooled boiling regime.

4.3 LLMP Series (450 mbar)

These tests were carried out at 450 mbar at low liquid level, the pool height was approximately 0.8 m. The tube heat fluxes in these tests were varied from 10-70 kW/m^2.

4.3.1 *Stream Temperature for the LLMP Series (450 mbar)*

Variation of stream temperature with stream location for heat fluxes of 10-70 kW/m^2 are shown in Figure 4.3. The saturation temperatures corresponding to the pressure at the free surface and the evaporator base are included. The behaviour for all applied heat fluxes looks similar. The difference between the base saturation temperature and the free surface saturation temperature is 3.7 K for all of the tests. The stream temperature is approximately the same for all heat fluxes, it varies by about 0.9 K at a heat flux of 10kW/m^2, 0.7 K at a heat flux of 20 kW/m^2, 0.8 K at a heat flux of 30 kW/m^2, 0.6 K at a heat flux of 40 kW/m^2, 0.6 K at a heat flux of 50 kW/m^2, 0.5 K at a heat flux of 60 kW/m^2 and 0.6 K at a heat flux of 70 kW/m^2. The stream temperature is close to the free surface saturation temperature for all cases. The stream temperature is less than the free surface saturation temperature by 1.3-2.2 K for a heat flux of 10 kW/m^2, 1.6-2.3 K for 20 kW/m^2, 1.6-2.4 K for 30 kW/m^2, 2.0-2.6 K for 40 kW/m^2, 2.1-2.7 K for 50kW/m^2, 1.8-2.3 K for 60 kW/m^2 and 1.9-2.5 K for 70 kW/m^2. In general, the stream temperatures varies by 0.5-0.9 K and the difference between the free surface saturation temperature and stream temperature was 1.3-2.7. Therefore, this reasonably uniform stream temperature suggests that recirculation is taking place within the pool, with fluid flashing to the saturation temperature at the free surface before returning to the depths of the pool.

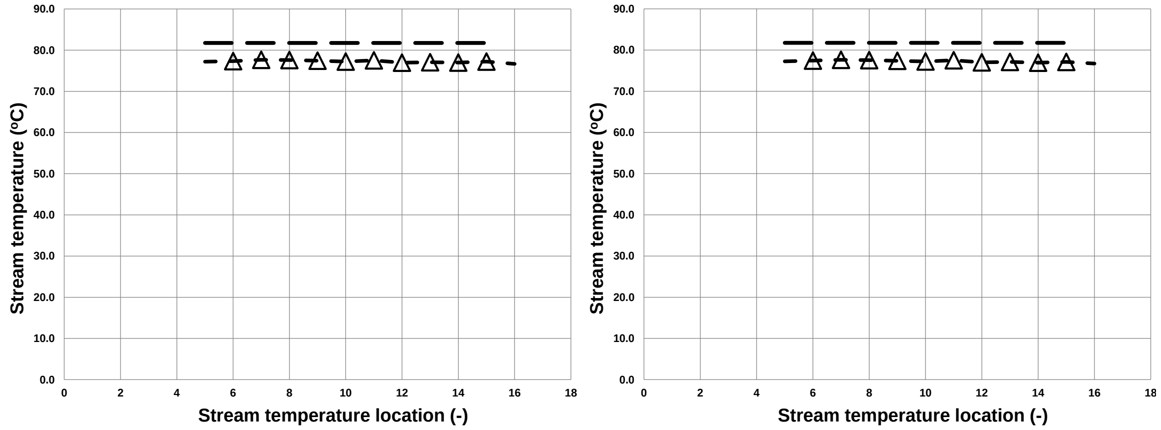

a)10 kW/m² *b)20 kW/m²*

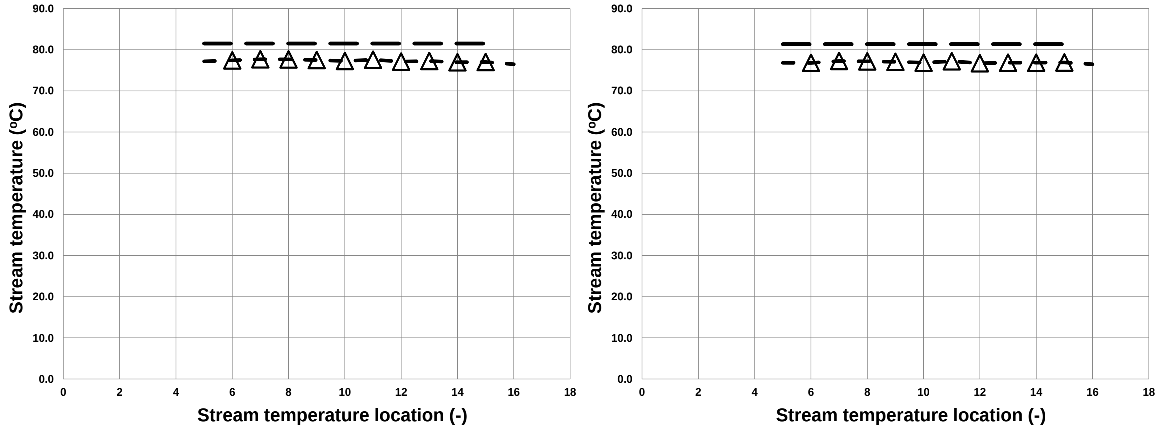

c) 30kW/m² *d) 40 kW/m²*

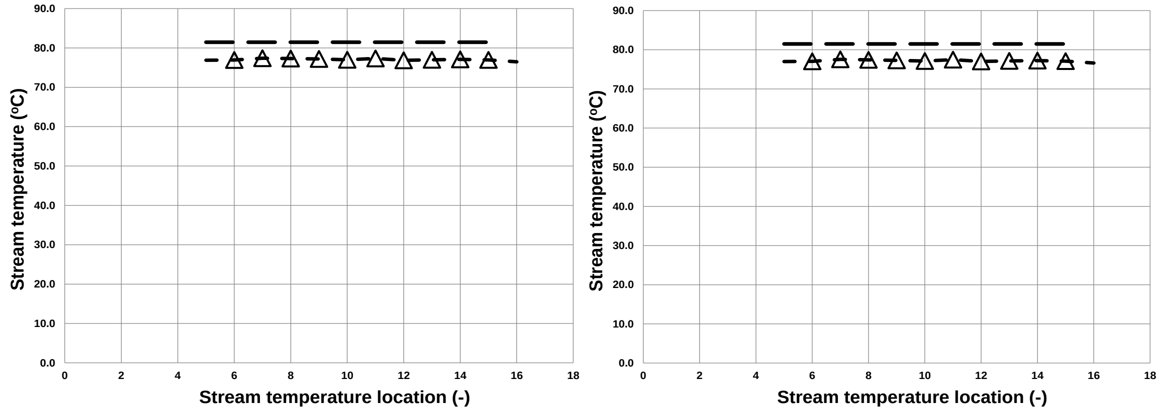

e) 50kW/m² *f) 60kW/m²*

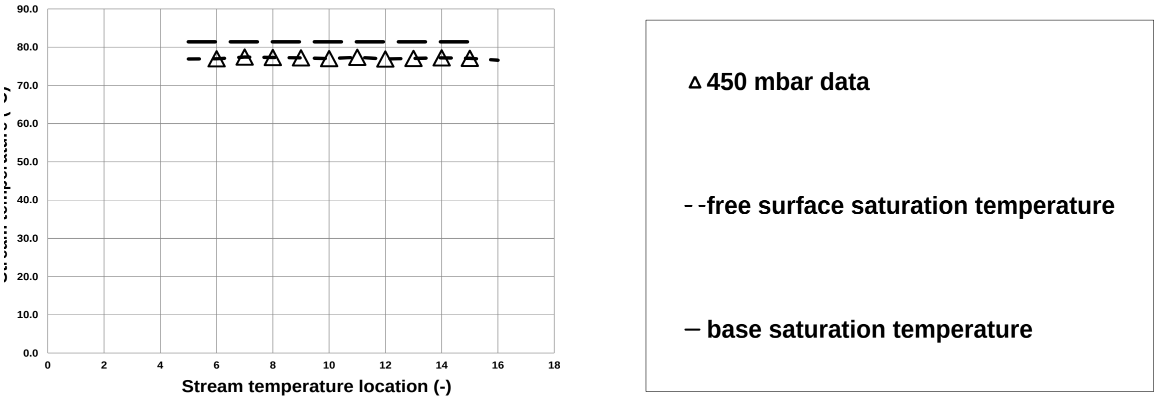

g) 70kW/m²

Figure 4-3: Variation of stream temperature with stream location

4.3.2 *Tube and Liquid Temperatures for the LLMP Series (450 mbar)*

Variation of liquid and tube temperatures with row number for the LLMP series are shown in Figure 4.4. Included in the figures are the onset boiling temperature for each column and the saturation temperature. For a heat flux of 10 kW/m^2, Figure 4.4a shows that in column 1 the degree of sub-cooling is about 2.6 K. The tube temperatures vary by about 3.9 K and they are all above the onset boiling temperature by 1.3-3.9 K. All the tubes are therefore in the sub-cooling boiling regime. The liquid temperatures in column 1 vary by about 0.6 K. In column 2 the sub-cooling is about 2.6 K and the liquid temperatures differs by 0.7 K. The tube temperatures vary by about 3.8 K and they are above the onset boiling temperature by 0.7-3.4 K. In column 3 the degree of sub-cooling is typically 3.1 K and varies within 3.1 K. The tube temperatures vary by about 2.0 K and exceed the boiling onset temperature by 0.8-2.0 K. For a heat flux of 20 kW/m^2, Figure 4.4b shows that column 1 was a degree of sub-cooling of about 2.6 K and that the liquid temperature varies within 0.4 K. The tubes temperatures vary by about 2.9 K and they are above the onset boiling temperature by 1.4-3.5 K. All the tubes are therefore boiling in the sub-cooled regime. Column 2 has a degree of sub-cooling of about 2.6 K and the liquid temperatures differ by 0.8 K. The tube temperatures vary by about 2.2 K and are above the onset boiling temperature by 2.1-2.8 K. All of the tubes are in sub - cooling boiling regime. Column 3 has a degree of sub-cooling of about 3.1 K with a 0.5K variation. The tube temperatures vary within 2.8 K and are above the onset boiling temperature by 1.6-4.1 K. The tubes are all boiling in the sub-cooled regime.

Figure 4.4c for a heat flux of 30 kW/m^2 Shows that Column 1 has a small degree of sub- cooling of about 2.4 K that varies within 0.4 K. The tube temperatures vary within 2.0 K and are above the onset boiling temperature by 3.4-5.1 K. The tubes are boiling in subcooled regime. Column 2 shows a small degree of sub-cooling of about 2.3 K with the liquid temperatures varying within 0.6 K. The tube temperatures vary by about 2.7K and are higher than the onset boiling temperature by 3.1-4.8 K. Thus, all the tubes are boiling in the sub-cooled regime. Column 3 shows that the liquid temperature is below the saturation temperature by about 2.8 K and varies within 0.5 K. The tube temperatures differ by 3.8 K and are above the onset boiling temperature by 3.4-6.5 K. All the tubes are in sub-cooled boiling regime.

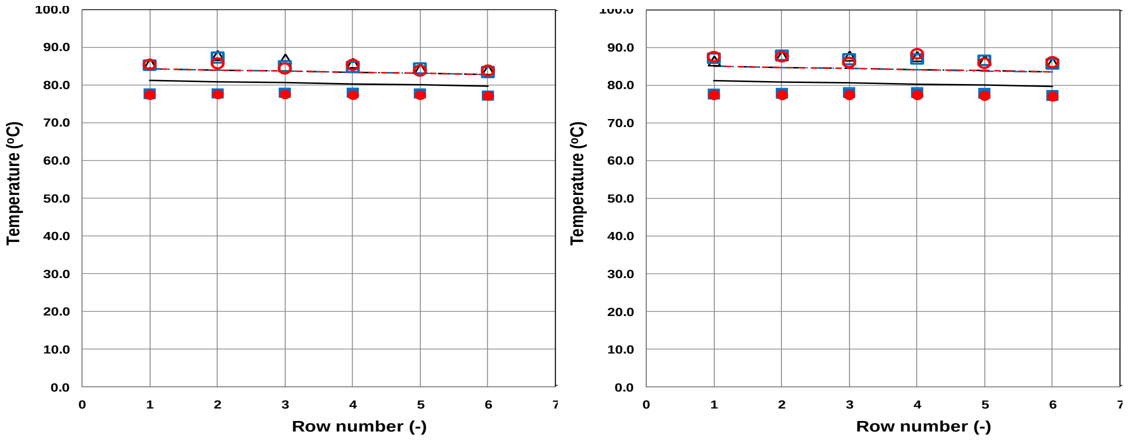

a) 10 kW/m²   *b) 20 kW/m²*

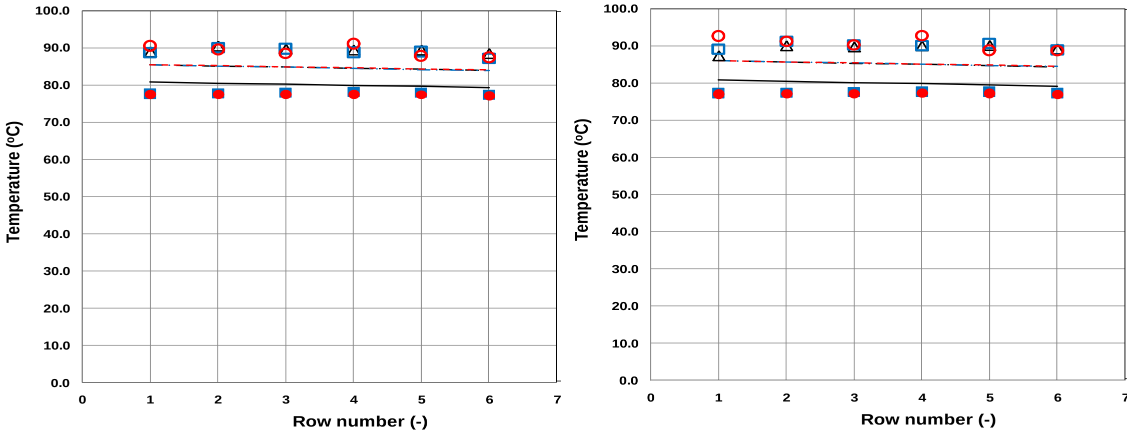

c) 30 kW/m²   *d) 40 kW/m²*

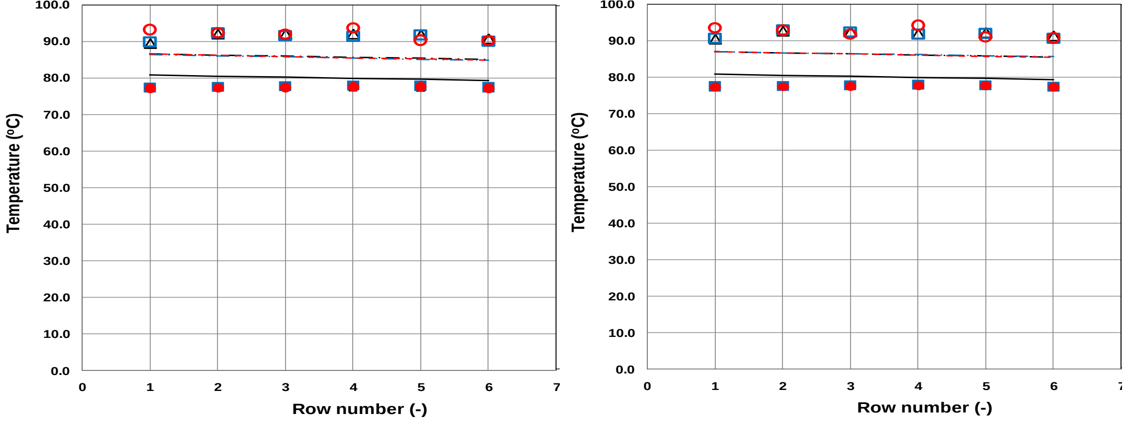

e) 50 kW/m²   *f) 60 kW/m²*

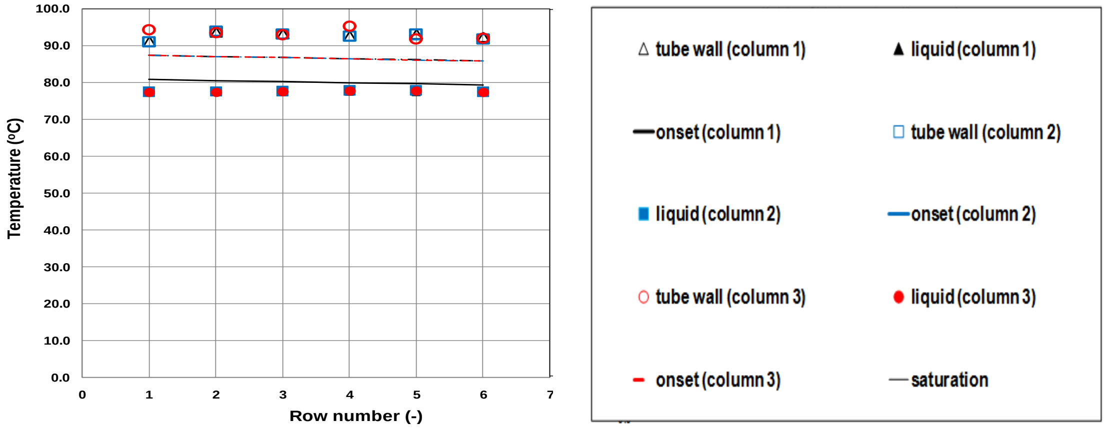

g) 70 kW/m²

Figure 4-4: Variation of tube and liquid temperatures with row number

For a heat flux of 40 kW/m^2, Figure 4.4c shows that Column 1 has a sub-cooling of about 2.7 K. The tube temperatures vary within 2.6 K and are above the onset boiling temperature by 1.4-5.4 K. All the tubes are boiling in the sub-cooled regime. The liquid temperatures are reasonably uniform and vary within 0.3 K. Column 2 has a sub-cooling of about 2.5 K. The liquid temperatures are nearly constant and vary within 0.5 K. The tubes temperatures differ by about 2.3 K and are above the onset boiling temperature by 3.1-5.9 K. All tubes are boiling and all of them are in the sub-cooled regime. Column 3 has sub-cooling of about 2.8 K and the liquid temperature varies within 0.3 K. The tube temperatures vary by about 3.9 K and are above the onset boiling temperature by 4.8- 7.6 K. Therefore all the tubes are boiling in the sub-cooled regime.

Figure 4.4d shows the variation of tube and liquid temperatures with row number for a heat flux of 50 kW/m^2. Column 1 has a sub-cooling of about 2.7 K. The tube temperatures differ by 2.6 K and are above the onset boiling temperature by 3.0-6.6 K. All the tubes are boiling and in the sub-cooled regime. The liquid temperatures in column 1 vary by about 0.3 K. Column 2 has a small degree of sub-cooling of 2.5 K and the liquid temperatures varies within 0.5 K. The tube temperatures differ by 2.5 K and are higher than the onset boiling temperature by 3.3-6.6 K. This means that all the tube are boiling in the sub-cooled regime. Column 3 has a sub-cooling of about 2.7 K. The tubes temperatures vary by about 2.9 K and are above the onset boiling temperature by 5.0 - 8.1 K. All the tubes are boiling in the sub-cooled regime. The liquid temperatures are reasonably constant in column 3 and differ by 0.4 K.

For a heat flux of 60 kW/m^2 Figure 4.4f shows that Column 1 shows a degree of sub-cooling of about 2.5 K. The tube temperatures vary by about 2.1 K and are above the onset boiling temperature by 3.5-6.5 K. The tubes all are boiling and in the sub-cooled regime. The liquid temperatures in column lare nearly constant and vary within 0.3 K. Column 2 has a sub-cooling of about 2.4 K. The temperatures of the tubes vary within 2.4 K and are higher than the onset boiling temperature by 3.7-6.3 K. All the tubes are boiling in the sub-cooled regime. The liquid temperatures in column 2 vary within 0.5K. Column 3 has a sub-cooling of about 2.6 K and the liquid temperatures vary within 0.4K. The tube temperatures are above the onset boiling temperature by 5.3-8.2 K. All the tubes therefore are boiling in the sub-cooled regime.

For a heat flux of 70 kW/m^2, Figure 4.4g shows that column 1 has a sub-cooling of about 2.6 K. The liquid temperature is reasonably constant and differs within 0.4 K. The tube temperatures are above the onset boiling temperature by 3.8-7.0 K and differ by 2.1K. All the tubes are boiling, in the sub-cooled regime. Column 2 has a sub-cooling of about 2.4 K and the liquid temperatures changes within 0.5 K. The tubes temperatures vary by about 2.2 K and are above the onset boiling temperature by 3.7-7.0 K. Thus, all tubes are boiling in the sub-cooled regime. Column 3 has a sub-cooling of about 2.6 K and the liquid temperature is reasonably uniform and changes within 0.4 K. The tube temperatures vary within 3.3 K and are above the onset boiling temperature by 5.7-8.8 K, as a result, all the tubes are boiling in the sub-cooled regime.

Overall, all the liquid temperatures for all heat fluxes are below the local saturation temperature and are consistent with the stream temperatures. The fluid temperature is approximately constant and therefore supports the concept of re-circulation within the evaporator. The LLMP data have a reasonably small degree of sub-cooling, typically 2.6K, and have a tube temperature that varies by about 2.9 K. All tube temperatures are shown to be above the boiling onset temperature and therefore all tubes are in the sub- cooled boiling regime. It is reasonable to conclude that all of the LLMP data lie in the sub-cooled boiling regime. Tubes in Column 3 have higher wall superheat than column 2, while the tubes in column 2 have higher wall superheat than tubes in column 1.

4.4 LLHP Series (850 mbar)

These tests were carried out at 850 mbar absolute pressure and at a low liquid level, the pool height was approximately 0.8 m. The tube heat fluxes in these tests were varied from 10-70 kW/m^2.

4.4.1 ***Stream Temperature for the LLHP Series (850 mbar)***

Variation of stream temperature with stream location for heat fluxes of 10-70 kW/m^2 are shown in Figure 4. 5. Stream temperature behaves similar to LLML series. In general, the stream temperature varies by 0.7-1.6 K and the difference between the free surface saturation temperature and stream temperature was 1.6-3.6 K. The stream temperatures are well distributed throughout the pool. These results are therefore indicative of fluid recirculation taking place, with fluid flashing to the saturation temperature at the free surface before returning to the depths of the pool.

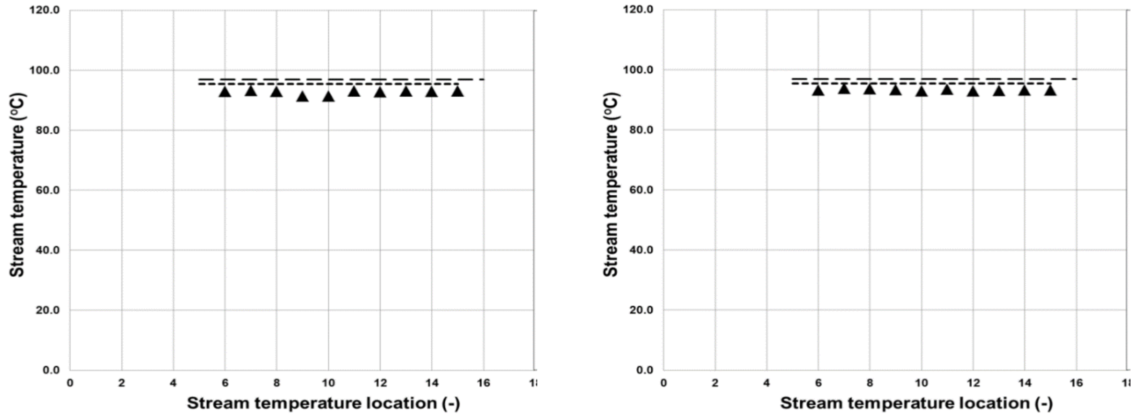

a) 10 kW/m² *b) 20 kW/m²*

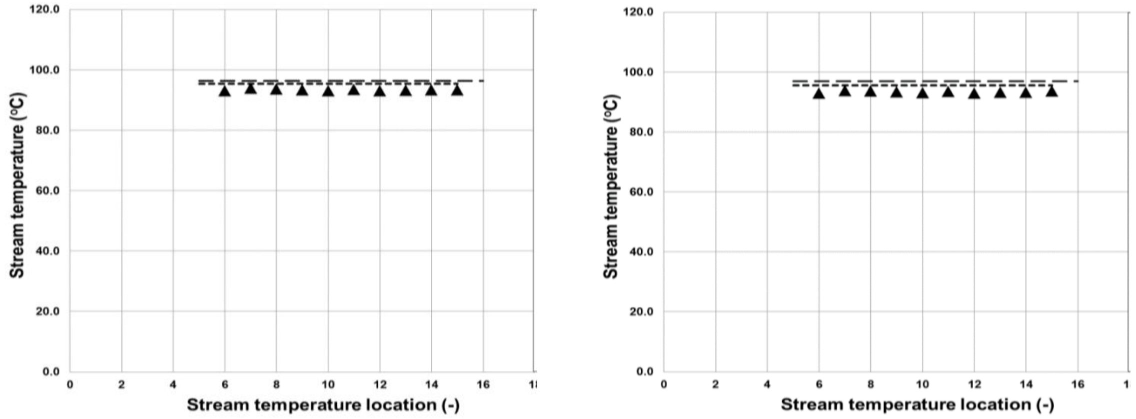

c) 30 kW/m² *d) 40 kW/m²*

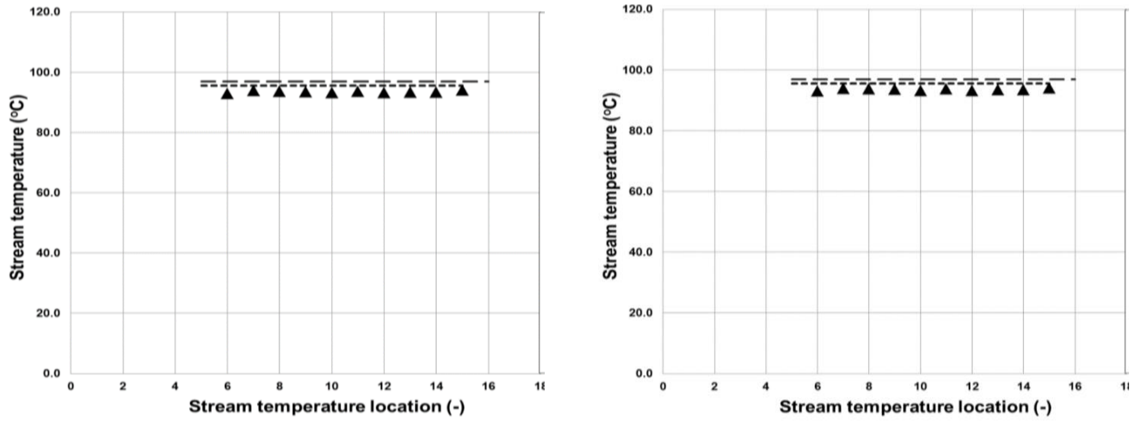

e) 50 kW/m² *f) 60 kW/m²*

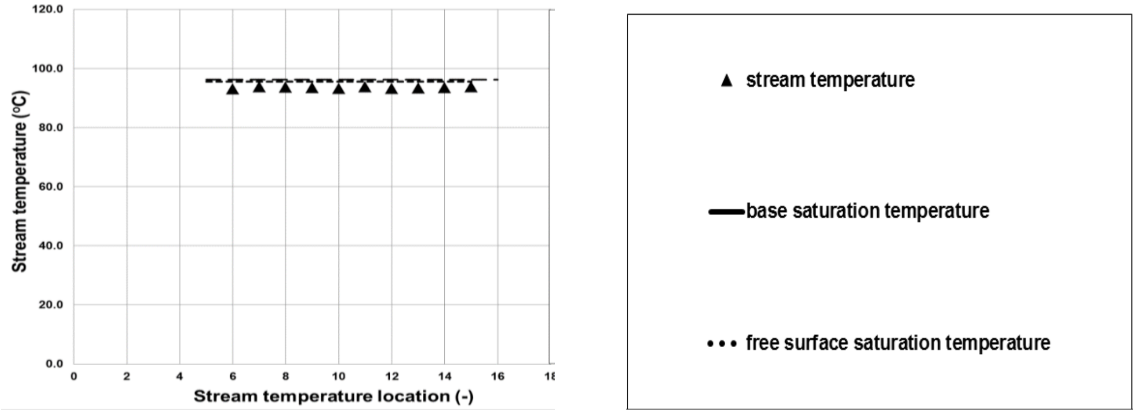

g) 70 kW/m^2

Figure 4-5: Variation of stream temperature with stream location

4.4.2 ***Tube and Liquid Temperatures for the LLHP Series (850 mbar)***

Variation of liquid and tube temperatures with row number for the LLHP series are shown in Figure 4.6. Included in the Figures is the onset boiling temperature for each column and the saturation temperature. Figure 4.6 shows that LLHP series behaves similar to LLMP with respect of slight difference of the tube and liquid temperatures which shown in Table 4.1.

All the liquid temperatures for all heat fluxes are below the local saturation temperature and are consistent with the stream temperatures. The fluid temperature is approximately constant and therefore supports the concept of re-circulation within the evaporator. The LLHP data have a reasonably small degree of sub-cooling, typically 2.4K, and have a wall temperature that varies by about 3.2 K. All tube temperatures are shown to be above the boiling onset temperature and therefore all tubes are in the sub-cooled boiling regime. It is reasonable to conclude that almost all of the HPLL data lie in the sub-cooled boiling regime. Tubes in Column 3 have higher wall superheat than column 2, while the tubes in column 2 have higher wall superheat than tubes in column 1.

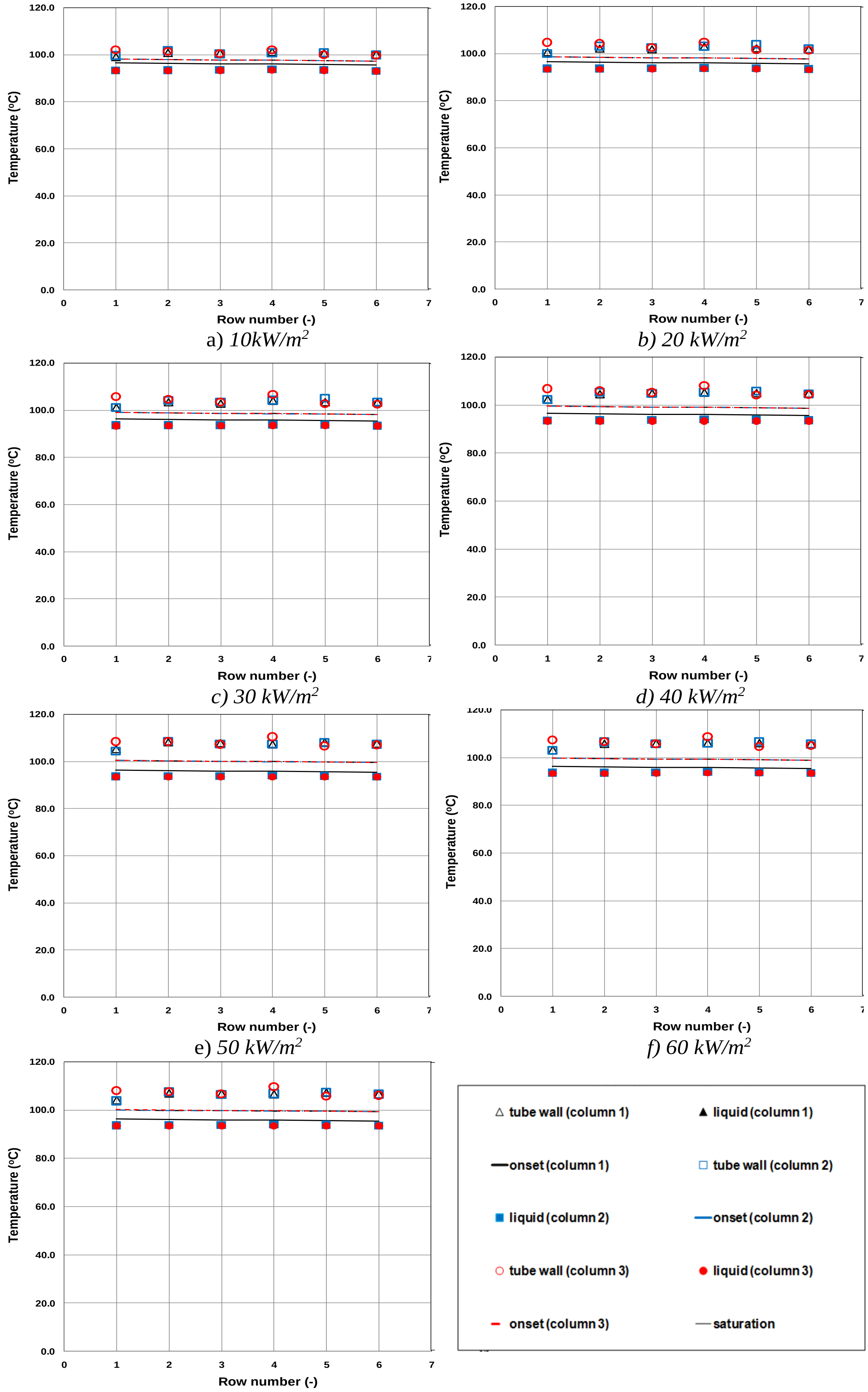

a) *10kW/m*^{2}

b) *20 kW/m*^{2}

c) *30 kW/m*^{2}

d) *40 kW/m*^{2}

e) *50 kW/m*^{2}

f) *60 kW/m*^{2}

g) *70 kW/m*^{2}

Figure 4-6: Variation of tube and liquid temperatures with row number

Table 4-1: Results of LLHP series

Heat flux kW/m^2	Column C	Sub-cooling (K)	Liquid temperatures variation (K)	Tube temperatures variation (K)	Regime
10	1	2.6	0.3	1.1	sub-cooled boiling regime
	2	2.6	0.6	2.4	sub-cooled boiling regime
	3	2.9	0.4	2.0	sub-cooled boiling regime
20	1	2.2	0.4	1.7	sub-cooled boiling regime
	2	2.3	0.5	3.7	sub-cooled boiling regime
	3	2.7	0.4	3.3	sub-cooled boiling regime
30	1	2.2	0.4	2.7	sub-cooled boiling regime
	2	2.2	0.5	3.7	sub-cooled boiling regime
	3	2.5	0.3	4.1	sub-cooled boiling regime
40	1	2.4	0.5	2.9	sub-cooled boiling regime
	2	2.3	0.3	3.5	sub-cooled boiling regime
	3	2.7	0.2	3.8	sub-cooled boiling regime
50	1	2.2	0.4	2.9	sub-cooled boiling regime
	2	2.1	0.4	2.4	sub-cooled boiling regime
	3	2.4	0.2	3.9	sub-cooled boiling regime
60	1	2.2	0.6	3.0	sub-cooled boiling regime
	2	2.0	0.3	3.8	sub-cooled boiling regime
	3	2.4	0.2	3.7	sub-cooled boiling regime
70	1	2.2	0.6	2.9	sub-cooled boiling regime
	2	2.1	0.4	4.0	sub-cooled boiling regime
	3	2.5	0.1	3.9	sub-cooled boiling regime

4.5 HLLP Series (50mbar)

These tests were carried out at 50 mbar absolute pressure at high liquid level, the pool height was approximately 2.0 m. The tube heat flux in these tests were varied from 10- 65 kW/m^2.

4.5.1 ***Stream Temperature for the HLLP Series (50mbar)***

HLLP tests for heat fluxes of 10, 25, 40, 55 and 65 kW/m^2 produced the stream temperature shown in Figure 4.7. The saturation temperatures corresponding to the pressure at the free surface and the evaporator base are included. The saturation temperature is shown to vary from 32^{o}C at the free surface to 64^{o}C at the evaporator base. Figure 4.7a shows the variation of stream temperature with stream location for a heat flux of 10 kW/m^2. The stream temperature is reasonably uniform and close to the free surface saturation temperature.

The difference between the saturation temperature at the free surface and the stream temperature increases as the heat flux increases at most locations, as shown in Figure 4.7, except locations 1, 2 and 18, which are close to the free surface saturation temperature. The stream temperatures fluctuate by 2.1 K for a heat flux of 10 kW/m^2, 3.4 K for a heat flux of 25 kW/m^2, 4.7 K for a heat flux of 40 kW/m^2, 5.6 K for a heat flux of 55 kW/m^2 and 6.2 K for a heat flux of 65 kW/m^2. The stream temperatures are well distributed throughout the pool. These results are therefore indicative of fluid recirculation taking place, with fluid flashing to the saturation temperature at the free surface before the liquid is returned to the depths of the pool.

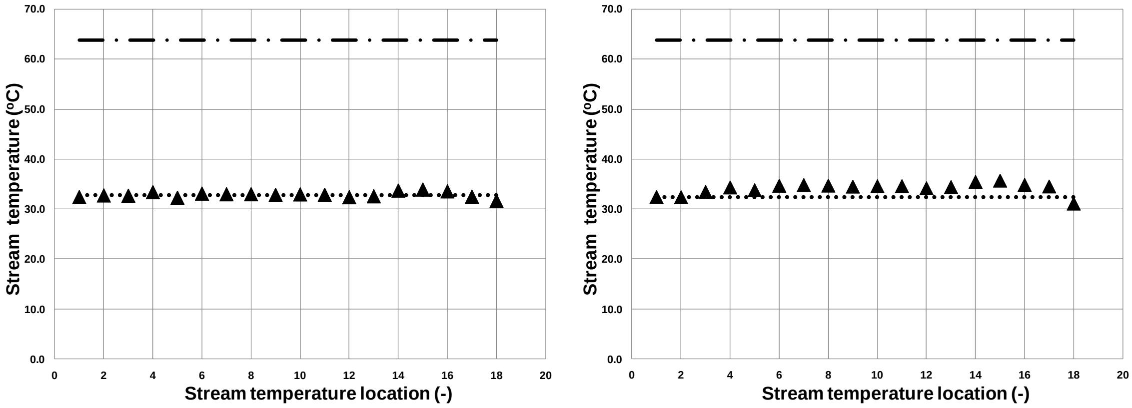

a) 10 kW/m^2

b) 25 kW/m^2

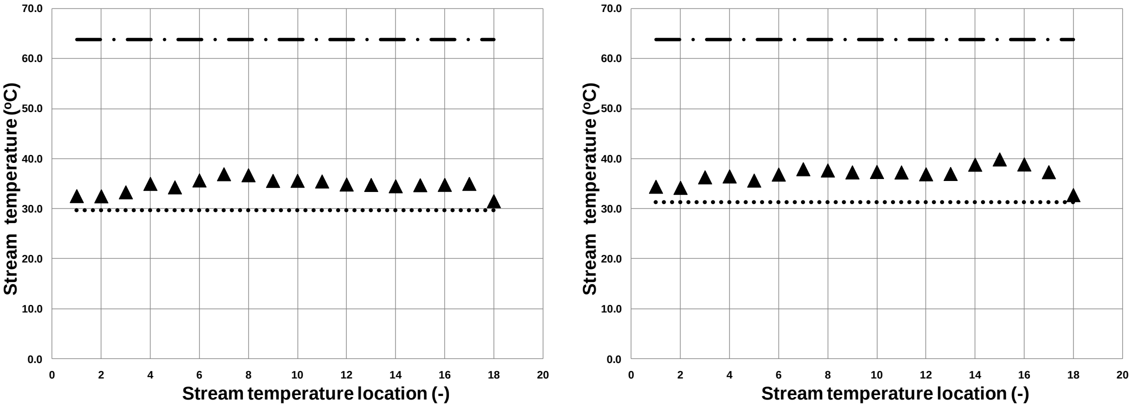

c) 40 kW/m^2

d) 55 kW/m^2

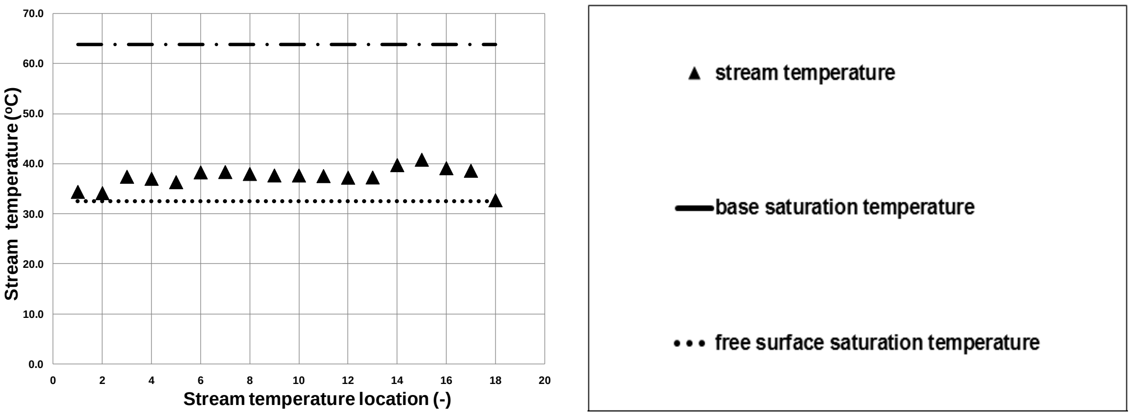

e) 65 kW/m^2

Figure 4-7: Variation of stream temperature with stream location

4.5.2 *Tube and Liquid Temperatures for the HLLP Series (50mbar)*

The variation of liquid and tube temperatures with row number is shown in Figure 4.8. Included in the Figures is the onset boiling temperature and the saturation temperature. Figure 4.6 shows that HLLP series behaves similar to LLLP with respect of slight difference of the tube and liquid temperatures which shown in Table 4.2. The liquid temperatures for all heat fluxes are below the local saturation temperature and are consistent with the stream temperatures. The liquid temperature is approximately uniform, and therefore supports the concept of re-circulation within the evaporator. The HLLP data have a high degree of sub-cooling, typically 26 K. Most tube temperatures for heat fluxes of 10, 25 and 40 kW/m^2 are shown to be below the boiling onset temperature and therefore are mostly in the single phase regime. Most of the tube temperatures at heat fluxes of 55 and 65 kW/m^2 are above the onset boiling temperature, and are in the sub- cooled boiling regime. Boiling heat transfer therefore starts at a heat flux between 40 and 55 kW/m^2.

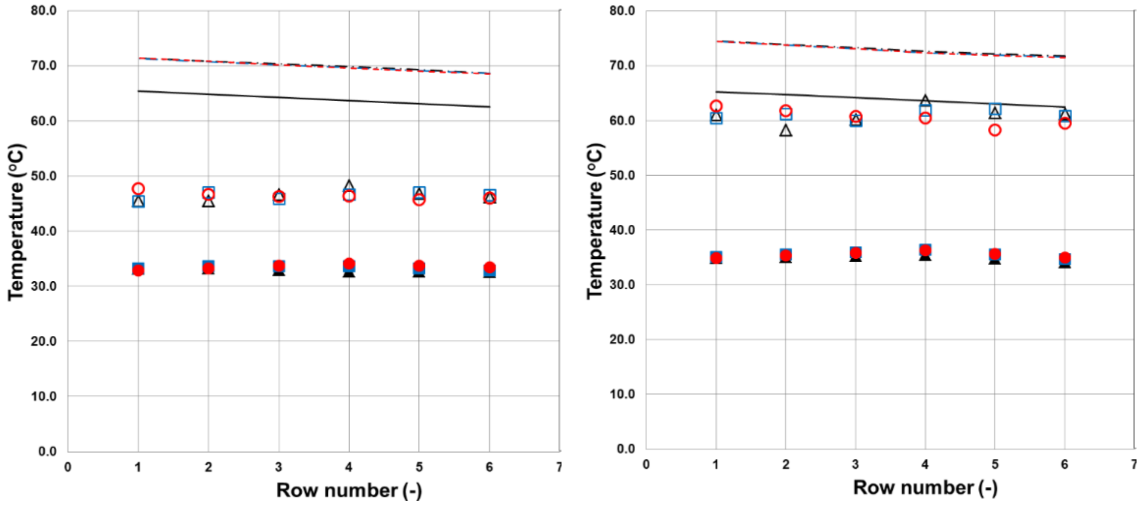

a) 10 kW/m² *b) 25 kW/m²*

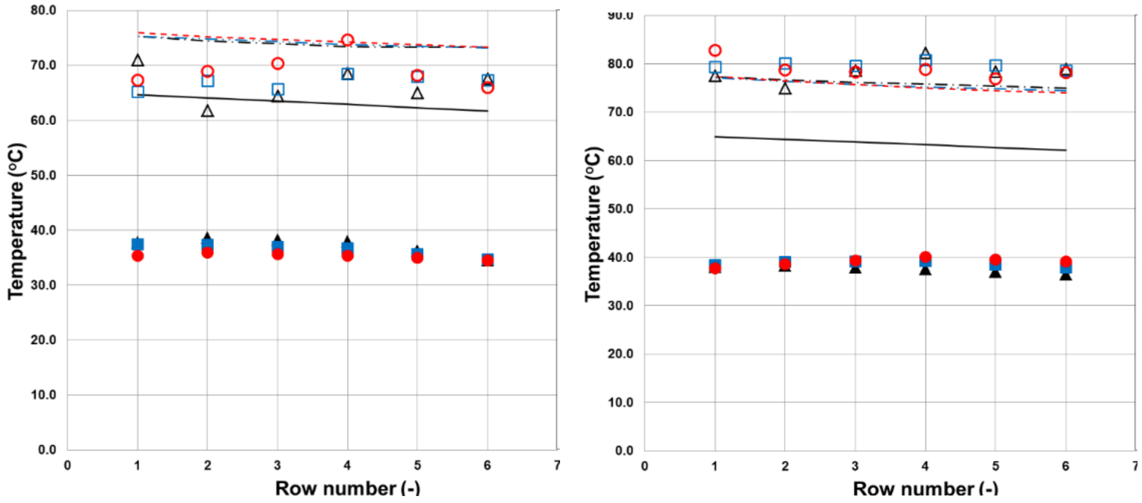

c) 40 kW/m² *d)55 kW/m²*

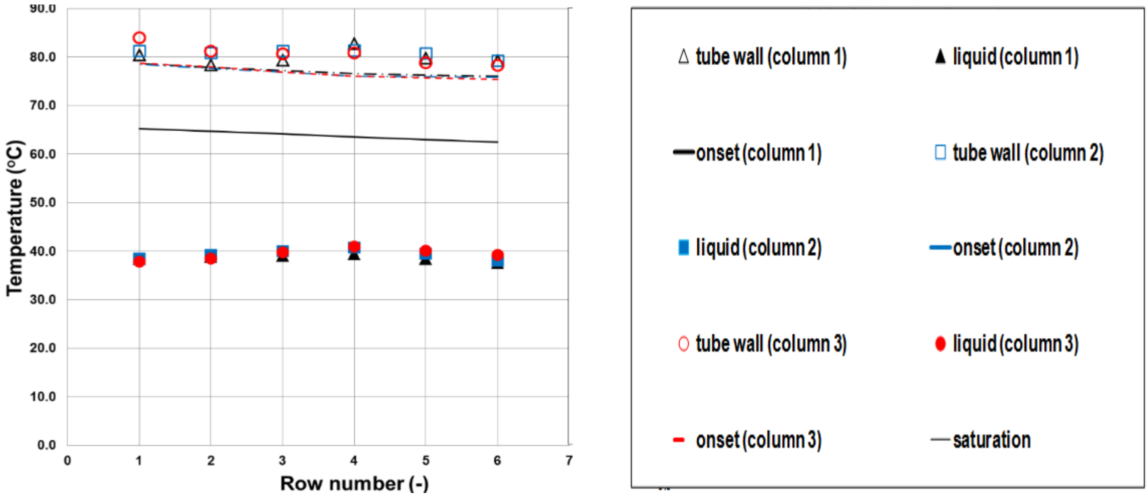

e) 65 kW/m²

Figure 4-8: Variation of tube and liquid temperatures with row number

Table 4-2: Results of Results of HLLP series

Heat flux kW/m^2	Column C	Sub-cooling (K)	Liquid temperature variation (K)	Tube temperature variation (K)	Regime
10	1	30	0.6	2.2	All the tubes are in single phase regime
	2	31	0.7	1.6	All the tubes are in single phase regime
	3	31.5	1.1	2.1	All the tubes are in single phase regime
25	1	30	1.4	3.1	All the tubes are in single phase regime
	2	29	1.4	1.4	All the tubes are in single phase regime
	3	29	1.5	3.2	All the tubes are in single phase regime
40	1	26	4.1	2.7	All the tubes are in single phase regime
	2	26.5	1.6	3.3	All the tubes are in single phase regime
	3	28	3.4	8.1	All the tubes are in single phase regime except that in fourth row, which in sub-cooling boiling regime.
55	1	26	1.8	7.7	All the tubes are in sub-cooled boiling regime except that in the second row which in single phase regime
	2	25	0.5	2.2	All the tubes are in sub-cooled boiling regime
	3	25	2.3	8.3	All the tubes are in sub-cooled boiling regime
65	1	25	1.8	3.1	All the tubes are in sub-cooled boiling regime
	2	24	2.5	2.4	All the tubes are in sub-cooled boiling regime
	3	24	3.1	5.7	All the tubes are in sub-cooled boiling regime

4.6 Discussion and Visual Observations

The results obtained show that the operation of the evaporator changes significantly as the pressure is reduced. This is evidenced by the stream temperatures. The stream temperatures indicate that some kind of re-circulation is occurring, irrespective of the pressure, because the pool temperature is similar to the saturation temperature corresponding to the pressure at the free surface. However, this produces small liquid sub-coolings at high pressure, LLHP, and large liquid sub-coolings at vacuum pressures, LLLP and HLLP. The LLMP and LLHP tests behaved as expected. However, the vacuum tests behave differently. The vapour density in Equation 3.1 means that vacuum heat fluxes require a significantly higher wall superheat to nucleate. This has meant that tube wall temperatures are lower than expected at the lower heat fluxes and are being cooled by single-phase flows. The single-phase cooling is enhanced as a result of the re- circulation, another source of the delay in nucleation. The tubes nucleate at the higher heat fluxes but only partial boiling is confirmed by the visual observations shown in Figures 4.29, 4.30, 4.31 and 4.32. The LLHP and the LLMP tests shows lots of bubbles whereas the HLLP and LLLP tests shows very few.

Photographs taken of the tube bundle at a pressure of 50 mbar during the LLLP series for various heat fluxes are shown in Figure 4.29. At a heat flux of 10 kW/m^2, bubbles were not evident so the photograph is excluded. Bubbles are evident as the heat flux increases. However, the bubbles are relatively large and attached to the tube wall. Larger heat fluxes led to a more frequent appearance of the bubbles. These photographs indicate that sub- cooled boiling happens at heat fluxes greater than 10 kW/m^2 but the information obtained does not allow any evidence of the presence or absence of convection to be confirmed. The HLLP series are shown in Figure 4.30 and looked similar to the LLLP series. However, bubbles were not observed until a heat flux of 40 kW/m^2.

Photographs taken of the tube bundle at a pressure of 450 mbar, the LLMP series, are shown in Figure 4.31 they looked similar to the LLHP series shown in Figure 4.32. At heat fluxes of 10 and 20 kW/m^2, small bubbles are evident towards the top of the tube bundle. As the heat flux increases to 30 kW/m^2, bubbles are evident further down in to the tube bundle. For heat fluxes greater than 30 kW/m^2, the LLMP series, and for the heat flux greater than 20 kW/m^2, the LLHP series show bubbles present from row 1 upwards, confirming that sub-cooled boiling is occurring. However, what cannot be deduced is the presence or absence of convective heat transfer. It is noticeable that, even at a heat flux of 70 kW/m^2, the void fraction is low.

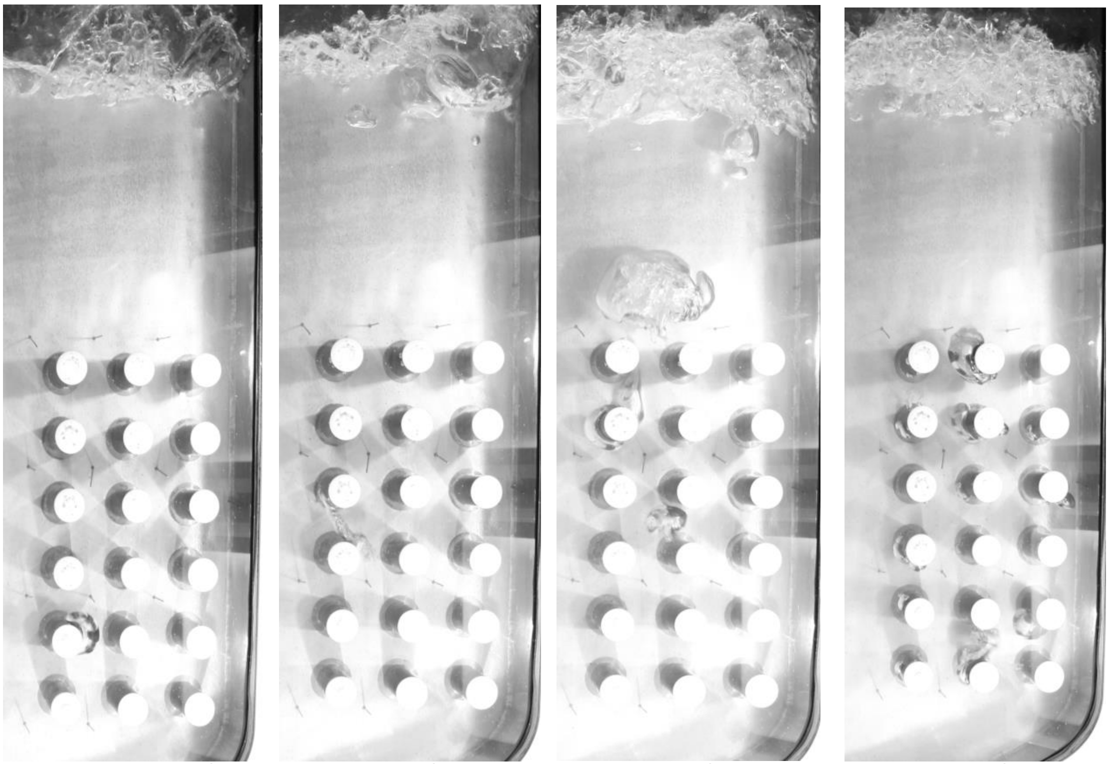

a) 25 kW/m^2 *b) 40 kW/m^2* *c) 55 kW/m^2* *d) 65 kW/m^2*

Figure 4-9: LLLP test

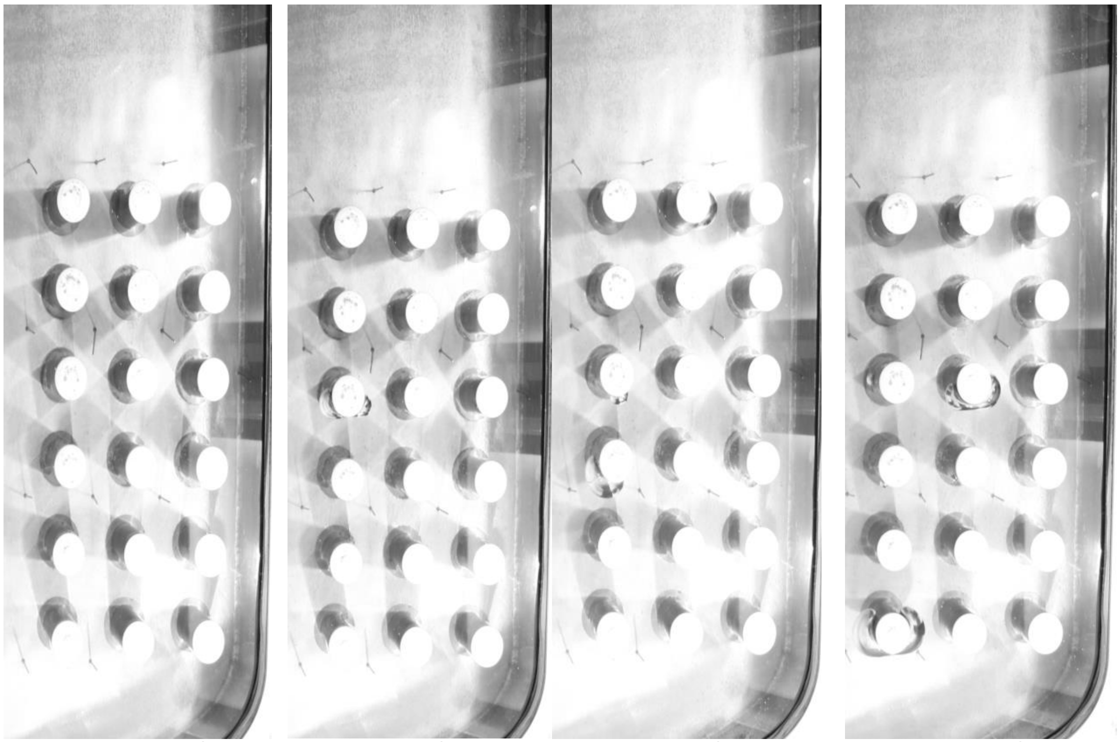

a) 25kW/m^2 *b) 40 kW/m^2* *c) 55 kW/m^2* *d) 65kW/m^2*

Figure 4-10: HLLP test

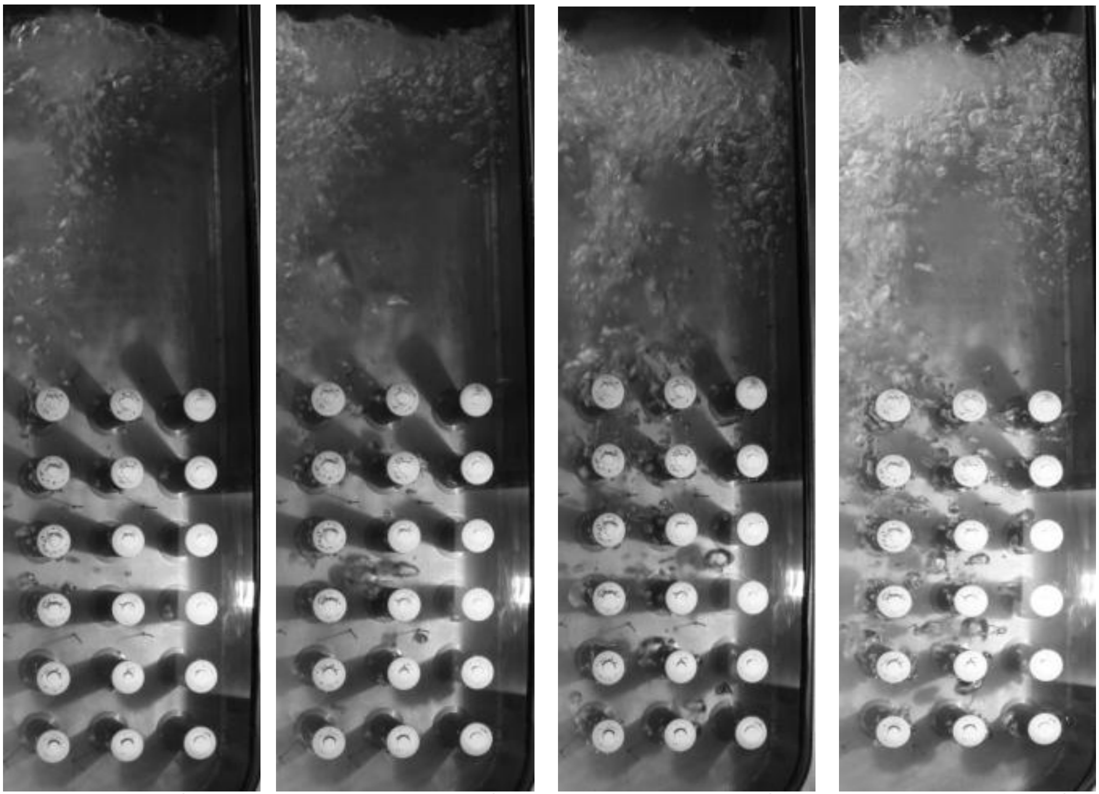

a) 10kW/m^2 *b) 20 kW/m^2* *c) 30 kW/m^2* *d) 40kW/m^2*

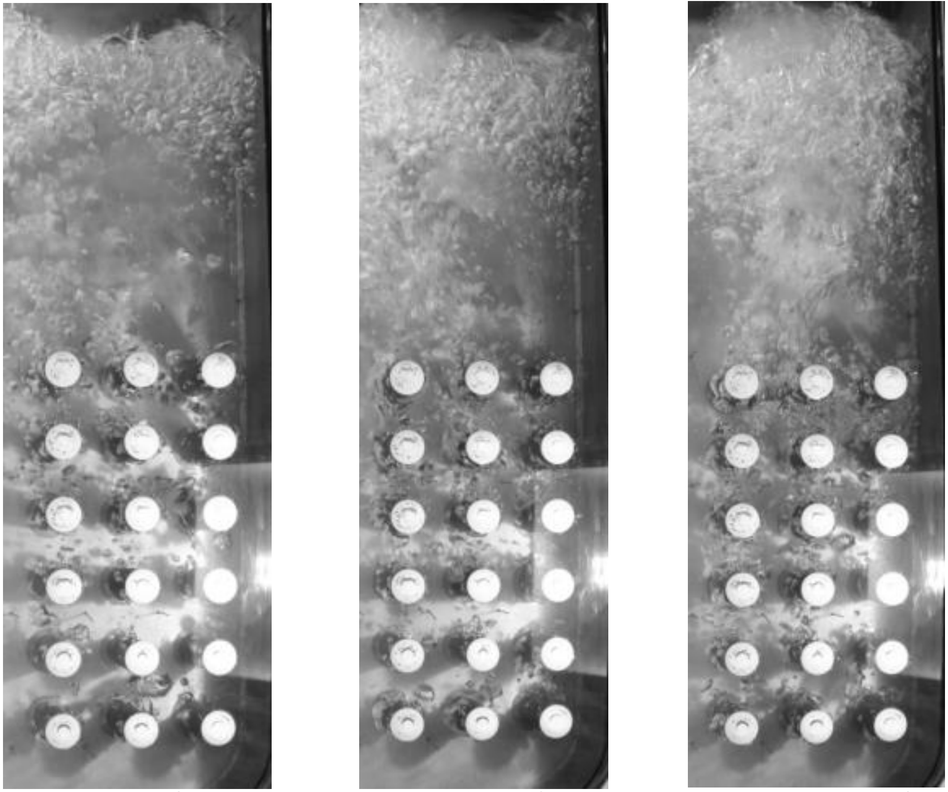

e) 50 kW/m^2 *f) 60 kW/m^2* *g) 70 kW/m^2*

Figure 4-11: LLMP test

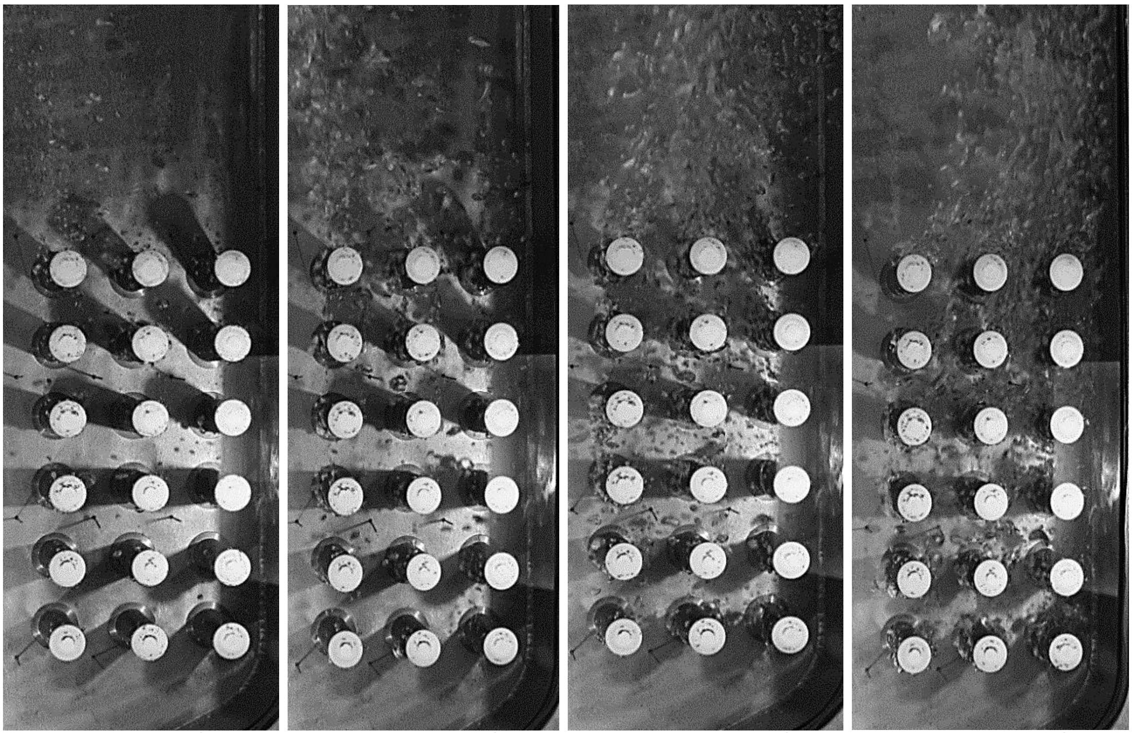

a) 10kW/m^2 b) 20kW/m^2 c) 30kW/m^2 d) 40kW/m^2

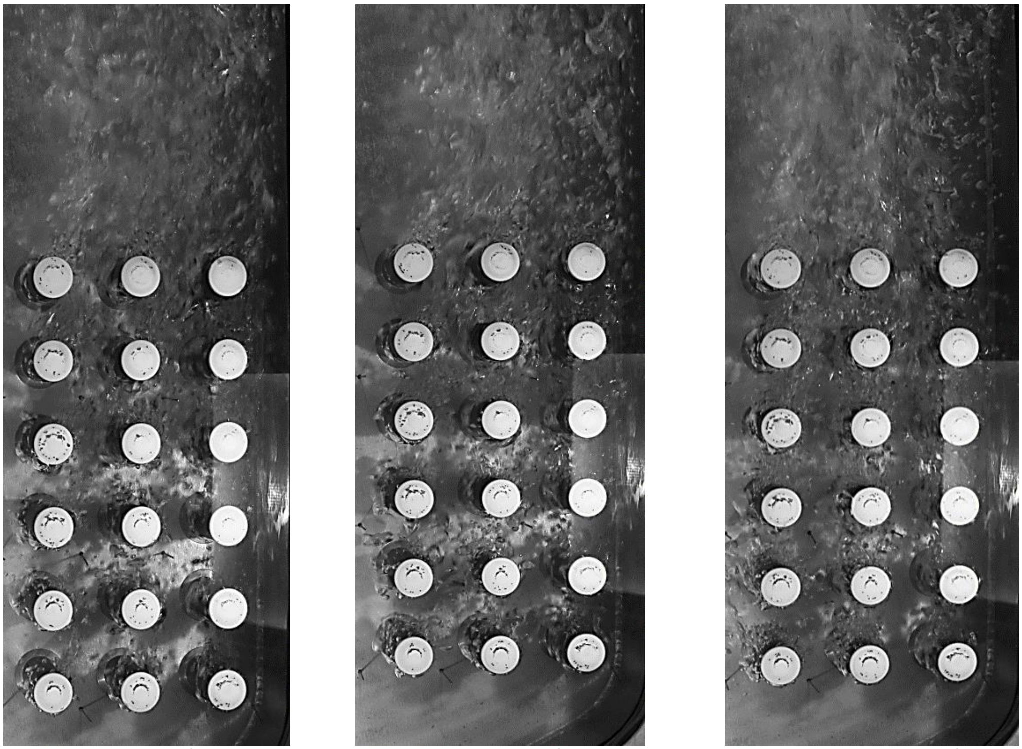

e) 50 kW/m^2 *f) 60 kW/m^2* *g) 70 kW/m^2*

Figure 4-12: LLHP test

Chapter 5 : HEAT-TRANSFER REGIME INVESTIGATION

5.1 Introduction

The non-equilibrium model studied by McNeil et al at the same condition for low pressure and high pressures, [80] suggested that the non-equilibrium scenario is very unlikely to have occurred. Two analyses were undertaken in an attempt to establish the heat-transfer mechanisms that occurring on the tube surfaces, the isolated tube analysis and the equilibrium one-dimensional column analysis.

5.2 The Isolated Tube Analysis

This analysis assumed that the tubes acted independent of each other in either natural convection or sub-cooled nucleate boiling. For a horizontal cylinder, Churchill and Chu [81] gave the natural convection, heat-transfer coefficient, h_{nc},as in Equation 2.31, Prandtl number, given in Equation 2.24 and Ra is the Rayleigh number, given by Equation 2.32. The fluid properties were evaluated at the film temperature, T_f, given by

$$T_f = \frac{(T_W + T_L)}{2} \qquad \textit{5-1}$$

Natural convection took place with increasing heat flux until the onset of nucleate boiling. This occurred when the wall superheat from natural convection balanced with the onset condition, Equation, i.e.

$$q_{onb} = \frac{k_L h_{fg} \rho_g (\triangle T_{onb})^2}{8\sigma T_{sat}} = h_{nc}(\triangle T_{onb} + \triangle T_{sub}) \qquad \textit{5-2}$$

with nucleate boiling continuing thereafter. The correlations considered for the boiling heat-transfer coefficient, h_{nc} were of the form

$$h_{nb} = \gamma q_{nb}^{n} \qquad \textit{5-3}$$

Three correlations were used, the Cooper [11] correlation, Equation 3.16, and Gorenflo [12] correlation, Equation 3.17, as they had been identified by Feldmann and Luke [54] as having some success at these reduced pressures and the Stephan and Abdelsalam [9] correlation, Equation 3.12. Two errors were used to indicate accuracy, the average and the root mean square errors. The average error was defined as

$$Error\ average = \frac{D_{measured} - D_{predicted}}{D_{measured}} \qquad 5\text{-}4$$

The root mean square error was defined as

$$rms = \sqrt{\frac{1}{n}\left(D1^2 + D2^2 + \cdots Dn^2\right)} \qquad 5\text{-}5$$

where D is the wall temperature difference, which is the difference between the wall and liquid temperatures. This temperature difference is used for the statistical comparisons for all of the models.

5.2.1 *Low Pressure Low Level Series LLLP*

At a pressure of 50 mbar, Equation 5.2 gave onset wall superheats of typically 3.9-6.4 K for the LLLP data series. This translates to the data taken at a heat flux of 10 kW/m^2, being in the natural convection regime while others were in the sub-cooled nucleate boiling regime. There are differences between the behaviors of the columns, with columns 1 running cooler than column 2, which, in turn is running cooler than column3.

5.2.1.1 *Cooper correlation based predictions*

A comparison between the measured and predicted wall superheats using the Cooper [11] correlation in the sub-cooled boiling regime for columns 1, 2 and 3 are shown in Figure 5.1. Data sets (a) and (b), taken at the same conditions ten minutes apart, are both shown. The upper and lower limits shown in Figure 5.2 are set at ± 30% with the data for columns 1, 2 and 3 shown in red, green and black respectively. The Cooper-based approach over- predicts the data with an error average difference of -23.1%, -15.8% and -8.9% for columns 1, 2 and 3 respectively. The corresponding root mean square differences (rms) are 27.9%, 19.0% and 16.6%. Thus, the Cooper [11] based approach predicts the wall temperatures in columns 3 better than those in columns 1 and 2. Overall, the average and rms differences are -15.9% and 21.6% respectively.

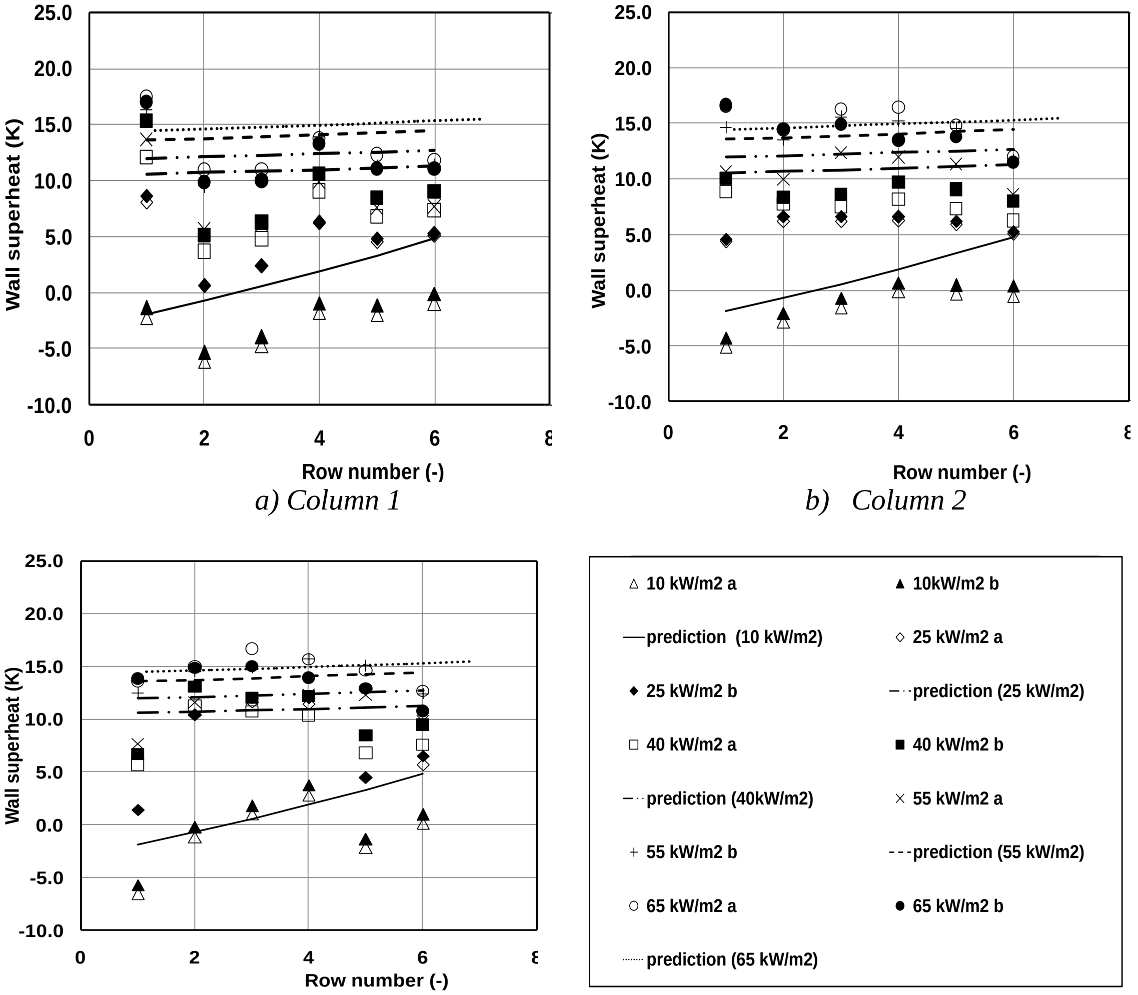

a) Column 1

b) Column 2

c) Column 3

Figure 5-1: variation of row number with wall superheat

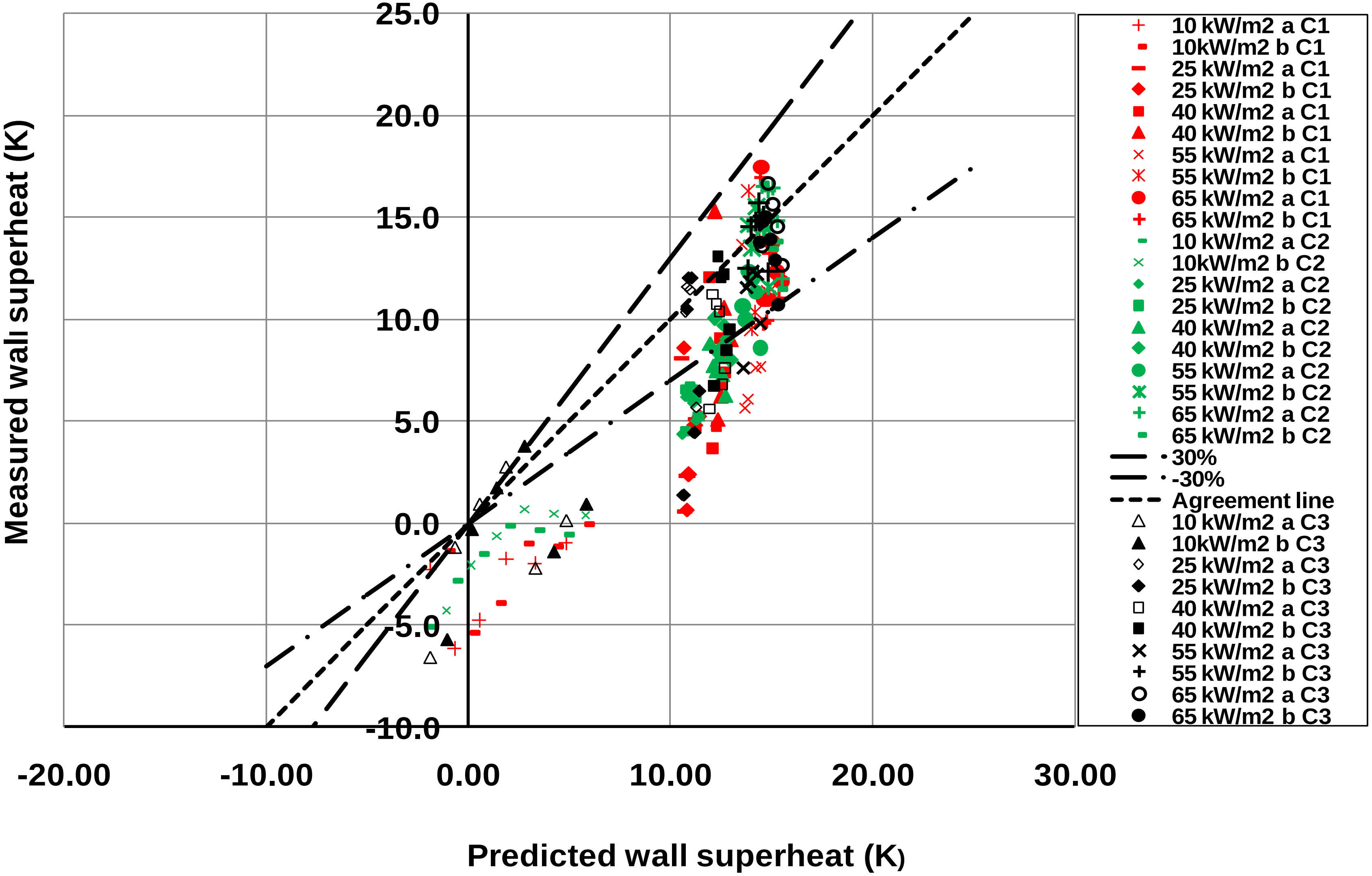

Figure 5-2: comparison of predicted with measured wall superheat

5.2.1.2 *Gorenflo correlation based predictions*

A comparison between the measured and predicted wall superheats using the Gorenflo [12] correlation in the sub-cooled boiling regime is shown in Figure 5.3 for column 1, 2 and 3 respectively. Predictions of the data occur with average differences of -35.7%, - 29.3% and -23.2% for columns 1, 2 and 3 respectively. The corresponding root mean square differences (rms) are 37.7%, 30.4% and 27.0%. Thus, the Gorenflo [12] based approach predicts the wall temperatures in column 3 better than those in columns 1 and 2. Overall, the average and rms differences are -29.4% and 32.0% respectively. The variation of predicted and measured wall superheat, Figure 5.4, shows that the Gorenflo [12] correlation gives poor agreement with wall superheat.

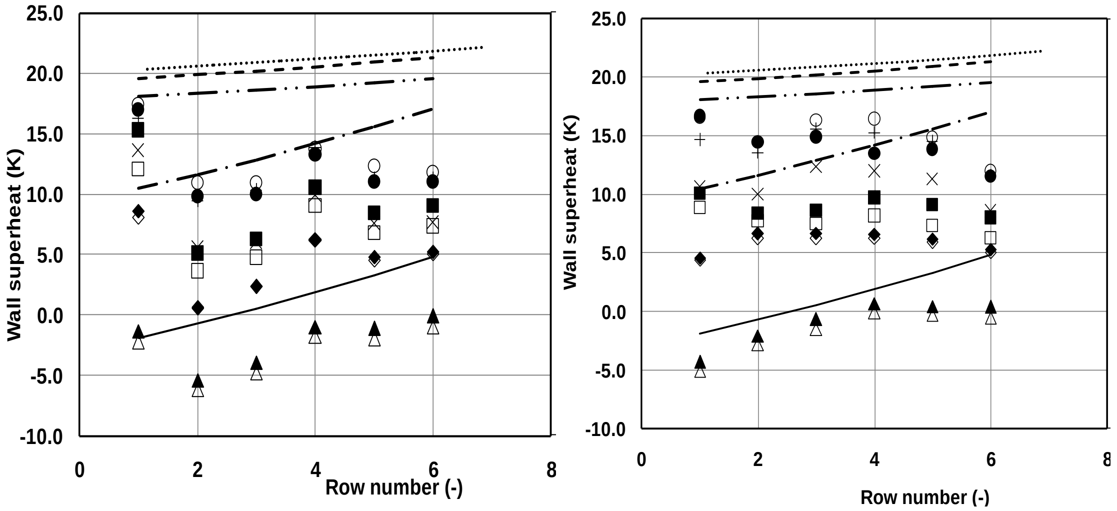

a) Column 1 b) Column 2

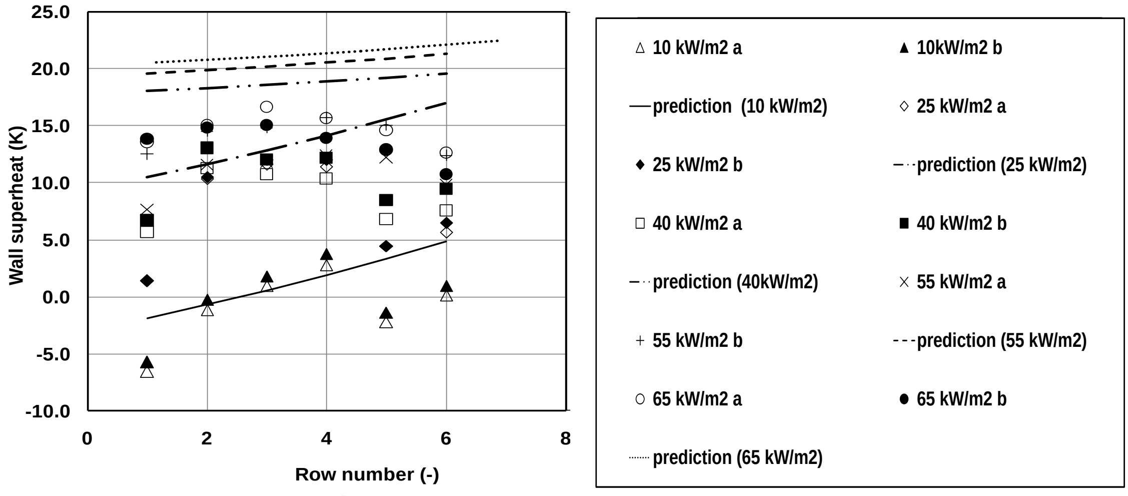

c) Column 3

Figure 5-3: variation of row number with wall superheat for

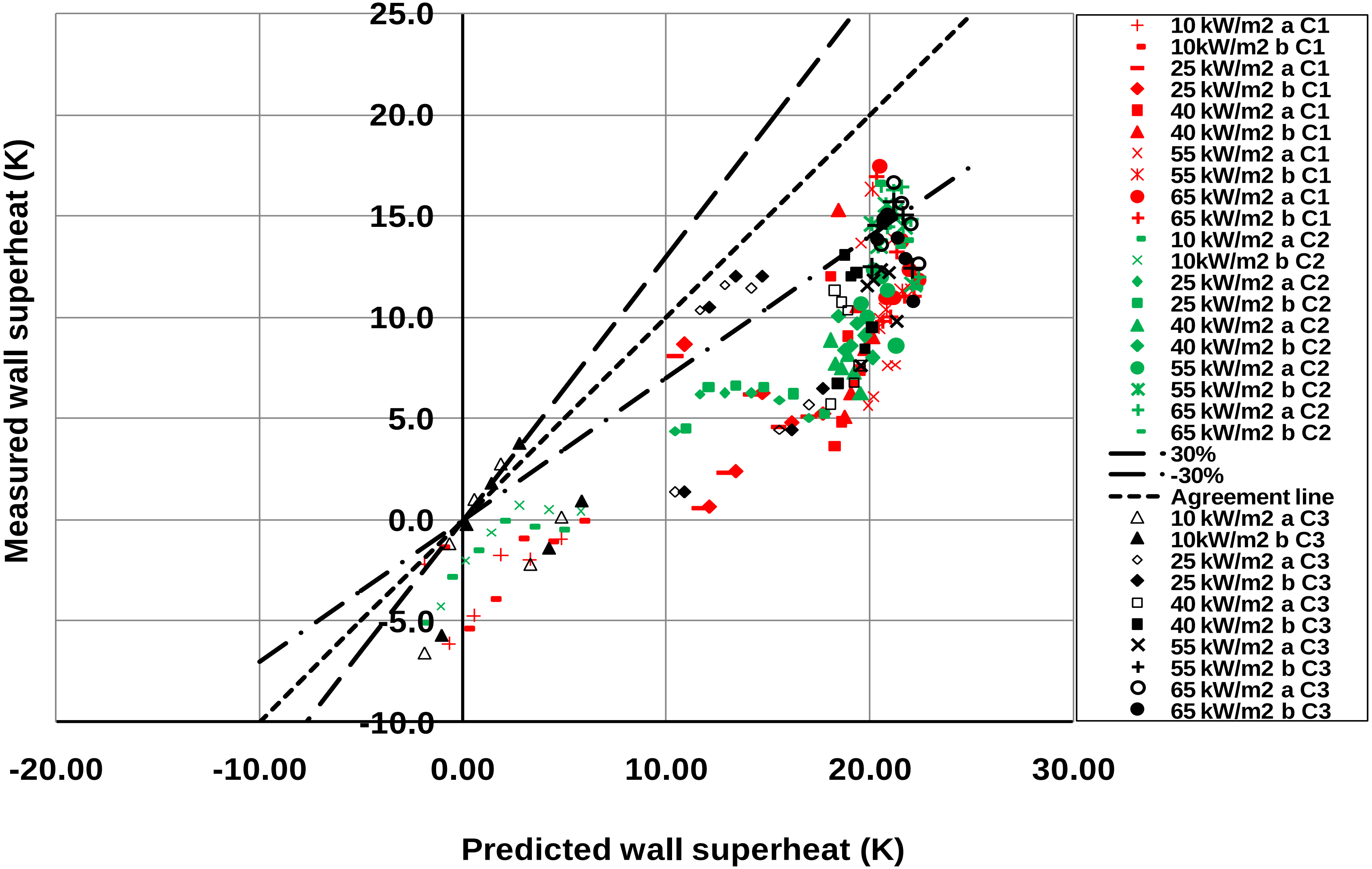

Figure 5-4: comparison of predicted with measured wall superheat

5.2.1.3 *Stephan and Abdelsalam correlation based predictions*

Figures 5.5 shows the comparison between the measured and predicted wall superheats using the Stephan and Abdelsalam [9] correlation in the sub-cooled boiling regime for column 1, 2 and 3 respectively. The Stephan and Abdelsalam [9]-based approach over- predicts the data with an average differences of -20.5%, -13.0% and - 5.9% for columns 1, 2 and 3 respectively. The corresponding root mean square differences (rms) are 26.4%, 17.3% and 15.3%. Thus, the Stephan and Abdelsalam [9] based approach predicts the wall temperatures in columns 3 better than those in columns 1 and 2. Overall, the average and rms differences are -13.1% and 20.3% respectively. The variation of all of the predicted and measured wall superheat is shown in Figure 5.6.

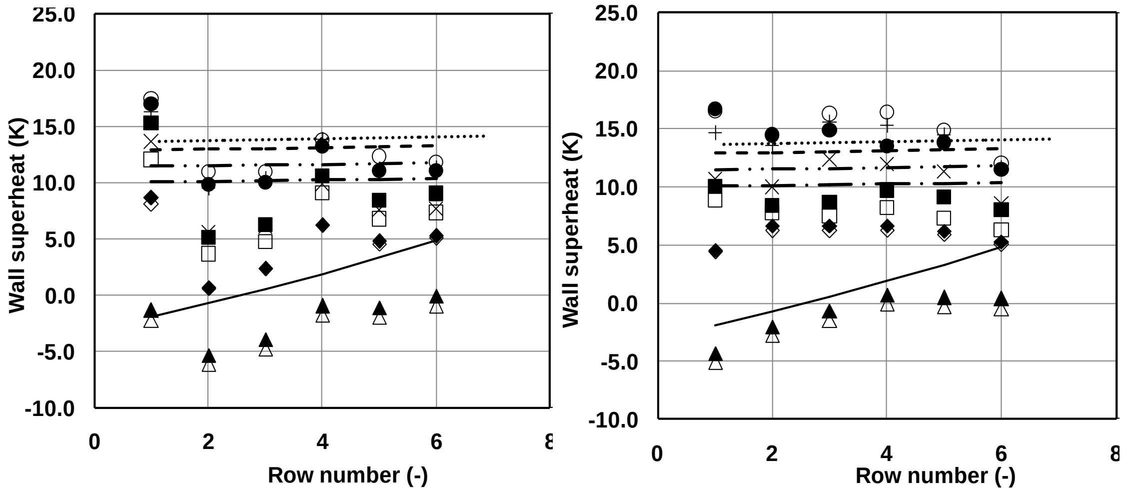

a) Column 1 *b) Column 2*

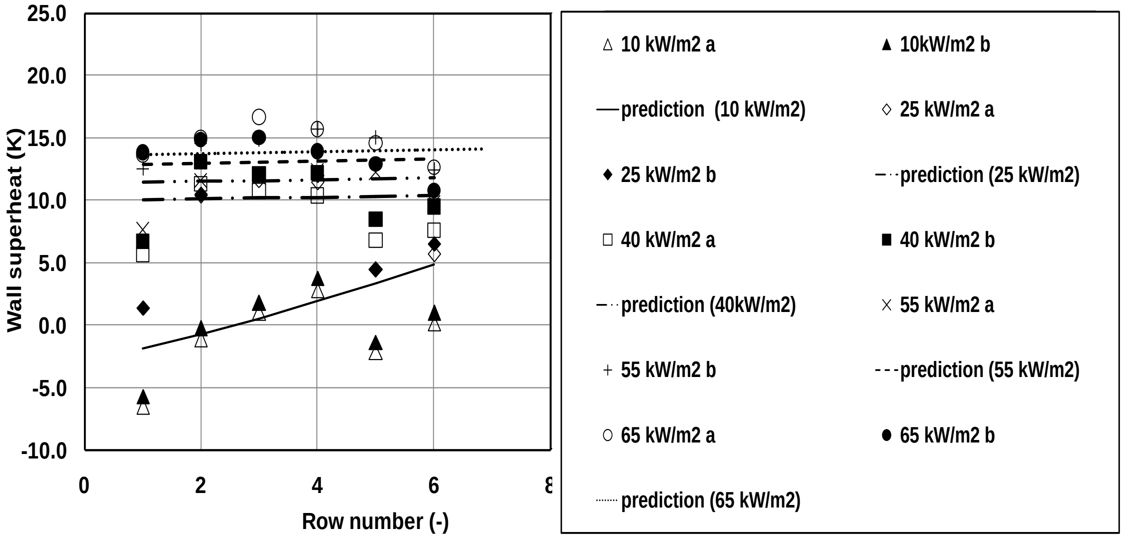

c) Column 3

Figure 5-5: Variation of row number with wall superheat for

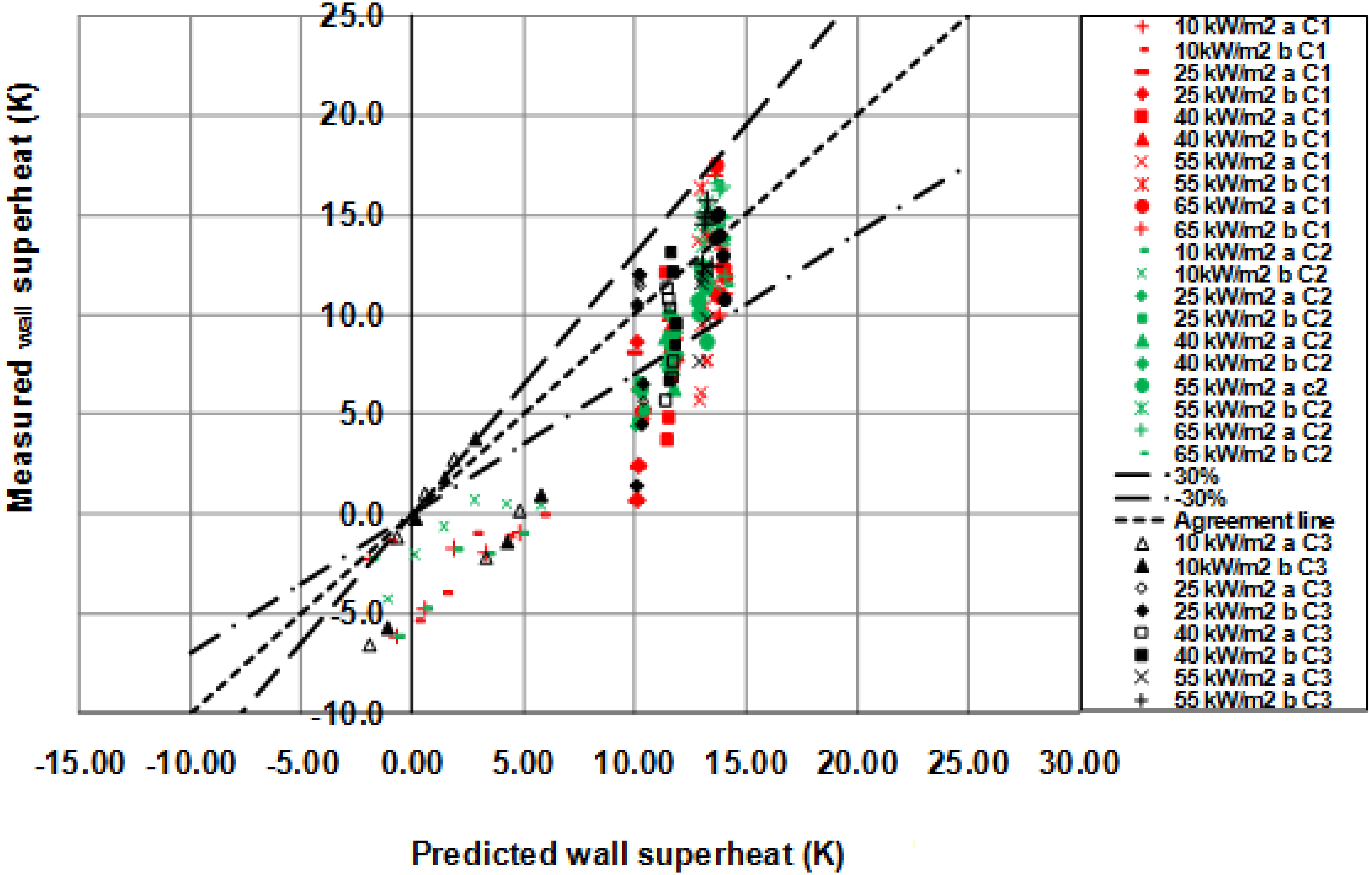

Figure 5-6: comparison of predicted with measured wall superheat

Overall, when this model is applied to the low level data at a pressure of 50 mbar, root mean square differences of 21.6% and an average error of -16% occur when the Cooper [11] correlation was used to describe the boiling element. The corresponding figures achieved for the Gorenflo [12] correlation were 32.0% and -29.4% and for the Stephan and Abdelsalam [9] correlation were 20.3% and -13.2%. Figures 5.2, 5.4 and 5.6 shows that the Stephan and Abdelsalam [9]-based approach predicts the data significantly better than the Cooper [11]-based approach, which is better than Gorenflo [12]-based approach.

5.2.2 *Low Pressure High Level Series HLLP*

At a pressure of 50 mbar, Equation 5.2 gave onset wall superheats of typically 6.1-7.2 K for the HLLP data series. This translates to the data taken at heat fluxes of 10 and 25 kW/m^2, being in the natural convection regime with those obtained at 55 and 65 kW/m^2 being in the sub-cooled nucleate boiling regime. Some of the data obtained at a heat flux of 40 kW/m^2 are in the natural convection regime while others are in the sub-cooled boiling regime.

5.2.2.1 *Cooper correlation based predictions*

A comparison between the measured and predicted wall superheats using the Cooper [11] correlation for the sub-cooled nucleate boiling regime are shown in Figure 5.7 for columns 1, 2 and 3 respectively. There is little difference in the behavior of the columns. The Cooper-based approach predicts the data with an average difference of 0.5%, 1.28% and 3.1% and the corresponding root mean square differences (rms) are 14.7%, 13.6% and 14.4% for columns 1, 2 and 3 respectively. The variations of the predicted and measured wall superheat are shown in Figure 5.8. The Cooper [11]-based approach predicts the wall temperatures in all columns equally well. Overall, the average difference and the corresponding root mean square differences (rms) are 1.6% and 14.3% respectively.

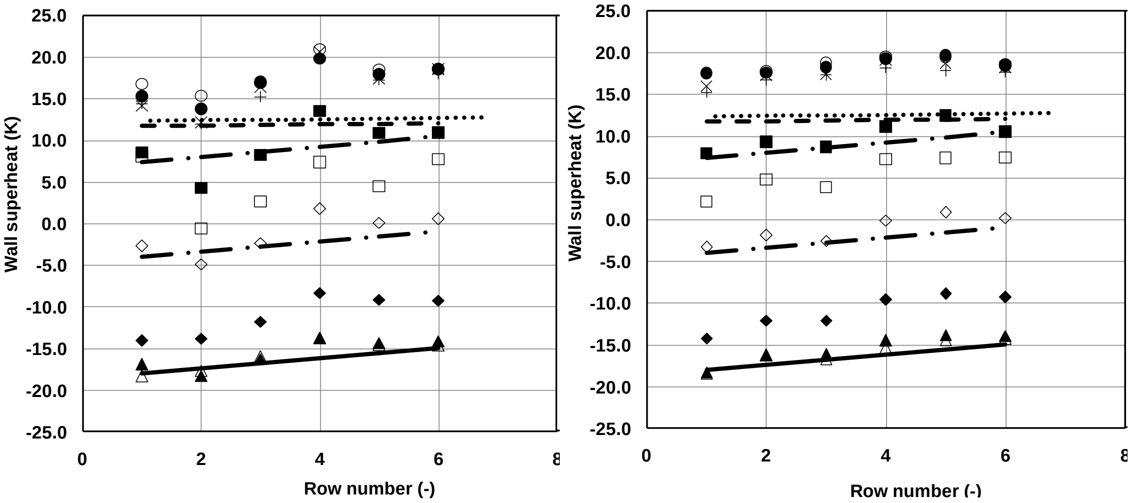

a) Column 1 *b) Column 2*

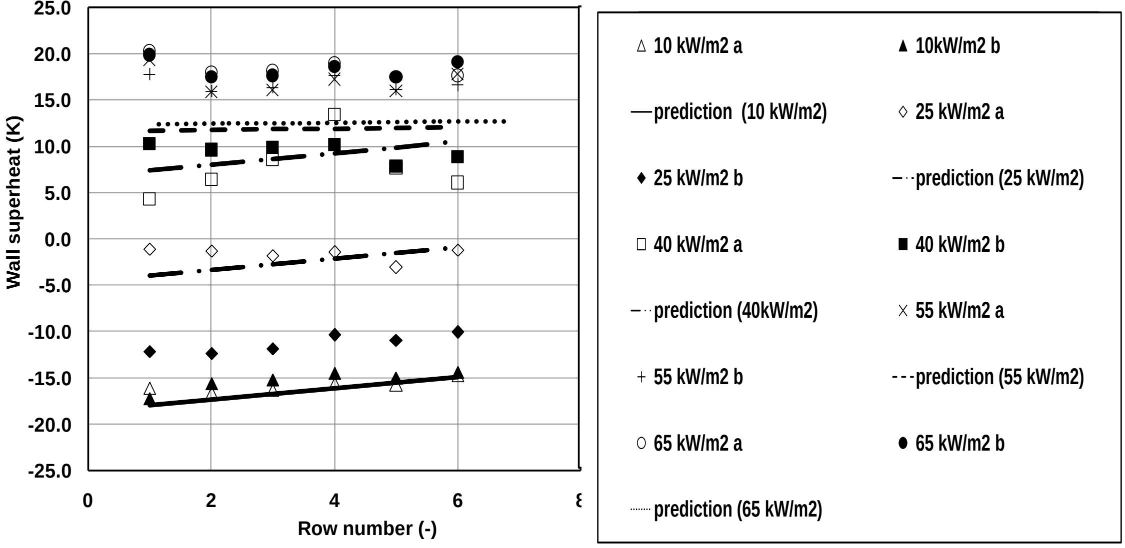

c) Column 3

Figure 5-7: variation of row number with wall superheat

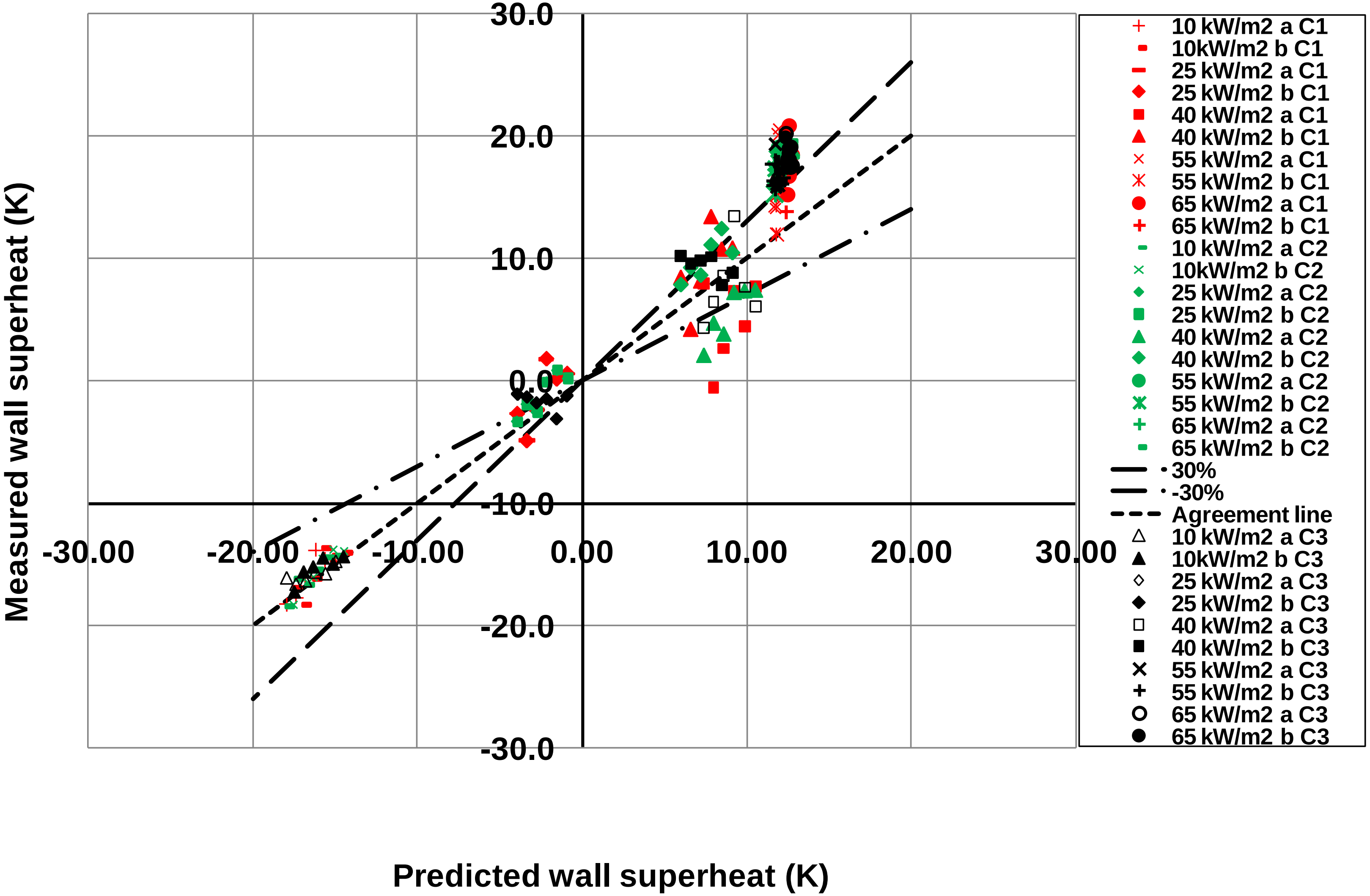

Figure 5-8: comparison of predicted with measured wall superheat

5.2.2.2 *Gorenflo correlation based predictions*

Using the Gorenflo [12] correlation in the sub-cooled nucleate boiling regime, Figure, 5.9 show little difference between the columns, with an average difference of -4.6%, -3.9% and 2.0% and with corresponding root mean square differences (rms) of 12.1%, 12.9% and 12.0% for columns 1, 2 and 3 respectively. Thus, the Gorenflo [12]-based approach also predicts the wall temperatures in all columns equally well. Overall, the average difference and the corresponding root mean square differences (rms) are -3.5% and 12.1% respectively. The variation of the predicted and measured wall superheat is shown in Figure 5.10.

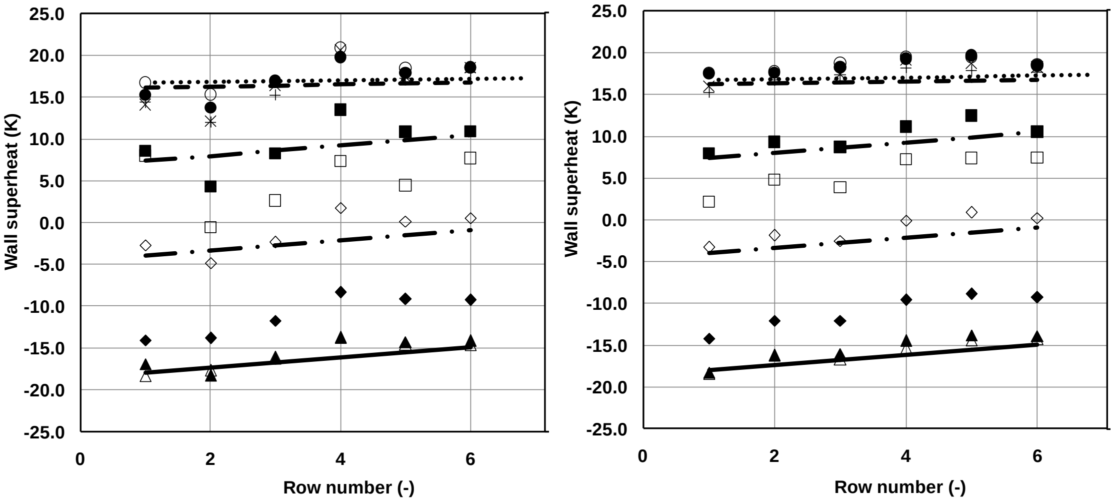

a) Column 1 *b) Column 2*

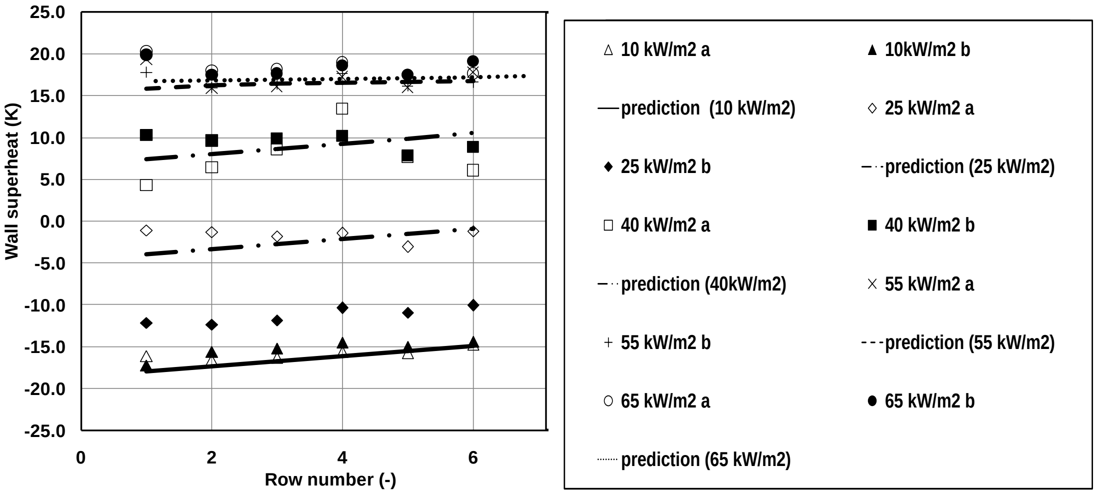

c) Column 3

Figure 5-9: variation of row number with wall superheat

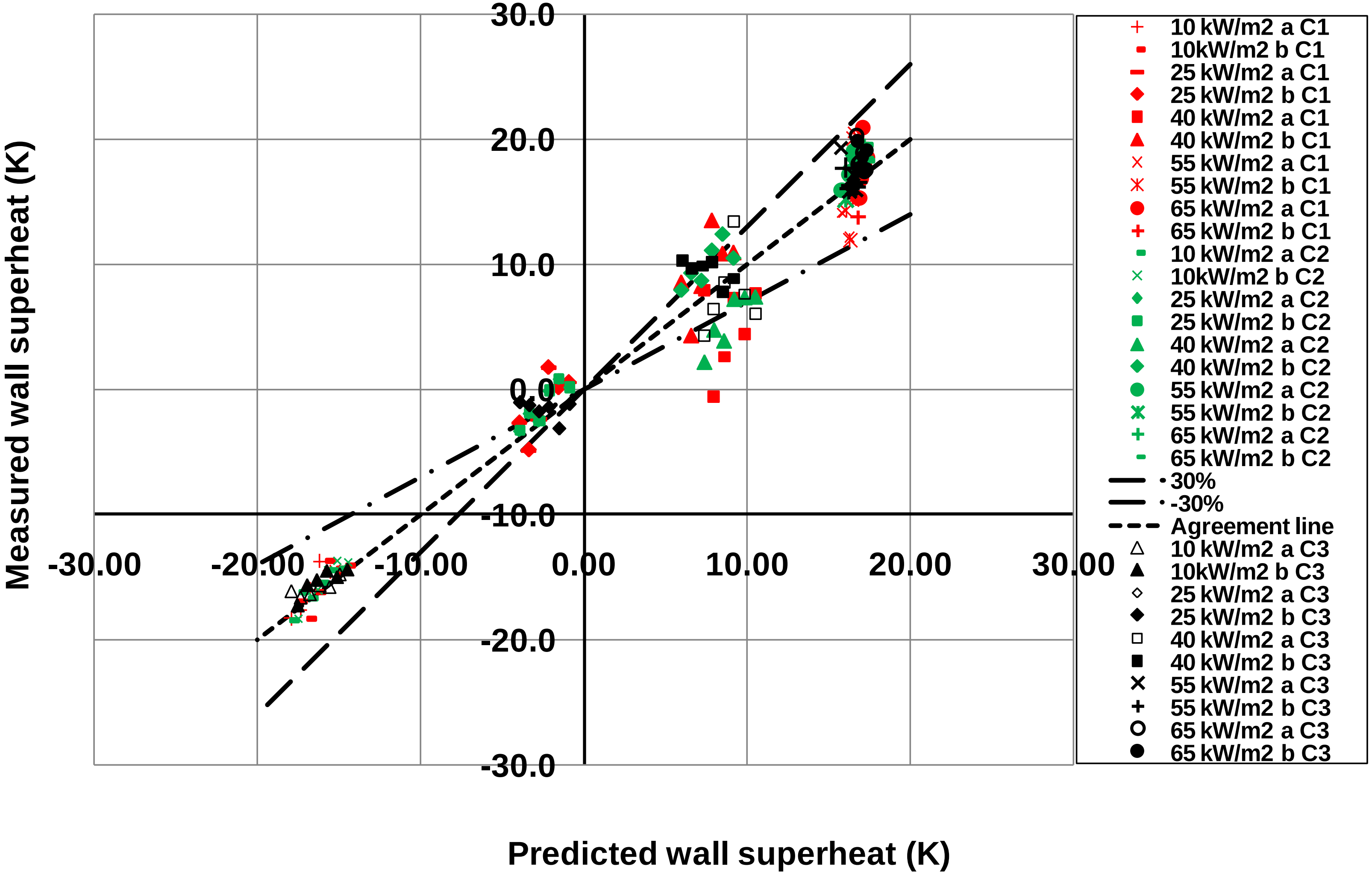

Figure 5-10: comparison of predicted with measured wall superheat

5.2.2.3 *Stephan and Abdelsalam correlation based predictions*

A comparison between the measured and predicted wall superheats using the Stephan and Abdelsalam [9] correlation for the sub-cooled nucleate boiling regime is shown in Figures 5.11 for columns 1, 2 and 3 respectively. The Stephan and Abdelsalam [9]-based approach predicts the data with an average difference of 0.3%, 1.7% and 2.9% while the corresponding root mean square differences (rms) are 14.6%, 13.4% and 14.2% for columns 1, 2 and 3 respectively. The variation of the predicted and measured wall superheat is shown in Figure 5.12. The Stephan and Abdelsalam [9]-based approach predicts the wall temperatures in all columns equally well. Overall, the average error and the corresponding root mean square differences (rms) are 1.4% and 14.1%, respectively.

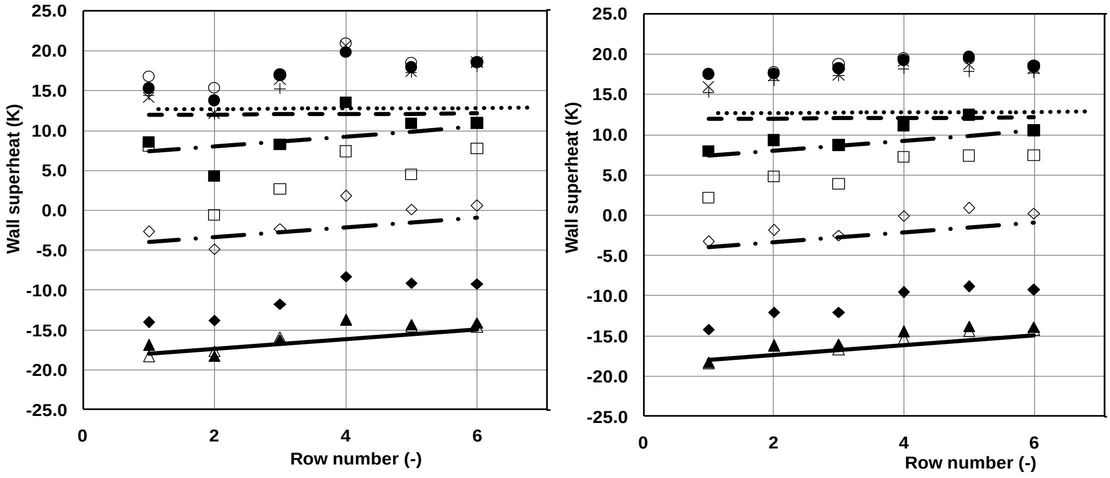

a) Column 1 *b) Column 2*

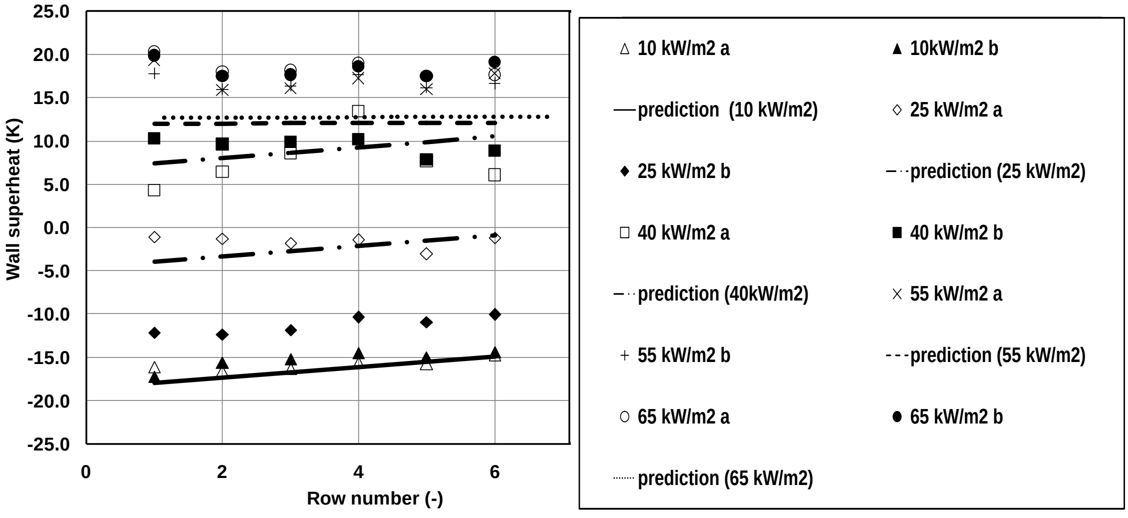

c) Column 3

Figure 5-11: variation of row number with wall superheat for

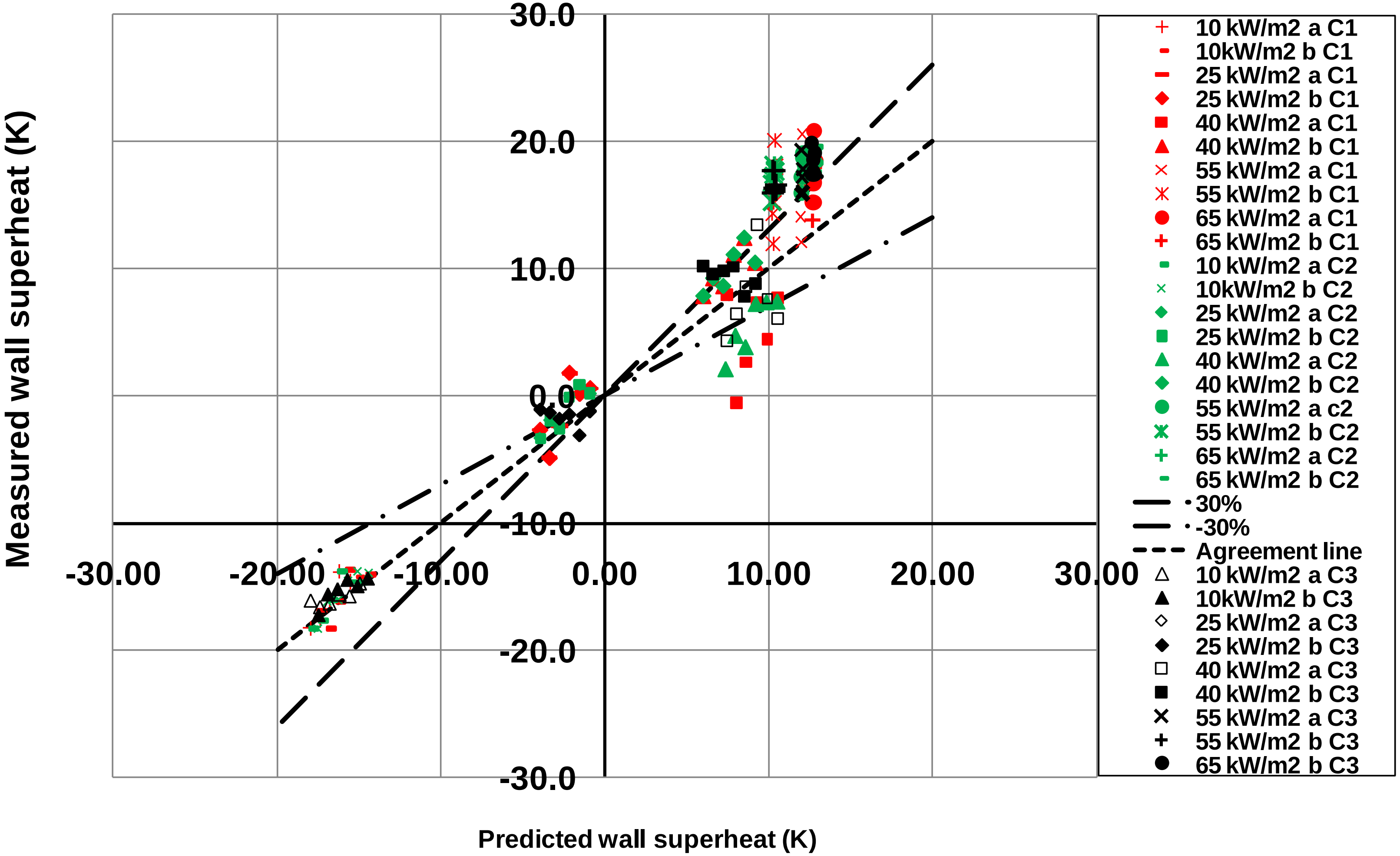

Figure 5-12: comparison of predicted with measured wall superheat

Overall, the Stephan and Abdelsalam [9]-based approach, Cooper [11]-based approach and the Gorenflo [12]-based approach predict the data equally well. However, a significant proportion of the good agreement comes from the natural convection predictions, which masks the boiling element. Boiling occurs at heat fluxes of 55 and 65 kW/m^2, for which the Gorenflo [12] correlation has an rms difference of 12.14% while the Stephan correlation has an rms difference of 14.14% and the Cooper correlation as the root mean square difference of 14.3%. Thus, the Gorenflo [12] correlation predicts the data better than the Stephan correlation, which predicted similarly to the Cooper [11] correlation.

5.2.3 ***Medium Pressure Low Level Series LLMP:***

At a pressure of 450 mbar, Equation 5.2 gave onset wall superheats of typically 0.9-1.2K, so that all of the LLMP data set is predicted to be boiling. This translates to the data taken at all heat fluxes being in the sub-cooled nucleate boiling regime. All the columns behave similarly, with column 3 slightly hotter than the other columns.

5.2.3.1 ***Cooper correlation based predictions***

Figure 5.13 shows a comparison between the measured and predicted wall superheats for the Cooper [11] correlation. The data behavior is consistent with pool boiling in that the wall superheat increases with increasing heat flux as shown in Figure 5.13. The Cooper [11]-based approach over-predicts the data with an average difference of 3.1%, 0.8% and 6.2% for columns 1, 2 and 3 respectively. The corresponding root mean square differences (rms) are 12.0%, 11.3% and 14.8%. Thus, the Cooper correlation predicts the wall temperatures in columns 1 and 2 better than those in column 3. Overall, the average and the corresponding root mean square differences are 3.1% and 12.8% respectively, Figure 5.13. The upper and lower limits shown in Figure 5.14 are set at ±30% with the data for columns 1, 2 and 3 shows good agreement between the predicted and measured wall superheat.

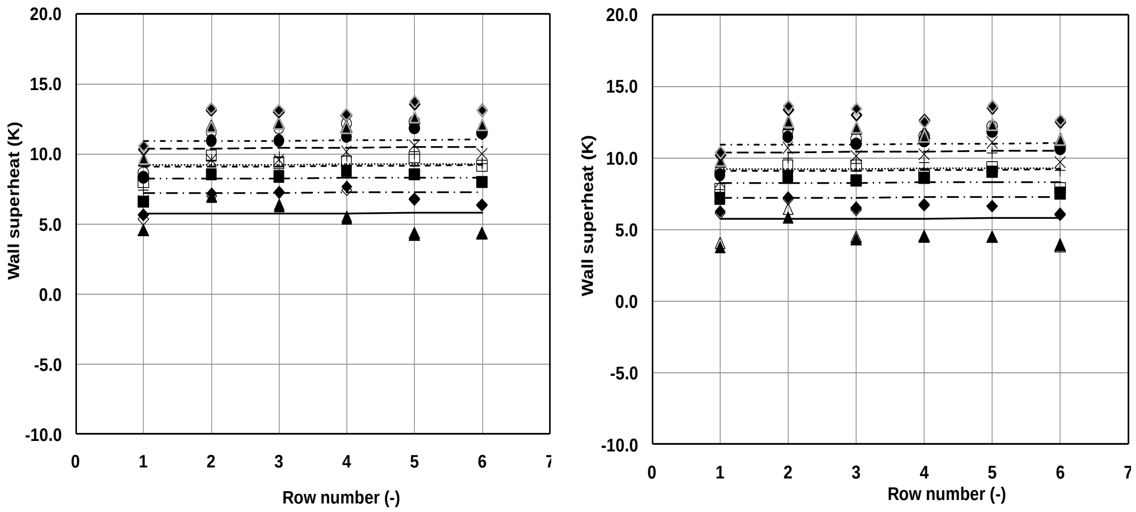

a) Column 1　　　*b) Column 2*

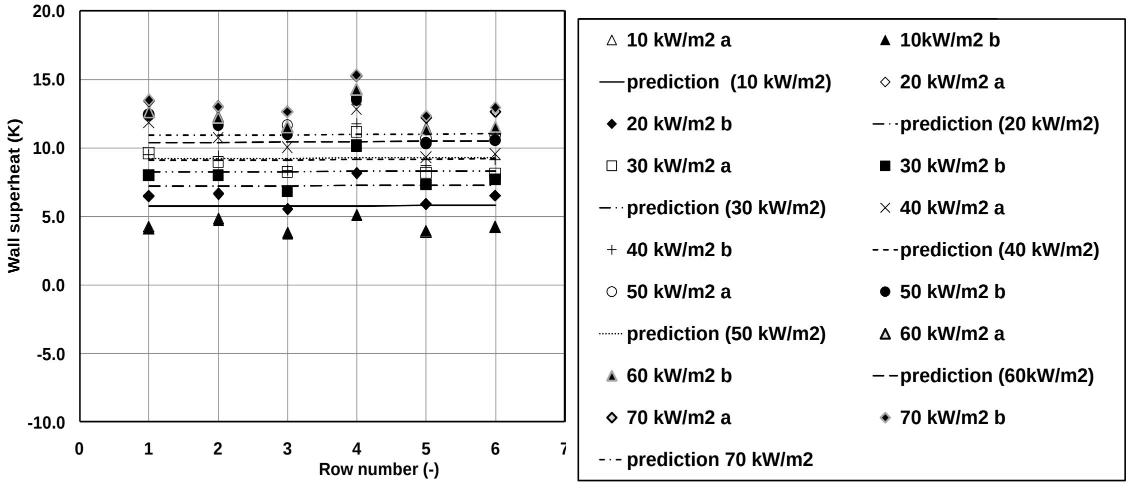

c) Column 3

Figure 5-13: variation of wall superheat with row number

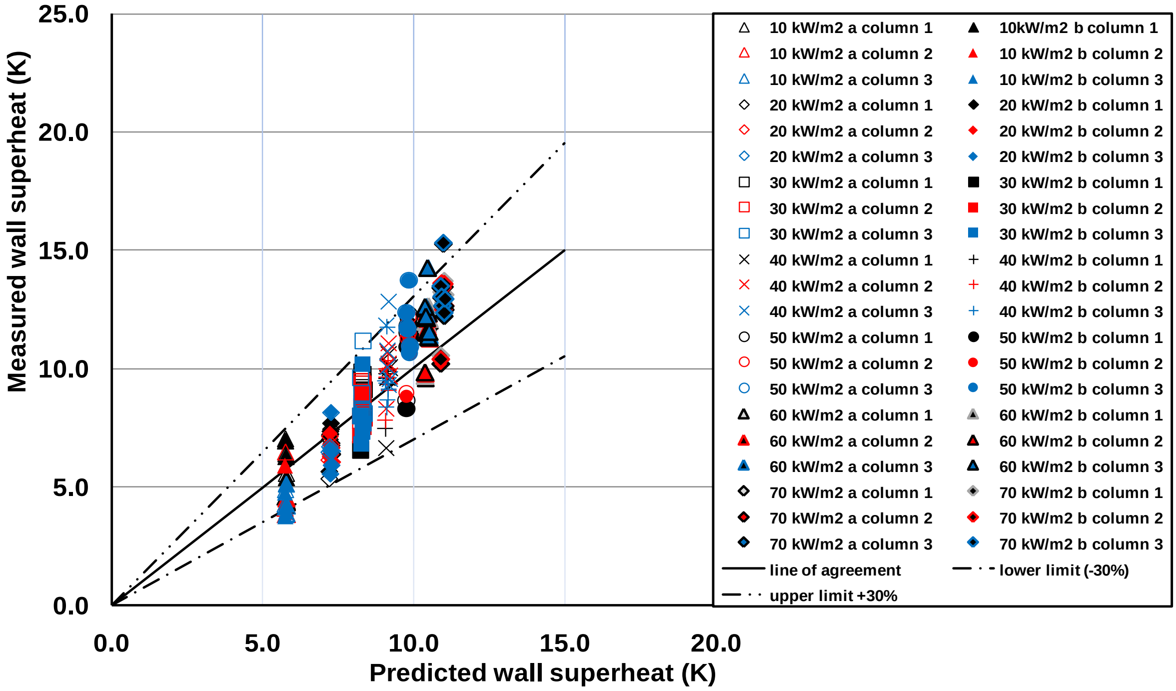

Figure 5-14: comparison of predicted with measured wall superheat

5.2.3.2 *Gorenflo correlation based predictions*

A comparison between the measured and predicted wall superheats for the Gorenflo [12] correlation is shown in Figure 5.15. The Gorenflo [12] correlation predicts the data with an average difference of -19.1%, -21.0% and -16.7% for columns 1, 2 and 3 respectively. The corresponding root mean square differences (rms) are 21.4%, 22.9% and 19.9%. Thus, the Gorenflo [12] correlation predicts the wall temperatures in column 3 better than those in columns1 and 2. Overall, the average and the corresponding root mean square (rms) differences are -18.0% and 21.48% respectively. A comparison of predicted with measured wall superheat, Figure 5.16, shows poor agreement.

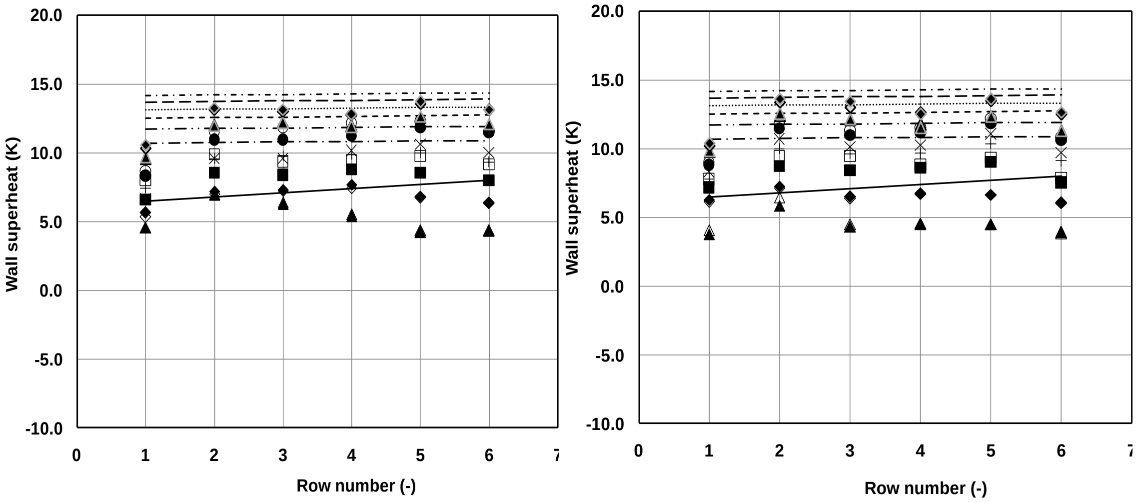

a) Column 1 *b) Column 2*

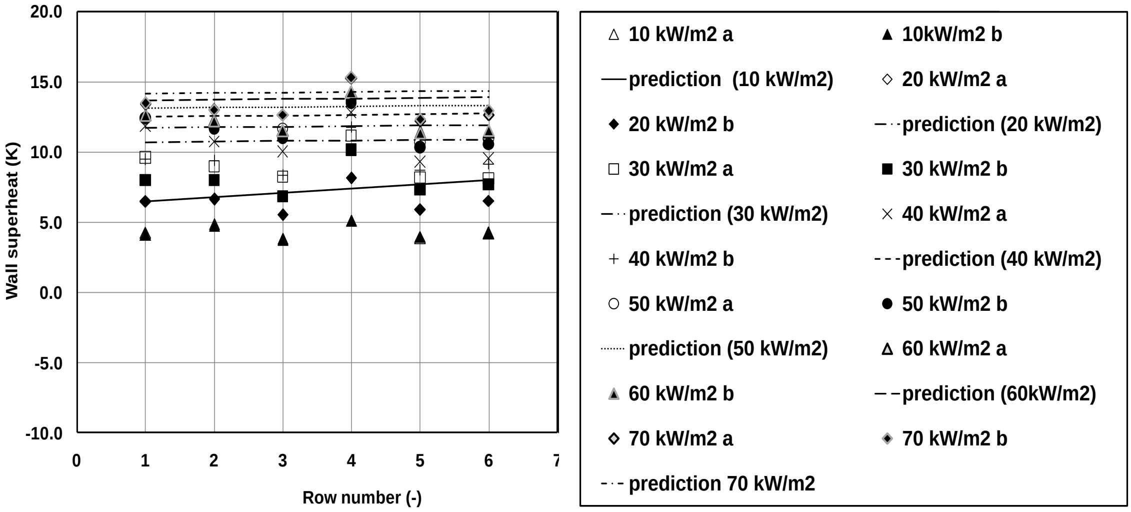

c) Column 3

Figure 5-15: variation of wall superheat with row number

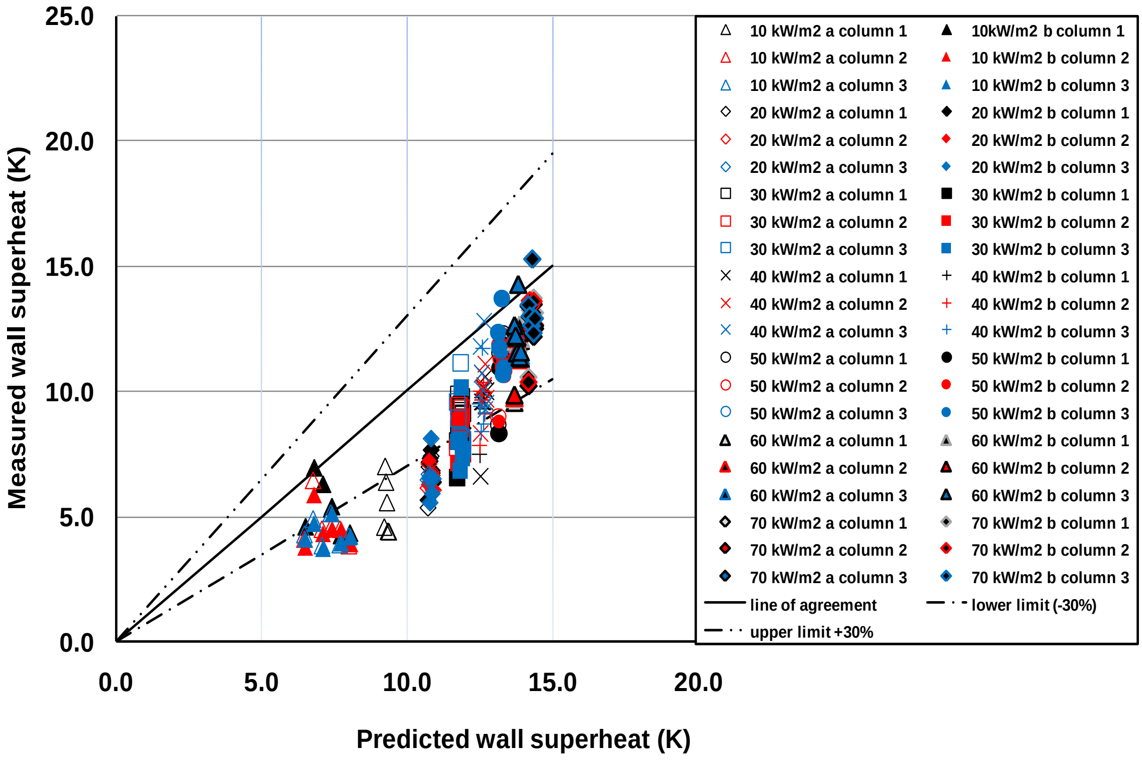

Figure 5-16: comparison of predicted with measured wall superheat

5.2.3.3 ***Stephan and Abdelsalam correlation based predictions***

Figure 5.17 shows a comparison between the measured and predicted wall superheats for the Stephan and Abdelsalam [9] correlation. A comparison of predicted with measured wall superheat are shown in Figure 5.18 for columns 1, 2 and 3. The Stephan and Abdelsalam [9] correlation predicts the data with an average difference of 0.5%, -1.7% and 3.6% for columns 1, 2 and 3 respectively. The corresponding root mean square differences (rms) are 10.9%, 10.7% and 13.1%. Overall, the average difference and root mean square differences are 0.8% and 11.6% respectively.

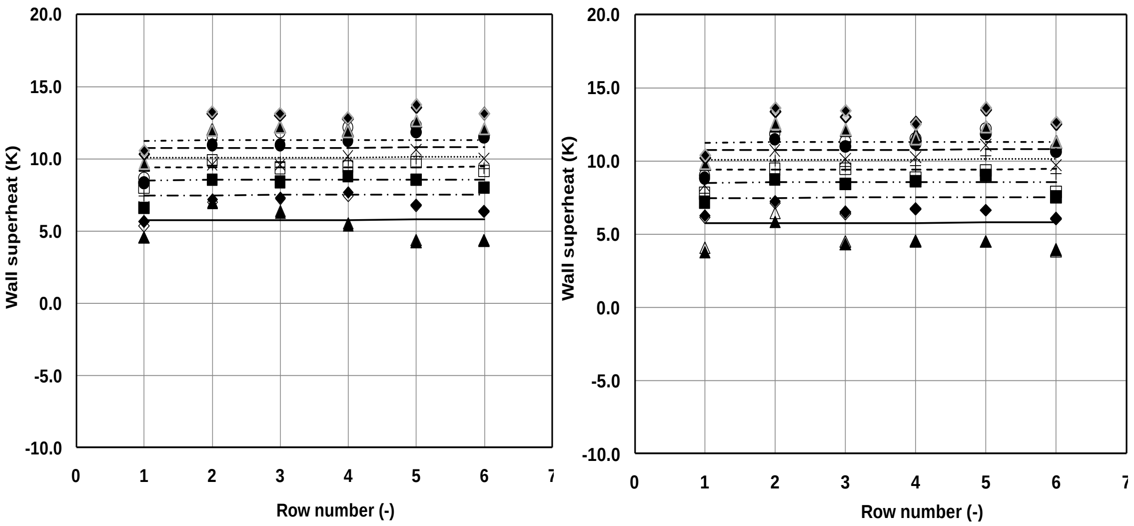

a) Column 1

b) Column 2

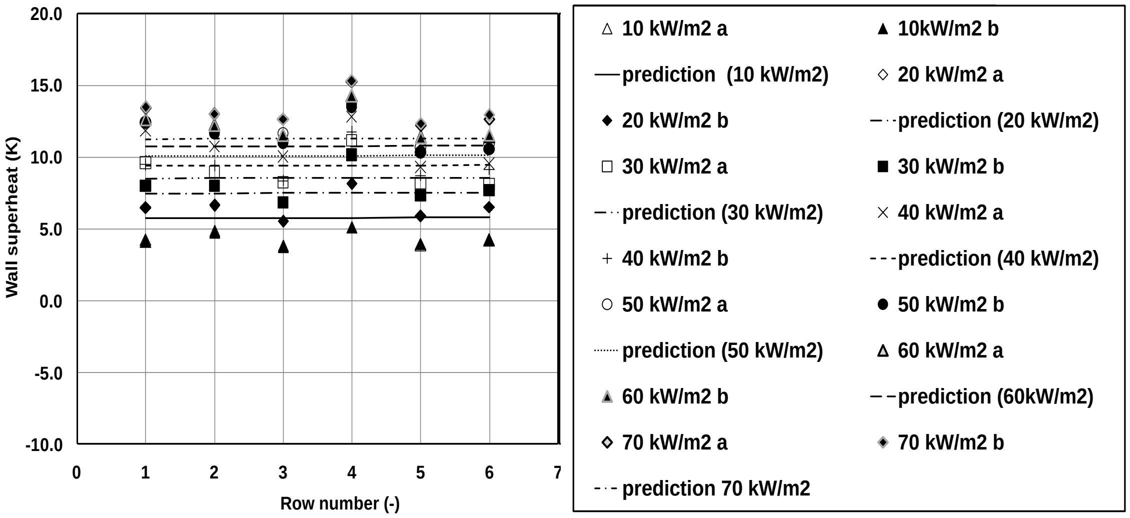

c) Column 3

Figure 5-17: variation of wall superheat with row number

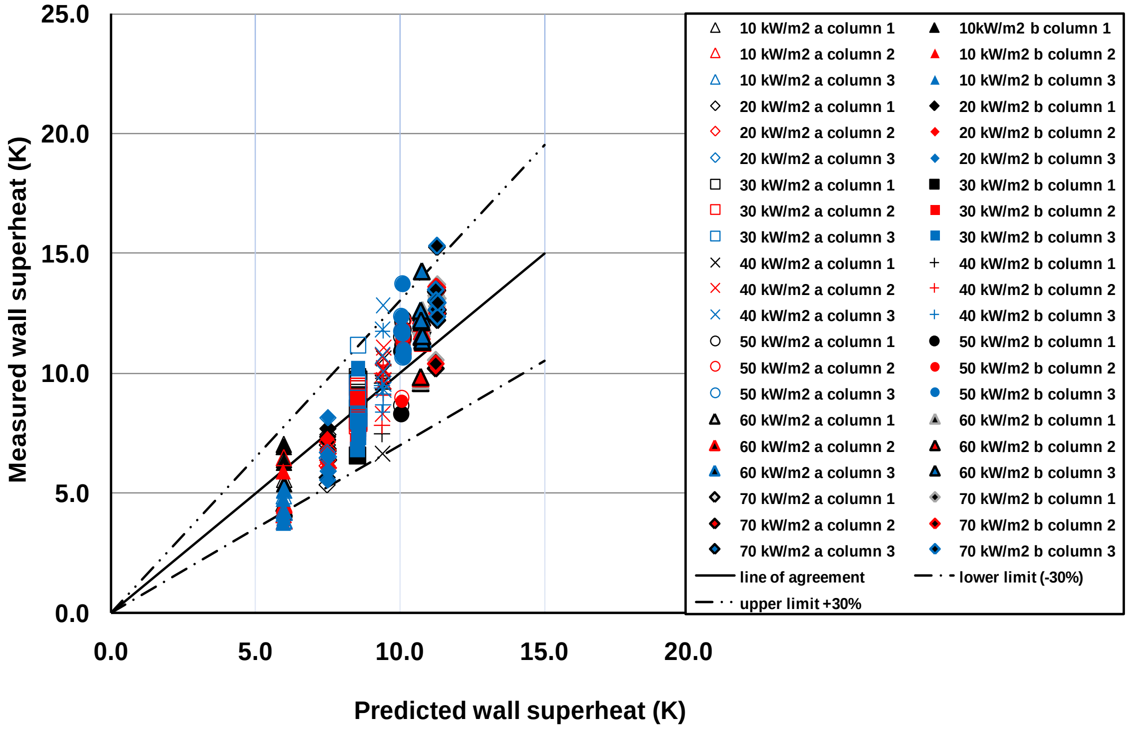

Figure 5-18: comparison of predicted with measured wall superheat

Overall, when this model is applied to the low level data at a pressure of 450 mbar, root mean square differences of 12.8 % and an average error of 3.1 % occur when the Cooper [11] correlation was used to describe the boiling element. The corresponding figures achieved when the Gorenflo [12] correlation was used were 21.5 % and -18.0 % and when the Stephan and Abdelsalam [9] correlation was used 11.6 % and 0.81 %. The Stephan and Abdelsalam [9] and Cooper [11] based approach, gives good agreement with the measured values.

5.2.4 ***High Pressure Low Level Series LLHP***

At a pressure of 850 mbar, Equation 5.2 gave onset wall superheats of typically 0.7 K, so that all of the LLHP data set is predicted to be boiling. This translates to the data taken at all heat fluxes being in the sub-cooled nucleate regime. All the columns behave similarly, with column 3 slightly hotter than the other columns.

5.2.4.1 ***Cooper correlation based predictions***

A comparison between the measured and predicted wall superheats for the Cooper [11] correlation shown in Figures 5.19. The Cooper [11] correlation predicts the data with an average difference of 3.1%, 5.07% and 15.5% for columns 1, 2 and 3 respectively. The corresponding root mean square differences (rms) are 15.1%, 14.9% and 21.0%. Thus, the Cooper [11] correlation predicts the wall temperatures in columns 1 and 2 better than those in column 3. Overall, the average and rms differences are 7.9% and 17.2% respectively. The data behavior is consistent with pool boiling in that the wall superheat increases with increasing heat flux. Figure 5.20 shows good agreement for the predicted wall superheat with measured value.

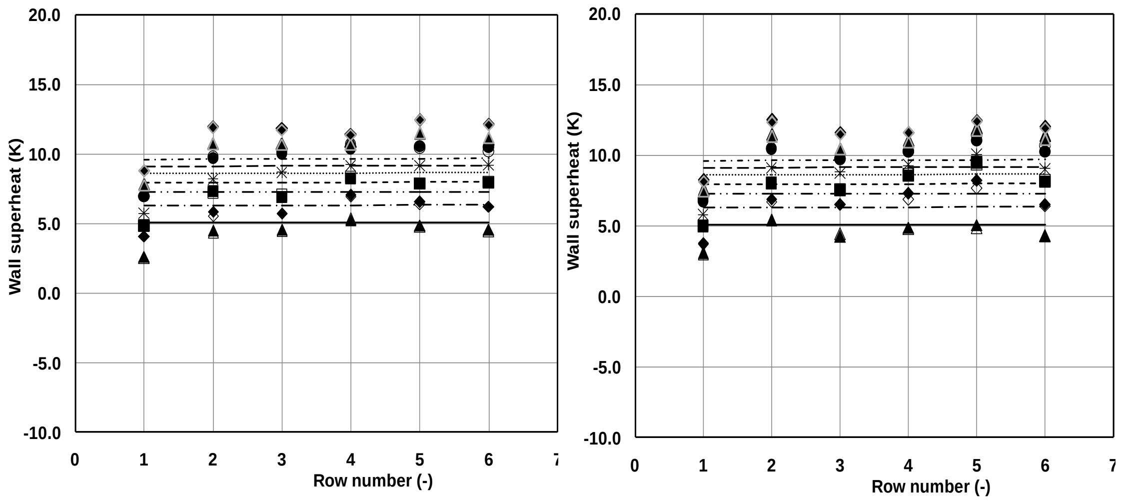

a) Column 1

b) Column 2

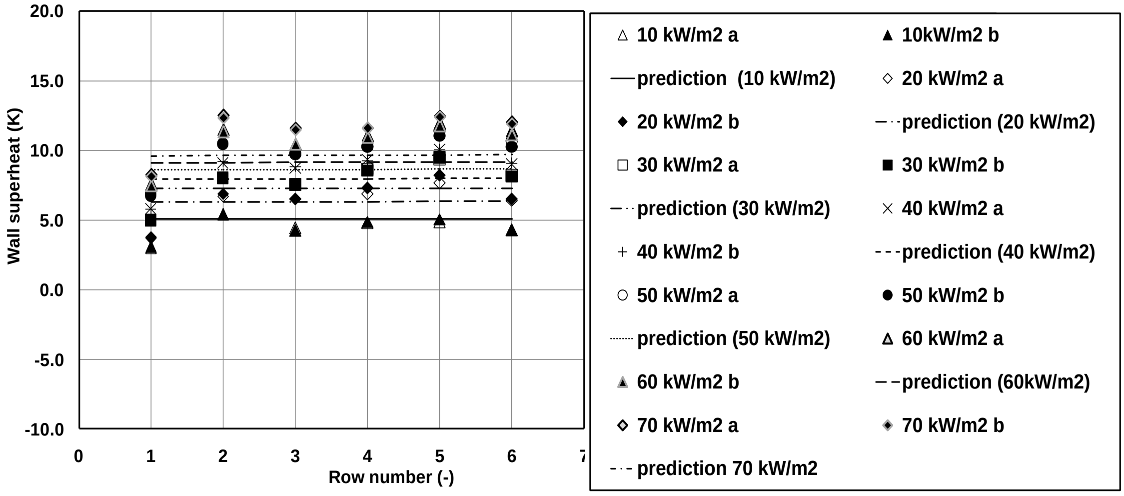

c) Column 3

Figure 5-19: variation of wall superheat with row number for

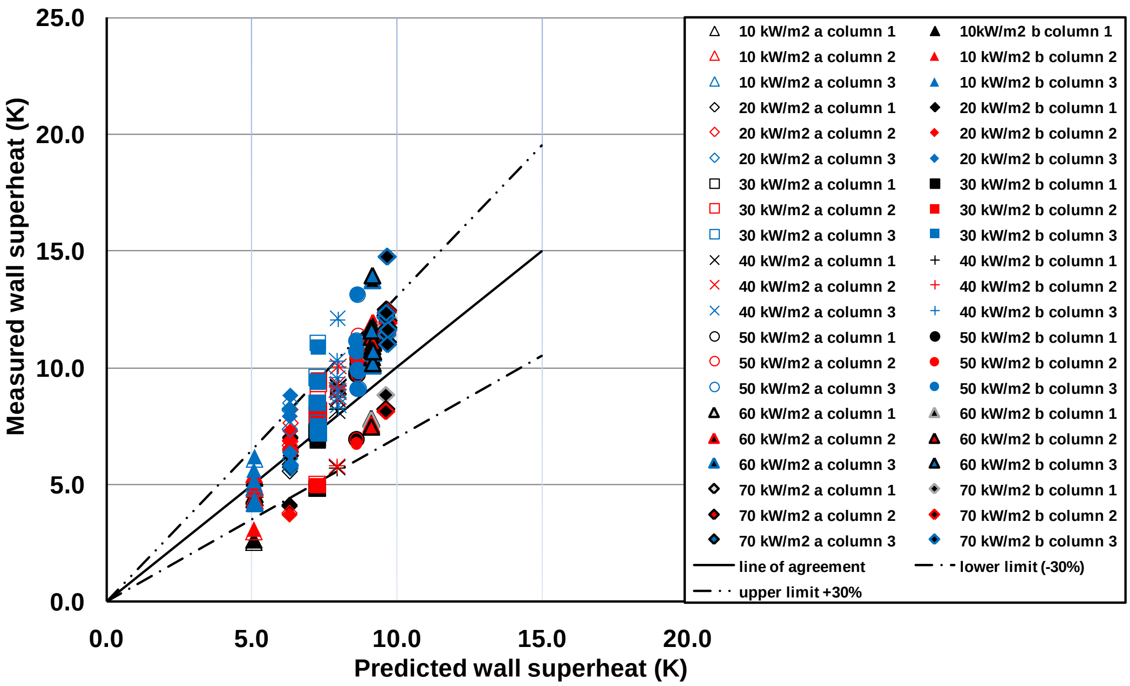

Figure 5-20: comparison of predicted with measured wall superheat

5.2.4.2 *Gorenflo correlation based predictions*

Figure 5.21 shows a comparison between the measured and predicted wall superheats for the Gorenflo [12] correlation. The Gorenflo [12] correlation predicts the data with an average difference of -18.9%, -17.4% and -9.2% for columns 1, 2 and 3 respectively. The corresponding root mean square differences (rms) are 23.0%, 21.3% and 15.9%. Thus, the Gorenflo [12] correlation predicts the wall temperatures in column 3 better than those in columns 1 and 2. Overall, the average and the corresponding root mean square differences are -15.0% and 20.3% respectively. Figure 5.22 shows poor agreement between the predicted and the measured wall superheat compare to cooper correlation.

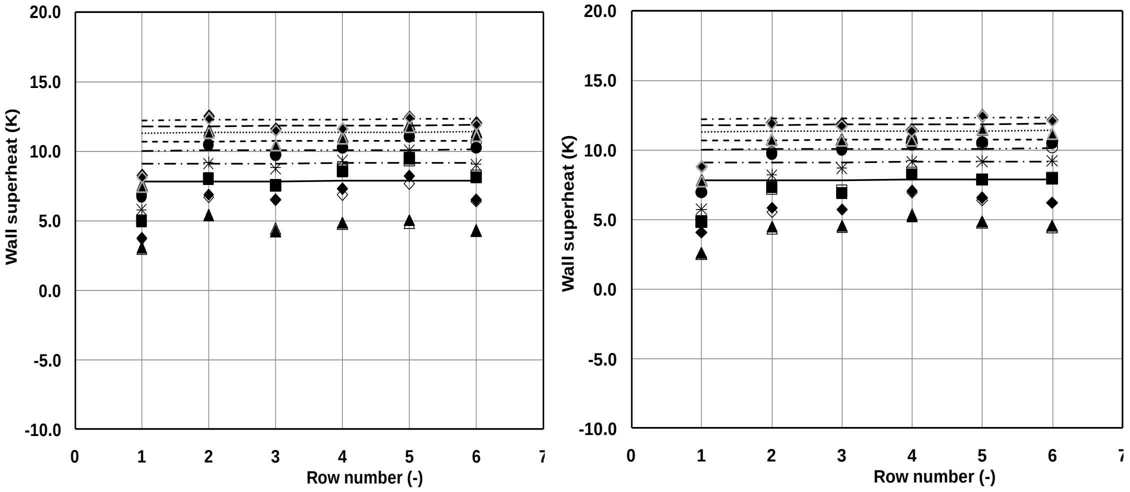

a) Column 1 *b) Column 2*

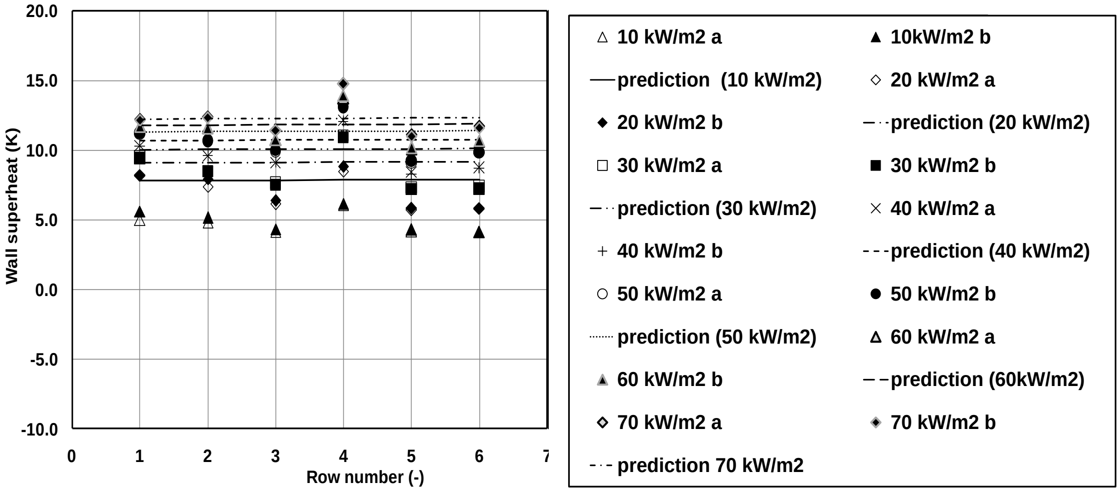

c) Column 3

Figure 5-21: variation of wall superheat with row number

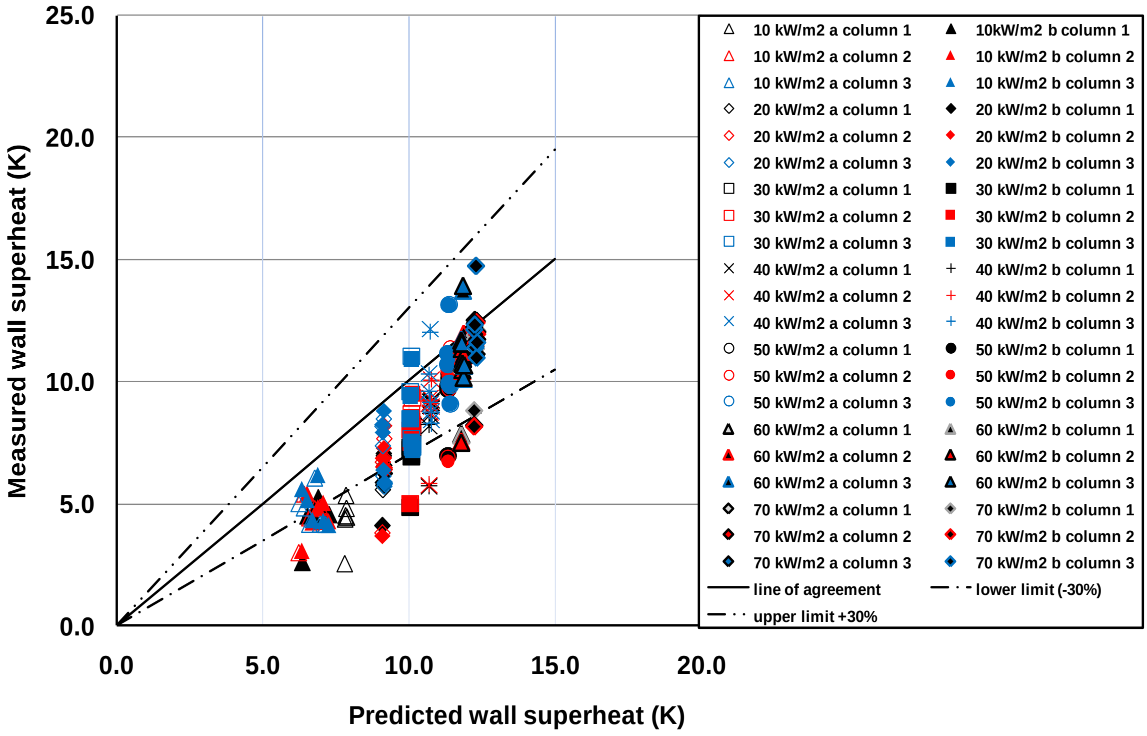

Figure 5-22: comparison of predicted with measured wall superheat

5.2.4.3 *Stephan and Abdelsalam correlation based predictions*

Figure 5.23 show a comparison between the measured and predicted wall superheats for the Stephan and Abdelsalam [9] correlation. The Stephan and Abdelsalam [9] correlation predicts the data with an average difference of -1.91%%, -0.04% and 9.9% for columns 1, 2 and 3 respectively. The corresponding root mean square differences (rms) are 14.1%, 13.3% and 16.7%. Overall, the average difference and rms differences are 2.6% and 14.8% respectively. A comparison between predicted and measured wall superheat is shown in Figure 5.24 for the data for columns 1, 2 and 3 shows better agreement than cooper and Gorenflo correlations.

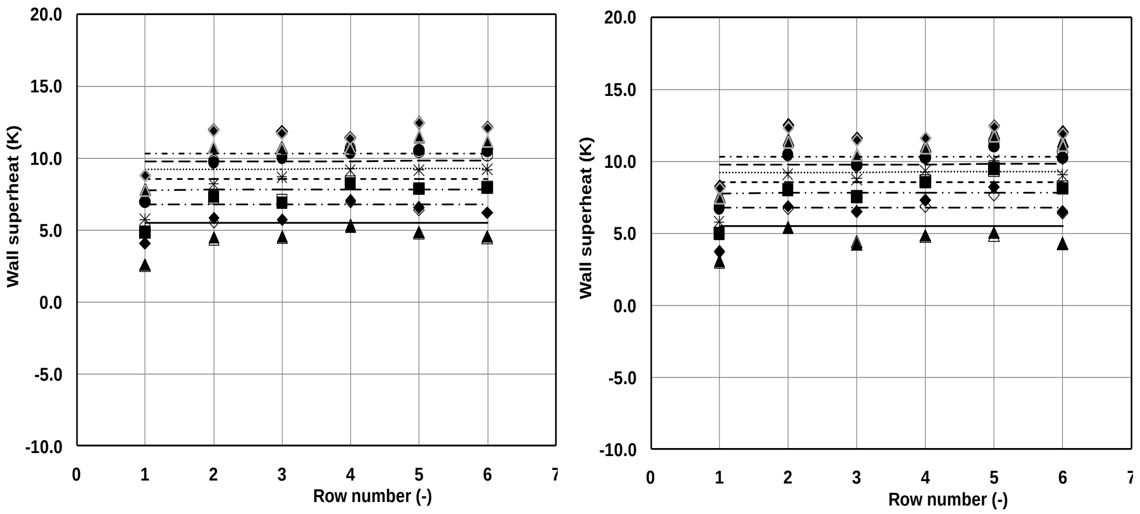

a) Column 1

b) Column 2

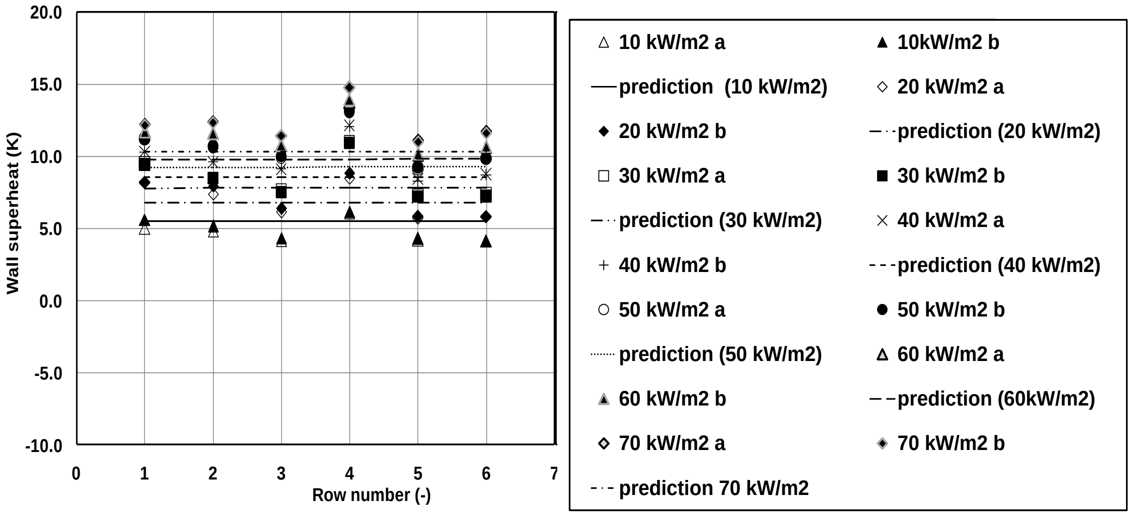

c) Column 3

Figure 5-23: variation of wall superheat with row number

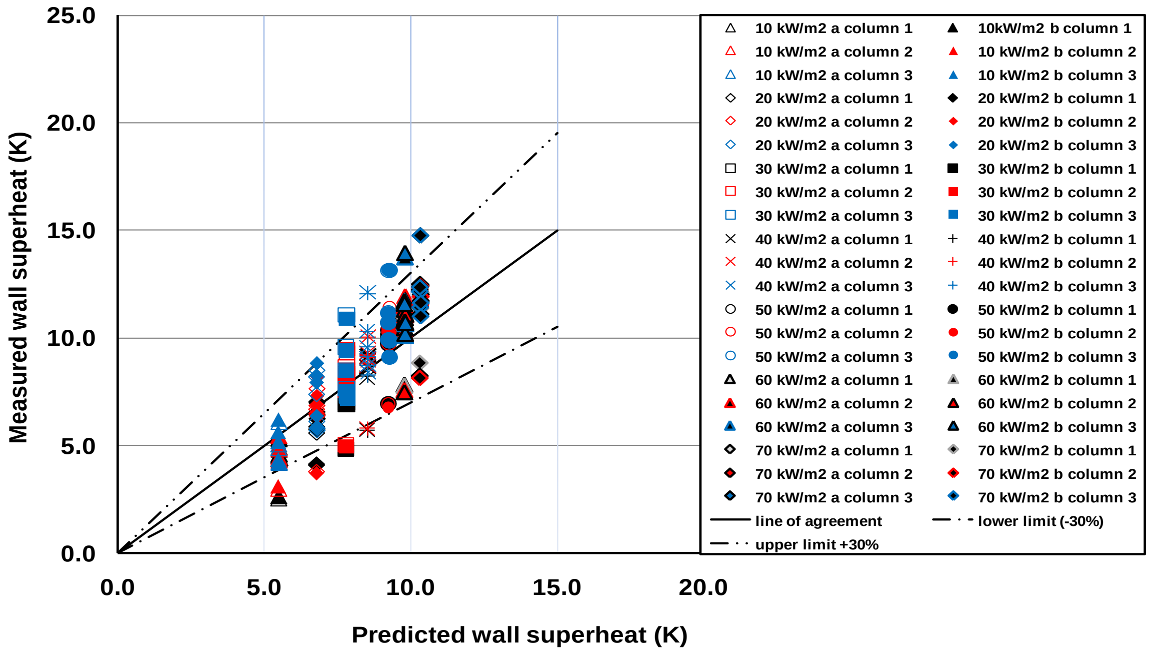

Figure 5-24: comparison of predicted with measured wall superheat

Overall, for the low level data at a pressure of 850 mbar, the model produced root mean square differences of 17.2 % and an average error of 7.9 % when the Cooper [11] correlation was used to describe the boiling element. The corresponding figures achieved when the Gorenflo [12] correlation was used were 20.3 % and -15.0 % . The Stephan and Abdelsalam [9] correlation gave a root mean square difference of 14.8 % and an average error of 2.7 %. The Stephan and Abdelsalam [9] correlation gives good agreement with the measured values and better than the other correlations used.

5.3 The Equilibrium, One-Dimensional Model

The one-dimensional model, as described by McNeil et al and Brisbane et al [75, 82] normally assumes that the liquid enters a column of tubes in a saturated state and evaporates as the fluid moves upwards across the tubes. This model in forced convection and assumes single phase convection caused by natural circulation. The mass flux upwards through the column is the value that balances the pressure drops in the tube column with the static liquid value outside of it. The pressure gradient, $\frac{dp}{dz}$ in the column has three components, $\left(\frac{dp}{dz}\right)_M$, the pressure gradient due to momentum, $\left(\frac{dp}{dz}\right)_F$, the pressure gradient due to friction and, $\left(\frac{dp}{dz}\right)_G$, the pressure gradient due gravity, i.e.

$$\frac{dp}{dz} = \left(\frac{dp}{dz}\right)_M + \left(\frac{dp}{dz}\right)_F + \left(\frac{dp}{dz}\right)_G \tag{5-6}$$

In the current application the pressure gradient due to momentum $\left(\frac{dp}{dz}\right)_M$ was neglected because the void fraction was very low.

The frictional pressure gradient was obtained from

$$\left(\frac{dp}{dz}\right)_F = -\frac{f_L}{2D\rho_L}m^2 \tag{5-7}$$

The single-phase friction factor, f_L, was found from the method of ESDU [83], Equation (2.55). In this model, the liquid temperature in the column was raised but was found not to reach the local saturation temperature. The driving force for the mass flux in the column was modified to use natural circulation caused by temperature differences in the liquid. Thus, for a sub-cooled liquid, the energy equation for a tube within a column, Figure 5.25, becomes

$$T_{LE} = T_{LI} + \frac{\pi D q}{m P_H c_{pL}} \qquad \textit{5-8}$$

The net pressure drop, Δp_{net}, which must be balanced by friction in the column, is given by

$$\triangle p_{net} = \sum_{i=1}^{N_{row}} g P_v \left(\rho_{LB} - \rho_{Lwi}\right) \qquad \textit{5-9}$$

where $\mathrm{N_{row}}$ is the number of rows, *i* is the row number, P_v is the vertical tube pitch, ρ_{LB} is the bulk fluid liquid density and ρ_{lw} is the liquid density at the wall temperature. The heat flux was assumed to partition into nucleate,q_{nb} and single-phase, q_{sp}, components, thus

$$q = q_{nb} + q_{sp} \qquad \textit{5-10}$$

The tube wall superheat, $\triangle T_{sup}$ was therefore found from the solution of

$$q = \left(\gamma \triangle T_{sup}\right)^{\frac{1}{(1-n)}} + h_{sp}\left(\triangle T_{sup} + \triangle T_{sub}\right) \qquad \textit{5-11}$$

where $\triangle T_{sub}$ is the liquid sub-cooling and h_{sp} was obtained from the ESDU [84] correlation

$$h_{sp} = RNu\, k_l / D \qquad \textit{5-12}$$

where RNu is the row Nusselt number , this is found from

$$RNu = f1 f4\, RNu_R \qquad \textit{5-13}$$

where $f1$ And $f4$ are correlation parameters and $f4$ depends on row number and $f1$ is defined as

$$f1 = \left(\frac{Pr}{Pr_w}\right)^{0.26} \qquad \textit{5-14}$$

in which Pr and Pr_w are the bulk flow Prandtl number and the wall flow Prandtl number respectively, Equation 2.25

RNu_R is the reference Nusselt number, which is given as:

$$RNu_R = 0.34 A\, C\, Re\, Pr \qquad \textit{5-15}$$

where A and C depend on Re, Reynolds number

- If $10 < Re < 300$ then A= 0.742 and C = 0.431
- If $300 < Re < 2.10^5$ then A= 0.211 and C = 0.651
- If $2.10^5 < Re < 2.10^6$ then A= 0.116 and C = 0.700

$$Re = \frac{m P_h D}{\mu_l (P_h - D)} \qquad \textit{5-16}$$

where P_h is the horizontal tube pitch and.

Three correlations were used for the nucleating boiling component, the Cooper [11] , Gorenflo [12] and Stephan and Abdelsalam [9] correlations.

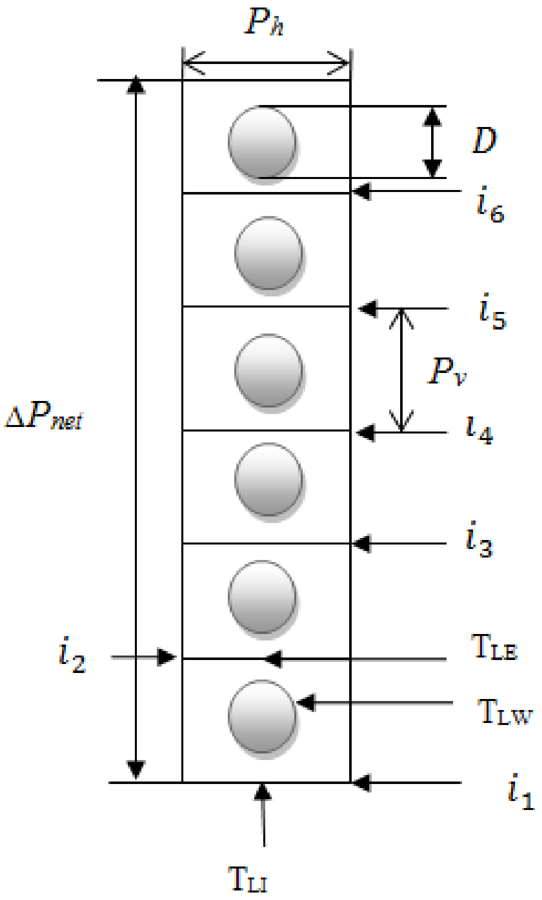

Figure 5-25: tube column from the evaporator

5.3.1 ***Low Pressure Low Level Series LLLP***

At a pressure of 50 mbar, Equation 5.4 gave onset wall superheats of typically 5.5-9.6 K for the LLLP data set, so that most of the data at heat fluxes of 10 and 25 kW/m^2 are in single-phase convection, with the remainder convecting and boiling.

5.3.1.1 *Cooper - ESDU combination*

Figure 5.26 shows a comparison between the measured and predicted wall superheats for the Cooper-ESDU [11] [84] combination. This combination predicts the data with an average difference of -0.7%, 9.4% and 19.8% for columns 1, 2 and 3 respectively. The corresponding root mean square differences (rms) are 14.7%, 13.2% and 28.1%. Thus, the Cooper - ESDU [11] [84] combination predicts the wall temperatures in columns 1 and 2 better than those in column 3

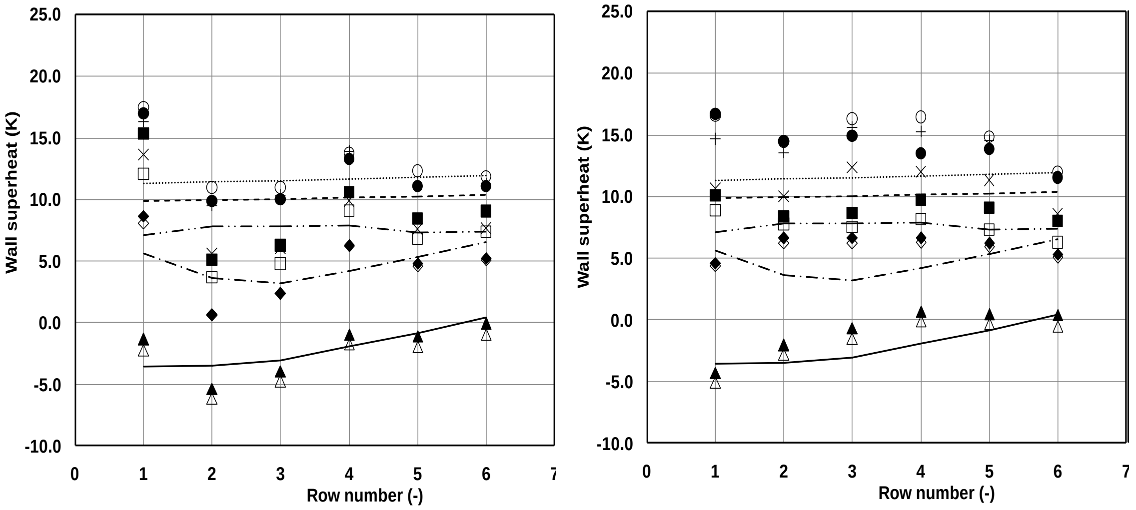

a) Column 1 *b) Column 2*

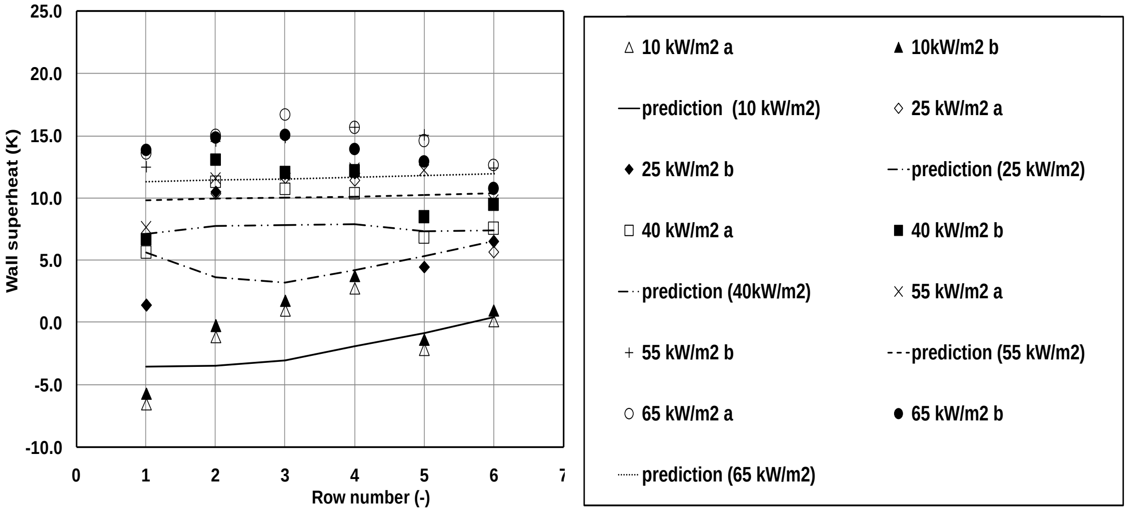

c) Column 3

Figure 5-26: variation of wall superheat with row number

Overall, the average and the corresponding root mean square differences (rms) are 9.3% and 19.8% respectively. A comparison of predicted with measured wall superheat is shown in Figure 5.27 for the data for columns 1, 2 and 3. This figure shows good agreement for the predicted wall superheat with the measured wall superheat.

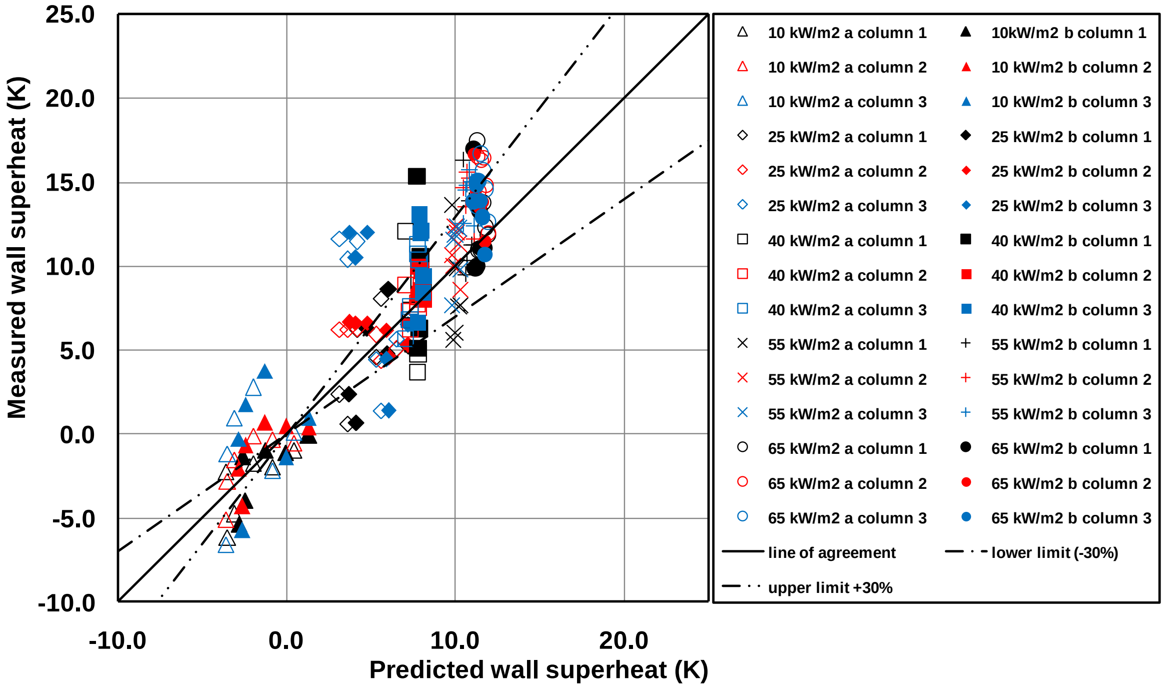

Figure 5-27: comparison of predicted with measured wall superheat

5.3.1.2 *Gorenflo –ESDU combination*

A comparison between the measured and predicted wall superheats for the Gorenflo - ESDU [12] [84] combination is shown in Figures 5.28 for columns 1, 2 and 3 respectively. The Gorenflo - ESDU [12] [84] combination predicts the data with an average difference of -10.0%, -0.48% and 9.07% for columns 1, 2 and 3 respectively. The corresponding root mean square differences (rms) are 15.8%, 10.3% and 25.0%. Overall, the average and the corresponding root mean square differences (rms) are -0.47% and 18.5% respectively. A comparison of predicted with measured wall superheat is shown in Figure 5.29. This Figure also shows good agreement for the predicted wall superheat with the measured wall superheat.

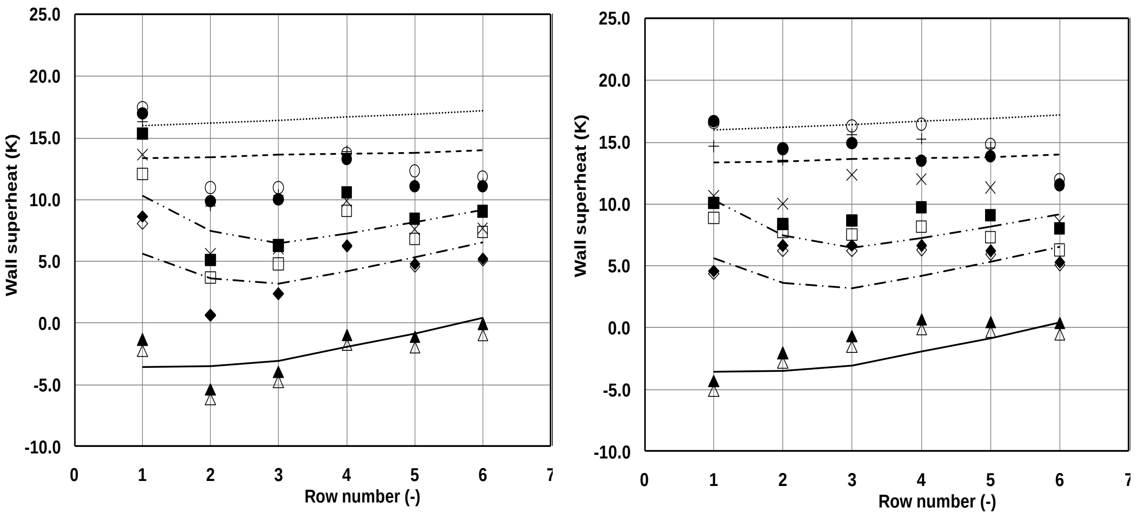

a) Column 1

b) Column 2

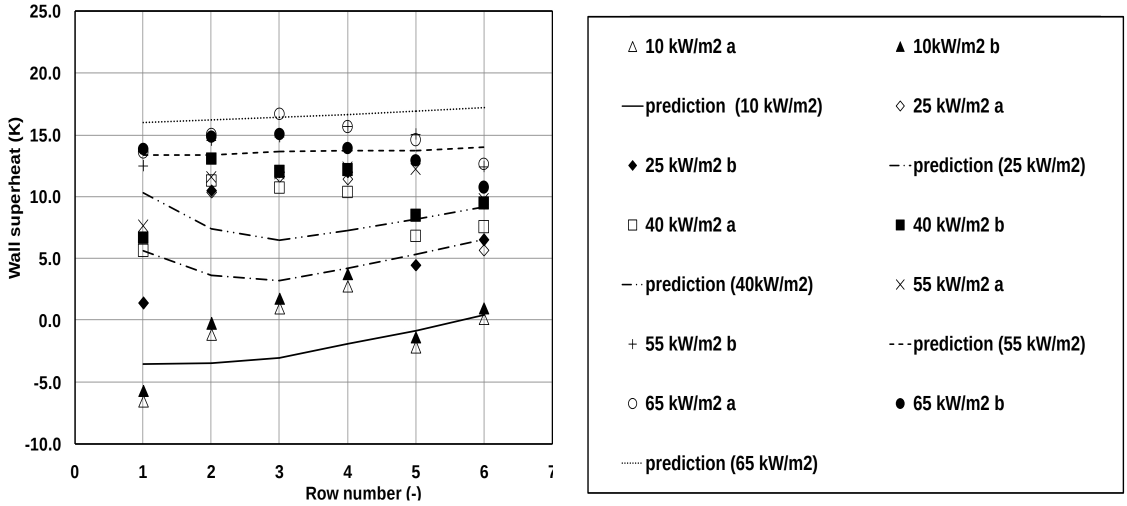

c) Column 3

Figure 5-28: variation of wall superheat with row number

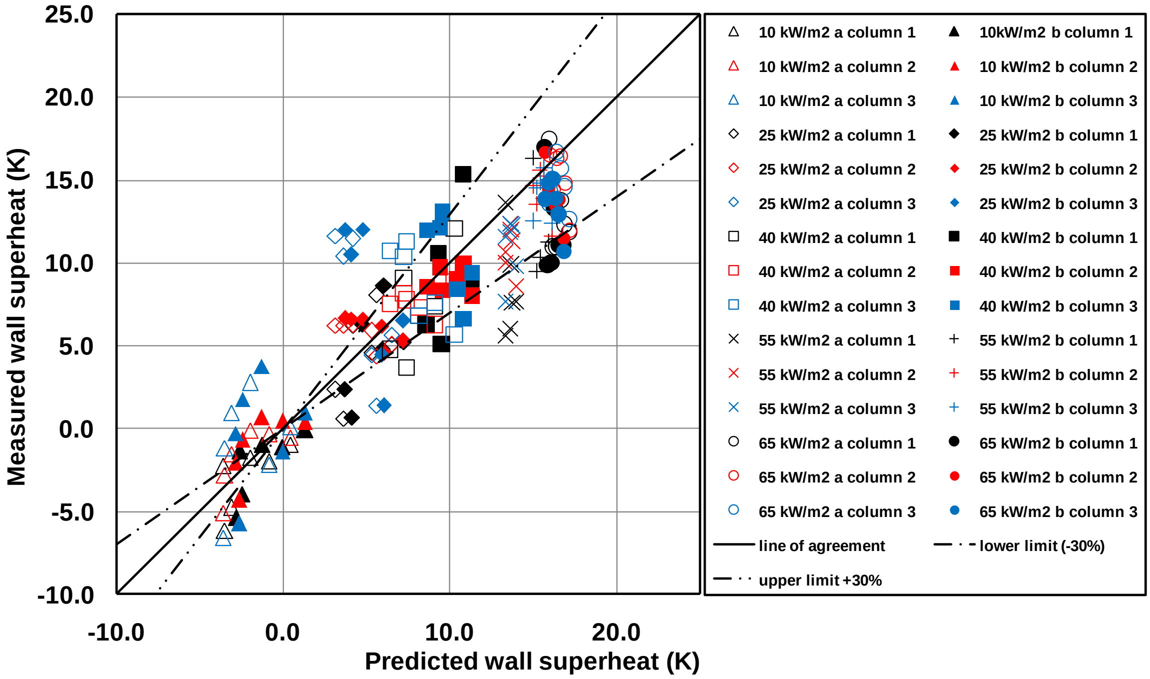

Figure 5-29: comparison of predicted with measured wall superheat

5.3.1.3 *Stephan and Abdelsalam – ESDU combination*

Figure 5.30 shows a comparison between the measured and predicted wall superheats for the Stephan and Abdelsalam - ESDU [9] [84] combination. The Stephan and Abdelsalam - ESDU [9] [84] combination predicts the data with an average difference of 0.5%%, 10.7% and 20.5% for columns 1, 2 and 3 respectively. The corresponding root mean square differences (rms) are 15.3%, 14.6% and 29.0%.

Overall, the average difference and rms differences are 10.6% and 20.7% respectively. A comparison of predicted with measured wall superheat shown in Figure 5.31.

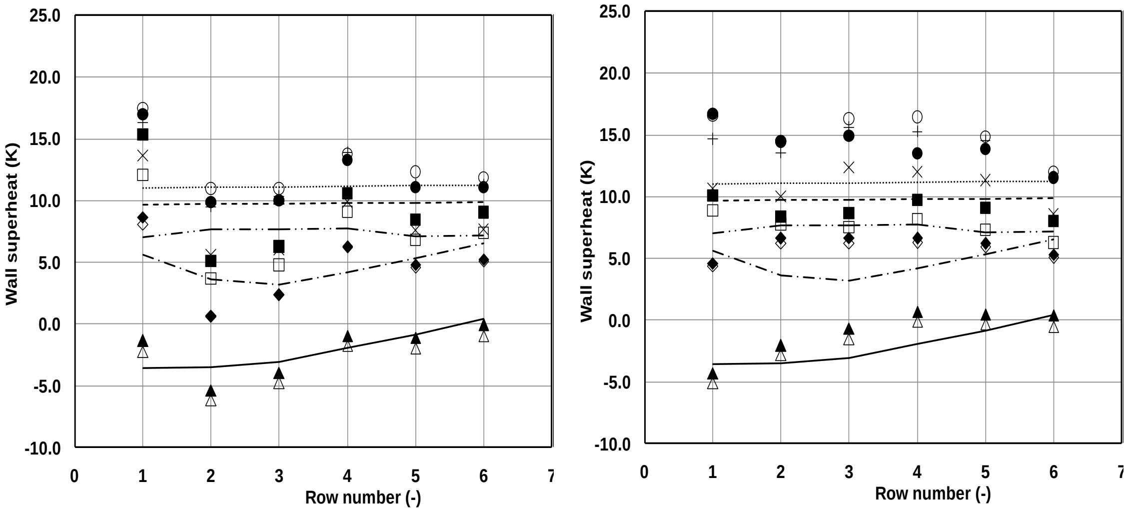

a) Column 1 *b) Column 2*

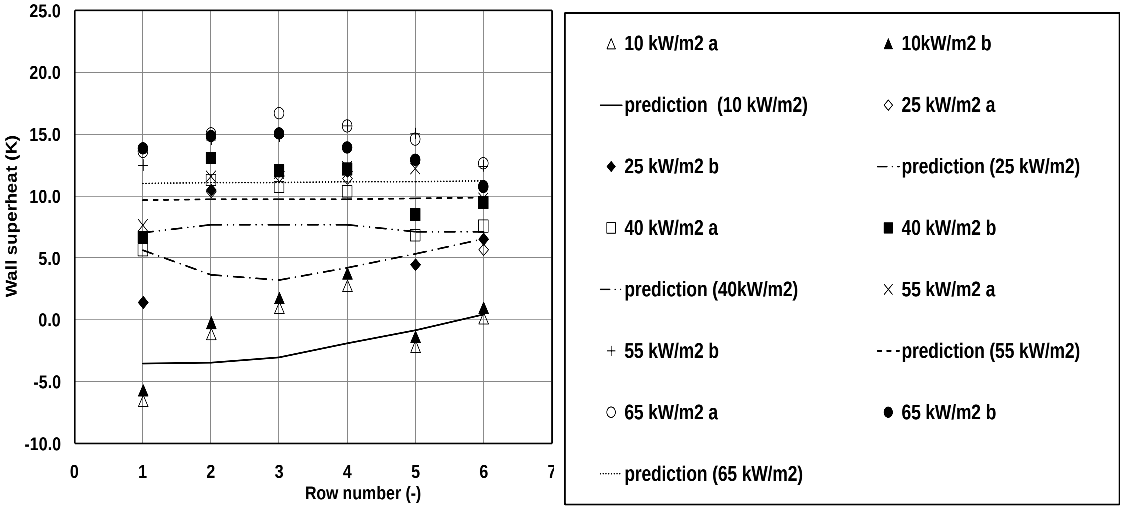

c) Column 3

Figure 5-30: variation of wall superheat with row number

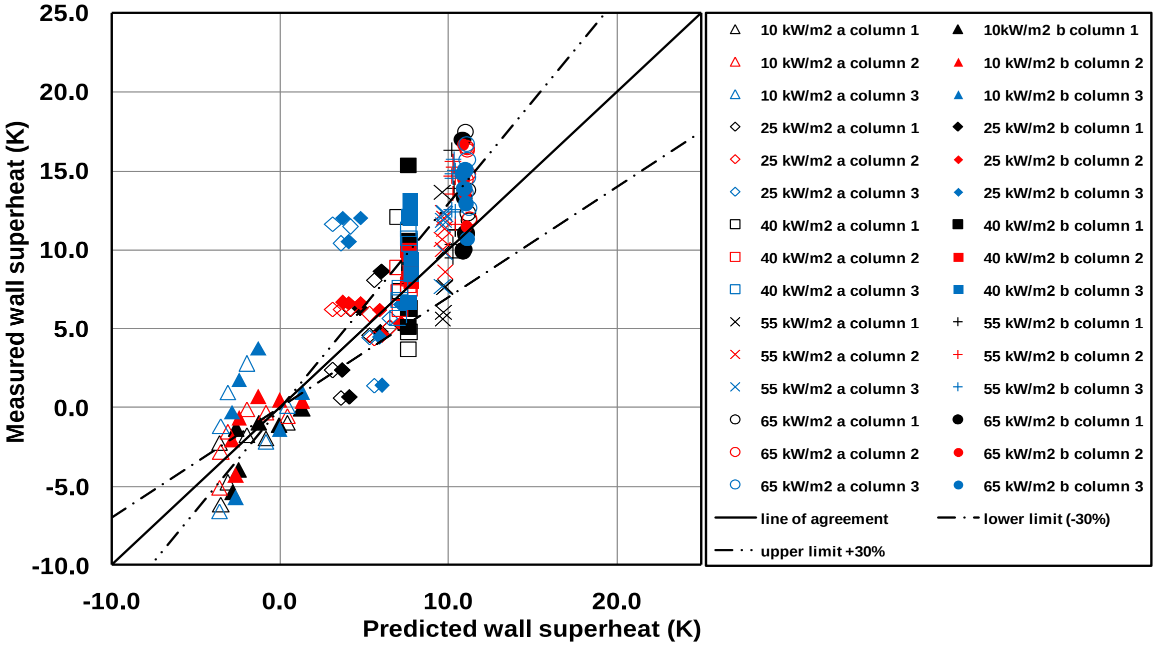

Figure 5-31: comparison of predicted with measured wall superheat

When this model is applied to the low level data at a pressure of 50 mbar, produced root mean square differences of 19.8 % and an average error of 9.3 % are obtained when the Cooper – ESDU [11] [84] combination was used. The corresponding figures achieved for the Gorenflo - ESDU [12] [84] combination was 18.5 % and -0.47 % and when the Stephan and Abdelsalam - ESDU [9] [84] combination was used 20.8 % and 10.6%. These results shows that the Gorenflo - ESDU [12] [84] combination gives good agreement and better than the other correlations used. The mass flux range required for this model is in the range of 29-65 kg/m^{2}s.

5.3.2 *Low Pressure High Level Series HLLP:*

At a pressure of 50 mbar, Equation 5.4 gave onset wall superheats of typically 5.2-7.7 K for the HLLP data set, so that virtually all of the data are in single-phase convection, with only row 1 data boiling at a heat flux of 65 kW/m^2, making the choice of boiling correlation somewhat irrelevant. A comparison between the measured and predicted wall superheats for the Gorenflo - ESDU [12] [84] combination is shown in Figure 5.32 for columns 1, 2 and 3 respectively. The Gorenflo - ESDU [12] [84] combination predicts the data with an average difference of 51%, 52% and 54% for columns 1, 2 and 3 respectively. The corresponding rms differences are 58%, 57% and 59%. Thus, the Gorenflo - ESDU [12, 84] combination predicts the wall temperatures in all columns similarly. Overall, the error average and root mean square differences are 52% and 58% respectively. The Cooper - ESDU [11] [84] combination and Stephan and Abdelsalam

– ESDU [9, 84] combination predicts the data similarly because virtually all of the predictions come from the ESDU correlation. A comparison of predicted with measured wall superheat is shown in Figure 5.33. This figure show poor agreement between the predicted wall superheat and the measured wall superheat. The mass flux required for this data set was in the range 29-87 kg/m^{2}s.

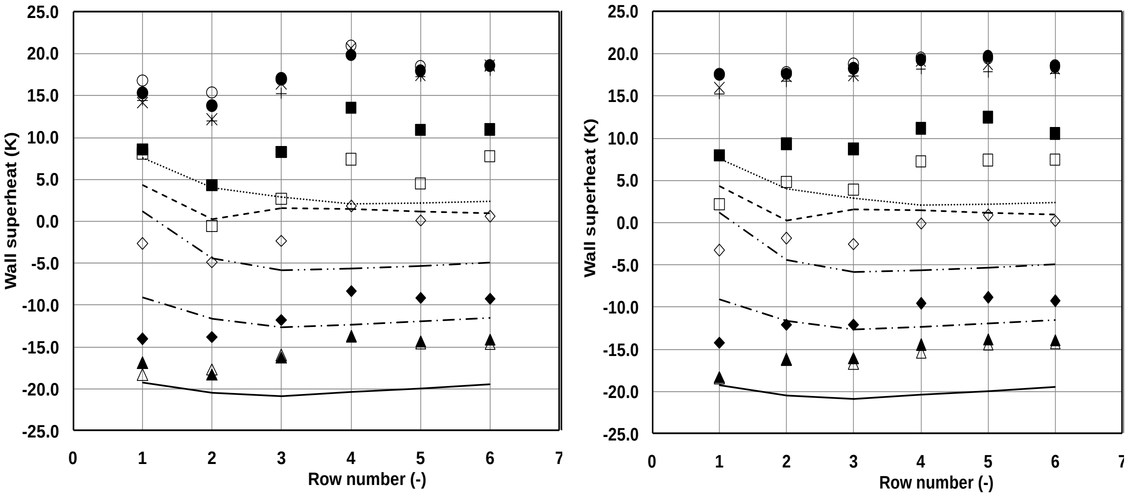

a) Column 1

b) Column 2

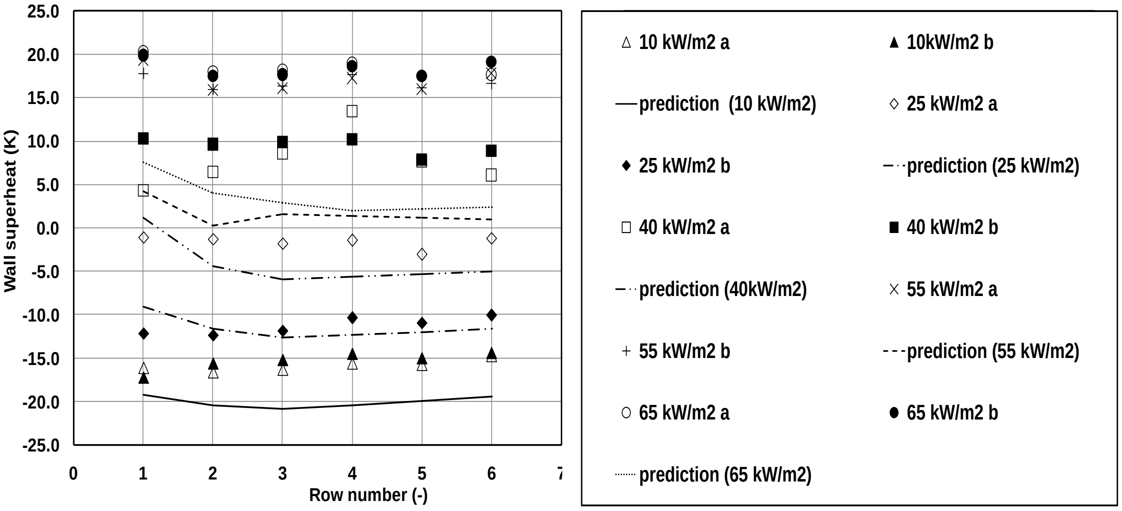

c) Column 3

Figure 5-32: variation of wall superheat with row number

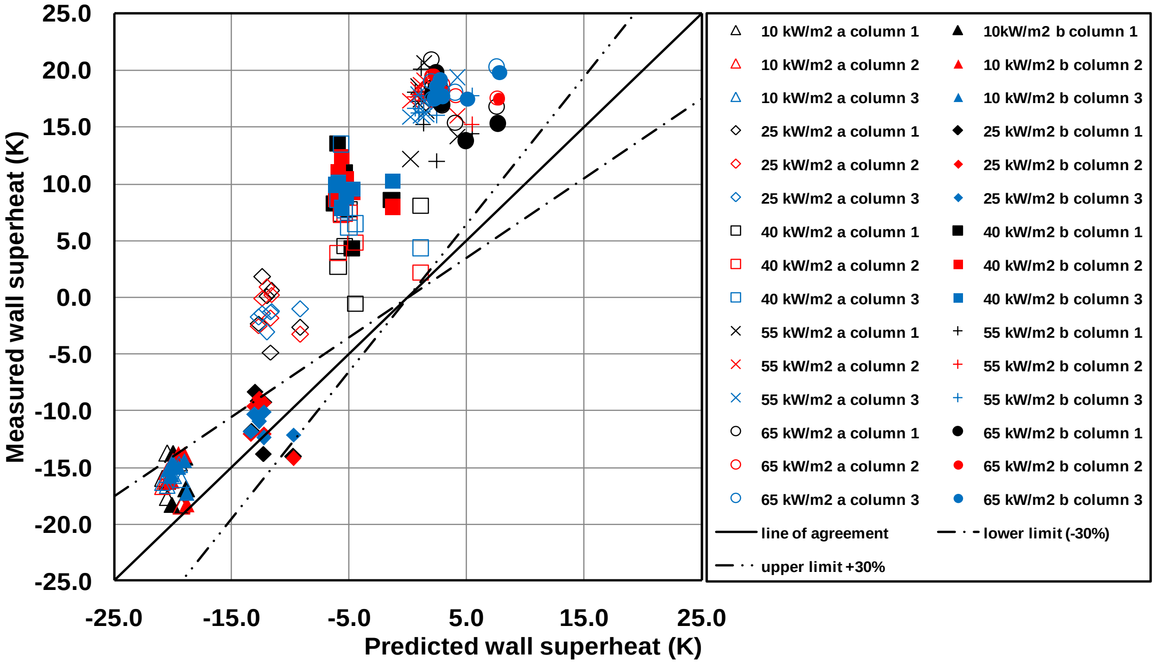

Figure 5-33: comparison of predicted with measured wall superheat

5.3.3 ***Medium Pressure Low Level Series LLMP:***

At a pressure of 450 mbar, Equation 5.4 gave onset wall superheats of typically 1-2 K, so that all of the LLMP data set is predicted to be boiling. This translates to the data taken at all heat fluxes being in the sub-cooled nucleate regime.

5.3.3.1 ***Cooper – ESDU combination***

Figure 5.34 shows a comparison between the measured and predicted wall superheats for the Cooper - ESDU [11] [84] combination for columns 1, 2 and 3 respectively. The Cooper - ESDU [11] [84] combination predicts the data with an average difference of 33.2%, 29.8% and 36.6% for columns 1, 2 and 3 respectively. The corresponding root mean square differences (rms) are 36.8%, 31.9% and 38.6%. Overall, the average and the root mean square differences are 33.2% and 35.9% respectively. A comparison of predicted with measured wall superheat is shown in Figure 5.35. This figure shows poor agreement for the predicted wall superheat compare to the measured wall superheat.

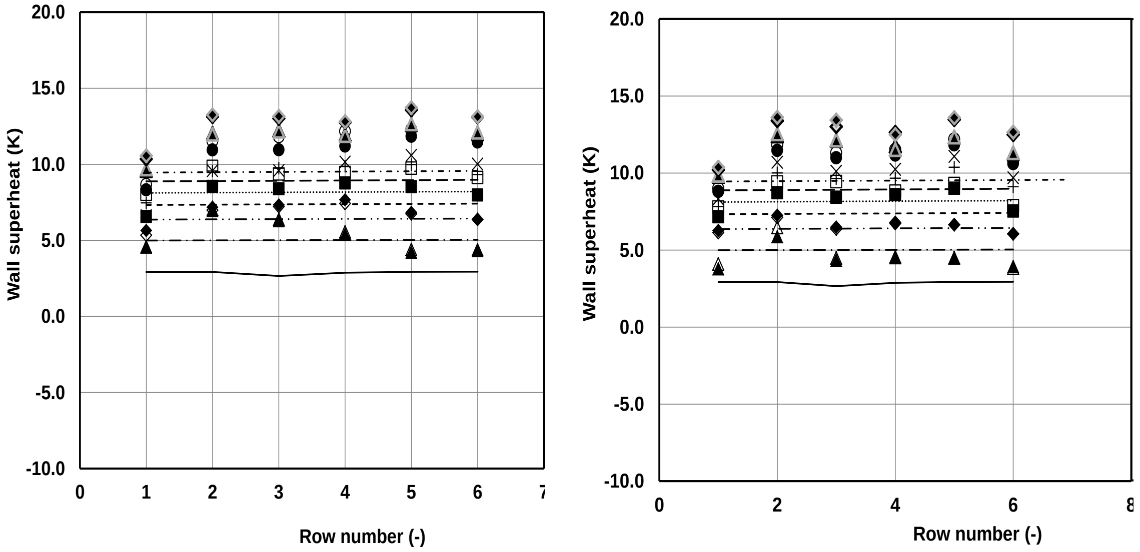

a) Column 1

b) Column 2

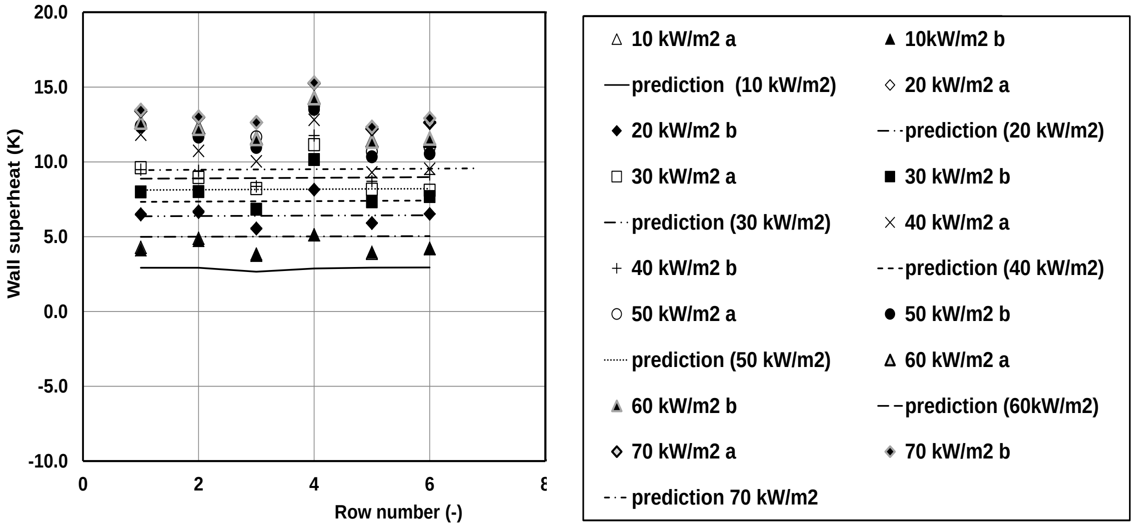

c) Column 3

Figure 5-34: variation of wall superheat with row number for

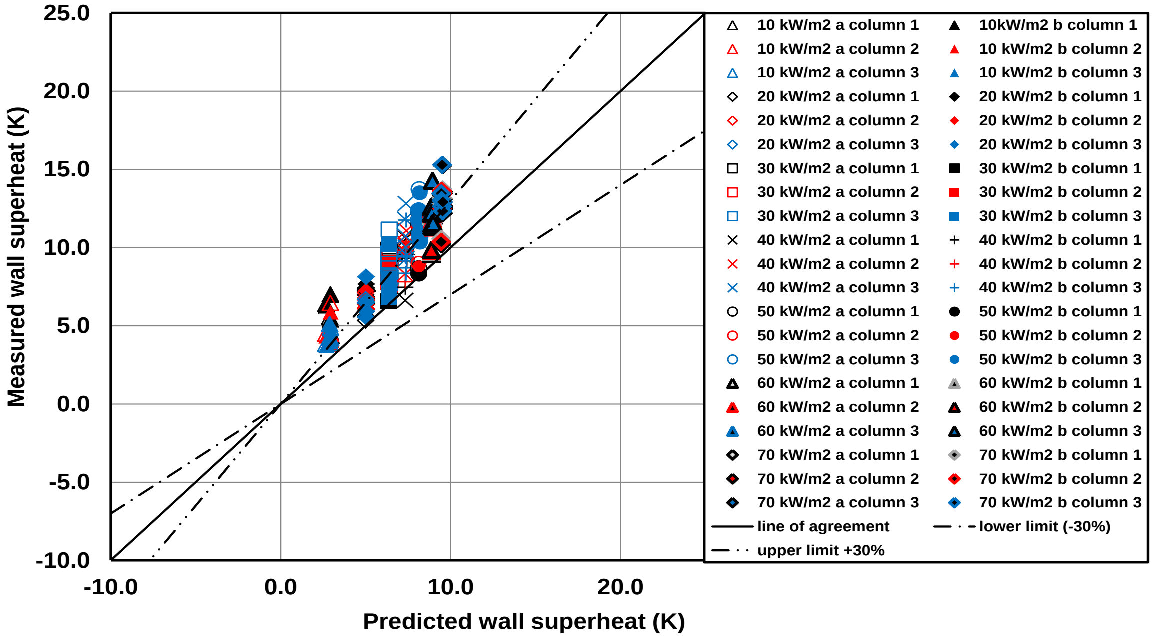

Figure 5-35: comparison of predicted with measured wall superheat

5.3.3.2 *Gorenflo - ESDU combination*

A comparison between the measured and predicted wall superheats for the Gorenflo - ESDU [12] [84] combination is shown in Figure 5.36 for the columns 1, 2 and 3 respectively. The Gorenflo - ESDU [12] [84] combination predicts the data with an average difference of 10.9%, 7.7% and 13.4% for columns 1, 2 and 3 respectively. The corresponding root mean square differences (rms) are 22.1%, 15.8% and 19.7%. Overall, the average and rms differences are 10.7% and 19.7% respectively. A comparison of predicted with measured wall superheat is shown in Figure 5.37.

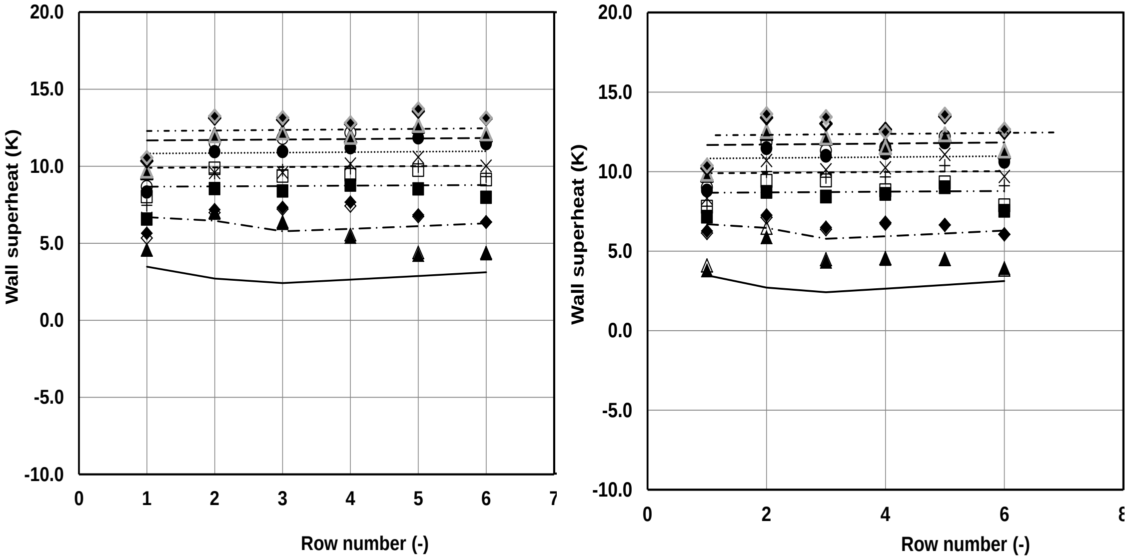

a) Column 1 *b) Column 2*

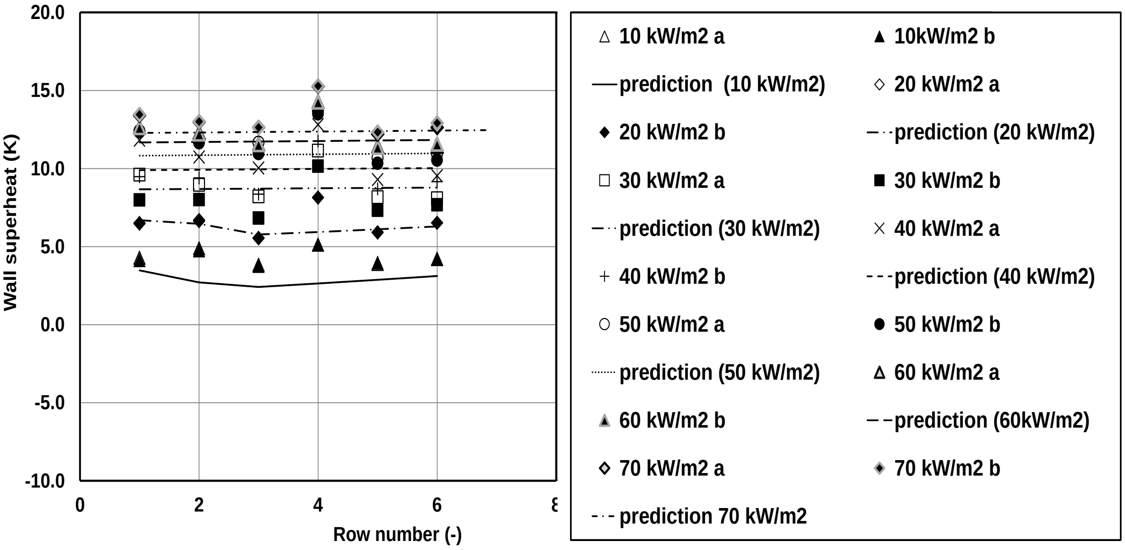

c) Column 3

Figure 5-36: variation of wall superheat with row number

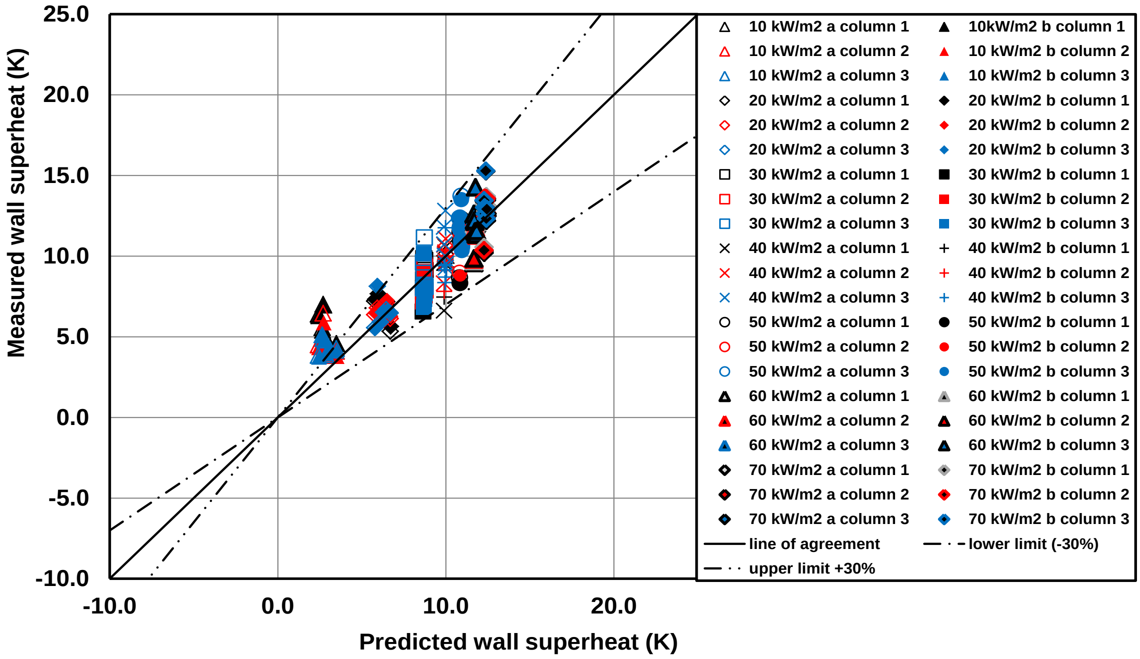

Figure 5-37: comparison of predicted with measured wall superheat

5.3.3.3 ***Stephan and Abdelsalam - ESDU combination***

Figure 5.38 shows a comparison between the measured and predicted wall superheats for the Stephan and Abdelsalam - ESDU [9] [84] combination. The Stephan and Abdelsalam - ESDU [9] [84] combination predicts the data with an average difference of 30.8%, 27.4% and 34.1% for columns 1, 2 and 3 respectively. The corresponding root mean square differences (rms) are 34.6%, 29.6% and 36.2%. Overall, the average difference and rms differences are 30.8% and 33.6% respectively. A comparison of predicted with measured wall superheat is shown in Figure 5.39.

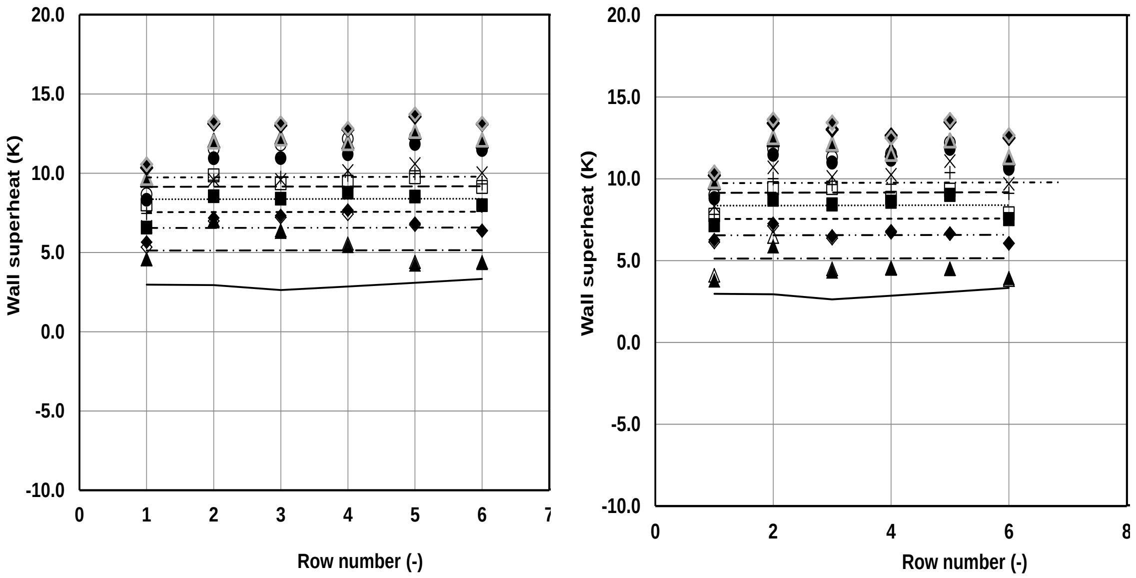

a) Column 1 *b) Column 2*

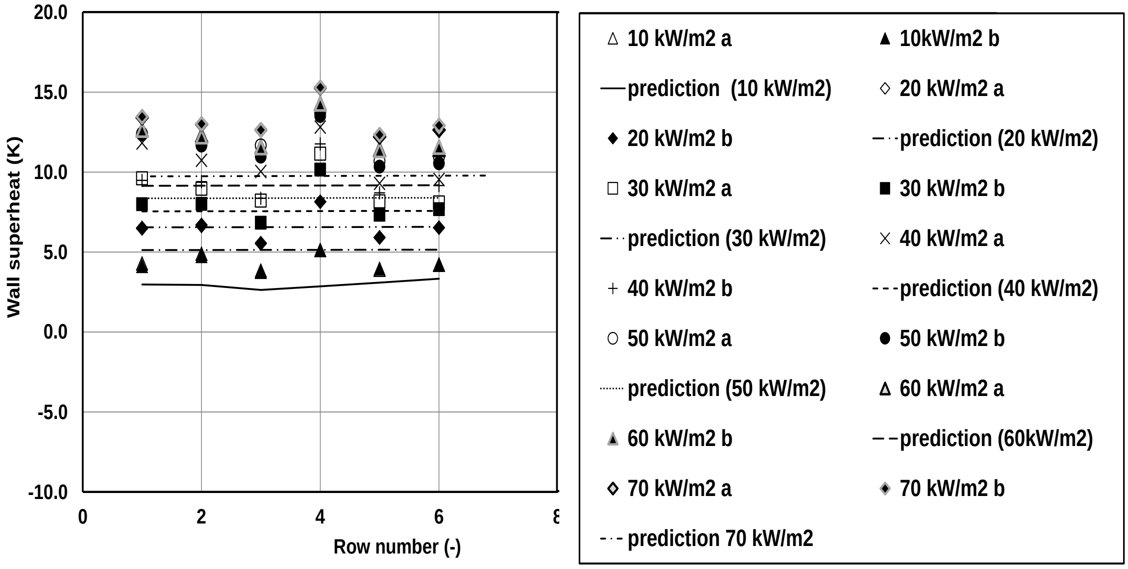

c) Column 3

Figure 5-38: variation of wall superheat with row number

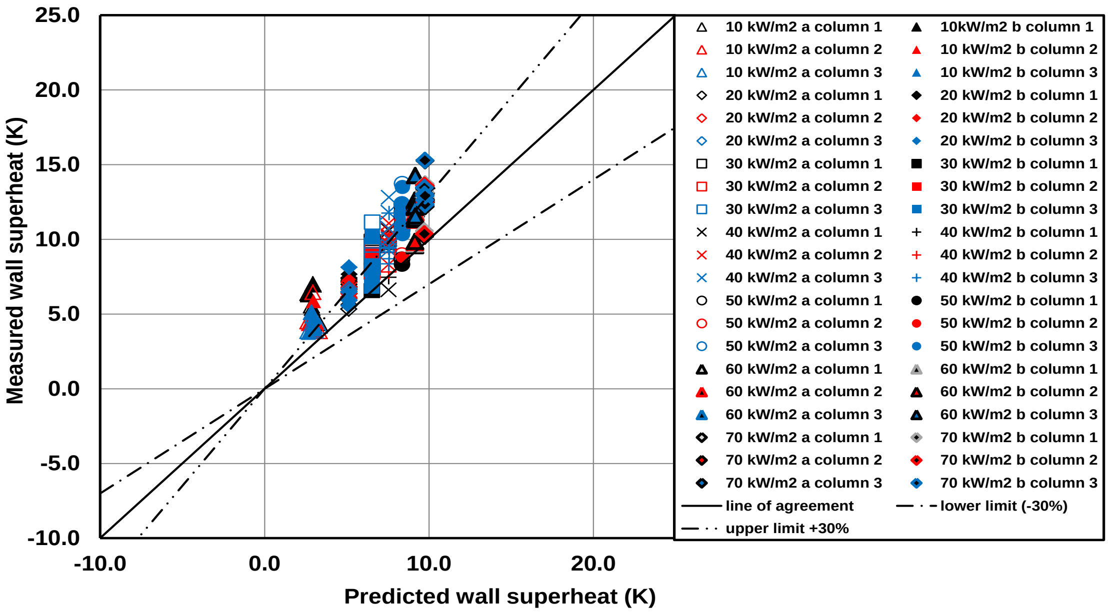

Figure 5-39: comparison of predicted with measured wall superheat

When this model analysis is applied to the low level data at a pressure of 450 mbar, root mean square differences of 35.9 % and an average error of 33.2 % are obtained for the Cooper - ESDU [11] [84] combination. The corresponding figures achieved when the Gorenflo - ESDU [12] [84] combination was used were 19.4 % and 10.7 % and when the Stephan and Abdelsalam - ESDU [9] [84] combination was used the root mean square differences was 33.6 % and an average error was 30.8%. These results shows that the Gorenflo - ESDU [12] [84] combination gives good agreement with the measurements better than the other correlations used.

5.3.4 ***High Pressure Low Level Series LLHP***

At a pressure of 850 mbar, Equation 3.2 gave onset wall superheats of 1.2-1.5 K, so that all of the HP data set is predicted to be convection and boiling.

5.3.4.1 ***Cooper – ESDU combination***

A comparison between the measured and predicted wall superheats for the Cooper - ESDU [11] [84] combination for columns 1, 2 and 3 are shown in Figure 5.40 respectively. The corresponding Cooper - ESDU [11] [84] combination predicts the data with an average difference of 32.1%, 34.5% and 47.1% for columns 1, 2 and 3 respectively. The root mean square differences (rms) are 38.2%, 39.5% and 49.3%. Overall, the average and rms differences are 34.5% and 39.5% respectively. A comparison of predicted with measured wall superheat is shown in Figure 5.41, showing poor agreement for the predicted wall superheat compared to the measured data.

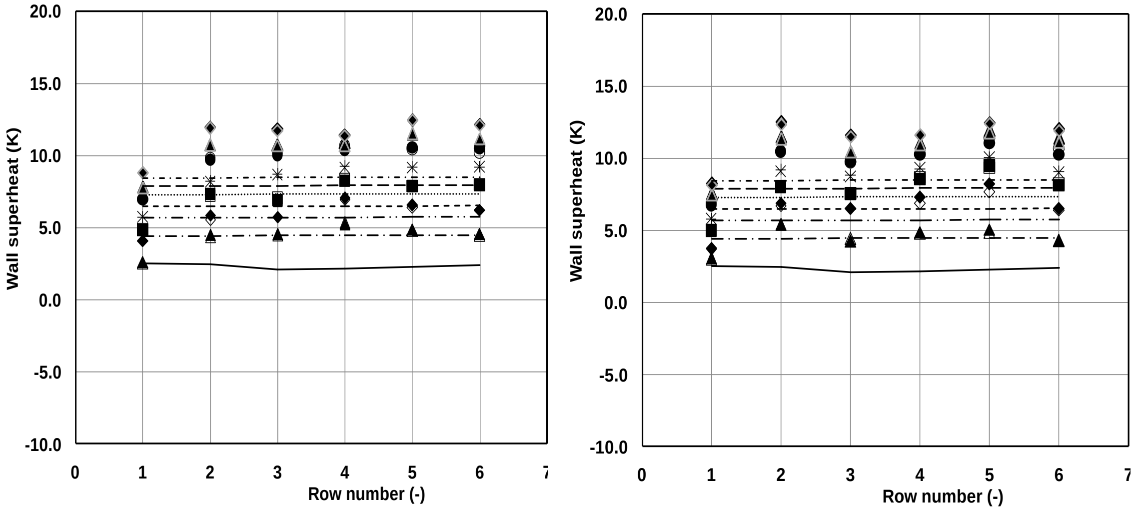

a) Column 1 *b) Column 2*

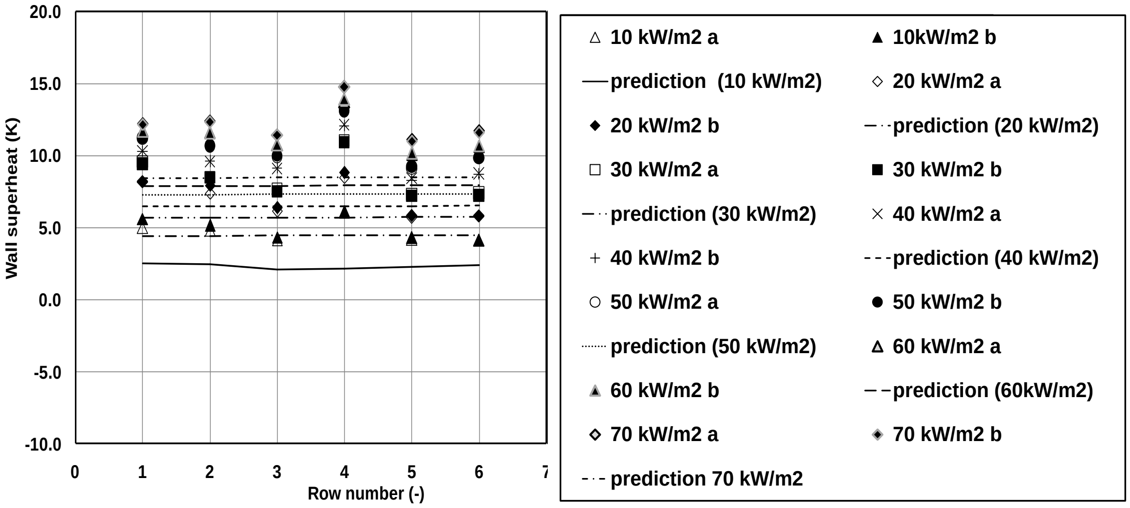

c) Column 3

Figure 5-40: variation of wall superheat with row number

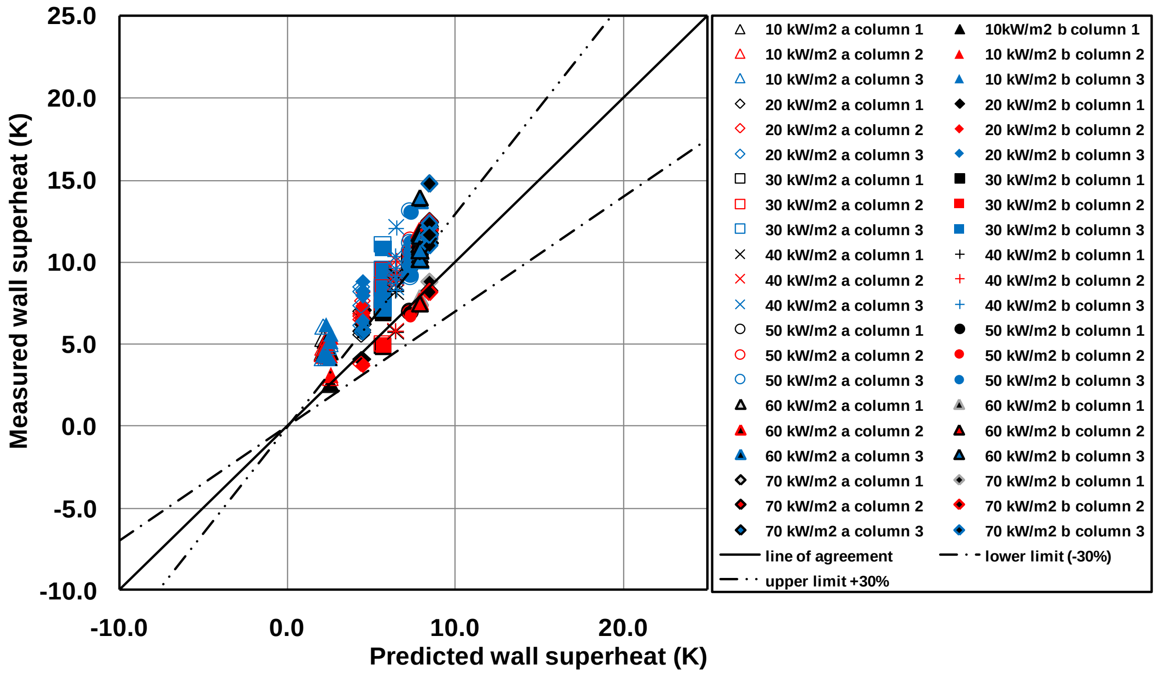

Figure 5-41: comparison of predicted with measured wall superheat

5.3.4.2 *Gorenflo – ESDU combination*

A comparison between the measured and predicted wall superheats, using the Gorenflo [12] correlation to describe boiling and the ESDU [84] correlations to describe convection, is shown in Figure 5.42. The Gorenflo - ESDU [12] [84] combination predicts the data with an average difference of 11.6%, 13.6% and 24.3% for columns 1, 2 and 3 respectively. The corresponding root mean square differences (rms) are 25.4%, 25.3% and 30.6%.

Overall, the average and rms differences are 16.5% and 27.3% respectively. A comparison of predicted with measured wall superheat is shown in Figure 543, showing good agreement for the predicted wall superheat compared to the measured data.

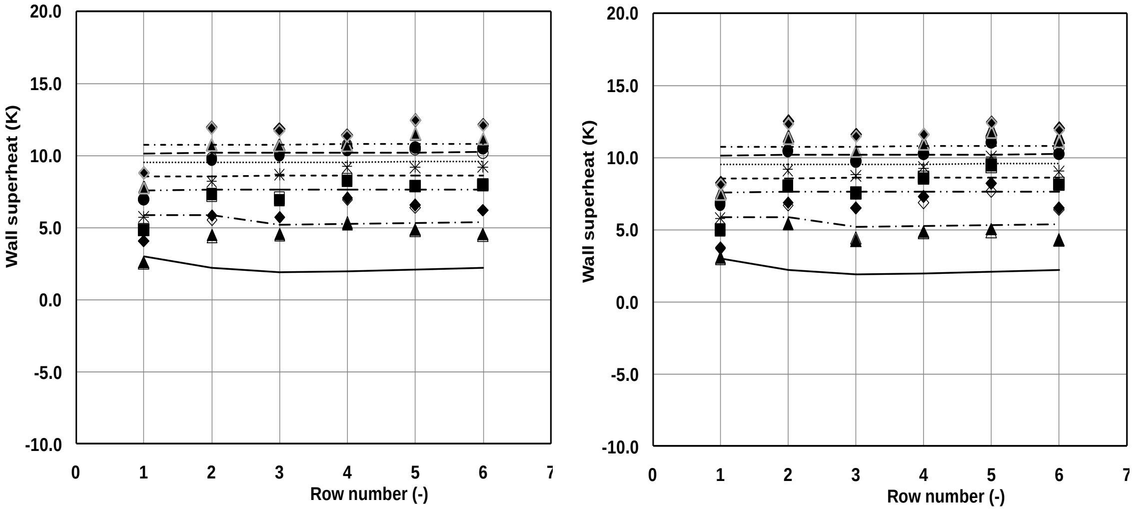

a) Column 1 *b) Column 2*

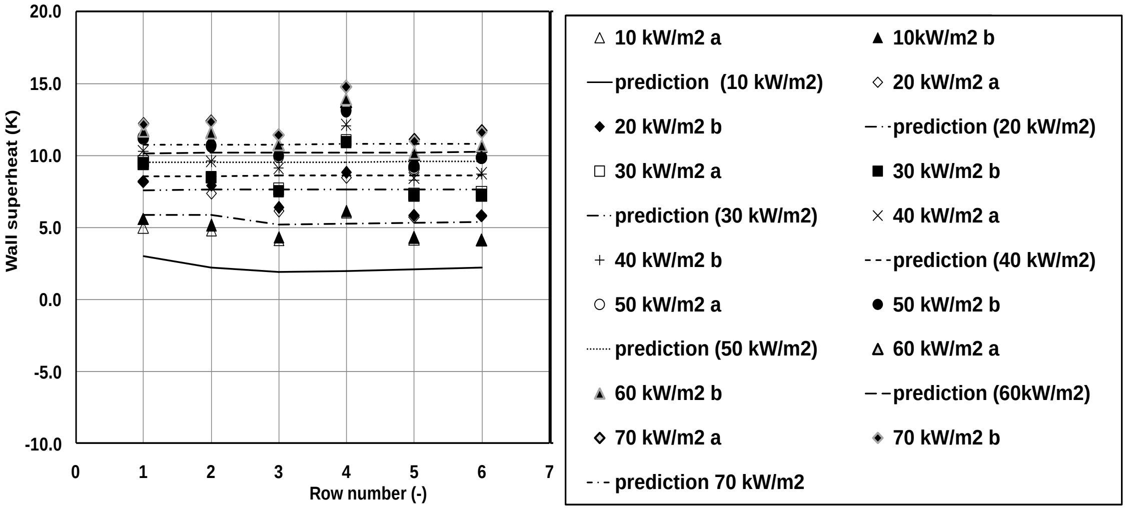

c) Column 3

Figure 5-42: variation of wall superheat with row number

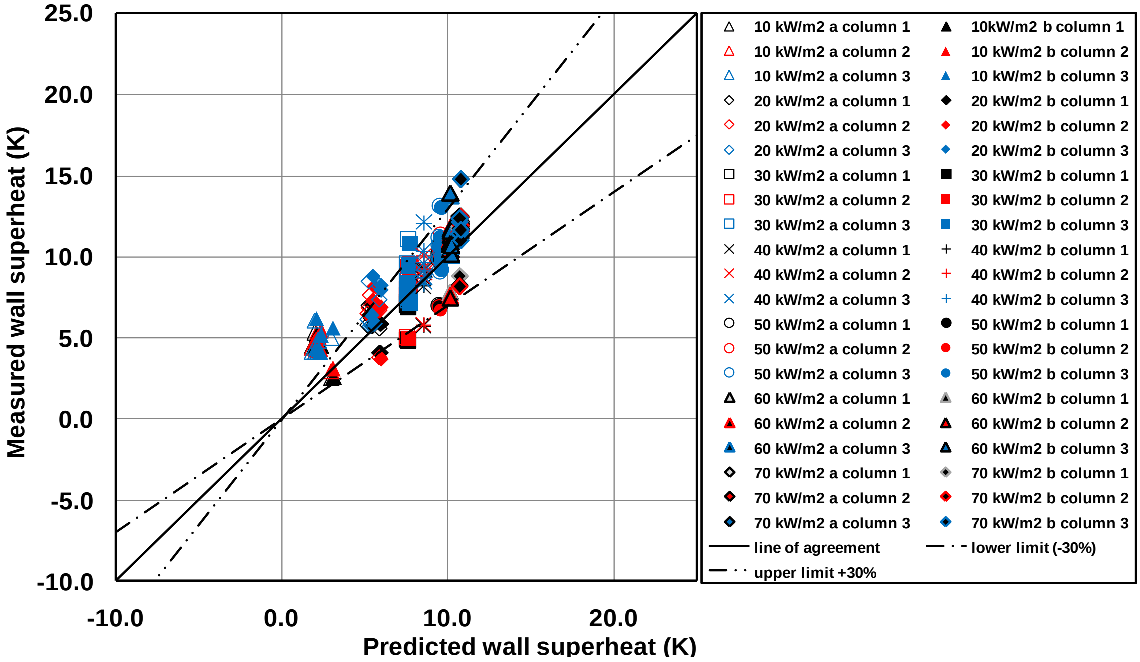

Figure 5-43: comparison of predicted with measured wall superheat

5.3.4.3 *Stephan and Abdelsalam – ESDU combination*

Figure 5.44 shows a comparison between the measured and predicted wall superheats for the Stephan and Abdelsalam - ESDU [9] [84] combination. The Stephan and Abdelsalam - ESDU [9] [84] combination predicts the data with an average difference of 27.4%%, 29.8% and 42.0% for columns 1, 2 and 3 respectively. The corresponding root mean square differences (rms) are 34.2%, 35.4% and 44.5%. Overall, the average difference and the corresponding root mean square differences (rms) are 33.1% and 38.3% respectively. A comparison of predicted with measured wall superheat is shown in Figure 5.45.

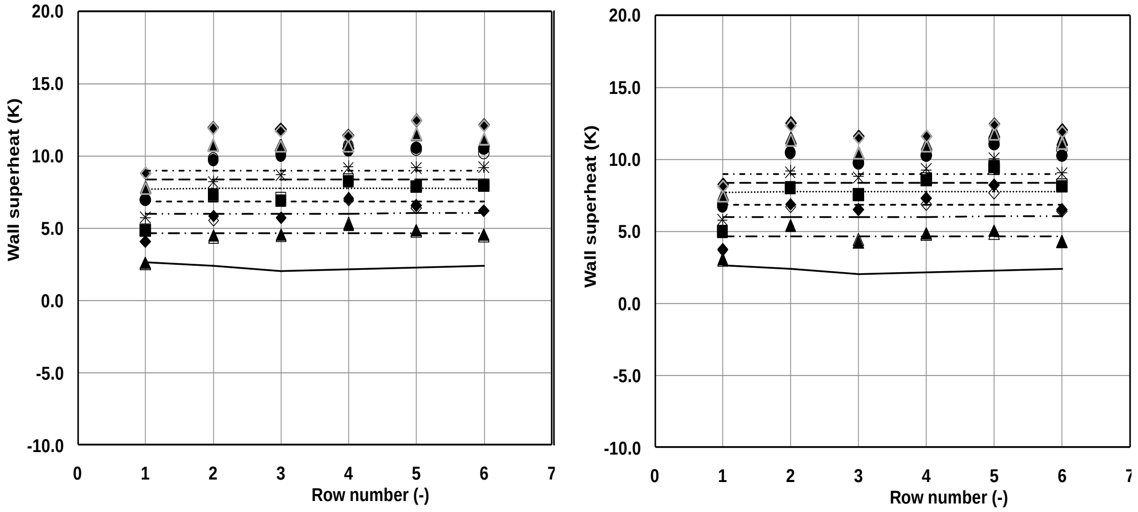

a) Column 1

b) Column 2

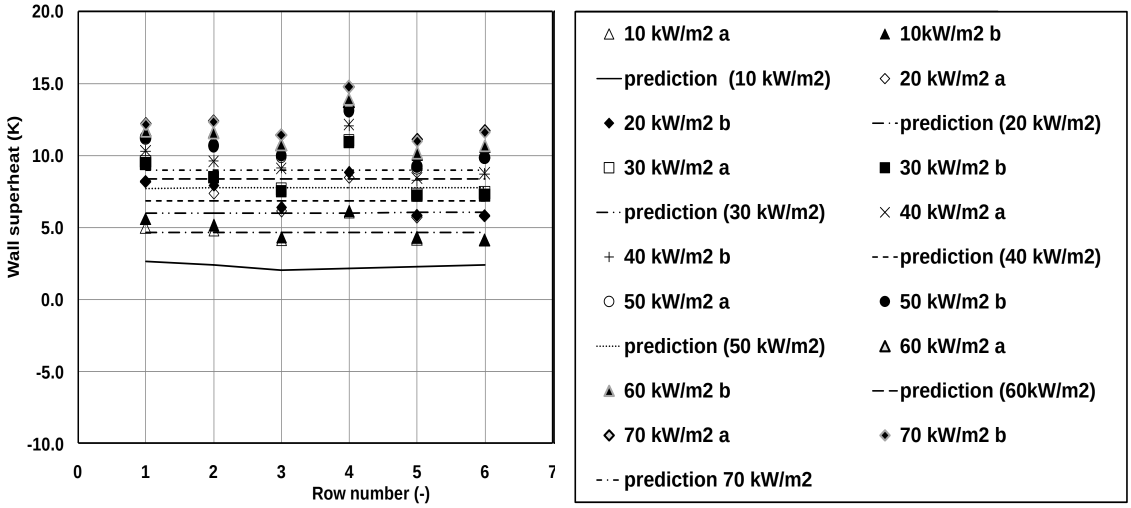

c) Column 3

Figure 5-44: variation of wall superheat with row number

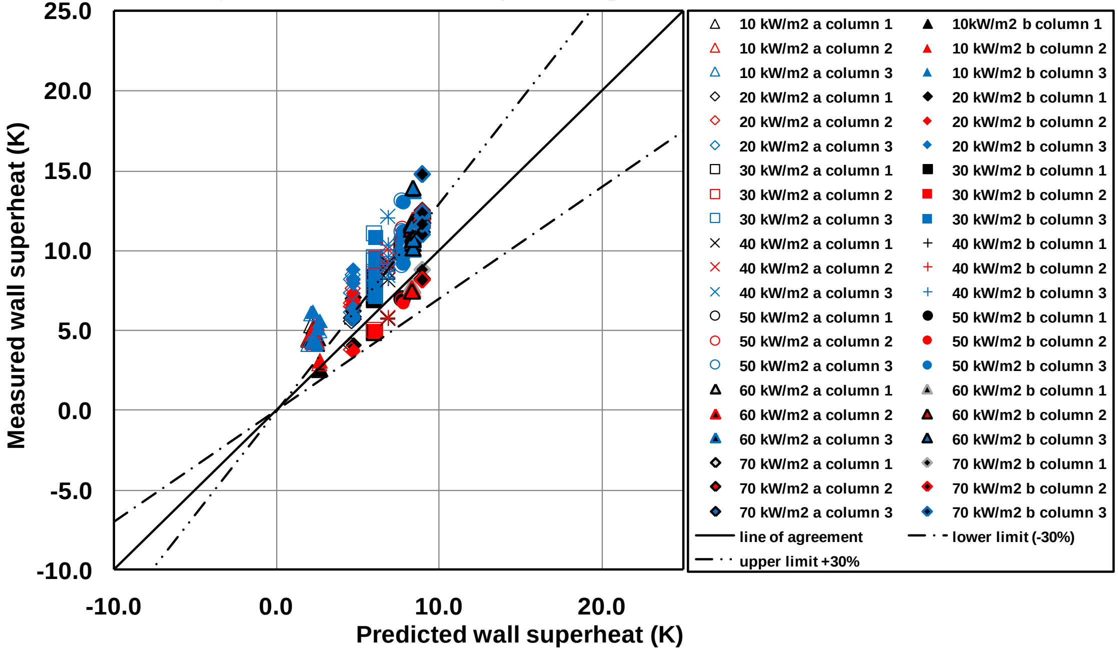

Figure 5-45: comparison of predicted with measured wall superheat

Overall, for to the low level data at a pressure of 850 mbar, the root mean square differences was 39.5% and the average error of 34.5 % when the Cooper – ESDU [11] [84] combination was used. The corresponding figures achieved when the Gorenflo - ESDU [12] [84] combination was used were 27.3 % and 16.5 % and when the Stephan and Abdelsalam - ESDU [9] [84] combination was used the root mean square differences was 33.4 % and an average error was 33.1%. These results shows that the Gorenflo - ESDU [12] [84] combination gives better agreement than the other correlations used. The mass flux range required for this model was in the range 48-80 kg/m^{2}s.

5.4 Discussion and Conclusion

The visual evidence presented in the experimental result chapter 4, Figures 4.29-4.32 show changes to the liquid pool behavior as the pressure is reduced. At a pressure of 450 and 850 mbar, the flow contains many bubbles, Figures 4.31 and 4.32, whereas few bubbles are evident at a pressure of 50 mbar, as shown in Figures 4.29 and 4.30. This is caused by the increase in sub-cooling that occurs at the lower pressure, a sub-cooling that is even larger when the pool height is increased. The increase in sub-cooling is produced by liquid re-circulating within the pool, as evidenced by the stream temperatures, Figures 4.1 and 4.15. The pool temperature is similar to the saturation temperature corresponding to the pressure at the free surface. This produces small liquid sub-coolings at a pressure of 450 and 850 mbar and large liquid sub-coolings at a pressure of 50 mbar. However, re-circulation requires a liquid velocity which means that convection and sub-cooled boiling could be present. What heat-transfer mechanism is dominating is less clear. Two analyses methods were used to help deduce what the heat-transfer mechanisms were. The statistics summarizing the comparison between the data and the models is given in Table 5.1.

The visual evidence at a pressure of 50 mbar, Figure 4.29, does not show bubbles rising up the columns. To get an indication of the flow patterns, 0.05 gram of neutrally buoyant particles 1 mm in diameter were added to the flow. These particles were observed to move chaotically, with streams of particles changing from vertically upwards through horizontally to vertically downwards at different parts of the ‘cycle’. The mean ‘cycle’ motion could not be identified, but ‘time of flight’ estimates from these particles indicated liquid velocities that were consistent with the predictions from the equilibrium model. The motion of the particles is supportive of a convective component of heat transfer.

(Comparison the results when these particles added and the test without it, showed that these particles did not have any effect).

When the models were applied to the low level data at a pressure of 50 mbar, an average differences of -16.0% and 9.3% and root mean square differences of 21.6% and 19.8% were obtained when the Cooper [11] correlation was used to describe the boiling element of the isolated tube and equilibrium models respectively. The corresponding figures achieved when the Gorenflo [12] correlation was used were -29.4% and -0.47% for the average differences and 32.0% and 18.5% for the root mean square differences. When the Stephan and Abdelsalam [9] correlation was used -13.2% and 10.6% were obtained for the average differences 20.3% and 20.8% for the root mean square differences. These results suggest that the isolated tube model is less likely than the equilibrium model. Velocity magnitudes supportive of the equilibrium model have been observed. Thus, at a pressure of 50 mbar, the equilibrium model with the Gorenflo - ESDU [12] [84] combination used to describe boiling gives the best results. This model doesn't predict vaporization to occur at any of the test conditions. At a heat flux of 10 kW/m^2, the isolated tube model, Figures 5-1, 5-3 does show good agreement with some of the data, while others agree with the equilibrium model, Figures 5-26, 5-28, 5-30. This could be further evidence that a minimum heat flux is required to fully-establish tube interaction, as described by the equilibrium model. In the low-level case, boiling is achieved at higher heat fluxes after tube interaction is established, giving flow boiling at these heat fluxes.

When the models were applied to the high level data at a pressure of 50 mbar, average differences of 1.6% and 53% and root mean square differences of 14.3% and 58% were obtained when the Cooper [11] correlation was used to describe the boiling element of the isolated tube and equilibrium models respectively. The corresponding figures achieved when the Gorenflo [12] correlation was used were -3.5% and 53% for the average differences and 12.1% and 58% for the root mean square differences. When the Stephan and Abdelsalam [9] correlation was used, 1.4% and 53% were obtained for the average differences and 14.1% and 58% for the root mean square difference. These results suggest that the equilibrium model behavior is unlikely and that isolated tube behavior is probable. The isolated tube model suggests that boiling only occurs at heat fluxes of 55 and 65 kW/m^2, for which the rms differences are 14.3 % , 12.1% and 14.1% for the Cooper [11], the Gorenflo [12] and the Stephan and Abdelsalam [9] correlations respectively. Thus, the Gorenflo [12] correlation seems to be more accurate at these low pressures.

The visual evidence at a pressure of 450 and 850 mbar, Figures 4.31 and 4.32 shows bubble rising up the columns. These bubbles exist in a sub-cooled liquid pool and are not taken into consideration in the equilibrium model. The fluid thermocouples are located at a reasonably large distance from the tube centers, typically 35 mm horizontally and 31 mm vertically, Figure 3.11. It is possible that these thermocouples are not detecting rises in fluid temperature from fluid nearer the top of each tube. However, the bubble locations suggest that this is unlikely. The presence of a moving bubble stream is supportive of a convective component of heat transfer.

When the models were applied at a pressure of 450 mbar, average differences of 3.1% and 33.2% and root mean square differences of 12.8% and 35.9% were obtained when the Coope [11] correlation was used to describe boiling heat transfer in the isolated tube and equilibrium models respectively. The corresponding figures achieved when the Gorenflo [12] correlation was used were -18% and 10.7% for the average differences and 21.5% and 19.4% for the root mean square differences, and when the Stephan and Abdelsalam [9] correlation was used 0.81% and 30.8% for the average differences and 11.6% and 35.9% for the root mean square differences.

When the models were applied at a pressure of 850 mbar, average differences of 7.9% and 34.5% and root mean square differences of 17.2% and 39.5% were obtained when the Cooper correlation was used to describe boiling heat transfer in the isolated tube and equilibrium models respectively. The corresponding figures achieved when the Gorenflo [12] correlation was used were -15% and 16.5% for the average differences and 20.3% and 27.3% for the root mean square differences and when the Stephan and Abdelsalam, 1980) [9] correlation was used were 2.7% and 33.1% for the average differences and 14.8% and 33.4 for the root mean square differences.

The results for 450 and 850 mbar suggest that the equilibrium scenario is less likely to have occurred and that isolated tube behavior is more likely. However, the low root mean square differences were obtained with the isolated tube model by a systematic change from over prediction at low heat flux to under-prediction at high heat flux, Figures 5.13, 5.15 and 5.17 for 450 mbar and Figures 5.19, 5.21 and 5.23 for 850 mbar. This is not the case for the equilibrium model, Figures 5.34, 5.36 and 5.38 for 450 mbar and 5.40, 5.42

and 5.44 for 850 mbar, which does give credible results when the Cooper [11], Gorenflo [12] or Stephan and Abdelsalam [9] correlations were used to describe boiling. The low pressure, high level measured wall superheats, Table 5.1, shows little difference between the columns. These data are consistent with the isolated tube model. In other words, when tubes at a similar vertical position are subjected to the same conditions, the wall superheats are similar. This is not the case for the low level results at 450 and 850 mbar, Table 5.1, where the columns behave differently. This suggests that a significant convective element is present. Also, the visual evidence, Figures 4.31 and 4.32, is suggestive of a convective contribution. The equilibrium model predictions suggest that two-phase flow does not occur but it is observed. The results for 450 or 850 mbar suggest that the Stephan and Abdelsalam [9] correlation based prediction seems to be more accurate at these pressures.

It seems likely that the low pressure, high level data is dominated by isolated tube behavior, where the heat-transfer mechanism is natural convection until the onset of boiling and nucleate boiling thereafter. The low pressure, low level data is dominated by tube interactions as described by the equilibrium model, where the heat-transfer mechanism is convection before the onset of boiling, with convection and nucleation afterwards. It is possible that the reduction in pressure changes the low level behavior of the heat exchanger and that the dominant mechanism at a pressure of 450 and 850 mbar is different from that at 50 mbar. But the data are inconclusive, particularly since the convective effect of the bubbles has not been accounted for the pressure drop.

The ratio of the convective to the total heat flux predicted by the equilibrium model is shown in Figures 5.46 and 5.47. The Gorenflo [12] correlation was used to evaluate the nucleate boiling component. At a pressure of 850 mbar, Figure 5.46, the heat flux is convective at a heat flux of 10 kW/m^2. The convective fraction reduces with increasing heat flux, reaching about 50% at a heat flux of 70 kW/m^2. At a pressure of 50 mbar, Figure 5.47, the heat flux is convective at a heat flux of 10 kW/m^2. The convective fraction reduces with increasing heat flux, reaching about 80% at a heat flux of 65 kW/m^2. Thus, even when boiling is present, low level flows are dominated by convection.

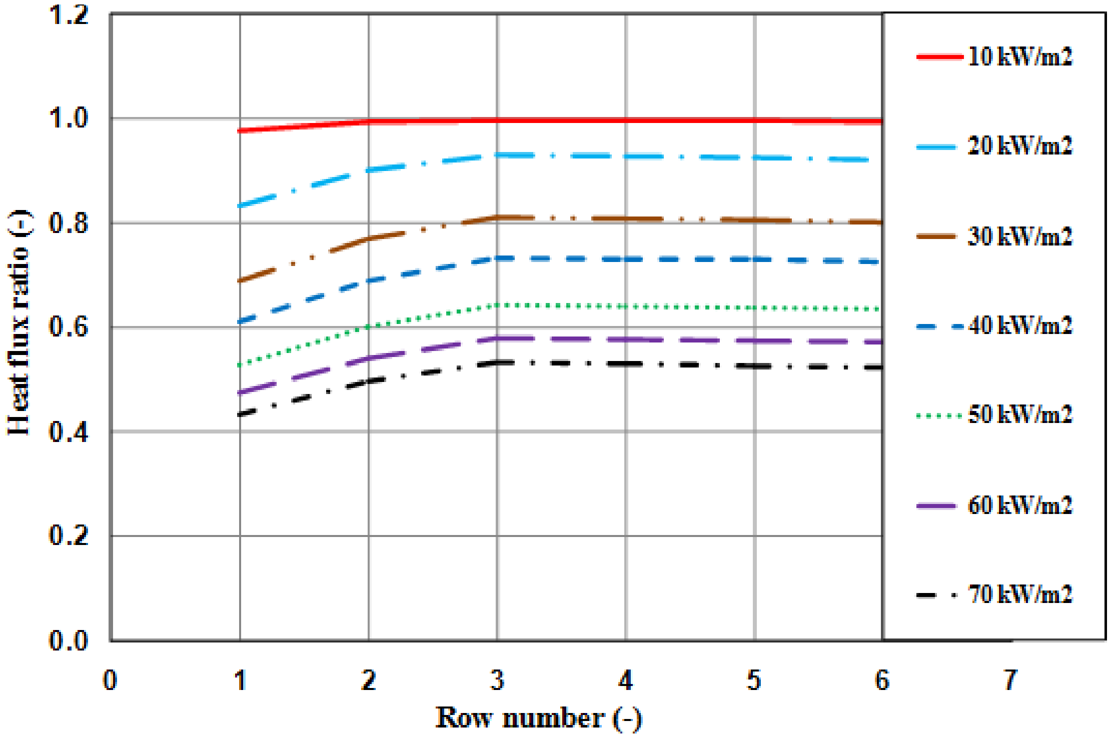

Figure 5-46: comparison of heat-flux ratio with position for pressure of 850 mbar

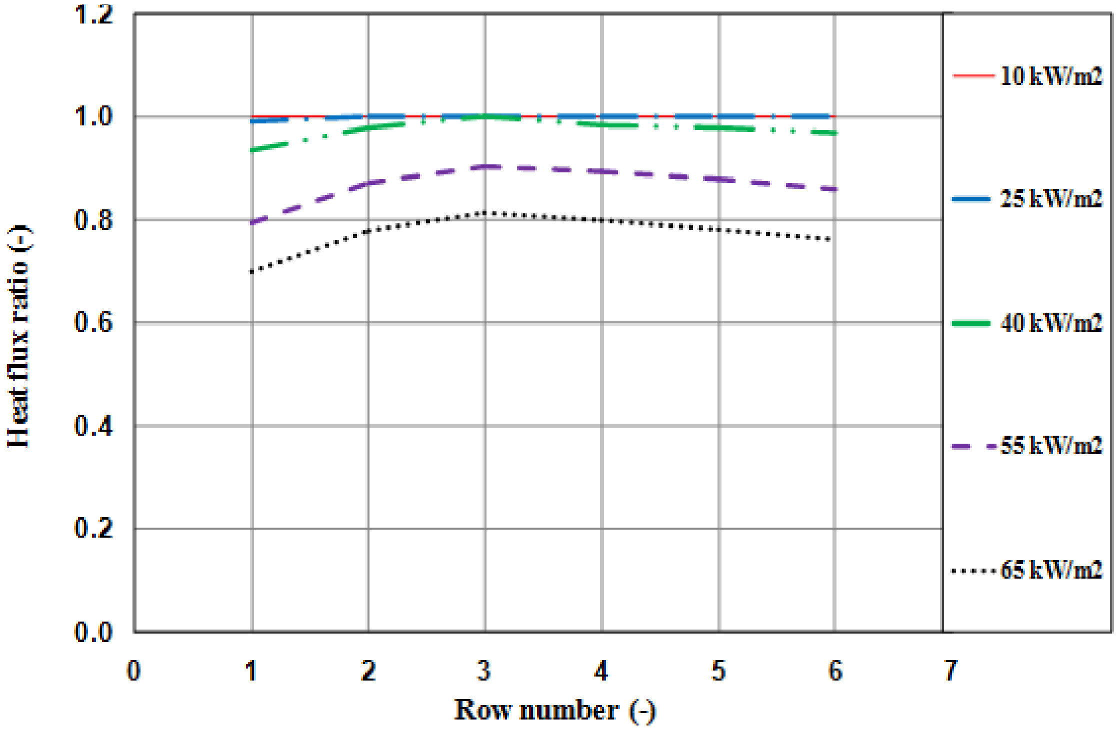

Figure 5-47: comparison of heat-flux ratio with position for pressure of 50 mbar

Table 5-1: summary of the average and RMS differences for all series

Test series	Analysis method	Boiling correlation	Column 1		Column 2		Column 3		All	
			Average error %	RMS error %	Average error %	RMS error %	Average error %	RMS error %	Average error %	RMS error %
50 mbar low level LLLP	**Isolated Tube**	**Cooper**	-23.1	27.9	-15.8	19.0	-8.9	16.6	-16.0	21.6
		Gorenflo	-35.7	37.7	-29.3	30.4	-23.2	27.0	-29.4	32.0
		Stephan	-20.6	26.4	-13.0	17.4	-5.9	15.3	-13.2	20.3
	Two Phase Equilibrium	**Cooper**	-0.69	14.7	9.4	13.3	19.8	28.1	9.3	19.8
		Gorenflo	-10.0	15.8	-0.48	10.3	9.07	25.0	-0.47	18.5
		Stephan	0.53	15.3	10.7	14.6	20.5	20.1	10.6	20.8
50 mbar high level HLLP	**Isolated Tube**	**Cooper**	0.50	14.7	1.3	13.7	3.14	14.5	1.6	14.3
		Gorenflo	-4.61	12.1	-3.9	13.0	2.0	12.1	-3.5	12.1
		Stephan	0.30	14.6	1.7	13.5	2.9	14.3	1.4	14.1
	Two Phase Equilibrium	**Cooper**	51	58	52	57	54	59	53	58
		Gorenflo	51	58	52	57	54	59	53	58
		Stephan	51	58	52	57	54	59	53	58
450 mbar low level LLMP	**Isolated Tube**	**Cooper**	3.12	12.1	0.80	11.3	6.3	14.8	3.1	12.8
		Gorenflo	-19.2	21.5	-21.0	22.9	-16.7	19.9	-18.0	21.5
		Stephan	0.55	10.9	-1.7	10.7	3.6	13.1	0.81	11.6
	Two Phase Equilibrium	**Cooper**	33.2	36.8	29.8	31.9	36.6	38.6	33.2	35.9
		Gorenflo	10.9	22,7	7.7	15.8	13.4	19.7	10.7	19.4
		Stephan	30.8	34.6	27.4	29.6	34.1	36.2	30.8	33.6
850 mbar low level LLHP	**Isolated Tube**	**Cooper**	3.1	15.1	5.1	15.0	15.5	21.0	7.9	17.2
		Gorenflo	-19.0	23.0	-17.5	21.4	-9.2	16.0	-15.0	20.3
		Stephan	-1.9	14.1	-0.04	13.3	9.9	16.8	2.7	14.8
	Two Phase Equilibrium	**Cooper**	32.1	38.2	34.5	39.5	47.1	49.3	34.5	39.5
		Gorenflo	11.65	25.5	13.7	25.4	24.3	30.7	16.5	27.3
		Stephan	27.5	34.2	29.8	35.4	42.0	44.6	33.1	33.4

Chapter 6 – **EXPERIMENTAL RESULTS WITH SOLIDS ON THE EVAPORATOR BASE**

This experimental campaign was carried out with 0.5-0.6 mm diameter glass spheres placed in a bed on the base of the evaporator. These are a stimulant for Barium Nitrate, a solid that occurs in the actual evaporator. All of the tests were carried out with water at a low liquid level at a pressure of 50 mbar absolute. Experimental data are reported for bed depths of 4, 8, 12, 16, 24 and 32 mm. During the tests, the tube heat flux was set to 65 kW/m^2 and the wall heat flux was varied from 0 to 45 kW/m^2.

6.1 Stream Temperature for a Bed Depth of 4 mm

The stream temperatures are shown in Figures 6.1 and 6.2 for a bed depth of 4 mm and for wall heat fluxes of 5 and 45 kW/m^2. Other wall heat fluxes behaved similarity. Included in figures are the saturation temperatures corresponding to the pressure at the free surface and the evaporator base. The tests show that the saturation temperature changes as the pressure increases, with the saturation temperature varying from 32 ^{o}C at the free surface to 47.5 ^{o}C at the evaporator base for a heat flux of 10 kW/m^2 and to 50.4^{o}C for a heat flux of 45 kW/m^2. The stream temperature for both cases are shown to be reasonably constant and close to the free surface saturation temperature, the stream temperature variation was 2.8 K at a heat flux of 10 kW/m^2 and was 3.6 K for a heat flux of 45 kW/m^2. These results indicate that liquid recirculation is taking place, with fluid flashing to the saturation temperature at the free surface before returning to the depths of the pool. The temperature at T_{s9}, shown as location 9 in Figure 3.11, looks different to the others because it is close to the solid bed. This is discussed as a bed temperature in the 6.2 section.

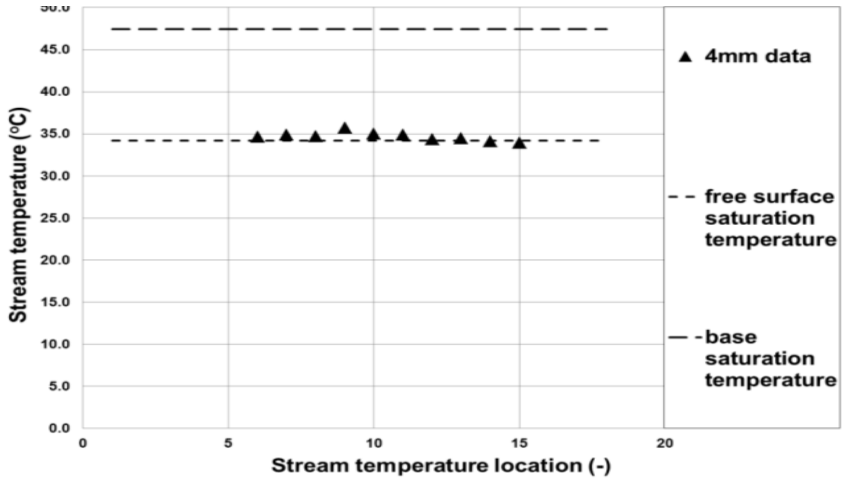

Figure 6-1: Variation of stream temperature with stream location at a heat flux of 5kW/m²

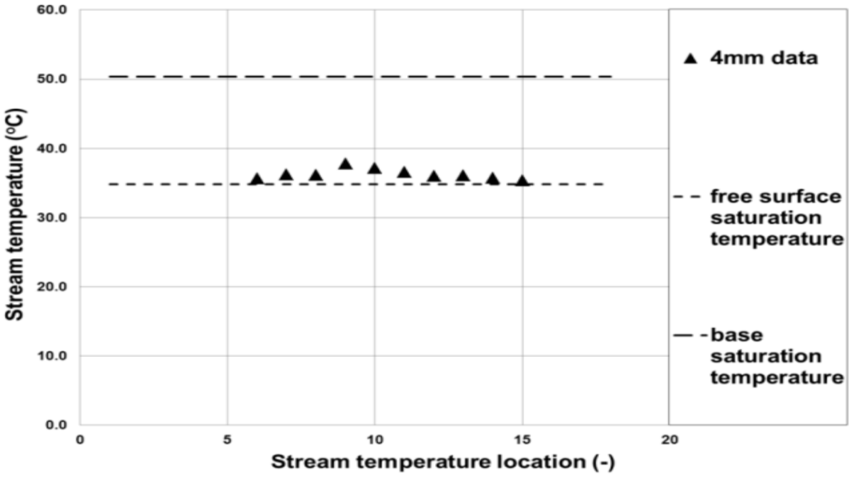

Figure 6-2: Variation of stream temperature with stream location at a heat flux of 45kW/m²

6.2 Wall and Bed Temperatures for a Bed Depth of 4 mm

The wall temperature T_{W1}, Figure 3.11 against heat flux for a 4 mm bed depth is shown in Figure 6.3. When the wall heat flux is zero, the wall temperature is sub-cooled. It becomes close to the saturation temperature at a heat flux of 5 kW/m². However boiling did not occur at a heat flux of 5 kW/m², but did above this. This suggests that the convection currents were sufficiently cooling the wall at 5 kW/m² to prevent boiling. The wall temperature is reasonably uniform for all heat fluxes once boiling is initiated. However, above a heat flux of 15 kW/m², the wall temperature does decrease with increasing heat flux. It is decrease by 5.2 K between heat fluxes 15 and 45 kW/m². The bed temperature was measured by T_{S9}, Figure. 3.11. Its value is also shown in Figure 6.3. The bed temperature is below the saturation temperature so that sub-cooled boiling is dominant at heat flux of higher than 5 kW/m² and single phase convection is dominant at a heat flux 5 kW/m². The bed temperature increases by 3.6 K over the heat fluxes range.

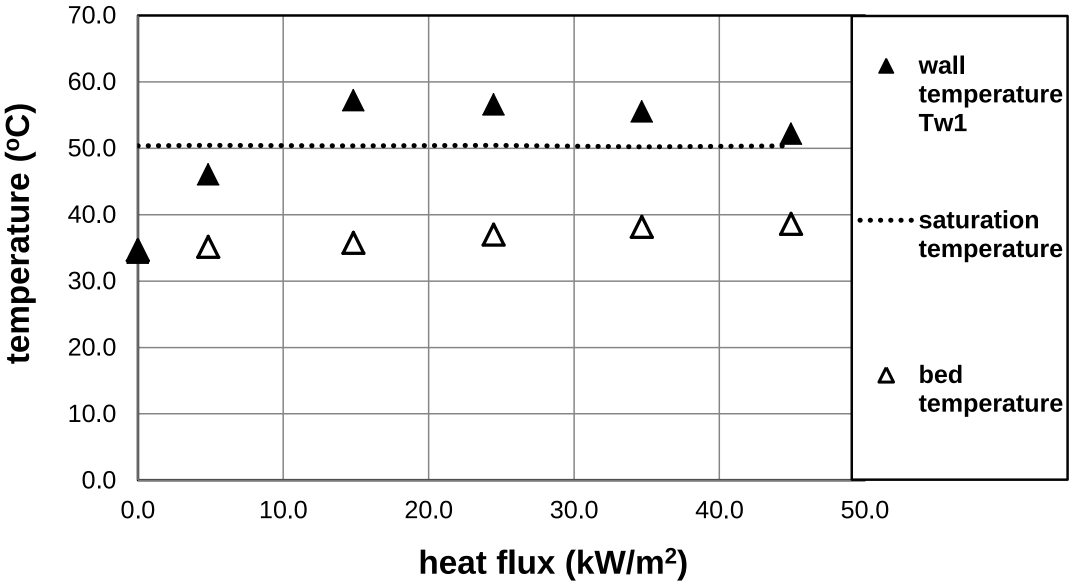

Figure 6-3: Variation of wall and bed temperature with heat flux

6.3 Stream Temperature for a Bed Depth of 8 mm

Figures 6.4 and 6.5 show the variations of stream temperature with stream location for a bed depth of 8 mm and at heat fluxes of 5 and 45 kW/m^2. The stream temperatures behave similarly to those at a bed depth of 4 mm, other than T_{s9}. The stream temperatures vary by 2.2 K for a heat flux of 5 kW/m^2 and by 1.6 K for a heat flux of 45 kW/m^2. The temperature at T_{s9} behaves differently to the other results because it is covered by the solid bed. This will be discussed as a bed temperature in section 6.4.

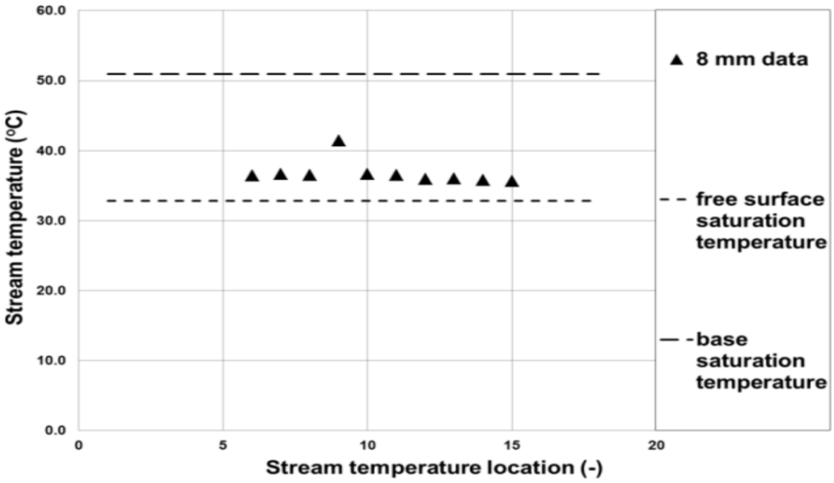

Figure 6-4: Variation of stream temperature with stream location at a heat flux of 5kW/m^2

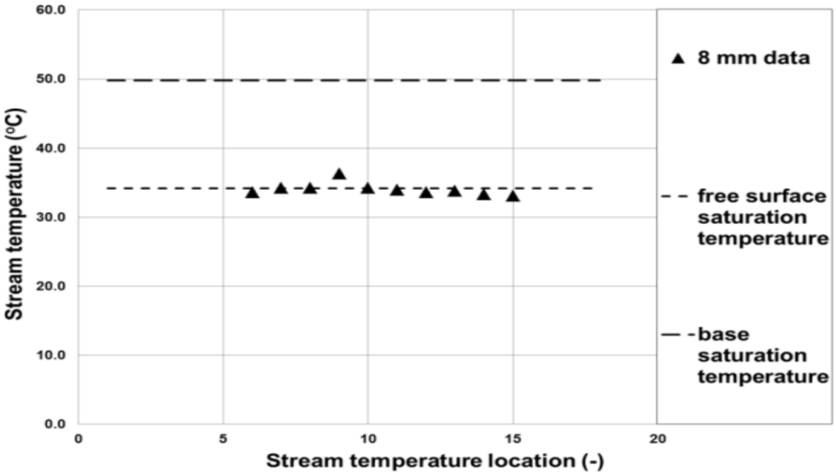

Figure 6-5: Variation of stream temperature with stream location at a heat flux of 45 kW/m²

6.4 Wall and Bed Temperatures for a Bed Depth of 8 mm

The wall temperature T_{W1} and the bed temperatures T_{S9}, Figure 3.11, against wall heat flux for an 8 mm bed depth are shown in Figure 6.6. When the wall heat flux is not applied, the wall temperature is sub-cooled. The wall temperature is reasonably uniform for all heat fluxes. However, the wall temperatures tend to decrease slightly with increasing heat flux, after a heat flux of 15 kW/m², as shown in Figure 6.6. It decreases by 1.9 K between the heat fluxes of 15 and 45 kW/m². The bed temperatures are below the saturation temperature so that sub-cooled boiling is dominant at all heat fluxes. The bed temperatures decrease by 4.6 K as the heat flux is increased from 5-45 kW/m².

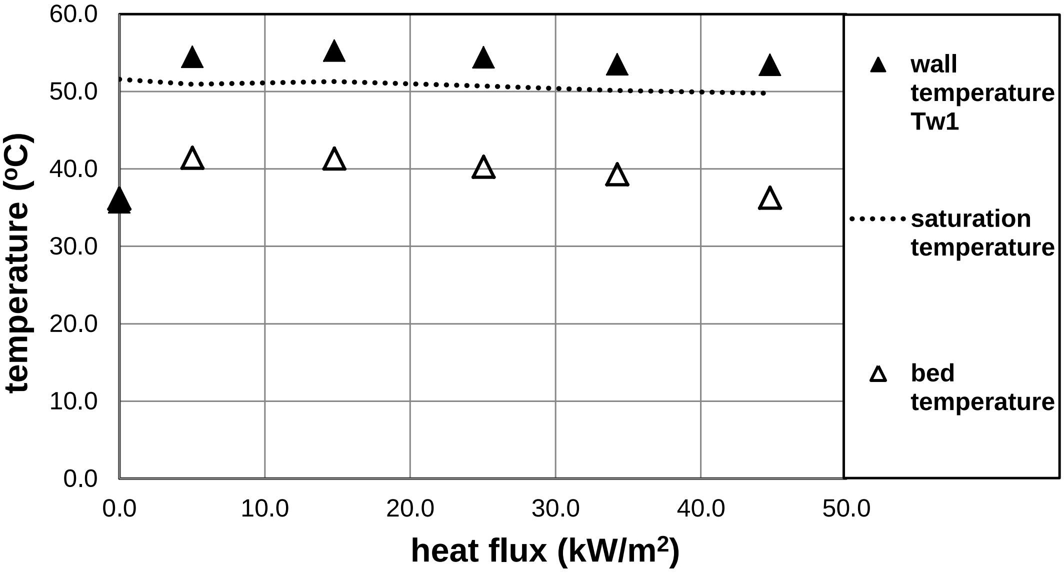

Figure 6-6: Variation of wall and bed temperature with heat flux

6.5 Stream Temperature for a Bed Depth of 12 mm

Figures 6.7 and 6.8 shows the variation of stream temperature with stream location for a bed depth of 12 mm and for heat fluxes of 5 and 45 kW/m^2. The stream temperatures behave similarly to those at a bed depth of 4 mm. The stream temperatures vary by 2.3 K for a heat flux of 5 kW/m^2 and 2.5 K for a heat flux of 45 kW/m^2. The temperature at T_{s9} is again different to the other results because it is covered by the solid bed and is discussed as a bed temperature in the section 6.6.

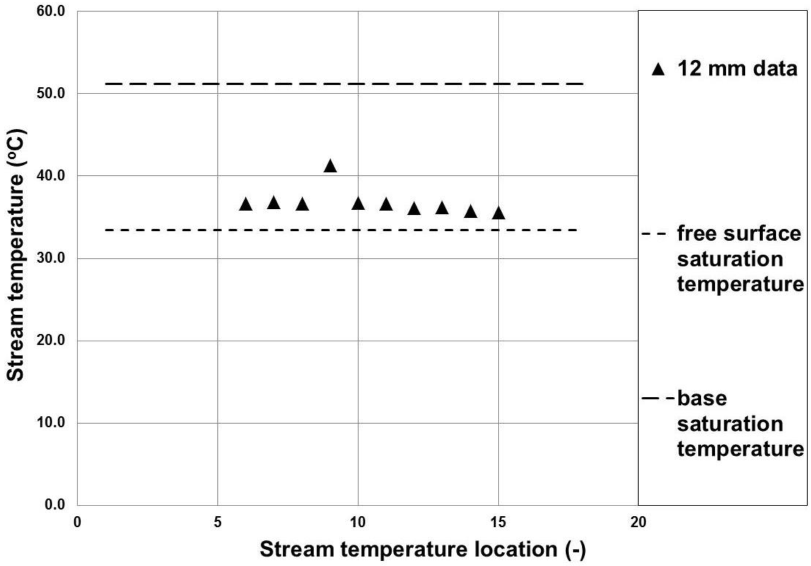

Figure 6-7: Variation of stream temperature with stream location at a heat flux of 5 kW/m^2

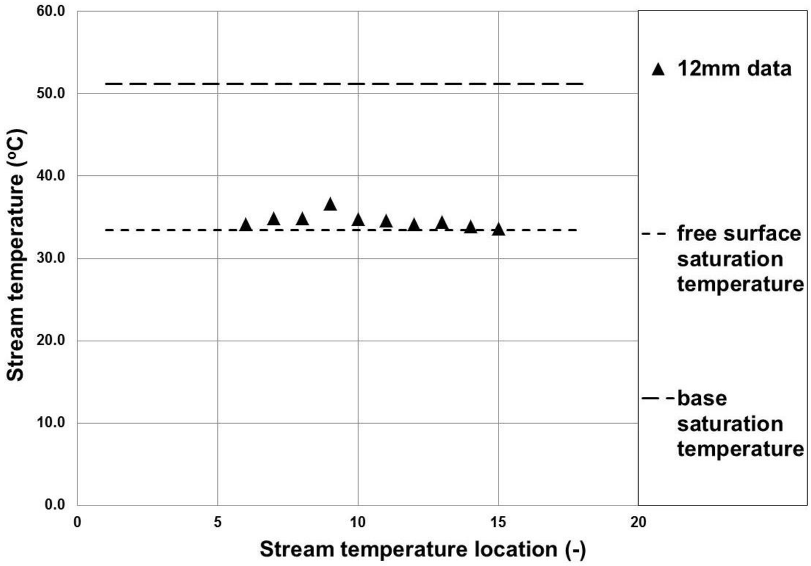

Figure 6-8: Variation of stream temperature with stream location at a heat flux of 45 kW/m^2

6.6 Wall and Bed Temperature for a Bed Depth of 12 mm

Figure 6.9 shows the variation of the wall temperature T_{W1} and the bed temperatures T_{S9} with heat flux for a 12 mm bed depth. The wall temperature is reasonably constant for all heat fluxes, but does decrease slightly after a heat flux of 15 kW/m^2. It decreases by 1.3 K between the heat fluxes of 5 and 45 kW/m^2. The bed temperature decreases as the heat flux increases. It decrease by 2.7 K over the heat flux range and is always below the saturation temperature so that sub-cooled boiling is dominant at all heat fluxes.

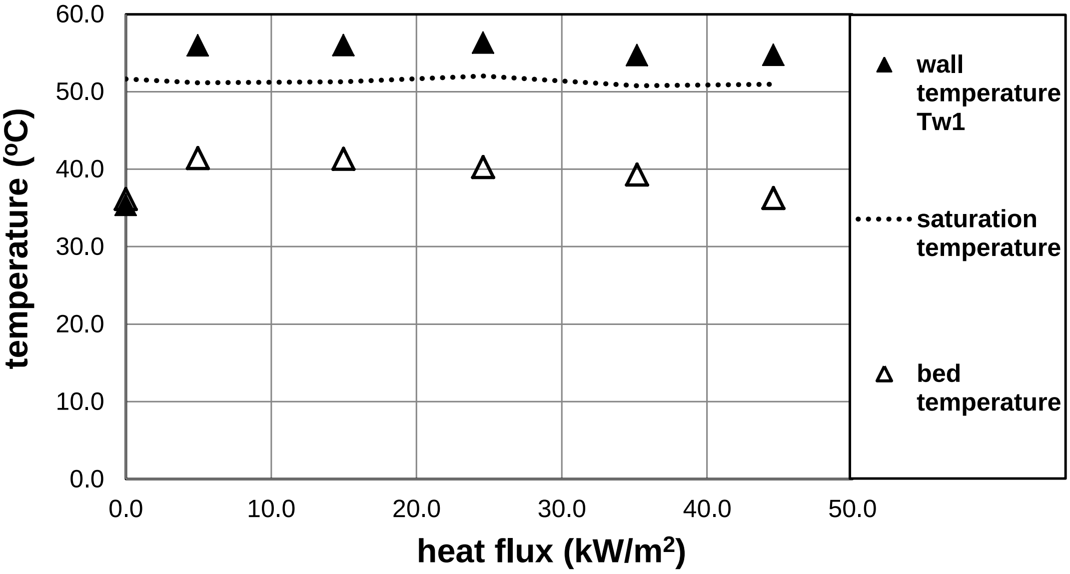

Figure 6-9: Variation of wall and bed temperature with stream location

6.7 Stream Temperature for a Bed Depth of 16 mm

Figures 6.10 and 6.11 show the variation of stream temperature with stream location for a bed depth of 16 mm at heat fluxes of 5 and 45 kW/m^2. The stream temperatures behave similar to those at a bed depth of 4 mm. The variation in the stream temperature was 2.5K at a heat flux of 5 kW/m^2 and 1.5 K for a heat flux of 45 kW/m^2. The temperature T_{s9} is again different because it is covered by the solid bed and will be discussed as a bed temperature in the section 6.7.

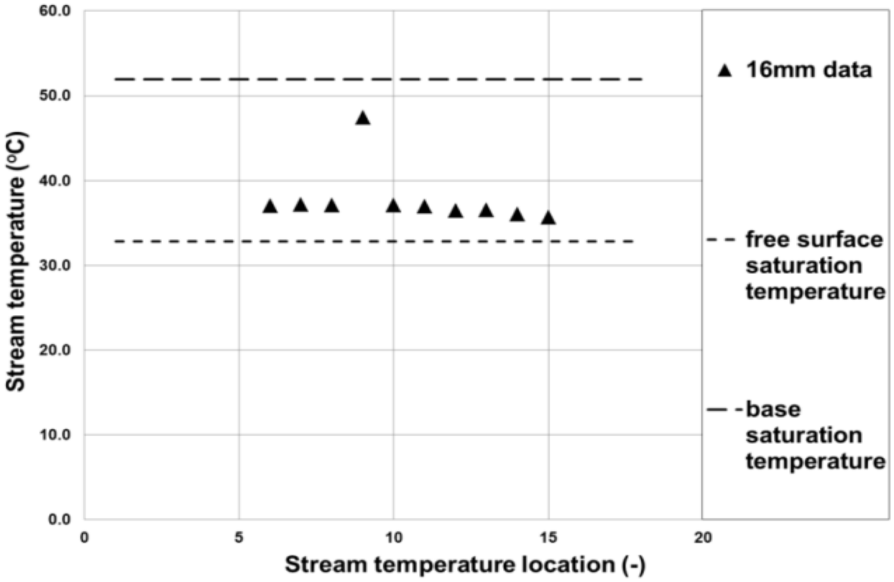

Figure 6-10: Variation of stream temperature with stream location at a heat flux of 5kW/m^2

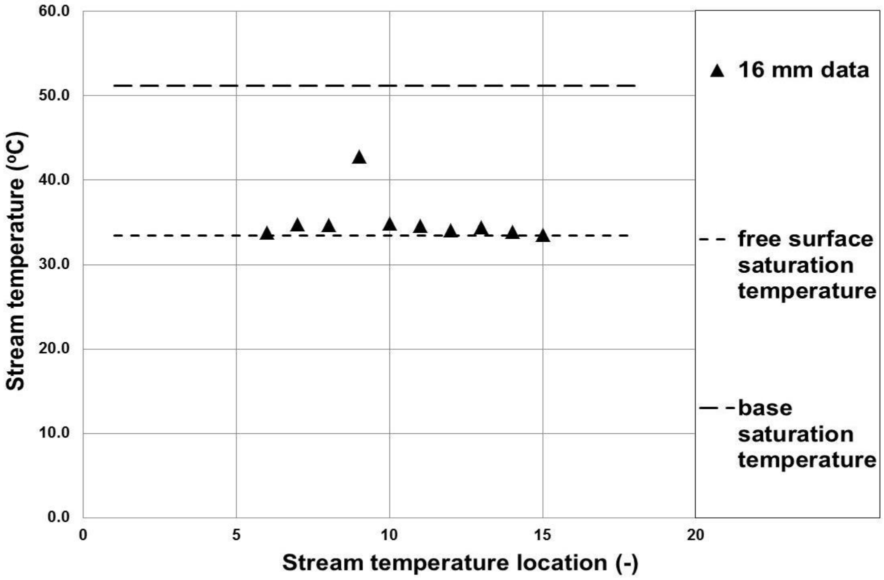

Figure 6-11: Variation of stream temperature with stream location at a heat flux of 45kW/m^2

6.8 Wall and Bed Temperatures for a Bed Depth of 16 mm

The wall temperature T_{W1} and the bed temperatures T_{S9}, Figure.3.11, are shown against heat flux for a 16 mm bed depth in Figure 6.12. After a heat flux of 5 kW/m^2, the wall temperatures decreases slightly with increasing heat flux, decreasing by 0.9 K between the heat fluxes of 5 and 45 kW/m^2, which is practically constant. The bed temperature is below the saturation temperatures so that sub-cooled boiling is dominant at all heat fluxes. It decreases as the heat flux increases by 4.7 K over the heat flux range.

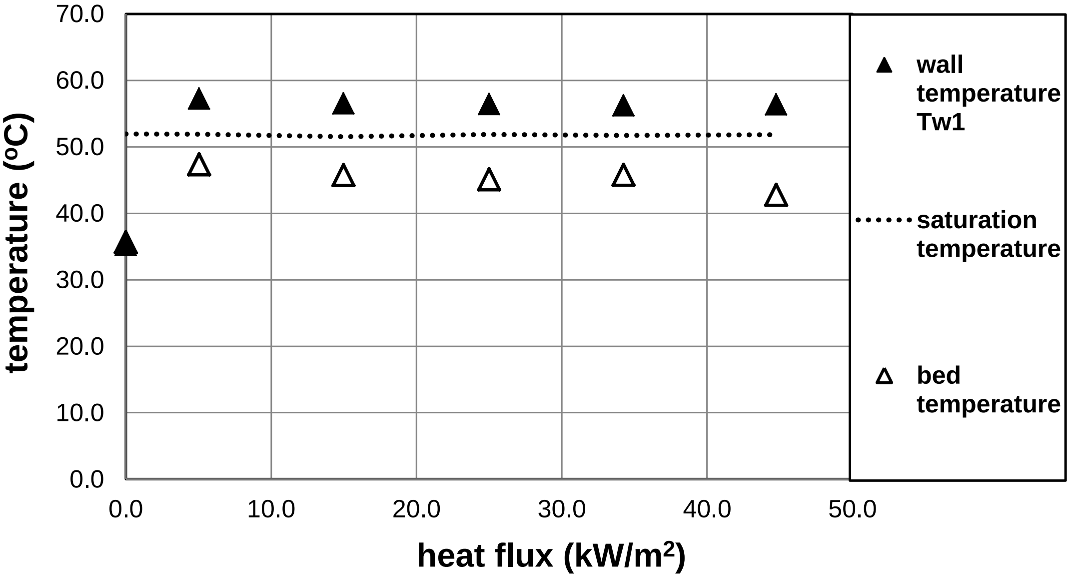

Figure 6-12: Variation of wall and bed temperature with heat flux

6.9 Stream Temperature for a Bed Depth of 24 mm

Figure 6.13 shows the variation of stream temperature with stream location for a bed depth of 24 mm at heat fluxes of 5 and 45 kW/m^2. The stream temperatures behave similar to those at a bed depth of 4 mm. The stream temperature varies within 2.8 K for a heat flux of 5 kW/m^2 and within 2.3 K for a heat flux of 45 kW/m^2. The temperature at T_{s9} and T_{s10} behave differently to the other results because they are covered by the solid bed and will be discussed as bed temperatures in section 6.9.

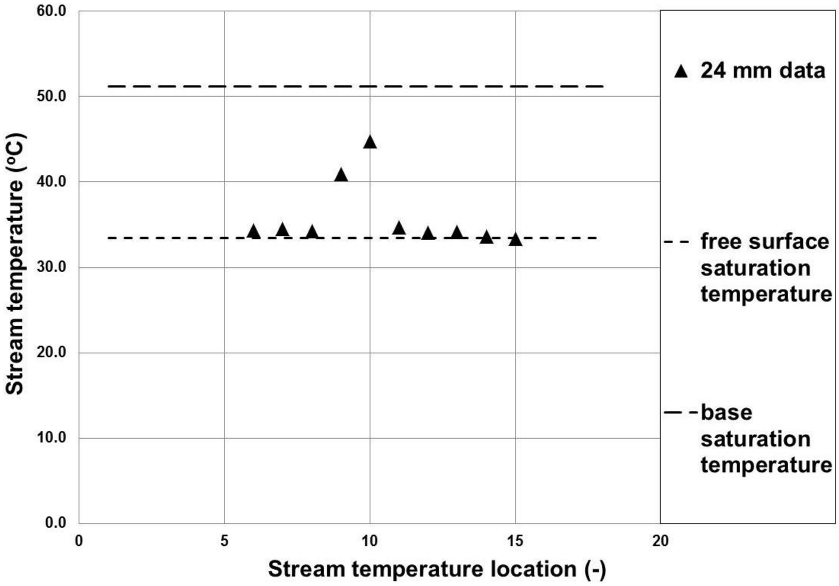

Figure 6-13: Variation of stream temperature with stream location at a heat flux of 5kW/m^2

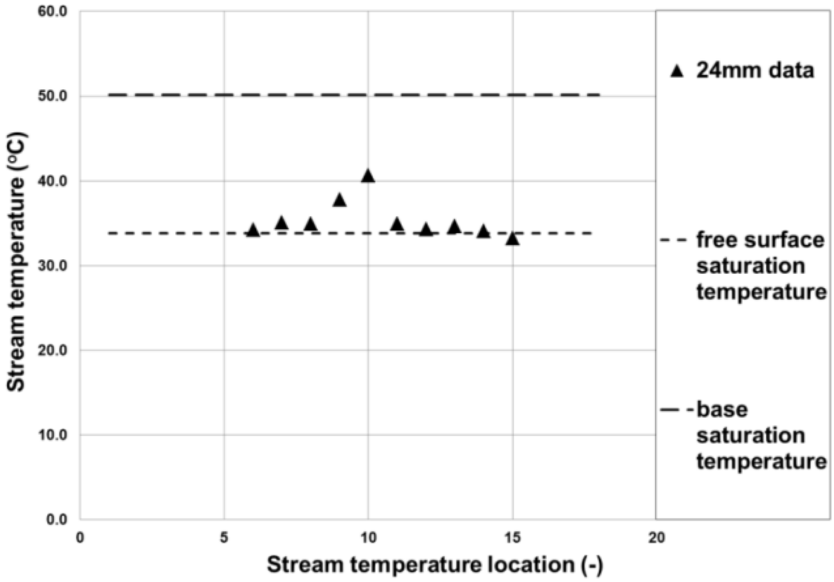

Figure 6-14: Variation of stream temperature with stream location at a heat flux of 45kW/m²

6.10 Wall and bed temperatures for a bed depth of 24 mm

Figure 6.15 shows the variation of the wall temperature and the bed temperatures with heat flux for a 24 mm bed depth. The wall temperature is reasonably uniform with heat flux, decreases slightly with increasing heat flux. It decreases by 3.5 K between the heat fluxes of 15 and 45 kW/m^2. The bed temperature also decreases as the heat flux increases and it is always below the saturation temperature, so that sub-cooled boiling is dominant at all heat fluxes. The decrease in the bed temperature was 3.2 K for the T_{s9} location and was 4.6 K for the T_{s10} location.

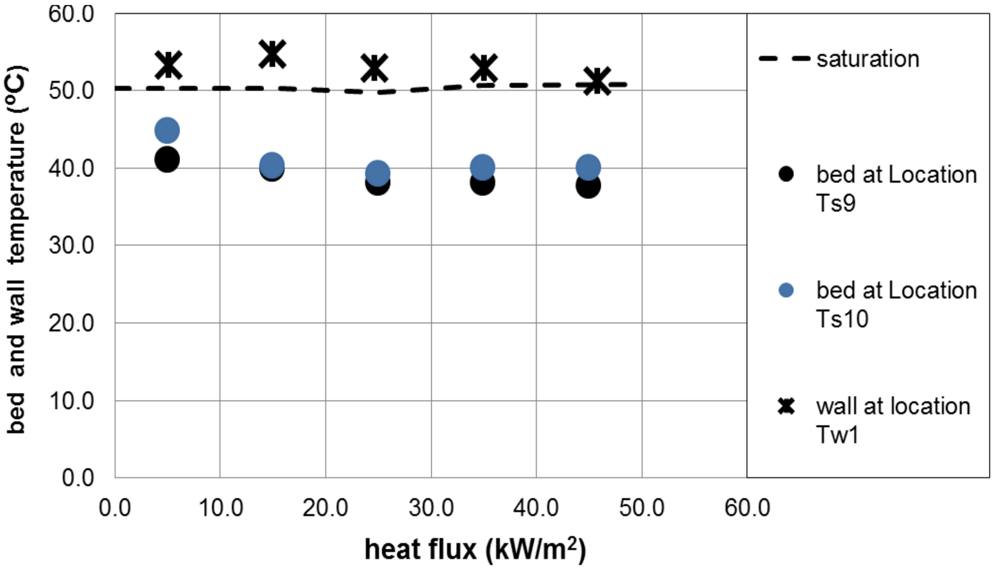

Figure 6-15: Variation of wall and bed temperature with heat flux

6.11 Stream Temperature for a Bed Depth of 32 mm

Figures 6.16 and 6.17 show the variation of stream temperature with stream location for a bed depth of 32 mm at heat fluxes of 5 and 45 kW/m^2. The stream temperatures behave similarly to those at previous bed depths. The stream temperature varies at a heat flux of 5 kW/m^2 to within 2.2 K and to within 2.1 K for a heat flux of 45 kW/m^2. The temperature at $T_{s9,}$ and T_{s10} behave differently to the other results, because they are covered by the solid bed and will be discussed as bed temperatures in the section 6.11.

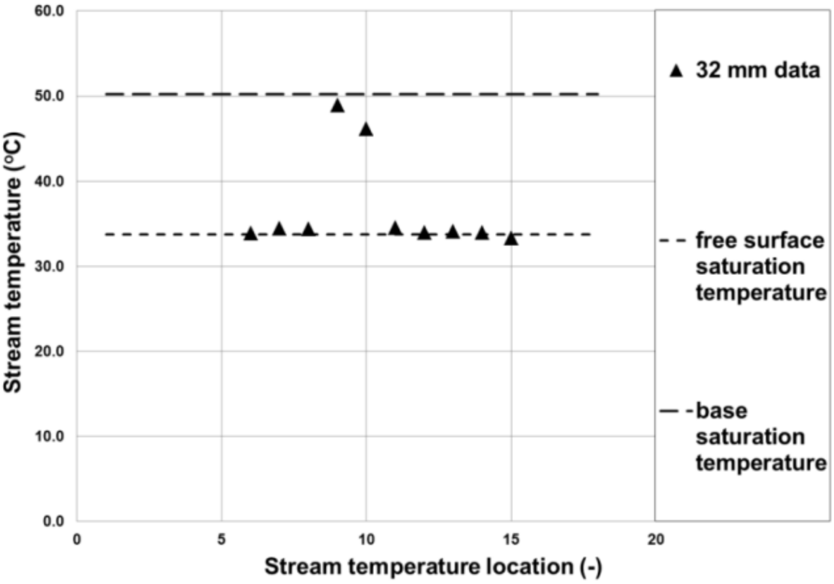

Figure 6-16: Variation of stream temperature with stream location at a heat flux of 5kW/m^2

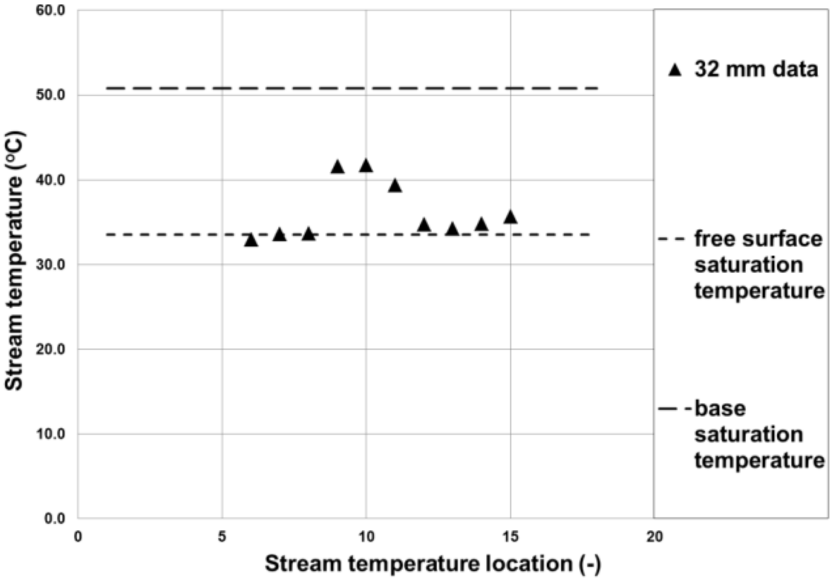

Figure 6-17: Variation of stream temperature with stream location at a heat flux of 45 kW/m^2

6.12 Wall and Bed Temperatures for a Bed Depth of 32 mm

Figure 6.18 shows the variation of the wall temperature T_{W1} and the bed temperatures T_{S9}, T_{S10}, and T_{S11} with heat flux for a 32 mm bed depth. The wall temperature is practically constant, vary within 0.7 K. The bed temperature for the location T_{S9} and T_{S10} decrease as the heat flux increases. Decreasing by 6.6 K for T_{S9} and by 5.8 K for T_{S10}. The bed temperature for location T_{S10} behaves similar to the 12 mm bed depth, which means the depth in this location about 12 mm. The bed temperature at location T_{S11} behaves similarly to the 4 mm bed depth. They are all below the saturation temperature so that sub-cooled boiling is dominant at all heat fluxes.

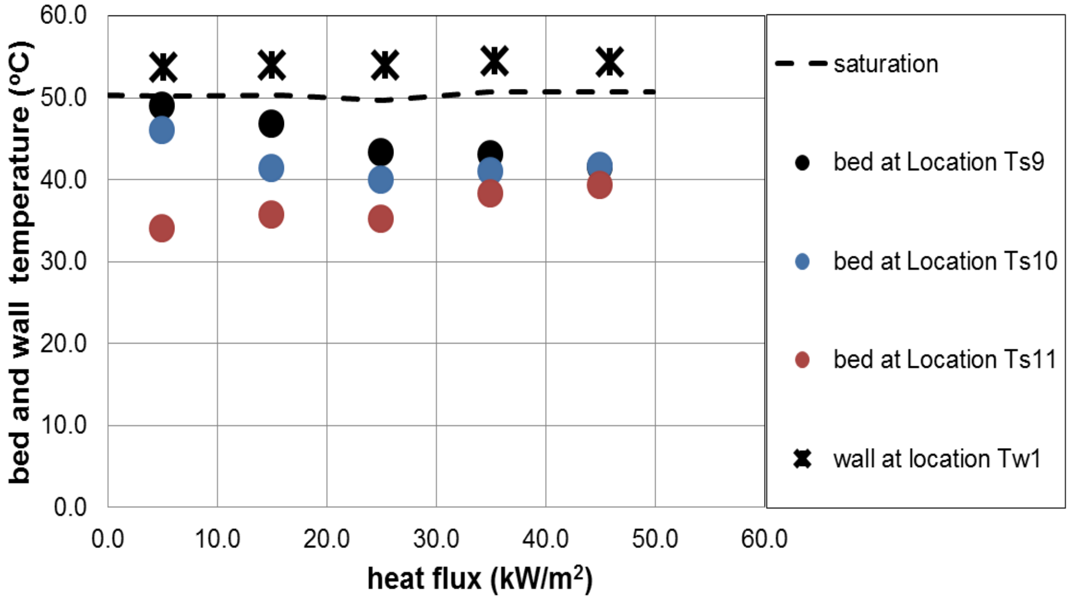

Figure 6-18: Variation of wall and bed temperature with heat flux

6.13 Discussion and Visual Observation

For the non-solids case, the base superheat, ΔT_{onb}, required to initiate nucleation can be estimated from Equation 6.1, [79].

$$q_{onb} = \frac{k_L h_{fg} \rho_g (\triangle T_{onb})^2}{8\sigma T_{sat}} = h_{sp}(\triangle T_{onb} + \triangle T_{sub}) \qquad \textit{6-1}$$

where h_{sp} is the single-phase, heat-transfer coefficient in the pool. The low vapour density produced at these low pressures, the large liquid sub-cooling in the liquid pool and the circulation within the pool, which increased the h_{sp} heat-transfer coefficient, all combined during these tests to require a large base superheat for the onset of nucleation. Hence, in the absence of solids, the base temperatures were lower than expected and nucleation was not observed. The solids bed isolated the heated base below it from the circulation in the liquid pool, reducing the heat-transfer coefficient h_{sp}within the bed. This increased the base temperature below the bed sufficiently to initiate boiling at much lower base superheats. The circulation within the pool was still happening. Thus, out with the bed, the base was being cooled as before. Thus, in general, boiling was observed below the bed but not on either side of it. When the bed depth was 4 mm and the heat flux was 5 kW/m^2, boiling was not observed on the base of the evaporator, within or out with the bed. The corresponding wall temperature, T_{W1}, as shown in Figure 6.3, was below the saturation temperature. However, when the wall heat flux was increased to 15 kW/m^2, boiling was initiated. The onset of nucleation caused the bed location to change with time, moving up the curved base to close to the vertical portion, Figure 3.1, before returning to the base minimum point and moving up the other side. Some of the locations of this oscillation are shown in Figure 6.19 for a heat flux of 45 kW/m^2. The bed and the location of the test section drain hole are highlighted to help clarify the movement. As the bed moved, the nucleation sites moved with it, restoring single-phase convection to where the bed, and boiling, had previously been. As the bed depth increased, the magnitude of this oscillation decreased, stopping completely at bed depths of 24 mm and above. However, significant bed oscillation only occurred at a bed depth of 4 mm, with minor or no oscillations present with deeper beds.

Images of the base are shown in Figure 6.20 for bed depths of 8-32 mm and for two base heat fluxes, 5 kW/m^2 and 45 kW/m^2. At a bed depth of 8 mm and at a base heat flux of 5 kW/m^2, Figure 6.20a, bubbles are shown to grow at one or two nucleation sites on the heated surface within the bed. These bubbles tended to coalesce, probably to produce the buoyancy force required to overcome the flow resistance of the particle in the bed and allow the vapour to escape into the pool, where the bubbles collapsed in the subcooled liquid. The number of nucleation sites decreases with increasing bed depth at high fluxes, as shown in Figure 6.20. For bed depths of 24 and 32 mm and at heat fluxes greater than 35 kW/m^2, the upward vapour flows were observed to ‘fluidise’ the bed. Particles were ejected from the bed by the vapour bubbles. These particles subsequently landed on the right or left side of the bed, depending on the direction of the liquid flow in the pool. The pool direction was observed to oscillate with time. Figure 6.21 shows that the bubble initiated on the base as a small bubbles and then these bubbles merged to became two bubbles, these pictures been taken from video reordering, the time between the each picture is 1/8 sec.

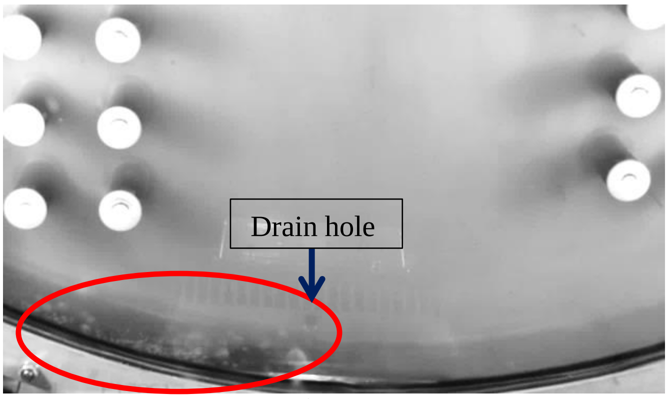

a) At 0 sec

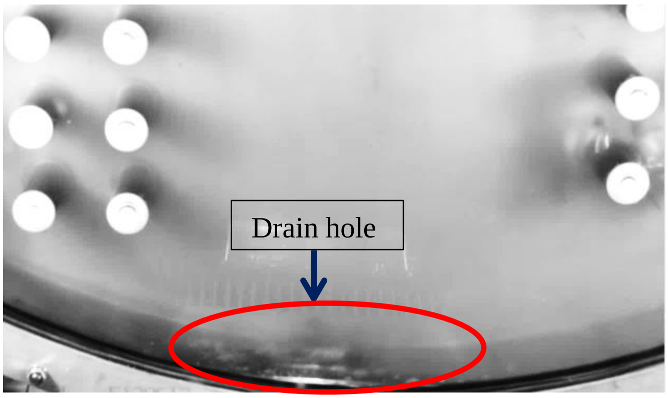

b) After 16 sec

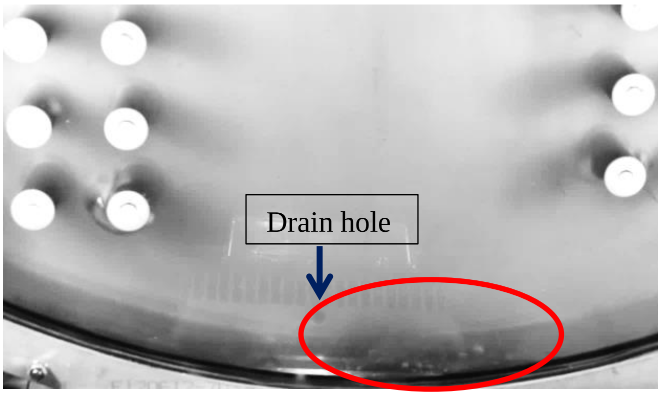

c) After 28sec

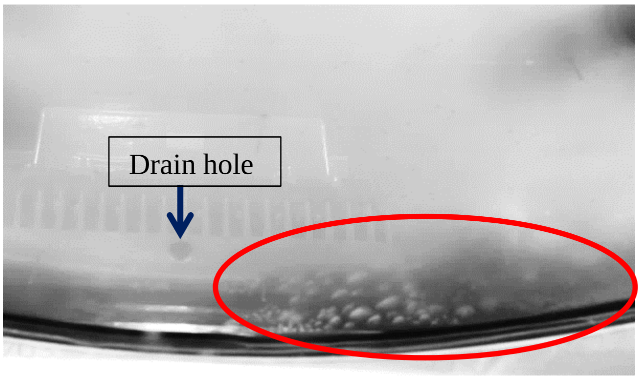

d) After 53 sec

Figure 6-19: Bed movement for 4 mm at a heat flux of 45kW/m^2

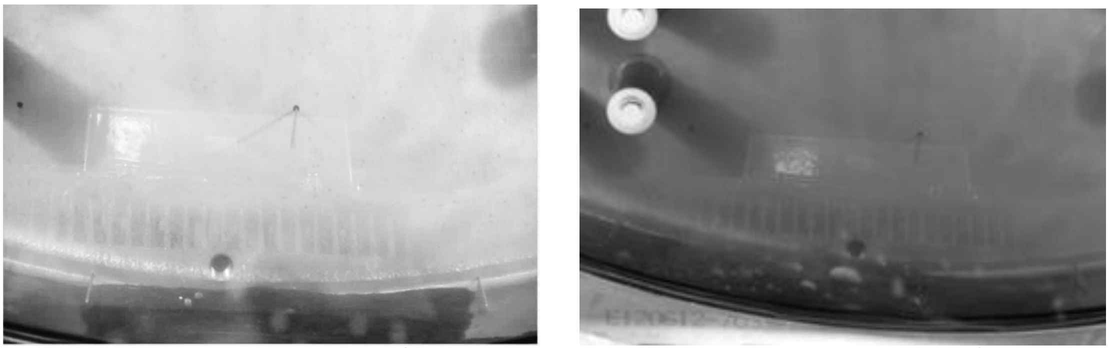

a) 8 mm at 5 kW/m^2 *b) 8 mm at 45 kW/m^2*

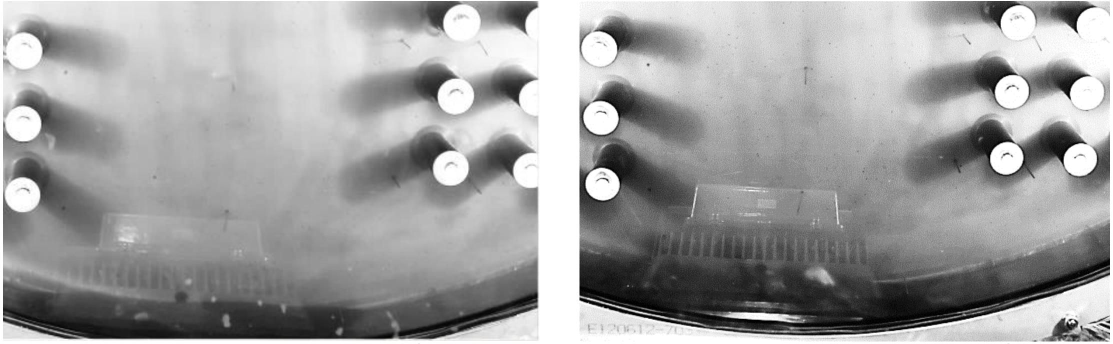

c) 16 mm at 5 kW/m^2 *d) 16 mm at 45 kW/m^2*

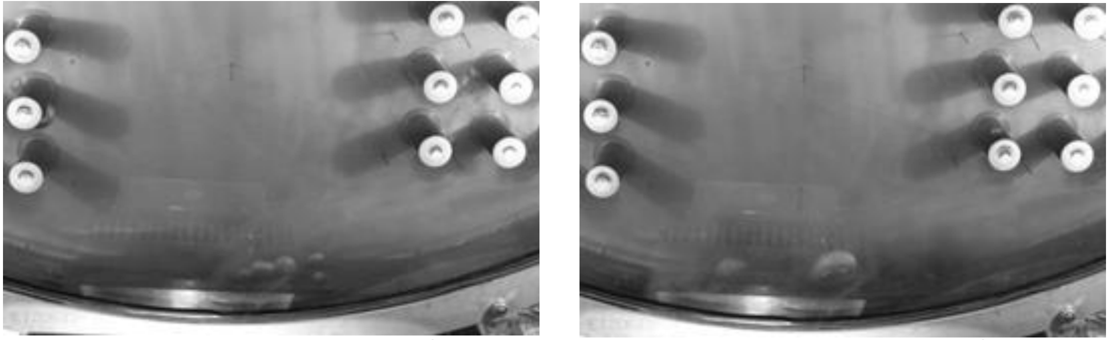

e) 24 mm at 5 kW/m^2 *f) 24 mm at 45 kW/m^2*

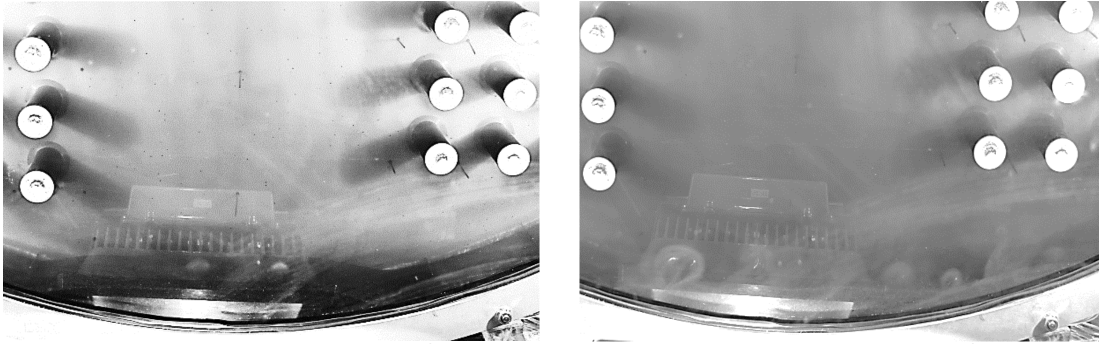

h) 32 mm at 5 kW/m^2 *j) 32 mm at 45 kW/m^2*

Figure 6-20: pictures at different heat flux and bed depth

a)

b)

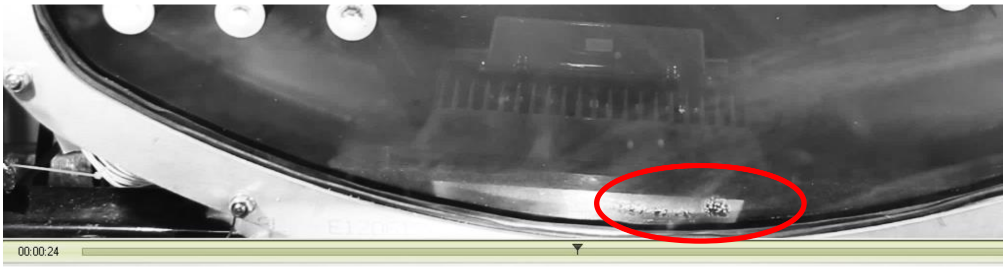

C)

d)

e)

F

h)

Figure 6-21: bubbles growth and merging (bed depth 32mm, q 5 kW/m^2)

Chapter 7 – **THE EFFECT OF SOLIDS ON WALL TEMPERATURES**

7.1 Introduction

This chapter studies the effect of particles placed centrally in a bed on the base of the evaporator, wall and bed temperatures were compared, bubble sizes and changes in the bed depth were investigated.

7.2 Wall Temperature Comparison

Wall temperature T_{W1} was located at the lowest point in the evaporator and T_{W5} was located at the interface between the curved and vertical portions of the base, Figure 3.11. In general, T_{W1} was covered by solids and T_{W5} was not. The variation of base temperature against heat flux for each bed depth is shown in Figure 7.1. The local saturation temperatures are included. Figure 7.1 shows that the base temperature in the central portion of the evaporator was affected by solids and Figure 7.2 shows that the effect was local.

In the central portion of the base, Figure 7.1, in the absence of solids, 0 mm case, the base is subcooled at low heat flux and moves closer to the saturation temperature as the heat flux increases. Boiling was not observed in the absence of solids on the base of the evaporator. This is because liquid circulation within the pool produces a cooling effect that is sufficient to prevent the onset of nucleate boiling. At a bed depth of 4 mm, Figure 7.1, boiling did not occur at a heat flux of 5 kW/m^2, but did at all heat fluxes above this. This suggests that the convection currents were sufficient to cool the base at a heat flux of 5 kW/m^2, but not at heat fluxes above this. Boiling occurred at all heat fluxes for bed depths of 8 mm and above, Figure 7.1. At these bed depths, the bed acts as a blanket, separating the base from the cooling convection currents in the liquid pool and causing the base temperature to rise. The base temperatures under the bed are reasonably uniform for all solid levels once boiling is initiated.

Note: as shown in Figures 7.1, 7.2 and 7.3, the saturation temperature is not the same due to the changes happened in the atomsperice pressure durring the day causes changing in the operating pressure from 50 to 62.5 mbar.

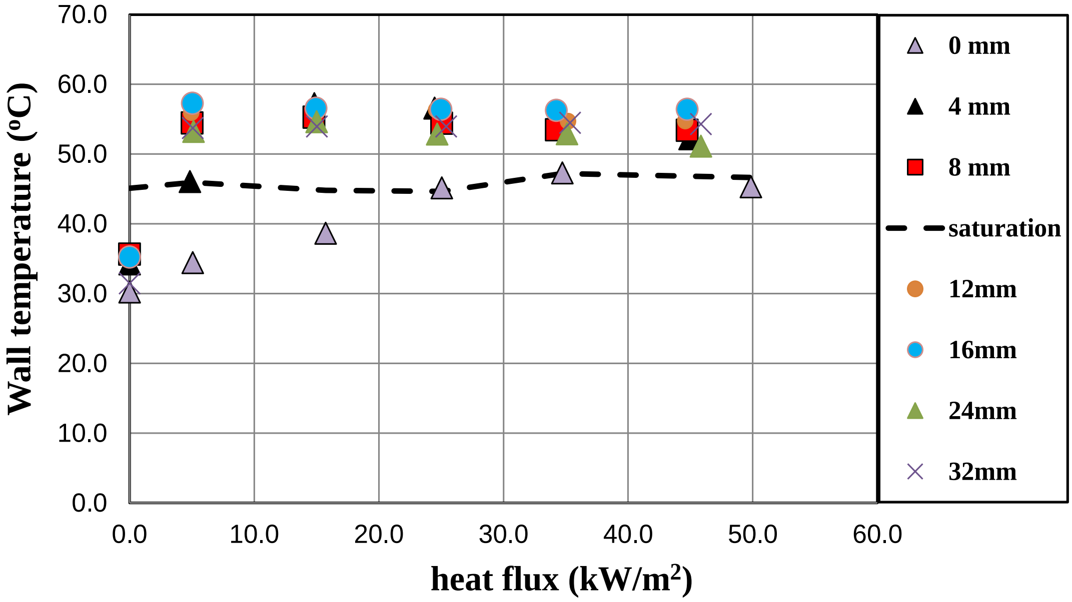

Figure 7-1: Variation of heat flux with wall temperature at location Tw₁

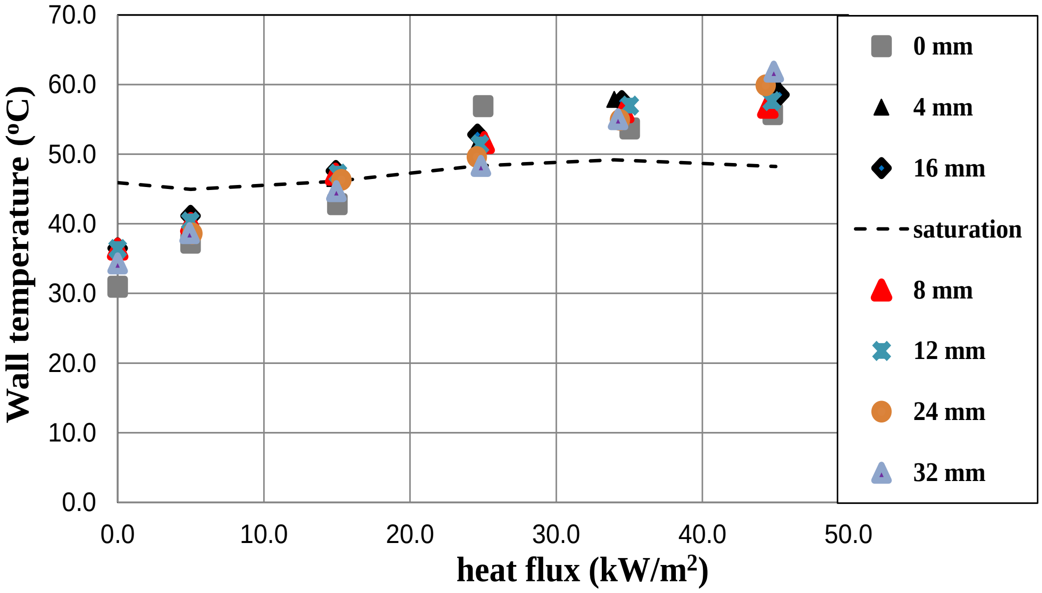

Figure 7-2: Variation of heat flux with wall temperature at location Tw₅

7.3 Bed Temperature Comparison

The variation of bed temperature, as measured by T_{S9} in Figure 3.11, with bed depth is shown in Figure 7.3. The local saturation temperature is also shown. All of the bed temperatures are below the saturation temperature so that, when boiling occurs, it is subcooled boiling. The bed temperature increases as the bed depth increases until a depth of 16 mm is reached, it decreases at 24 mm before increasing again at 32 mm. The variations of bed temperature with heat flux for each bed depth is shown in Figure 7.4. In the absence of a bed, the bed temperature increases with increasing heat flux, 0 mm case. For a bed depth of 4 mm, the bed temperature increases slightly as the heat flux increase. For all other bed depths, the bed temperature decreases as the base heat flux increases. The bed temperature moves close to the stream temperatures at high heat fluxes.

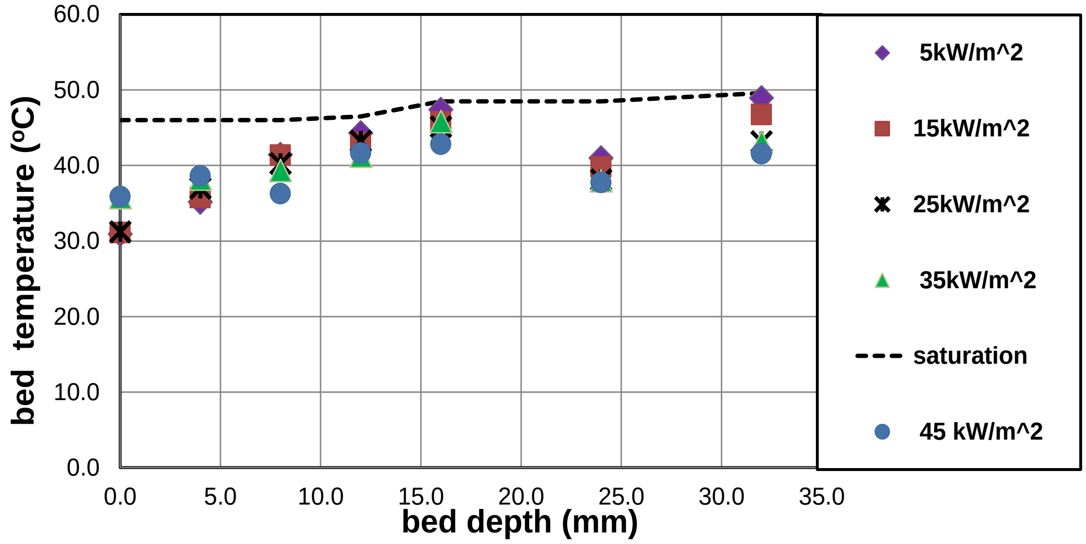

Figure 7-3: Variation of bed temperature with bed depth

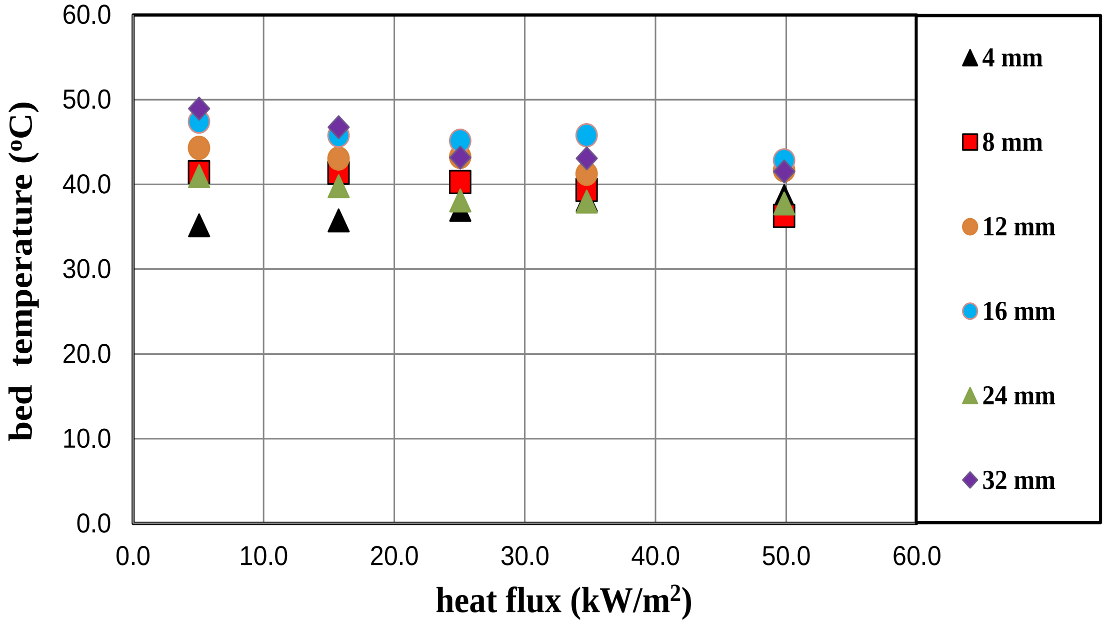

Figure 7-4: Variation of bed temperature with heat flux

7.4 Analysis of Solid Beds Containing Glass Particles

Bubble size was observed to increase with bed depth and heat flux and some fluidisation was observed to occur at the larger bed depths and heat fluxes. The camera used to record the visual images had a resolution of 5184 x 3456 pixels. The camera was focussed on the height of the test section, approximately 1 m. Thus, each vertical pixel represented approximately 0.29 mm of test section. This resolution is sufficient to allow the camera to be used to make estimates of bubble size and bed depth.

As is clear from the images, the camera angle was not ideally set up for this type of analysis. The analysis requires reference lengths to translate the pixels to physical sizes. Two reference distances were used. The first was the drain hole. This is the small hole shown above the solids bed in Figure 7.5 and is 13 mm in diameter. The second was the diameter of a heated tube. The tubes were manufactured in-house and had a diameter of 28.5 mm as shown in Figure 7.6. The analyses required appropriate software to make the measurements, Image J,[85] was used. These reference lengths were subjected to similar distortions as the measured quantities, making the measured quantities reasonably representative.

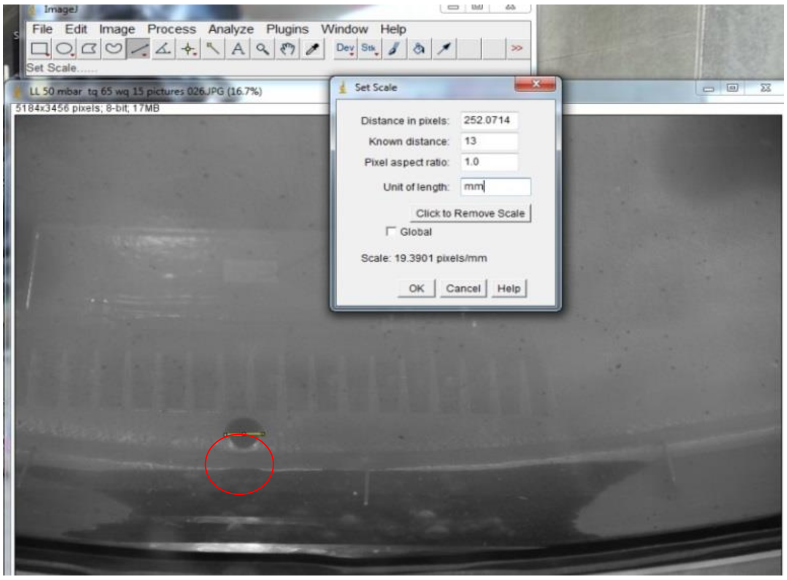

Distance in pixels: 252.0714
Known distance: 13
Pixel aspect ratio: 1.0
Unit of length: mm
☐ Global
Scale: 19.3901 pixels/mm

Figure 7-5: using drain hole’s diameter as a reference

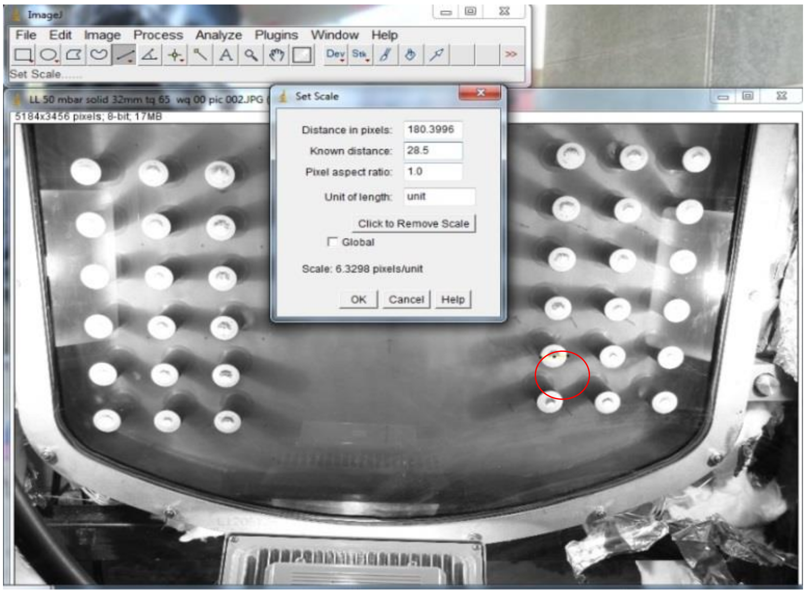

Distance in pixels: 180.3996
Known distance: 28.5
Pixel aspect ratio: 1.0
Unit of length: unit
☐ Global
Scale: 6.3298 pixels/unit

Figure 7-6: using tube diameter as a reference

7.4.1 *Bubble Diameter*

The bubbles measured were located in the centre of the base, where the bed depth was largest. Four images were selected for each measurement. An ellipse was used to measure the bubble size, as this best reflected the bubble shape. The equivalent diameter of the bubble on each image was taken as the average of the major and minor axes of the ellipse, the equivalent diameters for all the pictures for each depth shown in table 7.1. An example of the technique is given in Figure 7.7 for a bed depth of 8 mm and heat flux of 35 kW/m^2. The bubble diameter was taken as the average of the diameters from the four images.

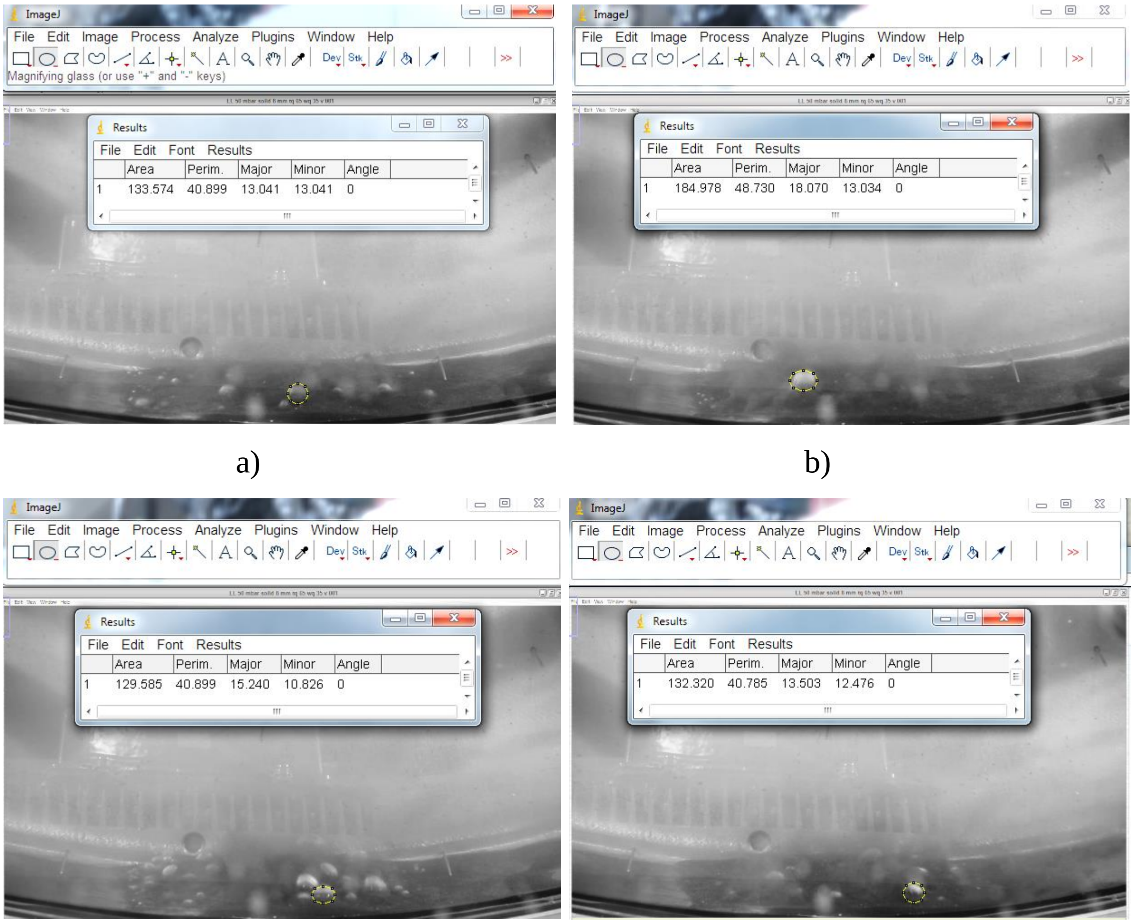

Magnifying glass (or use "+" and "-" keys)

```
   Area     Perim.   Major    Minor    Angle
1  133.574  40.899   13.041   13.041   0
```

```
   Area     Perim.   Major    Minor    Angle
1  184.978  48.730   18.070   13.034   0
```

```
   Area     Perim.   Major    Minor    Angle
1  129.585  40.899   15.240   10.826   0
```

```
   Area     Perim.   Major    Minor    Angle
1  132.320  40.785   13.503   12.476   0
```

a) b)

c) d)

Figure 7-7: four pictures for a bed depth of 8 mm at a heat flux of 35 kW/m^2

For a bed depth of 4 mm and at heat fluxes higher than 5 kW/m^2, the particles bring about nucleate boiling within the bed, while convective heat transfer is dominant at the sides. By using Image J software, the equivalent estimated bubble diameters were 2.8, 7.6, 10.9 and 9.7 mm for heat fluxes of 15, 25, 35 and 45 kW/m^2 respectively. Examples of these bubble diameters are given in Figure 7.8. A large numbers of bubbles are observed for the 4 mm bed at a heat flux of 45kW/m^2, as shown in Figure 7.8d.

For a bed depth of 8 mm, boiling started at a heat flux of 5 kW/m^2. The equivalent estimated bubble diameters increased as heat flux increased and were 7, 8.6, 10.7, 13.6 and 13.8 mm for heat fluxes of 15, 25, 35 and 45 kW/m^2 respectively. At bed depth higher than 12 mm the equivalent estimated bubble diameters increased significantly as heat fluxes increased, the results are shown in Table 7.1.

Figure 7.9 show the variation of estimated equivalent bubble diameter with the heat flux. The bubble diameter increases as the bed depth increases at the same heat flux. The equivalent estimated bubble diameter increases with increasing heat flux for the same bed depth, as shown in Figure 7.9. Similar measurements on the lower vertical wall, where there were no solids, gave bubble diameters of 20 mm at a heat flux 45 kW/m^2. Horizontal bubbles on the tube surfaces gave bubble diameters of 16 mm at a heat flux of 65 kW/m^2. These highlight just how large bubbles are at these low pressures and how much larger they can become in the presence of a solids layer. The nucleation sites decreased as the bed depth increased as shown in Figures 7.8d and 7.10f.

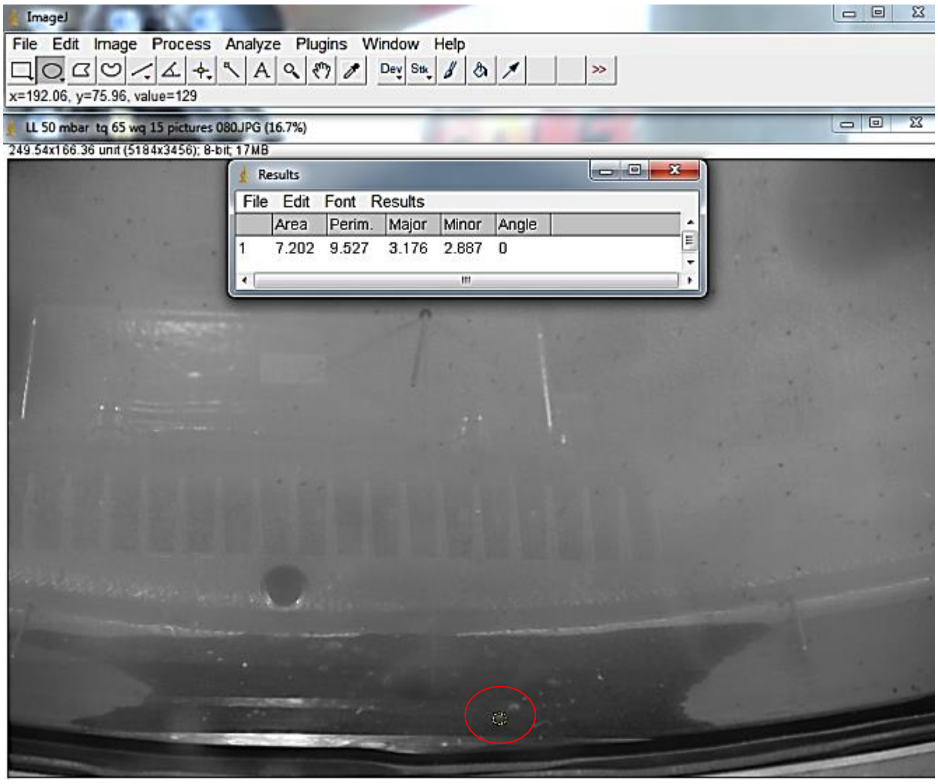

```
x=192.06, y=75.96, value=129
249.54x166.36 unit (5184x3456); 8-bit; 17MB
```

	Area	Perim.	Major	Minor	Angle
1	7.202	9.527	3.176	2.887	0

a) at heat flux of 15 kW/m^2

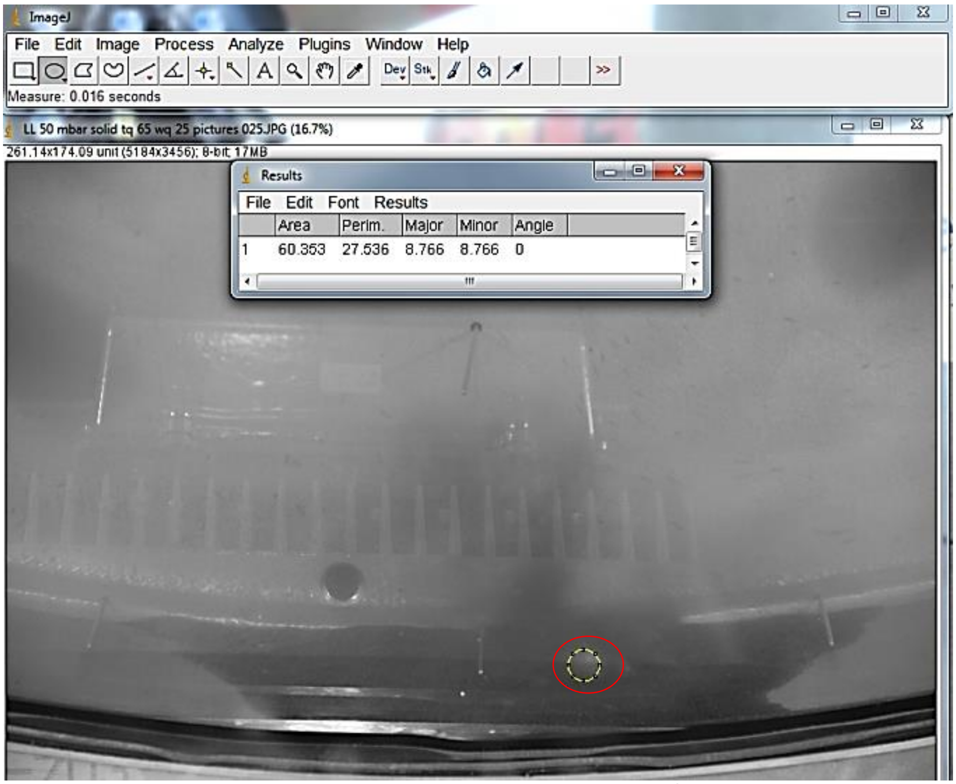

Measure: 0.016 seconds

LL 50 mbar solid tq 65 wq 25 pictures 025.JPG (16.7%)

261.14x174.09 unit (5184x3456); 8-bit; 17MB

	Area	Perim.	Major	Minor	Angle
1	60.353	27.536	8.766	8.766	0

b) at heat flux of 25 kW/m^2

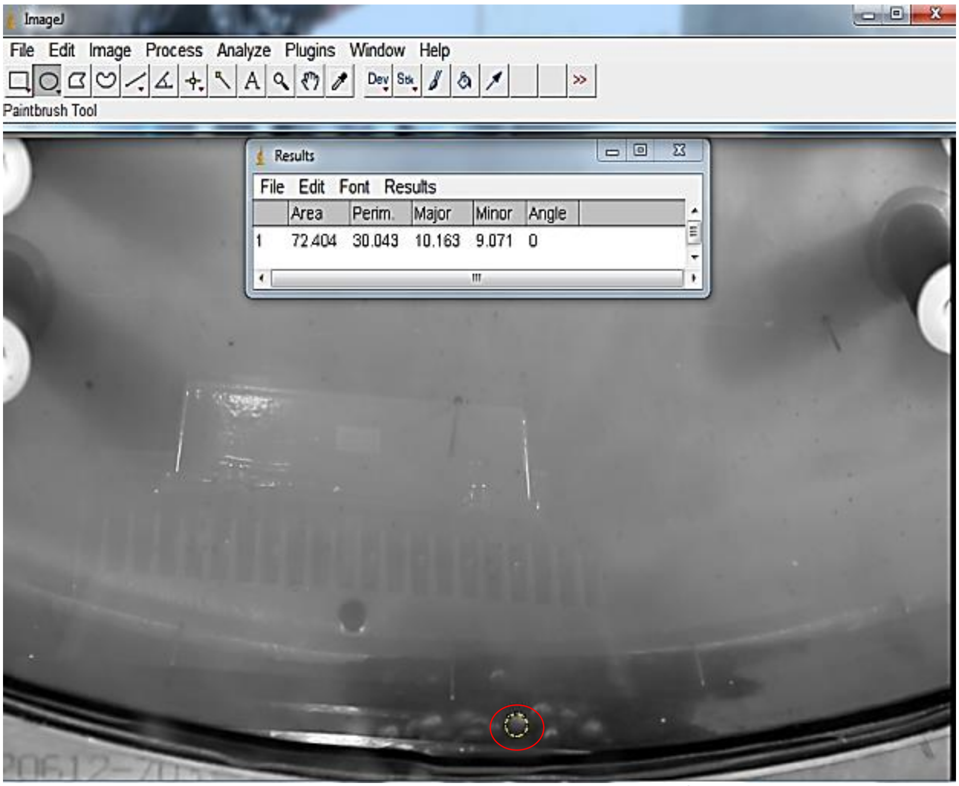

Paintbrush Tool

	Area	Perim.	Major	Minor	Angle
1	72.404	30.043	10.163	9.071	0

c) at heat flux of 35 kW/m^2

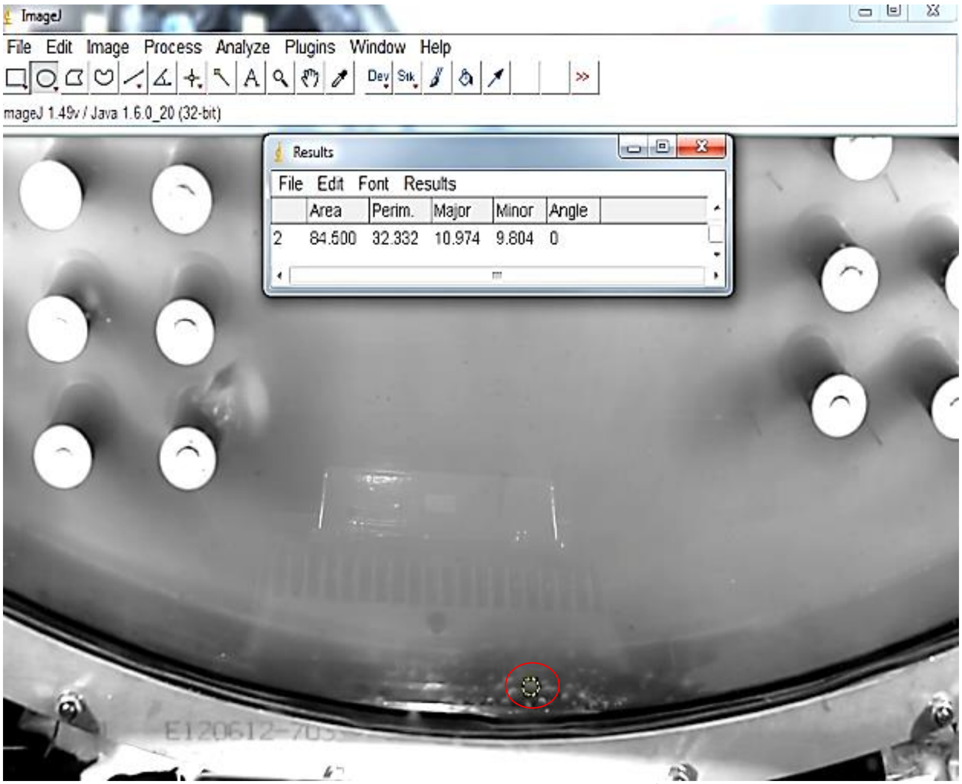

```
mageJ 1.49v / Java 1.6.0_20 (32-bit)
```

```
   Area    Perim.  Major   Minor  Angle
2  84.500  32.332  10.974  9.804  0
```

d) at heat flux of 45 kW/m^2

Figure 7-8: bubble behaver at a bed depth of 4 mm

Table 7-1: The equivalent estimated bubble diameters for each heat flux

Bed Depth	E.E. Bubble diameter at 5 kW/m^2 (mm)	E.E. Bubble diameter at 15 kW/m^2 (mm)	E.E. Bubble diameter at 25 kW/m^2 (mm)	E.E. Bubble diameter at 35 kW/m^2 (mm)	E.E. Bubble diameter at 45 kW/m^2 (mm)
4 mm	No bubbles	2.8	7.6	10.9	9.7
8 mm	7	8.6	10.7	13.6	13.8
12 mm	8.4	11.3	13.5	15.1	18.5
16mm	9.7	14.1	17.1	18.6	20.5
24 mm	14	15.7	20.7	25.5	30.1
32 mm	17.9	25	26.6	33.5	40.3

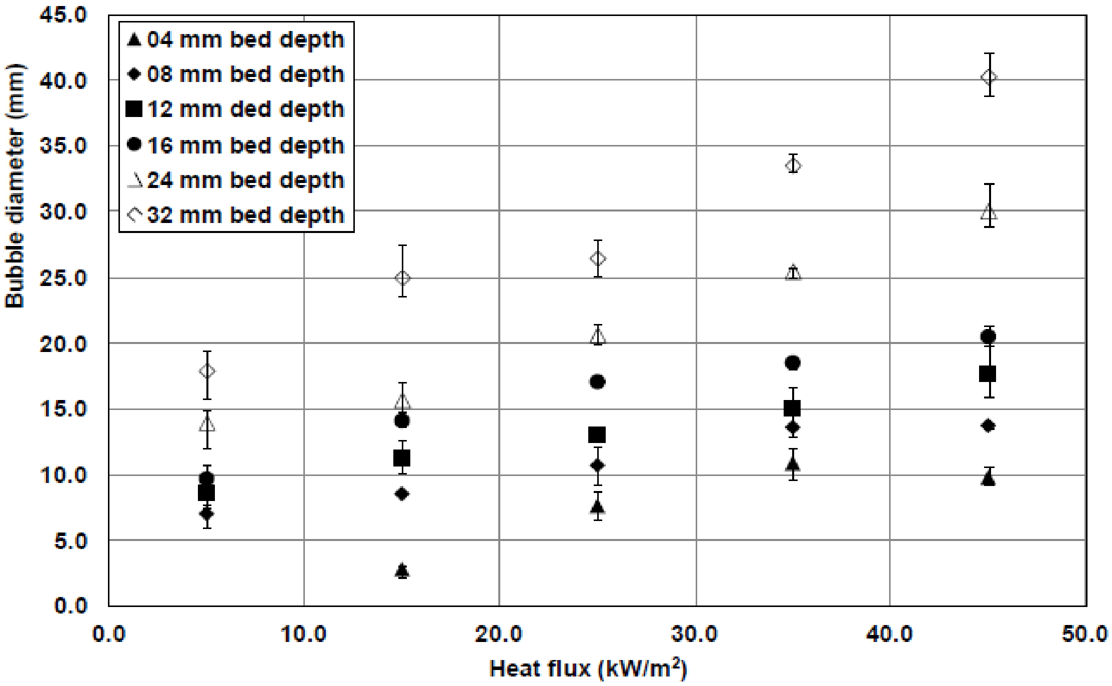

Figure 7-9: Variation of the estimated bubble diameter with the heat flux

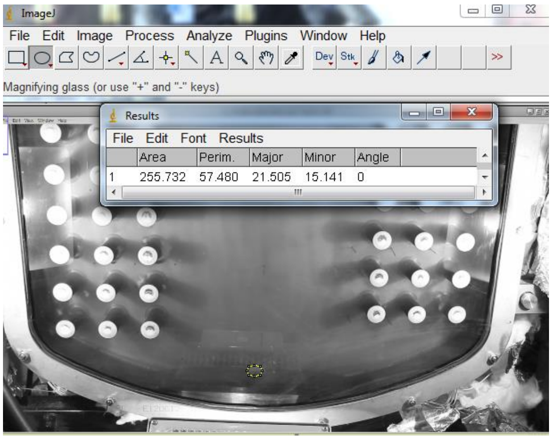

	Area	Perim.	Major	Minor	Angle
1	255.732	57.480	21.505	15.141	0

a) at heat flux of 5 kW/m^2

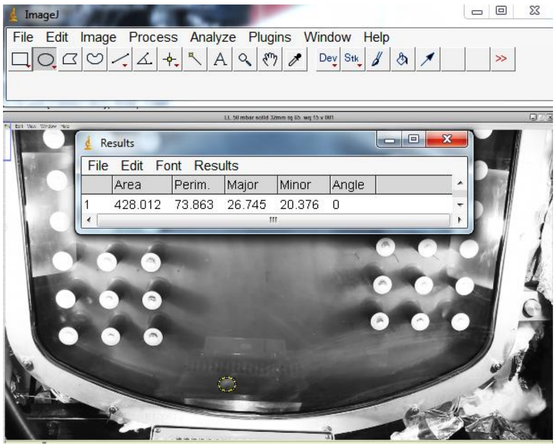

	Area	Perim.	Major	Minor	Angle
1	428.012	73.863	26.745	20.376	0

b) at heat flux of 15 kW/m^2

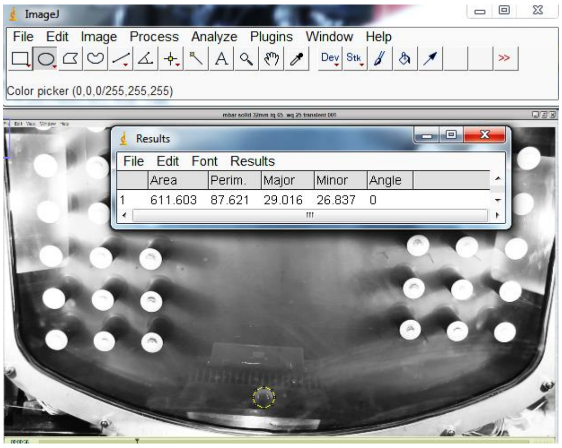

	Area	Perim.	Major	Minor	Angle
1	611.603	87.621	29.016	26.837	0

c) at heat flux of 25 kW/m^2

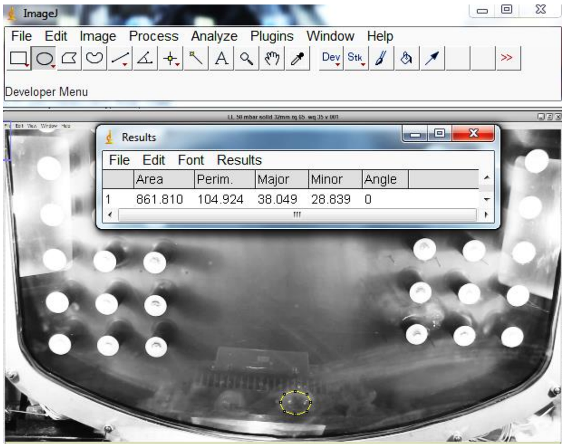

	Area	Perim.	Major	Minor	Angle
1	861.810	104.924	38.049	28.839	0

d) at heat flux of 35 kW/m^2

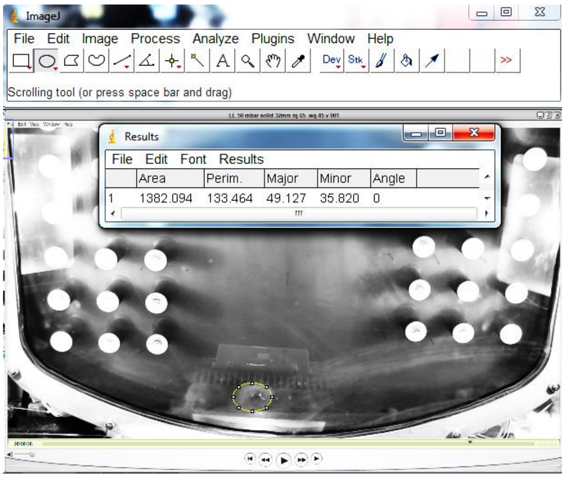

Scrolling tool (or press space bar and drag)

	Area	Perim.	Major	Minor	Angle
1	1382.094	133.464	49.127	35.820	0

f) at heat flux of 45 kW/m²

Figure 7-10: changing bubble size with the heat flux at bed depth of 32 mm

7.5 Changing in the Bed Depth (Fluidization)

Bed depths were also measured in the centre of the base, where it was largest. Five images were selected for each measurement. An example of a tube being used as the reference is shown in Figure 7.6. A line was used to measure the bed depth. An example of the technique is given in Figure 7.12. The bed depth was taken as the average of the depths from the five images.

The bed depth measurements are shown in Figure 7.11. Reliable estimates of the bed depth at 4 and 8 mm were not possible because of the movement of the bed. Measurements are shown for the bed depth before base heating was applied and at a heat flux of 45 kW/m^2. All 5 readings are included. These measurements show that only small variations were obtained from the different images. At bed depths of 12 and 16 mm, there is little difference between the values obtained at 0 and 45 kW/m^2. However, there is a significant difference between them at bed depths of 24 and 32 mm where decreases of about 2.5 and 5 mm were respectively obtained as shown in Figures 7.12 and 7.13. This is an indication of the partial fluidisation of the bed. Particles were observed to be irregularly driven from the centre of the bed surface by the rising vapour bubbles. These particles were temporarily distributed in the bulk liquid, before returning to the base. However, the majority of the particles remained in the bed and continued to provide nucleation sites to maintain the process.

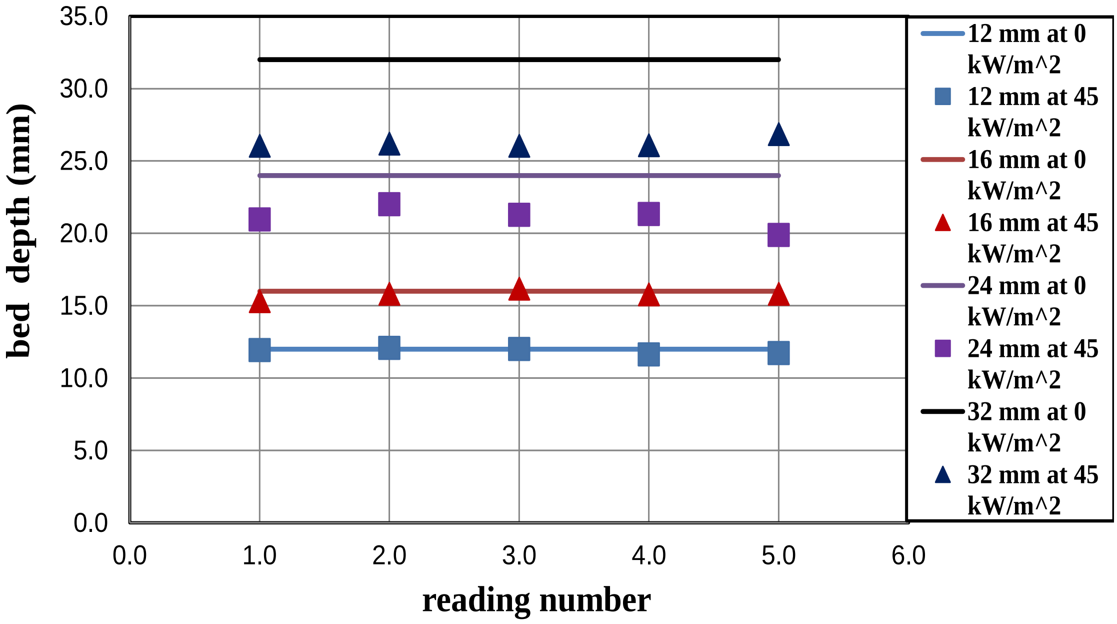

Figure 7-11: Variation of bed depth with the heat flux

Scrolling tool (or press space bar and drag)

HL 50 mbar solid 24mm tq 65 wq 05 pic 015.JPG (16.7%)

683.74x455.82 unit (5184x3456); 8-bit; 17MB

Area	Mean	Min	Max	Perim.	Angle	Length
3.149	104.420	34	196	23.741	-90	23.741

x=159.45, y=133.80, value=197

LL 50 mbar solid 24mm tq 65 wq 35 pic 001.JPG (16.7%)

598.98x399.32 unit (5184x3456); 8-bit; 17MB

Area	Mean	Min	Max	Perim.	Angle	Length
2.497	113.053	28	183	21.491	-90	21.491

a) *No heat flux applied*

b) *At a heat flux of 45 kW/m^2*

Figure 7-12: the bed depth estimation at a bed depth of 24 mm

LL 50 mbar solid 32mm tq 65 wq 05 pic 001.JPG (16.7%)
798.18x532.12 mm (5184x3456); 8-bit; 17MB

	Area	Mean	Min	Max	Perim.	Angle	Length
2	4.860	99.424	48	185	31.410	-90	31.410

x=386.63, y=404.53, value=118

LL 50 mbar solid 32mm tq 65 wq 45 pic 002.JPG (16.7%)
703.26x468.84 unit (5184x3456); 8-bit; 17MB

	Area	Mean	Min	Max	Perim.	Angle	Length
1	3.552	156.119	68	235	26.047	-90	26.047

a) No heat flux applied

b) At a heat flux of 45 kW/m^2, picture 1

LL 50 mbar solid 32mm tq 65 wq 45 pic 003.JPG (16.7%)
665.51x443.68 MM (5184x3456); 8-bit; 17MB

	Area	Mean	Min	Max	Perim.	Angle	Length
1	3.379	144.127	52	242	26.189	-90	26.189

x=278.49, y=172.63, value=142

LL 50 mbar solid 32mm tq 65 wq 45 pic 005.JPG (16.7%)
703.54x469.03 unit (5184x3456); 8-bit; 17MB

	Area	Mean	Min	Max	Perim.	Angle	Length
1	3.555	153.306	65	226	26.057	-90	26.057

c) At a heat flux of 45 kW/m^2, picture 2

d) At a heat flux of 45 kW/m^2, picture 3

LL 50 mbar solid 32mm tq 65 wq 45 pic 006.JPG (16.7%)
682.95x455.30 MM (5184x3456); 8-bit; 17MB

	Area	Mean	Min	Max	Perim.	Angle	Length
1	3.454	150.779	48	226	26.085	-90	26.085

LL 50 mbar solid 32mm tq 65 wq 45 pic 007.JPG (16.7%)
703.26x468.84 MM (5184x3456); 8-bit; 17MB

	Area	Mean	Min	Max	Perim.	Angle	Length
2	3.662	153	65	224	26.860	-90	26.860

d) At a heat flux of 45 kW/m^2, picture 4

f) At a heat flux of 45 kW/m^2, picture 5

Figure 7-13: the bed depth estimation at a bed depth of 32 mm

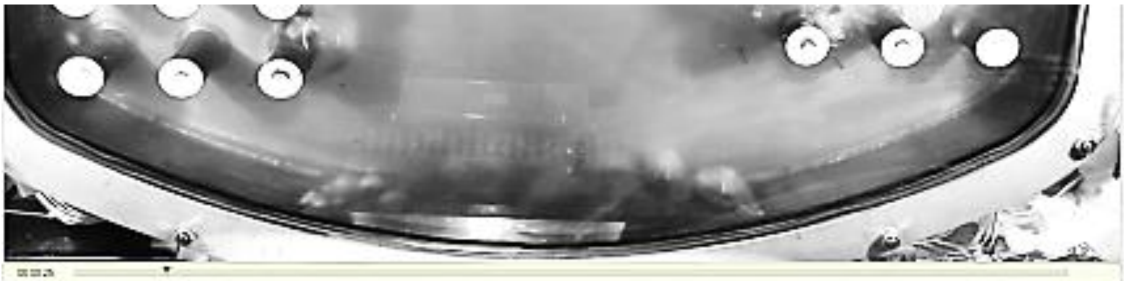
1

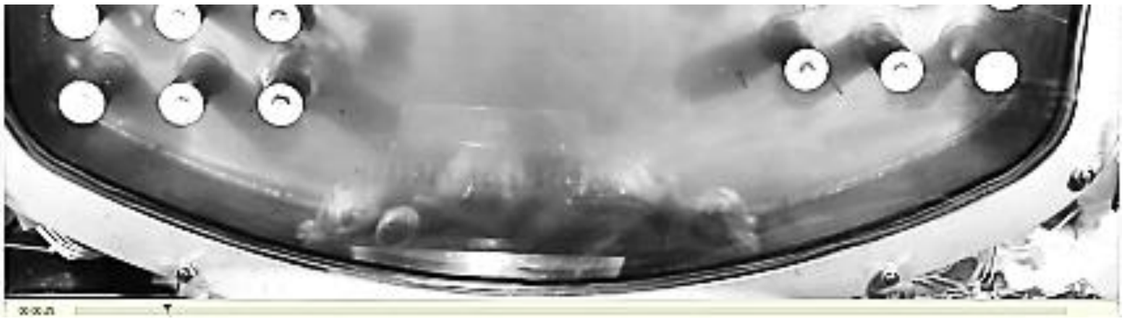
2

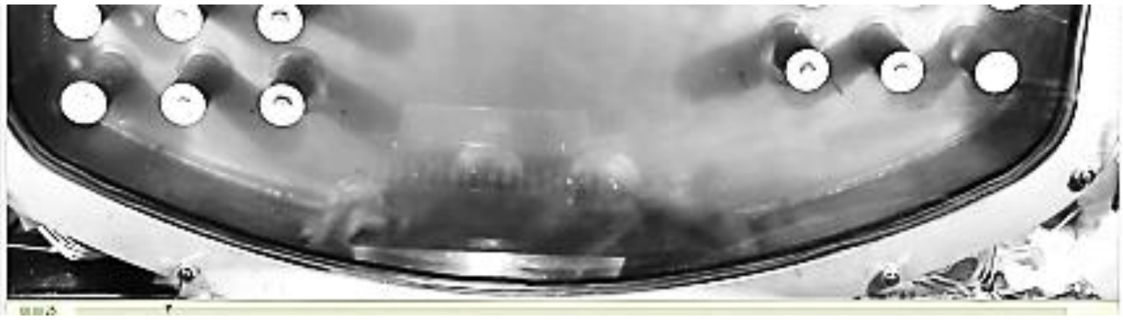
3

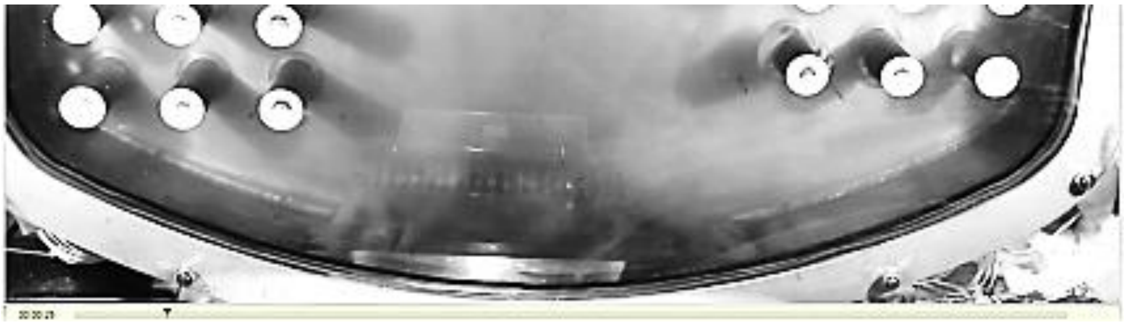
4

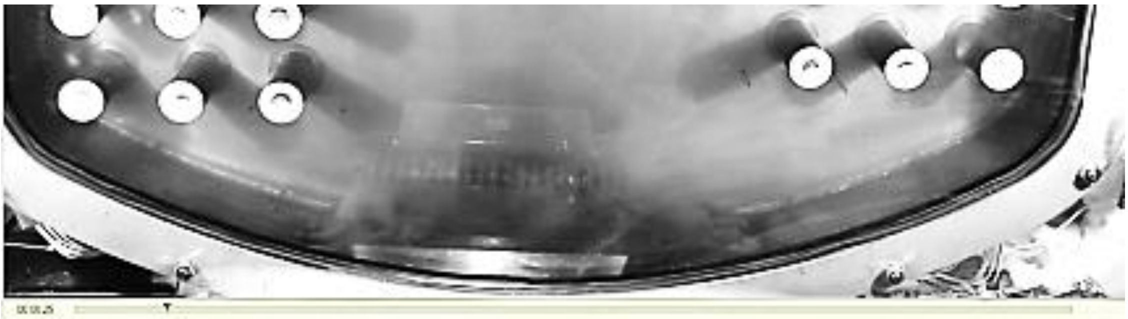
5

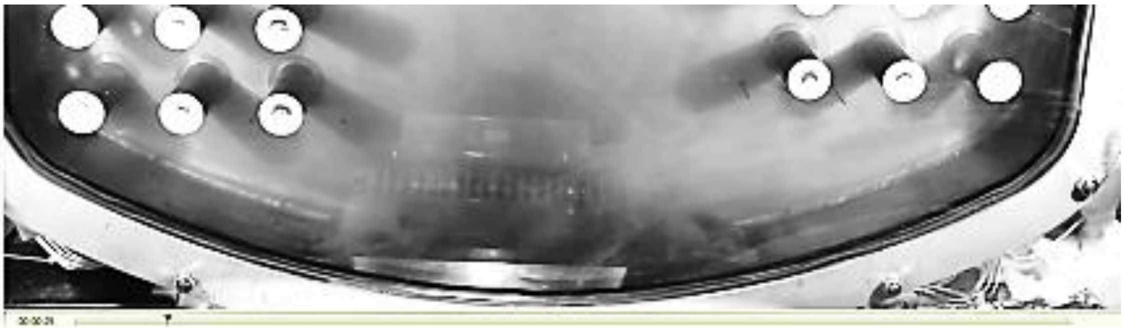

6

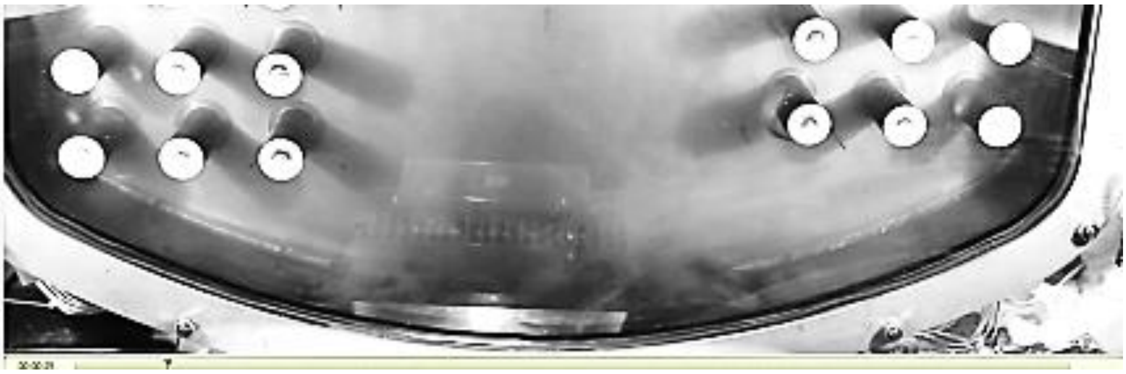

7

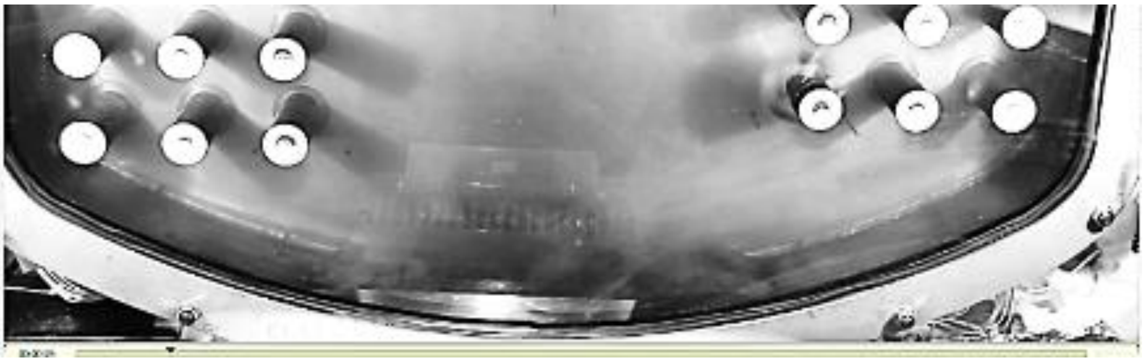

8

9

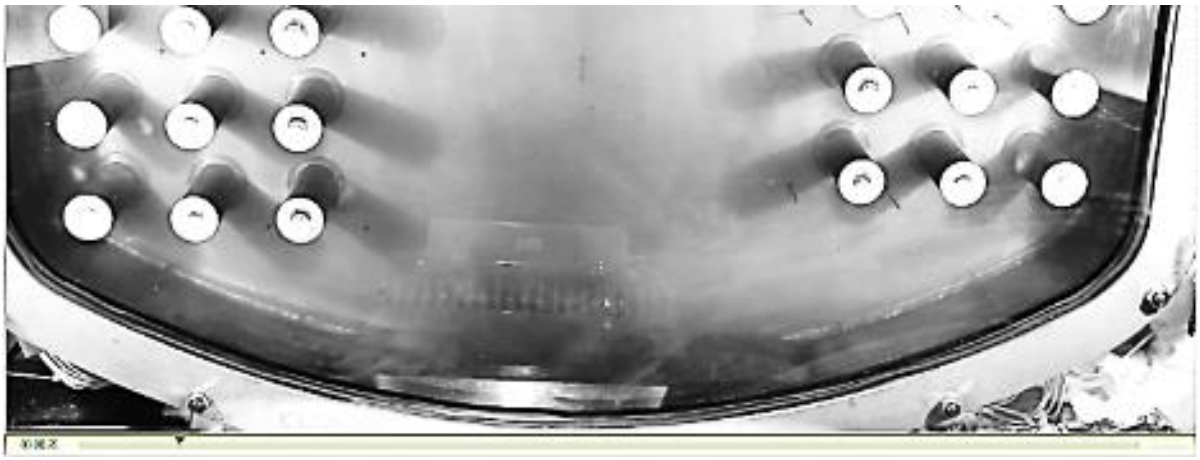

10

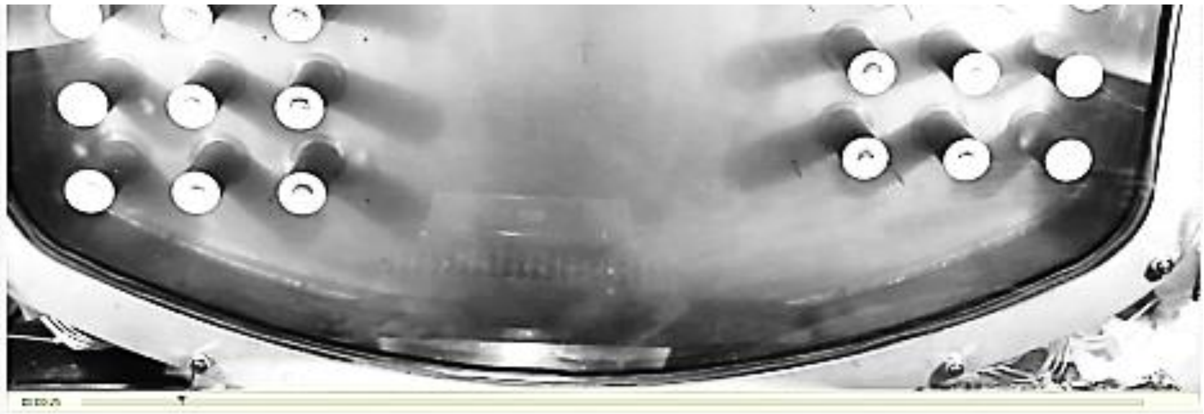

11

Figure 7-14: Fluidization at a bed depth of 32 mm with heat flux of 45 kW/m^2

7.6 Wall Superheat

The variation of base superheat with bed depth is shown in Figure 7.15. For a bed depth of 4 mm, the base superheat is negative at a heat flux of 5 kW/m^2, thus boiling was not happening at this heat flux. The base superheat increases to 9 K when the heat flux is increased to 15 kW/m^2, before reducing steadily at the heat flux is further increased. This was due, in part, to the bed moving around the base. For bed depths greater than 4 mm, the base superheat changes with increasing heat flux are less significant. However, the base superheat is shown to increase with increasing bed depth until 16 mm, before reducing.

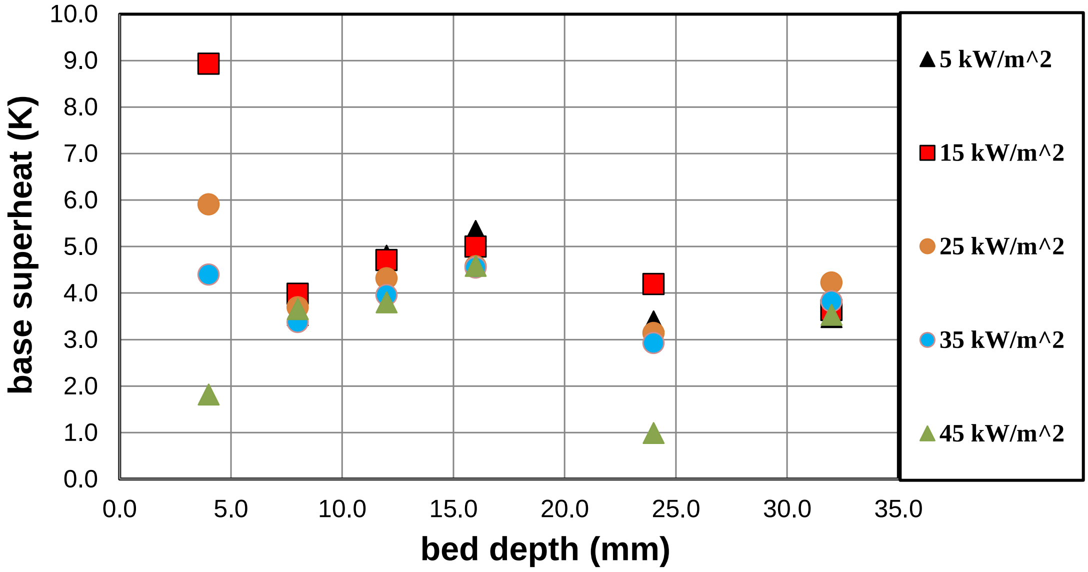

Figure 7-15: variation of the base superheat with the bed depth

7.7 Summary

The temperatures measured throughout the liquid pool were reasonably uniform at the saturation temperature of the free surface, irrespective of the particle type, Figures 6.1 and 6.2. This is an indicator that liquid circulation occurred within the pool, with flashing occurring at the free surface. This happens when the particles remain in a bed or when they were 'fluidised'.

In the absence of particles, the base temperatures were below the saturation temperature, Figures 7.1. However, the presence of the glass particles induced boiling below the bed. At bed depths of 16 mm and below, the liquid temperature within the bed, and the base superheat below it, increased with bed depth, Figures 7.3 and 7.15, and reduced at larger bed depths. The change in behaviour was probably caused by the onset of fluidisation of the bed, Figure 7.11.

Without solid particles, boiling did not occur because of convective cooling by the liquid circulating in the pool. When added, the deposited particles acted like a blanket, preventing the cooling effect of the pool and causing the base temperature below the bed to rise until boiling was initiated. Visual observations showed that bubbles were generated in the gaps between the heated surface and the particles, Figure 6.21. The vapour bubbles generated by the glass particles, Figure 7.9, are much larger than the particles in the bed, which were 0.5-0.6 mm in diameter, and they completely surrounded them. The number of bubbles produced by the glass particles was much larger at low bed depths than at larger depths. An estimate from the images obtained showed 60-80 bubbles present at a heat flux of 45 kW/m^2 and a bed depth of 4 mm. This was reduced to 5-15 bubbles at the same heat flux but at a bed depth of 32 mm. Deeper beds have a greater flow resistance, restricting the liquid flow through the bed to the heated surface and reducing vapour flow into the pool. The latter was overcome by small bubbles joining together to become large bubbles, Figure 7.9. Normally an increase in bubble departure diameter occurs with a decrease in bubble frequency and the higher the bubble frequency the stronger the boiling heat transfer, [65]. Therefore, larger bubble diameters imply a decrease in the heat transfer performance.

The evaporator tested operates at a low pressure to reduce the saturation temperature and thus the base temperature. This is done to reduce the corrosion rate of the evaporator base. These tests indicate that the presence of any particles on the base significantly increases the base temperature and therefore the corrosion rate. The glass particles were mainly on the base. The literature reviewed, and the observations from these tests, suggest that the presence of particles may change the boiling heat transfer rate. It is not clear whether it will be improved or degraded, i.e., the corrosion rate may be increased or reduced, relative to the plain base boiling performance.

Chapter 8- SUMMARY OF THE CONCLUSIONS AND RECOMMENDATIONS FOR FUTURE WORK

8.1 Summary of the Conclusions

The experimental results show that the operation of the evaporator changes significantly as the pressure is reduced. This is evidenced by the visual observations, the stream temperatures and the heat-transfer measurements. The stream temperatures indicate that re-circulation is occurring, irrespective of the pressure, because the pool temperature is similar to the saturation temperature corresponding to the pressure at the free surface. However, this produces small liquid sub-coolings at high pressure, as seen in the LLHP and LLMP data series, and large liquid sub-coolings at vacuum pressures, as seen in the LLLP and HLLP data series. The LLMP and LLHP tests behaved as expected, with bubbles generated and moving upwards in the liquid pool. However, the vacuum tests behave differently. The vapour density in Equation 3.1 means that vacuum heat fluxes require a significantly higher wall superheat to nucleate. This has meant that tube wall temperatures are lower than expected at the lower heat fluxes and are being cooled by single-phase flows. The single-phase cooling is enhanced as a result of the re-circulation, another source in the delay in nucleation. The tubes nucleate at the higher heat fluxes but only partial boiling was obtained.

The visual evidence shows

- For the LLLP series, bubbles were evident at heat fluxes greater than 10 kW/m^2. However, the bubbles were relatively large and attached to the tube wall. Larger heat fluxes led to a more frequent occurrence of the bubbles.

- For the HLLP series, bubbles were not observed until a heat flux of 40 kW/m^2.

- For the LLMP and LLHP series, small bubbles were evident towards the top of the tube bundle at heat fluxes of 10 kW/m^2. As the heat flux increases, bubbles were evident further down in to the tube bundle.

- The liquid pool changed as the pressure was reduced. At a pressure of 450 and 850 mbar the pool contained many bubbles, whereas few bubbles were evident at a pressure of 50 mbar.

- It is noticeable that, even at high heat fluxes, the void fraction is low.

Re-circulation requires a liquid velocity which means that convection and sub-cooled boiling could be present. However, which heat-transfer mechanism is dominating is less clear. Two analyses methods, the equilibrium model and isolated tube model, were used to help deduce what the heat-transfer mechanisms were.

- When the models were applied to the low level data at a pressure of 50 mbar, the analysis suggested that the isolated tube model was less likely than the equilibrium model. Velocity magnitudes supportive of the equilibrium model were observed. Thus, at a pressure of 50 mbar, the equilibrium model with the Gorenflo - ESDU [12] [84] combination used to describe boiling gave the more credible results.

- When the models were applied to the high level data at a pressure of 50 mbar, the isolated tube with the Gorenflo [12] correlation used to describe boiling gave the more credible results.

- When the models were applied at a pressure of 450 and 850 mbar, it is suggested that the equilibrium model is less likely to have occurred and that the isolated tube behavior is more likely. The results for 450 and 850 mbar suggest that the Stephan and Abdelsalam [9] correlation are more accurate at these pressures. However, caution must be exercised because the tube columns did not behave the same and the presence of the bubbles was not taken into account in the equilibrium model.

The low pressure, high level data show isolated tube behavior, where the heat-transfer mechanism is natural convection until the onset of boiling and nucleate boiling thereafter. The visual evidence and the models results supported that the low pressure, low level data is dominated by tube interactions as described by the equilibrium model, where the heat-transfer mechanism is convection before the onset of boiling, with convection and nucleation afterwards. It is probable that the reduction in pressure changes the low level behavior and that the dominant mechanism at a pressure of 450 and 850 mbar is different from that at 50 mbar. However, caution must be exercised as explained above.

The effect on base temperature of increasing the bed depth has been investigated for water boiling at a pressure of 50 mbar absolute. The bed depth was varied from 0-32 mm using glass particles 500-600 μm in diameter.

The visual evidence shows that

- The average bubble size increases with increasing bed depth. These bubbles are much greater than those present without particles.
- The bed was observed to oscillate from one side of the base to the other. The magnitude of oscillation decreased with increasing thickness and stopped moving at bed depth of 24 mm.
- The number of nucleation sites decreases with increasing bed depth
- For a bed depth of 24 and 32 mm, at heat fluxes greater than 35 kW/m^2, the vapour flows upward and fluidizes the particles, the fluidization produced significant decreases in the bed depths.
- The bubbles are initiated on the base as small bubbles, which subsequently merge.

The major effect of particles on nucleate boiling heat transfer can be analysed as follows. Firstly, with no solid particles, boiling is not observed, because of convective cooling by the liquid circulating in the pool. The solid particles act like a blanket, preventing the cooling effect of the pool and causing the wall temperature to rise until boiling is initiated. Secondly, according to visual observations, additional bubbles were provided on the heated surface by the particles in contact with the surface. This is dominant at low depth and decreases as the depth increases. The liquid flow to the surface is restricted by the bed flow resistance. For the same reasons vapour needs larger buoyancy forces to escape. This is achieved by small bubbles joining together to become larger bubbles. Once the bubble escapes the vacuum effect causes liquid to rush in to the bed.

8.2 Recommendation for Future Work

- Further controlled experiments should be undertaking to obtain boiling curve and convective coefficients for water at controlled flow rates, pressure and temperature across electrically heated tubes and walls.
- The fluid properties can be modified by the use of additives, e.g. the viscosity can be changed by adding glycerol to see the difference in the evaporator behaviour.

- Simulation using a CFD model is recommended.

- Deeper beds need to be investigated to see how fluidization progresses.

- Further study on particle shape is required to fully understand the particle effect.

- Different sizes of particles with different thermal conductivities are required to better understand the effect of the particles.

- Further work is required to investigate the magnitude of the heat-transfer coefficient during boiling in the presence of solids.

REFERENCES

1. Committee, S.L.M.S., *Radiological Safety Assessment of Breakthrough of HAL into Evaporator C Heating / Cooling Water Circuits. HALES* 2014. p. 022.

2. ONR's, *Hazard and Risk reduction from Highly Active Liquor Regulatory Judgement on the Justification for Evaporator C Continued Operations,*, ONR-SEL-PAR-15-009, Editor. 2015.

3. Stephan, I.P. and D.-I.J. Hammer, *A new model for nucleate boiling heat transfer.* Heat and Mass Transfer, 1994. **30**(2): p. 119-125.

4. Rohsenow, W.M., *A method of correlating heat transfer data for surface boiling liquids.* Journal of Heat Transfer, 1952. **74**: p. 969–976.

5. R.I.Vachon, G.H.N.a.G.E.T., *Evaluation of constants of the Rohsenow pool-boiling correlation.* Heat transfer 1968. **90**(2): p. 239-246.

6. Montinski, *application of the rule of corresponding states for calculation of the heat transfer and critical heat flux.* teploenergetika, 1963. **4**: p. 66.

7. Rice, P. and W.F. Calus, *POOL BOILING - SINGLE COMPONENT LIQUIDS.* Chemical Engineering Science, 1972. **27**(9): p. 1677-1686.

8. Borishanskii V. M., B.G.I., Minchenko F. P., *heat transfer from a tube to water and to enthanol in nucleate pool boiling.* In Kutateladze S. S., editor, Problems of heat transfer and hydraulics of two-phase media, 1969. **chapter 7**: p. 85-106.

9. Stephan, K. and M. Abdelsalam, *HEAT-TRANSFER CORRELATIONS FOR NATURAL CONVECTION BOILING.* International Journal of Heat and Mass Transfer, 1980. **23**(1): p. 73-87.

10. Nishikawa, K., Fujita, Y., Ohta, H., Hidaka, S. *Effect of the surface roughness on the nucleate boiling heat transfer over the wide range of pressure*. in *Proceedings of the 7th International Heat Transfer Conference*. 1982. München 1982.

11. Cooper, M.G., *HEAT FLOW RATES IN SATURATED NUCLEATE POOL BOILING - A WIDE-RANGING EXAMINATION USING REDUCED PROPERTIES.* Advances in Heat Transfer, 1984. **16**: p. 157-239.

12. Gorenflo, D., *Pool Boiling.* VDI–Heat Atlas, VDI–Verlag, 1993. **D¨usseldorf (English version)**.

13. Cornwell, K. and S. Houston, *Nucleate pool boiling on horizontal tubes: a convection-based correlation.* International journal of heat and mass transfer, 1994. **37**: p. 303-309.

14. Pioro, I. *Boiling heat transfer characteristics of thin liquid layers in a horizontally flat two-phase thermosyphon*. in *Preprints of the 10th International Heat Pipe Conference, Stuttgart, Germany*. 1997.

15. Choon, N.K., et al., *New pool boiling data for water with copper-foam metal at sub-atmospheric pressures: experiments and correlation.* Applied Thermal Engineering, 2006. **26**(11): p. 1286-1290.

16. Merk, H.J., and Prins, J.A., *Thermal Convection Laminar Boundary Layer* Applied Scientific Research, 1954a. **A4**.

17. Merk, H.J., and Prins, J.A., *Thermal Convection Laminar Boundary Layer III.* Applied Scientific Research 1954b. **A4,**.

18. Churchill, S.W. and H.H. Chu, *Correlating equations for laminar and turbulent free convection from a horizontal cylinder.* International journal of heat and mass transfer, 1975. **18**(9): p. 1049-1053.

19. Collier, J.G. and J.R. Thome, *Convective boiling and condensation*. 1994: Clarendon Press.

20. Cornwell, K., *The influence of bubbly flow on boiling from a tube in a bundle.* International Journal of Heat and Mass Transfer, 1990. **33**(12): p. 2579-2584.

21. Palen, J., *Shell and tube reboilers.* Heat Exchanger Design Handbook, 1983. **3**: p. 3.6.

22. Fujita, Y., et al. *Nucleate boiling heat transfer on horizontal tubes in bundles*. in *Proc. 8th IHTC*. 1986.

23. Jensen, M., M. Reinke, and J.-T. Hsu, *The influence of tube bundle geometry on cross-flow boiling heat transfer and pressure drop.* Experimental Thermal and Fluid Science, 1989. **2**(4): p. 465-476.

24. Cornwell, K., S.D. Houston, and A.J. Addlesee. *Sliding bubble heat transfer on a tube under heating and cooling conditions*. in *Proceedings of the Engineering Foundation Conference on Pool and External Flow Boiling, March 22, 1992 - March 27, 1992*. 1992. Santa Barbara, CA, USA: Publ by ASME.

25. Hwang, T. and S. Yao, *Forced convective boiling in horizontal tube bundles.* International journal of heat and mass transfer, 1986. **29**(5): p. 785-795.

26. Chen, J.C., *A proposed mechanism and method of correlation for convective boiling heat transfer with liquid metals*. 1963, Brookhaven National Lab., Upton, NY.

27. Bennett, D., M. Davis, and B. Hertzler, *Suppression of saturated nucleate boiling by forced convective flow.* 1980.

28. Cornwell, K., J. Einarsson, and P. Andrews. *Studies on boiling in tube bundles*. in *Proceedings of the eighth international heat transfer conference*. 1986.

29. Zukauskas, A. and J. Ziugzda, *Heat transfer of a cylinder in crossflow.* Washington, DC, Hemisphere Publishing Corp., 1985, 219 p. Translation., 1985. **1**.

30. Nukiyama, S., *Maximum nd Minimum Values of Heat Transmitted from a Metal to Boiling Water under Atmospheric Pressure.* Japanese Society of Mechanical Engineers, Japan, 1934. **37**: p. 367-373.

31. Ishihara, K., J.W. Palen, and J. Taborek, *CRITICAL REVIEW OF CORRELATIONS FOR PREDICTING TWO-PHASE FLOW PRESSURE DROP ACROSS TUBE BANKS.* Heat Transfer Engineering, 1980. **1**(3): p. 23-32.

32. Cornwell, K., N.W. Duffin, and R.B. Schueller, *EXPERIMENTAL STUDY OF THE EFFECTS OF FLUID FLOW ON BOILING WITHIN A KETTLE REBOILER TUBE BUNDLE.* American Society of Mechanical Engineers (Paper), 1980(80 -HT-45).

33. Fair, J. and A. Klip, *Thermal design of horizontal reboilers.* Chem. Eng. Prog.;(United States), 1983. **79**(3).

34. Schrage, D.S., J.T. Hsu, and M.K. Jensen, *TWO-PHASE PRESSURE DROP IN VERTICAL CROSSFLOW ACROSS A HORIZONTAL TUBE BUNDLE.* AIChE Journal, 1988. **34**(1): p. 107-115.

35. Dowlati, R., M. Kawaji, and A.M.C. Chan, *Two-phase crossflow and boiling heat transfer in horizontal tube bundles.* Journal of Heat Transfer, 1996. **118**(1): p. 124-131.

36. Feenstra, P.A., D.S. Weaver, and R.L. Judd, *An improved void fraction model for two-phase cross-flow in horizontal tube bundles.* International Journal of Multiphase Flow, 2000. **26**(11): p. 1851-1873.

37. Ribatski, G. and J.R. Thome, *Two-Phase Flow and Heat Transfer across Horizontal Tube Bundles-A Review.* Heat transfer engineering, 2007. **28**(6): p. 508-524.

38. Zukauskas, A.a.U., R, *Heat Exchanger Design Handbook.* 1983.

39. ESDU, *Crossflow Pressure Loss over Banks of Plain Tubes in Square and Triangular Arrays Including Effects of Flow Direction.* Engineering Sciences Data Unit, 1979. **79034**: p. 17.

40. Huang, X., Wang, L., and Jia, F, *Study of two-phase flow regime identification in horizontal tube bundles under vertical upward cross-flow condition using wavelet*

transform. Frontiers of Energy and Power Engineering in China, 2008. **2(3)**: p. 333–338.

41. Van Stralen, S.J.D., *Heat transfer to boiling binary liquid mixtures at atmospheric and subatmospheric pressures*, in *Chemical Engineering Science*. 1956. p. 290-296.

42. I. A. Raben, R.T.B., and G. E. Commerford. , *A Study of Heat Tranfer in Nucleate Pool Boiling of Water at Low Pressure.*

, ed. C.E.P.S. 61(57):249-257. 1965.

43. Ponter, A.B.a.H., C. P, *The boiling crisis in saturated and subcooled pool boiling at reduced pressures.* International Journal of Heat and Mass Transfer

1969. **12**: p. 429-437.

44. Miyauchi, T.a.Y., M, *The mechanism of nucleate boiling heat transfer*, *Heat Transfer* in *Japanese Research*. 1972: Japanese. p. 109-118.

45. van Stralen, S.J.D., et al., *BUBBLE GROWTH RATES IN NUCLEATE BOILING OF WATER AT SUBATMOSPHERIC PRESSURES.* International Journal of Heat and Mass Transfer, 1975. **18**(5): p. 655-669.

46. Joudi, K.A. and D.D. James, *INCIPIENT BOILING CHARACTERISTICS AT ATMOSPHERIC AND SUBATMOSPHERIC PRESSURES.* Journal of Heat Transfer, 1977. **99 Ser C**(3): p. 398-403.

47. Fath, H.S. and R.L. Judd, *INFLUENCE OF SYSTEM PRESSURE ON MICROLAYER EVAPORATION HEAT TRANSFER.* Journal of Heat Transfer, 1978. **100**(1): p. 49-55.

48. Tewari, P.K., et al., *Nucleate boiling in a thin film on a horizontal tube at atmospheric and subatmospheric pressures.* International Journal of Heat and Mass Transfer, 1989. **32**(4): p. 723-728.

49. McGillis, W.R., Carey, V. P., Fitch, J. S. and Hamburgen, W. R. *Pool boiling enhantechniques for water at low pressure*. in *Proceedings of the Seventh IEEE SEMI-THERM Symposium*. 1991.

50. Rainey, K.N., S.M. You, and S. Lee, *Effect of pressure, subcooling, and dissolved gas on pool boiling heat transfer from microporous surfaces in FC-72.* Journal of Heat Transfer, 2003. **125**(1): p. 75-83.

51. McGillis, W.R., et al. *Pool boiling enhancement techniques for water at low pressure*. in *Semiconductor Thermal Measurement and Management Symposium, 1991. SEMI-THERM VII. Proceedings., Seventh Annual IEEE*. 1991. IEEE.

52. Liu, Z.H. and L. Liao, *Enhancement Boiling Heat Transfer Study of a Newly Compact In-line Bundle Evaporator under Reduced Pressure Conditions.* Chemical engineering & technology, 2006. **29**(3): p. 408-413.

53. Barbosa Jr, J.R., L.W. Cheah, and G.F. Hewitt, *Flow boiling of water in a vertical tube at sub-atmospheric pressures.* Journal of the Brazilian Society of Mechanical Sciences and Engineering, 2007. **29**(4): p. 401-409.

54. Feldmann, H. and A. Luke, *Nucleate boiling in water for different pressures.* 2008.

55. Chan, M.A., C.R. Yap, and K.C. Ng, *Pool boiling heat transfer of water on finned surfaces at near vacuum pressures.* Journal of Heat Transfer, 2010. **132**(3): p. 031501.

56. Giraud, F., et al. *Experimental study of water pool boiling at very low pressure on a vertical or horizontal heated surface*. in *4th IIR Conference on Thermophysical Properties and Transfer Processes of Refrigerants*. 2013.

57. Yu, L.-H., et al., *Experimental Research on Water Boiling Heat Transfer on Horizontal Copper Rod Surface at Sub-Atmospheric Pressure.* Energies, 2015. **8**(9): p. 10141-10152.

58. Giraud, F., et al., *Experimental evidence of a new regime for boiling of water at subatmospheric pressure.* Experimental Thermal and Fluid Science, 2015. **60**: p. 45-53.

59. Zajaczkowski, B., T. Halon, and Z. Krolicki, *Experimental verification of heat transfer coefficient for nucleate boiling at sub-atmospheric pressure and small heat fluxes.* Heat and Mass Transfer, 2016. **52**(2): p. 205-215.

60. Yang, Y.M. and J.R. Maa, *Boiling of suspension of solid particles in water.* International Journal of Heat and Mass Transfer, 1984. **27**(1): p. 145-147.

61. Yamaguchi, H. and D. James. *Boiling heat transfer from glass beads covered flat heating surface*. in *International Symposium on Transport Phenomena in Thermal Engineering*. 1993.

62. Ma, C., et al., *Experimental study of boiling heat transfer in liquid saturated porous bed with emphasis on departure from natural convection.* J. Beijing Polytech. University, 1989. **15**: p. 39-49.

63. Chuah, Y. and V. Carey, *Boiling Heat Transfer in a Shallow Fluidized Particulate Bed.* Journal of Heat Transfer, 1987. **109**(1): p. 196-203.

64. Shi, M., Y. Zhao, and Z. Liu, *Study on boiling heat transfer in liquid saturated particle bed and fluidized bed.* International journal of heat and mass transfer, 2003. **46**(24): p. 4695-4702.

65. Kim, T.Y. and S.V. Garimella, *Investigation of boiling heat transfer in water using a free-particles-based enhancement technique.* International Journal of Heat and Mass Transfer, 2014. **71**: p. 818-828.

66. Kim, T.Y., J.A. Weibel, and S.V. Garimella, *A free-particles-based technique for boiling heat transfer enhancement in a wetting liquid.* International Journal of Heat and Mass Transfer, 2014. **71**: p. 808-817.

67. Jakob, M., *Heat transfer in evaporation and condensation*. 1937: University of Illinois.

68. Chaudhri, I. and I. McDougall, *Ageing studies in nucleate pool boiling of isopropyl acetate and perchloroethylene.* International Journal of Heat and Mass Transfer, 1969. **12**(6): p. 681-688.

69. Bergles, A. and M. Chyu, *Characteristics of nucleate pool boiling from porous metallic coatings.* Journal of Heat Transfer, 1982. **104**(2): p. 279-285.

70. Ayub, Z. and A. Bergles, *Pool boiling enhancement of a modified GEWA-T surface in water.* Journal of heat transfer, 1988. **110**(1): p. 266-268.

71. Chyu, M.-C. and A. Bergles, *Horizontal-tube falling-film evaporation with structured surfaces.* Journal of Heat Transfer, 1989. **111**(2): p. 518-524.

72. Bamardouf, K. and D.A. McNeil, *Experimental and numerical investigation of two-phase pressure drop in vertical cross-flow over a horizontal tube bundle.* Applied Thermal Engineering, 2009. **29**(7): p. 1356-1365.

73. Whalley, P. and D. Butterworth. *A simple method for calculating the recirculating flow in vertical thermotyphon and bettle reboilers*. in *National heat transfer conference. 21*. 1983.

74. AHMAD, H., P. Nelson, and B. Burnside. *Boiling Water and Three Immiscible Organic Liquids over a Small Tube Bundle at Atmospheric Pressure*. in *Proc. 8th Int. heat Mass Transfer Conf., San Francisco USA*. 1986.

75. Brisbane, T., I. Grant, and P. Whalley, *A prediction method for kettle reboiler performance.* ASME paper, 1980(80-HT): p. 42.

76. Jensen, M. *A model for the recirculating flow in a kettle reboiler*. in *AIChE Symp. Ser*. 1988.

77. Palen, J. and C. Yang. *Circulation boiling model for analysis of bettle and internal reboiler performance*. in *National heat transfer conference. 21*. 1983.

78. Burnside, B., et al., *Heat transfer coefficient distributions in an experimental kettle reboiler thin slice*. Chemical Engineering Research and Design, 2001. **79**(4): p. 445-452.

79. Matsumurs, T.S.a.H., *On the condition of incipient subcooled boiling and forced convection.* Bull JSME, 1963: p. 392-398

80. McNeil, D.A., et al., *Shell-side boiling of water at sub-atmospheric pressures.* International Journal of Heat and Mass Transfer, 2015. **85**: p. 488-504.

81. Churchill, S.W. and H.H. Chu, *Correlating equations for laminar and turbulent free convection from a vertical plate.* International journal of heat and mass transfer, 1975. **18**(11): p. 1323-1329.

82. McNeil, D., K. Bamardouf, and B. Burnside, *Two-dimensional flow modelling of a thin slice kettle reboiler*. International Journal of Heat and Mass Transfer, 2011. **54**(9): p. 1907-1923.

83. ESDU, *Crossflow Pressure Loss over Banks of Plain Tubes in Square and Triangular Arrays Including Effects of Flow Direction.* Engineering Sciences Data Unit,, 1979 **79034**: p. 17.

84. ESDU, *Convective heat transfer during crossflow of fluids over plain tube banks*. 1973, The Engineering Science Data Unit.

85. Image J. http://imagej.net/Welcome.